Electrical generation of spin polarization in strained III-V semiconductors

by

Benjamin Michael Norman

A dissertation submitted in partial fulfillment
of the requirements for the degree of
Doctor of Philosophy
(Physics)
in the University of Michigan
2014

Doctoral committee:

Assistant Professor Vanessa Sih, Chair
Assistant Professor Emanuel Gull
Professor Cagliyan Kurdak
Professor Roberto D. Merlin
Professor Roseanne J. Sension

# Contents

# List of Figures

# List of Tables

# Abstract

For the advancement of spin-based electronics applications, as well as the advancement of semiconductor technology in general, an understanding of spin-related phenomena in semiconductors is of crucial importance. This work focuses on two effects, namely the manipulation of electron spins via spin-orbit coupling, and the generation of spin polarization using an all electrical means known as current-induced spin polarization. Optical measurements via Faraday/Kerr rotation are systematically conducted on strained n-type InGaAs epilayers. The anisotropic spin-orbit splitting is mapped for several samples taken from the same wafer, and is represented as a spin-orbit effective magnetic field. Measurements of electrically generated spin polarization are performed on the same sample locations. In accordance with previous predictions, spins are dynamically polarized along the direction of the spin-orbit field. However, contrary to previous predictions, the steady-state spin polarization is deviated from the spin-orbit field direction. This is characterized quantitatively in this work presenting a new model based on the anisotropic spin relaxation rate. Furthermore, the magnitude of current-induced spin polarization is not proportional to the spin-orbit splitting, but rather the two obey a negative differential relationship. That is, the crystal direction having the weakest spin-orbit splitting exhibits the strongest current-induced spin polarization. This is characterized phenomenologically by introducing a term that allows for spin-dependent scattering accompanied by a spin flip. This is the first work to establish a relationship between current-induced spin polarization and an anisotropic spin-orbit split-

ting. Our model agrees with previous measurements in the field. Furthermore, the crystal directions corresponding to a spin polarization and spin-orbit field maxima are nearly orthogonal. We point out that this phenomenon has the potential to be extremely useful for the advancement of spintronics applications, as it allows for independent spin polarization and manipulation by application of orthogonal electric fields.

# Chapter 1

# Introduction

The intrinsic angular momentum of a particle, known as its spin, and the magnetic dipole moment it represents, establishes a class of physical properties that have sparked interest since its discovery over a century ago [1]. Peculiar quantum mechanical aspects of spins include the quantization of measured spin projections [2], as well as the statistical properties obeyed by particles of a certain spin class, namely that integer spin particles obey Bose-Einstein statistics [3], while half-integer spin particles obey Fermi-Dirac statistics [4, 5]. A particularly interesting mathematical construct, and physical realization is the Pauli exclusion principle [6] obeyed by Fermions (objects with half-integer spin), requiring that a well-defined quantum mechanical state can be occupied by no more than a single particle at any given time. This property is crucial for the existence of semiconductors.

Since the discovery and advancement of semiconductor technology in the past century, spin-related phenomena in semiconductors has become a field of increasing interest. Both quantum mechanical aspects, such as quantized spin projections and interactions with photons and phonons (quanta of light and sound energy, respectively), as well as classical aspects, i.e. manipulation of spins as classical magnetic dipoles, have undergone increasingly

thorough investigation. Recently, a computational paradigm utilizing the two-state nature of an electron spin (or other spin 1/2 systems) has been proposed and is becoming of increasing interest as the lower size scale limits for classical (charge-based) computation based on heating, and eventually quantum mechanical effects, are being reached [7]. Spintronics (spin-based electronics) is a such a paradigm that utilizes the quantum and classical nature of the two-state spin system.

Crucial to the development of a spintronics platform is the coherent generation and detection of spin polarization, as well as manipulation of spins on a time scale that is fast compared to the spin relaxation time [8]. In this dissertation we explore and characterize electrical generation of spin polarization as it pertains to spin-orbit interactions in the conduction band of strained III-V semiconductors.

## 1.1 Background

The electron spin is the closest realization of a pure magnetic dipole moment (a magnetic dipole defined at a zero-dimensional point in space). Semiconductors are a natural platform for the investigation and manipulation of the electron spin. Through semiconductor structure engineering, the electron effective mass and g-factor (coupling strength between the spin and a magnetic field) can be manipulated. Electron confinement can be achieved in zero-dimensional (quantum dot), one-dimensional (quantum wire), and two-dimensional (quantum well) semiconductor structures. Transport properties, namely the electron mobility, can be manipulated through sample growth (such as by varying the doping density) and device fabrication. The interaction of electrons with photons and phonons can be tuned, primarily through the band gap and optical selection rules, by the choice of semiconductor alloy components and growth conditions. Finally, manipulation of spins can be achieved through spin-orbit interactions induced by the symmetry of the semiconductor alloy [9],

heterostructure engineering [10], and strain [11].

Early optical investigation of electron spin phenomena in semiconductors [11] was able to elucidate common carrier scattering mechanisms as well as the relevant spin relaxation mechanisms [12, 13, 14, 15]. Exploiting these relaxation mechanisms, coherence times in $n$-type GaAs were measured in excess of 100 ns [16]. Coherence times were found to be extended in (001) [17] and (111) [18] quantum wells. Coupling between the electron and nuclear spin systems was shown in Ref. [19], and proposed as a method for long term storage of computational memory [20].

With the advent of pulsed laser technology, time-resolved optical measurements of spin polarization [21] were conducted in which the manipulation of electron [16] and hole [22] spin systems was observed. This was achieved via application of external magnetic fields, through magnetic impurities [23], through mechanical strain [24], and through the use of spin-orbit interactions [25, 26]. In the latter, it was found that the spin-orbit coupling in semiconductor heterostructures could be manipulated using all-electrical means [27].

As a method of generating spin polarization, much work has been conducted on ferromagnetic spin injection [28], optical spin orientation [11], and electrical spin polarization [29]. In semiconductors exhibiting the latter effect, it was shown that a spin-Hall current could also be generated transverse to the electrical current [30, 31]. Spin selective readout was shown to be possible with giant magnetoresistance [32, 33], as well as through optical means such as polarized photoluminescence [34] and Faraday/Kerr rotation of linearly polarized light [35]. The latter effect allowed for an extremely high resolution measurement of electron spin polarization with spin coherence times greatly exceeding the carrier recombination time. Faraday rotation was also shown as a method of coupling electron spin states to optical polarization [36].

This dissertation will focus on generating spin polarization using an electrical current. The inverse of such an effect was proposed [37] in the context of a photogalvanic current in-

duced upon absorption of circularly polarized light. It was first measured by the polarization of holes in Tellurium induced by the application of a current [38]. It was proposed that such an effect should be observable in semiconductors which exhibit a momentum-dependent spin splitting [39]. This was measured in strained bulk InGaAs [29] as well as AlGaAs quantum wells [40]. Believed to be an effect due to the spin-orbit interaction, it was, however, surprisingly found in bulk GaN [41] having a weak spin-orbit splitting, and in ZnSe [42] in which the spin-orbit splitting was immeasurable. Investigation of previous measurements [29] exhibit no clear trend between current-induced spin polarization (CISP) and spin-orbit interactions, and, as such, the mechanism that gives rise CISP remains an open question.

## 1.2 Results

This dissertation will focus on the investigation of current-induced spin polarization for the purposes of direct comparison with the strength of spin-orbit interactions. Measurements were conducted on the zincblende III-V semiconductor alloy $In_xGa_{1-x}As$. Samples consisted of 500 nm epilayers of Si-doped ($n$-type) InGaAs on (001) GaAs substrates. Indium substitution on all samples in this work are either $x = 3$ or 4 %, and the doping concentration is $n = 3 \times 10^{16}$ cm$^{-3}$. Strain, and strain relaxation, due to lattice mismatch results in an anisotropic spin-orbit effective magnetic field in the (001) plane. This is measured systematically on samples patterned in a four-contact geometry allowing for arbitrary orientation of the electron momentum in the (001) plane, as well as in an orthogonal dual channel geometry allowing for orientation of the electron momentum along the supposed spin-orbit field maximum and minimum.

Using optical pump-probe measurements, the spin-orbit field is mapped as a function of the magnitude and orientation of the electron momentum ($\vec{k}$). In accordance with previous expectations, we find that the spin-orbit field is linear in momentum, indicating that strain-

induced spin-orbit interactions dominate over the $\vec{k}$-cubic Dresselhaus interaction inherent to zincblende semiconductors. However, we find that for bulk samples, the measured spin-orbit splitting magnitude does not obey the previously expected mapping, with the maximum deviated by as much as 30° from the [110] or [1$\bar{1}$0] crystal axis. We attribute this to an additional strain axis resulting from anisotropic strain relaxation for InGaAs grown beyond the critical thickness. We also observe that for several samples taken from the same wafer, the magnitude and orientation of the spin-orbit field is strongly inhomogeneous. Due to these effects we point out the necessity to directly measure the spin-orbit effective magnetic field for each momentum direction in each sample, rather than extrapolating based on measurements along [110] and [1$\bar{1}$0], as has been done in the past [26].

Steady-state and time-resolved current-induced spin polarization measurements are conducted on the same samples and along the same orientations as the spin-orbit field measurements so that a direct comparison can be made. We find, in accordance with previous measurements and expectations, that the magnitude of the current-induced spin polarization is proportional to the electron velocity and that spins are dynamically oriented along the spin-orbit effective magnetic field. Contrary to previous predictions, however, we show that the steady-state spin polarization deviates from the spin-orbit field direction based on the orientation of the electron momentum. We build a theoretical model to explain this effect using the framework of an anisotropic spin relaxation tensor with eigenvectors along the [1$\bar{1}$0], [110], and [001] crystal axes. We find the deviation of the steady-state spin polarization from the spin-orbit field to be zero for $\vec{k} \parallel [1\bar{1}0], [110]$ and maximized for $\vec{k} \parallel [100]$. The model we present shows excellent agreement with experimental observations.

Finally, we show that, contrary to previous predictions, the magnitude of the current-induced spin polarization is not proportional to the magnitude of spin-orbit splitting, but rather the two obey a negative differential relationship. That is, for momentum along the direction having the weakest spin-orbit splitting, the current-induced spin polarization is

strongest, and vice versa. Furthermore, we show from measurements of different samples taken from the same wafer, that the current-induced spin polarization does not have a simple functional form with the spin-orbit splitting, but rather that the spin-orbit field anisotropy plays an influential role. The mechanism that gives rise to this effect is investigated based on a qualitative model presented in this work.

We point out the remarkable nature of our discovery. The momentum directions corresponding to the current-induced spin polarization and spin-orbit field maxima are found to be nearly orthogonal to each other. This effect has been exploited very recently by Stepanov, *et. al.* [43] in which orthogonal pairs of gates were used to rapidly seed a net spin polarization and then manipulate it using up to a $\pi$ rotation pulse. This was achieved without the use of any external magnetic fields. We propose that by incorporating such a scheme into a sample exhibiting a spin helix state [44], one could take advantage of the weak modulation fields required to rapidly switch between large current-induced spin polarizations when momentum is nearly along the direction for which the spin-orbit field vanishes. Such a device would have a far reaching impact on the advancement of semiconductor spintronics applications.

## 1.3 Organization

This dissertation is organized as follows. Chapter 2 builds the framework for the concepts of electron spin and spin polarization. Lifted spin degeneracy, due to spatial inversion or time reversal symmetry breaking, is investigated, and the time-dependent Bloch representation of spin polarization is presented. The zincblende band structure, in particular for GaAs, is investigated at the $\Gamma$ point, and the concepts of parabolic bands and carrier effective masses are introduced. Chapter 2 concludes with an introduction of the different types of spin-orbit interactions, including their momentum dependence, and a spatial map of the anistotropic spin-orbit effective magnetic field due to these interactions.

Chapter 3 introduces the concepts of carrier scattering in semiconductors. The relevant scattering mechanisms for electrons in the conduction band are investigated, and numerical evaluations of the energy dependent scattering time, as well as the energy and momentum relaxation times, are presented. Low field transport is discussed with an introduction of the Boltzmann transport equation and numerical evaluation of the carrier mobility, which shows excellent agreement with the measured values. From this we determine ionized impurity and polar optical phonon scattering are the dominant scattering mechanisms for low and high temperature, respectively, in our region of interest. Finally the relevant spin relaxation mechanisms are introduced. We investigate the anisotropic nature of the D'yakonov-Perel spin relaxation rate, which we will ultimately take to be the dominant mechanism.

Chapter 4 introduces the experimental paradigm used throughout the work presented in this dissertation. Optical spin generation is presented, with a discussion of the relevant equipment, and an introduction to the optical selection rules for zincblende semiconductors. We then present the optical spin polarization detection routine, namely Faraday and Kerr rotation. Practical aspects involving the measurement of Faraday/Kerr rotation are discussed in reference to the balanced photodiode bridge and digital signal processing techniques. Time- and spatially resolved measurement techniques are introduced, with a presentation of the optical setup and relevant measurements of material properties. Chapter 4 is concluded with a discussion of steady-state spin polarization measurements.

Chapter 5 is devoted to presenting our measurements of the spin-orbit effective magnetic fields. The relevant sample design and experimental geometry is presented. Practical aspects of the experimental setup are introduced, including the spatial overlap of the probe with the pump-induced spin packet. The components of the spin-orbit effective magnetic field are independently measured, from which the magnitude and orientation of the spin-orbit field are deduced. Finally the anisotropic spin-orbit effective magnetic field is spatially mapped as a function of electron momentum. This set of measurements is conducted for several samples

from the same wafer, at which point we make note of the inhomogeneity of the spin-orbit splitting.

Chapter 6 is devoted to presenting the measurements of current-induced spin polarization for direct comparison with the spin-orbit field measurements presented in Ch. 5. The experimental geometry as it pertains to the sample design and spin polarization is presented. We introduce a model that allows for anisotropic spin relaxation in the context of the Bloch equation. The time-dependent and steady-state behavior, with and without precession, is investigated numerically based on the anisotropic spin-relaxation rate. The experimental results are then presented. The practical aspects, including dependence on laser power, wavelength, and electric field modulation frequency, are investigated. Finally the current-induced spin polarization is mapped as a function of the electron momentum and compared to the measurements of the spin-orbit fields.

The observed negative differential relationship between current-induced spin polarization and the spin-orbit splitting is discussed as it pertains to spin generation and manipulation devices and ultimately as its usefulness as a tool for spintronics applications.

# Chapter 2

# Spin Splitting in Semiconductors

## 2.1 Introduction

This chapter will be devoted to providing the framework for understanding spin-related phenomena in semiconductors. It will be organized as follows. Sec. 2.2 will introduce the concept of spin, defining what it means for spins to be polarized. This will be approached in the presence of a constant and uniform magnetic field in terms of the Zeeman interaction, and in the presence of an electron momentum ($\vec{k}$) dependent magnetic field in terms of spin-orbit interactions. The concept of symmetry breaking will be discussed as it pertains to Kramers degeneracy, and the Bloch representation of spin polarization will be introduced. In Sec. 2.3, I will introduce the zincblende crystal structure, in particular gallium arsenide (GaAs). I will build the state wave functions for conduction and valence band electrons at the $\Gamma$ ($\vec{k} = 0$) point, and expand around this point to show the parabolic nature of the bands for low $\vec{k}$. At this point, the concepts of electron and hole effective masses as well as the nearly free electron will be introduced. Finally, in Sec. 2.4, I will discuss spin-orbit splitting in the conduction band as it pertains directly to the measurements and analysis in Chs. 5

and 6. The spin-orbit effective magnetic field will be introduced and mapped as a function of electron momentum $\vec{k}$ at which point the spin-orbit field anisotropy will be discussed.

## 2.2 Spin polarization

The term "spin" is used to describe the intrinsic angular momentum of a particle and the magnetic moment it represents. The nomenclature is due to the original thought that the magnetic moment observed was the result of a spinning charged particle [45]. Dirac showed soon after, with the Dirac equation providing a relativistic treatment of the quantum mechanical electron, that the intrinsic angular momentum and magnetic moment were necessary properties of the electron [46]. The Stern-Gerlach experiment [2] observed that silver atoms passing through a magnetic field gradient would experience deflections based on the projection of the spin of the atom along this gradient, and that the deflection took on two discrete values, rather than a continuum. This was important as it indicated the quantized nature of particle spin projections.

Defining the spin quantum number as $s$, it was shown that the projection of the spin along a particular axis of quantization, once measured, could only take on discrete values given by $m_s = -s, -s+1, ..., s-1, s$, where integer separation is required. The two-state spin system is extremely common in modern physics experiments [47] and consists of manipulations of spin 1/2 particles. An electron is such a particle with $s = 1/2$. It is typical to describe "spin up" as the spin species which minimizes the interaction Hamiltonian and "spin down" as that which maximizes it. With ensembles of spins, the term spin polarization is used to describe the net alignment of carrier spins along such an axis of quantization and is usually described by $S = (n_\uparrow - n_\downarrow)/(n_\uparrow + n_\downarrow)$, with $n_{\uparrow(\downarrow)}$ the density of up (down) spins. In this context the spin polarization falls in the range $-1 \leq S \leq 1$.

### 2.2.1 Zeeman interaction

To see how the effect of an external magnetic field can give rise to a spin-splitting, consider the most general, free space Hamiltonian in the presence of a magnetic field $\vec{B}$ [48]:

$$H = \frac{\vec{P}^2}{2m} = \frac{1}{2m}\left(\vec{p} + e\vec{A}\right)^2 \tag{2.1}$$

where $\vec{P}$ is the canonical (conserved) momentum, $\vec{p}$ is the quantum mechanical momentum operator defined by $\vec{p} = -i\hbar\nabla$, $e$ and $m$ are the magnitudes of the electron charge and mass respectively, and $\vec{A}$ is the vector potential defined by $\vec{B} = \nabla \times \vec{A}$. In this case we explicitly take the electric (scalar) potential to be zero (i.e. in the absence of sources). To understand the equilibrium behavior we will begin with the time-independent Schrödinger equation [49] $H\psi = \varepsilon\psi$, which gives us

$$-\frac{\hbar^2}{2m}\nabla^2\psi - \frac{ie\hbar}{2m}\left[\nabla\cdot\left(\vec{A}\psi\right) + \vec{A}\cdot\nabla\psi\right] + \frac{e^2\vec{A}^2}{2m}\psi = \varepsilon\psi, \tag{2.2}$$

where $\varepsilon$ is the energy eigenvalue corresponding to the Hamiltonian $H$. In regards to the vector potential $\vec{A}$, the physical quantity is the magnetic field $\vec{B}$. We are free to choose $\vec{A}$ up to gauge transformation, as long as the proper magnetic field $\vec{B} = \nabla \times \vec{A}$ is recovered. We will begin by using the Coulomb gauge given by $\nabla\cdot\vec{A} = 0$. Then the first term in square brackets becomes $\nabla\cdot(\vec{A}\psi) = (\nabla\cdot\vec{A})\psi + \vec{A}\cdot\nabla\psi = \vec{A}\cdot\nabla\psi$. If we further assume that the magnetic field is uniform in space, we can define the vector potential as

$$\vec{A} = -\frac{1}{2}\left(\vec{r}\times\vec{B}\right) \tag{2.3}$$

with $\vec{r}$ the usual spatial vector. We can see this satisfies both our Coulomb gauge $\nabla\cdot\vec{A} = 0$ and the definition of the magnetic field $\vec{B} = \nabla\times\vec{A}$. Eq. 2.2 becomes

$$-\frac{\hbar^2}{2m}\nabla^2\psi + \frac{ie\hbar}{2m}\left(\vec{r}\times\vec{B}\right)\cdot\nabla\psi + \frac{e^2}{8m}\left(\vec{r}\times\vec{B}\right)^2\psi = \varepsilon\psi. \tag{2.4}$$

The first term on the left is the normal kinetic term for a free electron, while the last term on the left is generally neglected except in the case of extremely large magnetic fields [48]. Focusing on the middle term, we can use the familiar vector relation $\vec{A}\cdot\vec{B}\times\vec{C} = \vec{A}\times\vec{B}\cdot\vec{C}$ to show that $(\vec{r}\times\vec{B})\cdot\nabla\psi = -\vec{B}\cdot(\vec{r}\times\nabla\psi)$. Remembering that $\nabla = i\vec{p}/\hbar$, and defining the angular momentum operator $\vec{L}$ using the relation $\vec{L} = \vec{r}\times\vec{p}$, Eq. 2.4 becomes

$$\left(-\frac{\hbar^2}{2m}\nabla^2 + \frac{e}{2m}\vec{L}\cdot\vec{B}\right)\psi = \varepsilon\psi. \tag{2.5}$$

The Zeeman Hamiltonian is [50]

$$H = H_0 + H_Z = \frac{p^2}{2m} - \vec{\mu}\cdot\vec{B} \tag{2.6}$$

with $H_0$ the free electron Hamiltonian, $H_Z$ the Zeeman contribution, $\vec{\mu}$ the angular momentum vector defined by $\vec{\mu} = -e\vec{L}/(2m) = -\mu_B\vec{L}/\hbar$, and $\mu_B$ the Bohr magneton. The negative sign in the definition of $\vec{\mu}$ arises from the fact that the "current loop" that arises from the angular momentum of an electron has the opposite sign due to its negative charge. For an atomic system, $\vec{\mu}$ will have both orbital angular momentum and spin components. In this case we must include a spin term and the magnetic moment becomes $\vec{\mu} = -\mu_B(\vec{L} + g\vec{S})/\hbar$, where $g$ is the electron g-factor and describes the strength with which the electron spin interacts with magnetic fields. The fact that it is nearly two, rather than simply one as is the case for the orbital angular momentum, requires a relativistic treatment and the use of the Dirac equation [46]. The Hamiltonian becomes

$$H = \frac{p^2}{2m} + \frac{\mu_B}{\hbar}\left(\vec{L} + g\vec{S}\right)\cdot\vec{B} \tag{2.7}$$

For the moment, the interaction between the spin and orbital angular momenta will be ignored.

The total magnetic moment will in general be defined by the particular quantum numbers describing the orbital ($l$) and spin ($s$) states of the system. For these quantum numbers we will take the prescription that capital letters ($L$, $S$, $J$) correspond to the observable quantity of interest, in this case the angular momentum, having units of $\hbar$, and the corresponding lowercase letters ($l$, $s$, $j$) their respective unitless quantum numbers, such that $S = \hbar s$ and so on.

The total angular momentum is defined by $J = L \pm S$ with projections along the axis of quantization $m_j = -j, -j+1, ..., j-1, j$. In the simplest case of a discrete two-state system, we take $l = 0$ (s-like orbital) and $s = \sigma/2$ for which $m_j = m_s = \pm 1/2$. Here $\sigma$ are the two-state Pauli matrices given by

$$\sigma_x = \begin{pmatrix} 0 & 1 \\ 1 & 0 \end{pmatrix} \qquad \sigma_y = \begin{pmatrix} 0 & -i \\ i & 0 \end{pmatrix} \qquad \sigma_z = \begin{pmatrix} 1 & 0 \\ 0 & -1 \end{pmatrix} \tag{2.8}$$

As the magnetic field is the only direction of interest, we will choose its direction as the axis of quantization ($\vec{B} = B\hat{z}$). The Schrödinger eigenvalue equation for the Zeeman component of the Hamiltonian becomes

$$H_Z \left|\uparrow (\downarrow)\right\rangle = \frac{g\mu_B B}{2}\sigma_z \left|\uparrow (\downarrow)\right\rangle = \varepsilon_{\uparrow(\downarrow)} \left|\uparrow (\downarrow)\right\rangle \tag{2.9}$$

The energy eigenvalues are $\varepsilon_{\uparrow(\downarrow)} = \mp g\mu_B B/2$. The Zeeman splitting for a two-state electron spin system is then

$$\Delta = \varepsilon_\downarrow - \varepsilon_\uparrow = g\mu_B B. \tag{2.10}$$

The spin polarization that results from this spin splitting will depend on the distribution

function of the electron. In equilibrium this will be described by the Fermi-Dirac distribution function. In the case of a non-degenerate semiconductor (i.e. low doping concentrations and high temperatures), this can usually be approximated by a Maxwell-Boltzmann distribution function [51]. In non-equilibrium cases, the distribution function must be calculated using other means, such as the Boltzmann transport equation. In general, to determine the average value of some observable quantity $a$ for a system described by distribution function $f(\varepsilon)$, we use the formula

$$\langle a \rangle = \frac{\sum_s a_s D\left(\varepsilon_s\right) f\left(\varepsilon_s\right)}{\sum_s D\left(\varepsilon_s\right) f\left(\varepsilon_s\right)} \tag{2.11}$$

where $s$ defines the state of the system, with $a_s$, $\varepsilon_s$, and $D(\varepsilon_s)$ the observable, energy eigenvalue, and corresponding density of states, respectively, for that particular state. Assuming a constant density of states we can define the fractional occupation of a given state $i$ as

$$n_i = \frac{f\left(\varepsilon_i\right)}{\sum_s f\left(\varepsilon_s\right)}. \tag{2.12}$$

In a two-state spin system we are interested in the polarization, defined by $P = (n_\uparrow - n_\downarrow)/(n_\uparrow + n_\downarrow)$. Using Eq. 2.12, the polarization is given in terms of the distribution function and spin splitting by

$$P = \frac{f\left(-\Delta/2\right) - f\left(\Delta/2\right)}{f\left(-\Delta/2\right) + f\left(\Delta/2\right)} \tag{2.13}$$

### 2.2.2 Spin-orbit interaction

The spin-orbit interaction stems from a concept of special relativity, that an electron with velocity perpendicular to an electric field in the lab frame observes an additional magnetic field in the rest frame of the electron. Using a *prime* notation to denote the vector quantities in the rest frame of the electron, and the lack of a *prime* to denote the lab frame, we have

the following set of relations for the electric ($\vec{E}$) and magnetic ($\vec{B}$) fields.

$$\vec{E}' = \gamma\left(\vec{E} + \vec{v}\times\vec{B}\right) - \frac{\gamma^2}{c^2\left(1+\gamma\right)}\vec{v}\left(\vec{v}\cdot\vec{E}\right) \tag{2.14}$$

$$\vec{B}' = \gamma\left(\vec{B} - \frac{1}{c^2}\vec{v}\times\vec{E}\right) - \frac{\gamma^2}{c^2\left(1+\gamma\right)}\vec{v}\left(\vec{v}\cdot\vec{B}\right) \tag{2.15}$$

where $\gamma = \left[1-(v/c)^2\right]^{-1/2}$, $v$ is the electron velocity in the lab frame, and $c$ is the speed of light. We will begin by making a few assumptions. The first is that the electron velocity is significantly less than the speed of light. For the purposes of this dissertation, $v/c \sim 3\times10^{-6}$. In this case, we ignore terms of order $(v/c)^2$, in which case $\gamma \sim 1$ and the last terms on the right are ignored. Furthermore, for now, we will take there to be no magnetic field in the lab frame, that is, $\vec{B} = 0$. The fields in the electron rest frame become

$$\vec{E}' = \vec{E} \tag{2.16}$$

$$\vec{B}' = -\frac{1}{c^2}\vec{v}\times\vec{E} = \frac{1}{mc^2}\vec{p}\times\nabla V \tag{2.17}$$

where in the last step, I used the electron momentum $\vec{p} = m\vec{v}$ and the definition of the electric potential $\vec{E} = -\nabla V$. Eq. 2.17 is the spin-orbit effective magnetic field seen from the rest frame of the electron. We use the term "orbit" because such a spin-orbit interaction is typical of the fine structure splitting in atoms, for which an electron is taken to orbit around a nucleus. For example, in Hydrogen, using a potential gradient of

$$\vec{E} = \frac{e}{4\pi\epsilon_0}\frac{\vec{r}}{r^3} \tag{2.18}$$

the spin-orbit magnetic field is

$$\vec{B}_{SO,Hydrogen} = \frac{\alpha\hbar}{emc}\frac{\vec{L}}{r^3} \tag{2.19}$$

with the fine structure constant defined by $\alpha = e^2/(4\pi\epsilon_0\hbar c)$ and the orbital angular momentum $\vec{L} = \vec{r} \times \vec{p}$. Analogous to the Zeeman splitting, we can define a spin-orbit Hamiltonian as $H_{SO} = -\vec{\mu} \cdot \vec{B}_{SO} = (g\mu_B/\hbar)\vec{S} \cdot \vec{B}_{SO}$. In this case, we explicitly only include the spin angular momentum in the definition of $\mu$. This is because the spin-orbit magnetic field is defined in the rest frame of the electron, in which there is no orbital angular momentum. The spin-orbit Hamiltonian is

$$H_{SO,Hydrogen} = \frac{1}{2}\frac{g\hbar\alpha}{2m^2c}\frac{\vec{S} \cdot \vec{L}}{r^3}. \tag{2.20}$$

The factor of $1/2$ arises due to relativistic effects and taking a proper Lorentz transform to the non-rotating electron rest frame. This introduces an additional factor of $g - 1$ and is known as Thomas precession [52].

For semiconductors, there is no "orbital" angular momentum in the strictly spherically symmetric sense, as with hydrogen, yet using Eq. 2.17 we see the analogous definition of linear momentum in a transverse electric potential gradient. The general form of the spin-orbit Hamiltonian in semiconductors is

$$H_{SO,Semiconductor} = \frac{\hbar}{4m^{*2}c^2}\left(\nabla V \times \vec{p}\right) \cdot \vec{\sigma} \tag{2.21}$$

where $m^*$ is the effective mass (Sec. 2.3.2) and $\vec{\sigma} = \vec{S}/(2\hbar)$ are the Pauli matrices.

### 2.2.3 Kramers degeneracy

In the last two sections, we stumbled upon the breaking of Kramer's degeneracy. Here it will be explained in a little more detail. For an in-depth discussion consult Ref. [53]. In general we

can define the time reversal operator $\Theta$ acting on a particular quantum mechanical operator $A$ by the following

$$\Theta A \Theta^{-1} = \pm A \tag{2.22}$$

where the $+A(-A)$ corresponds to an operator that is even (odd) under time reversal symmetry. It is, of course, easy to envision which operators are even or odd. For example, the position operator is even under time reversal, while momentum and angular momentum are odd. The time reversal operator is antiunitary, with $\{\Theta, i\} = \Theta i + i\Theta = 0$. For an arbitrary electron state defined by angular momentum quantum numbers $|j, m_j\rangle$, the time reversal operator acting on the state gives [53]

$$\Theta \, |j, m_j \rangle = i^{2m_j} \, |j, -m_j \rangle. \tag{2.23}$$

We can see the time reversal operator changes the sign of the angular momentum of the system. Using the above equation and the antiunitary property of the time reversal operator, we can build the following set of operations for systems having integer and half integer spin:

$$\Theta^2 \, |j, m_j\rangle = |j, m_j\rangle \qquad \text{integer j} \tag{2.24}$$

$$\Theta^2 \, |j, m_j\rangle = - \, |j, m_j\rangle \qquad \text{half integer j.} \tag{2.25}$$

For a Hamiltonian that is even under time reversal (i.e. the Hamiltonian commutes with the time reversal operator) it can be shown that if a state $|n\rangle$ is an eigenstate of the Hamiltonian such that $H \, |n\rangle = \varepsilon_n \, |n\rangle$ then $\Theta \, |n\rangle$ is also an eigenstate of $H$, where $|n\rangle$ and $\Theta \, |n\rangle$ refer to the same state if and only if the following is true:

$$\Theta^2 \, |n\rangle = |n\rangle \tag{2.26}$$

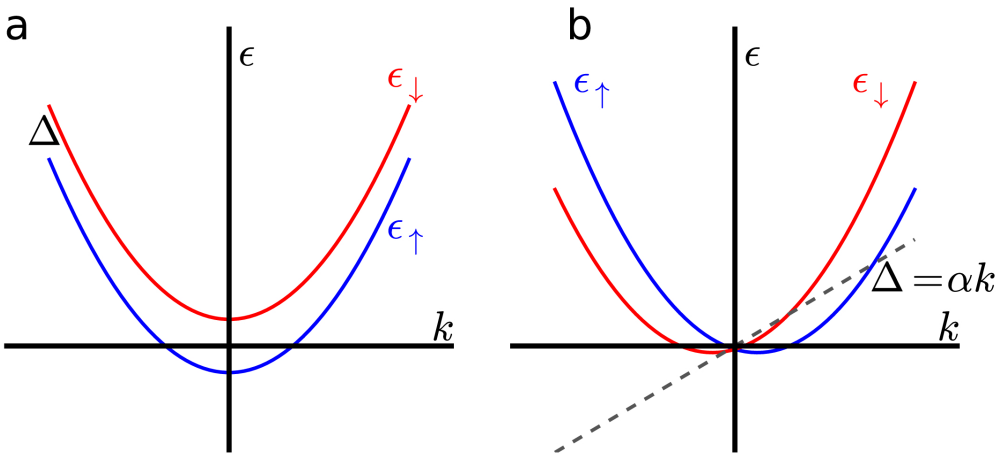


**Figure 2.1: Spin splitting:** Energy splitting for constant (a) and $k$-linear (b) spin-splitting terms. Time reversal symmetry is broken in (a) while spatial inversion symmetry is broken in (b).

But from Eqs. 2.24 and 2.25 this can only be true if $j$ is an integer. This result is the definition of Kramer's degeneracy [54, 55]; for half integer spin systems that have a Hamiltonian that is even under time reversal, there are two distinct and degenerate states $|n\rangle$ and $\Theta|n\rangle$. If we include a spatial inversion symmetry argument as well, we have the following pair of equations defining the degeneracy of spin states

$$\begin{aligned} \varepsilon_\uparrow(\vec{p}) &= \varepsilon_\uparrow(-\vec{p}) \qquad \text{spatial inversion symmetry} \\ \varepsilon_\uparrow(-\vec{p}) &= \varepsilon_\downarrow(\vec{p}) \qquad \text{time reversal symmetry} \end{aligned} \tag{2.27}$$

We can see that with combined time reversal and spatial inversion symmetry, the spin states of a spin 1/2 system are two-fold degenerate (i.e. $\varepsilon_\uparrow(\vec{p}) = \varepsilon_\downarrow(\vec{p})$). However, by breaking either symmetry the spin degeneracy is lifted. It is common to view the inclusion of an external magnetic field (i.e. Zeeman splitting) as breaking of time reversal symmetry. However, the spin degeneracy can be lifted by breaking spatial inversion symmetry as well. This is common in semiconductor systems lacking a spatial inversion centre, such as zincblende structures. In this case, a gradient in the periodic lattice potential acts as an effective magnetic field, as described by Eq. 2.21, and the degeneracy is lifted.

Fig. 2.1 displays the energy dispersion for a parabolic Hamiltonian lacking spin degeneracy. The parabolic term is simply the energy for a free electron, given by $\varepsilon_0 = \hbar^2 k^2/(2m^*)$, where here we use $\vec{k}$ to denote the electron momentum, defined by $\vec{p} = \hbar\vec{k}$. Panel (a) shows a spin-splitting that is a constant with respect to $k$, such as with the application of an external magnetic field. We see that spatial inversion symmetry is maintained, $\varepsilon_\uparrow(k) = \varepsilon_\uparrow(-k)$, but time reversal symmetry is broken, $\varepsilon_\uparrow(k) \neq \varepsilon_\downarrow(-k)$.

For semiconductor systems, it is common to have a spin-orbit splitting that is linear in the electron momentum. This is depicted in Fig. 2.1(b). We notice that the sum of the two energy states recovers the free electron energy, while the difference gives the spin-orbit splitting. This corresponds to a splitting in $k$-space between the up and down spin bands. Notice that time reversal symmetry is maintained, $\varepsilon_\uparrow(k) = \varepsilon_\downarrow(-k)$, while spatial inversion symmetry is broken, $\varepsilon_\uparrow(k) \neq \varepsilon_\uparrow(-k)$. How spatial inversion asymmetry gives rise to a spin-orbit splitting for specific cases will be discussed in Sec. 2.4. It is worth pointing out that it is also common to have spin-orbit splitting that is cubic in momentum, in which case the energy dispersion for each spin can no longer be parabolic.

### 2.2.4 The Bloch sphere

We derived in Sec. 2.2.1 the form of the Hamiltonian in the presence of an external magnetic field as

$$H = H_0 + H_Z = \frac{p^2}{2m} + \frac{g\mu_B}{2}\vec{\sigma}\cdot\vec{B} \tag{2.28}$$

where here we have restricted ourselves to the two-state spin system (i.e. in the absence of orbital angular momentum and the fine structure). According to the Heisenberg picture of quantum mechanics, we can cast the time dependence of any operator $A$ by the following prescription:

$$\frac{\partial A}{\partial t} = -\frac{i}{\hbar}[A, H] \tag{2.29}$$

where $[,]$ denotes the commutator given by $[A, H] = AH - HA$. In general, we are interested in the time dependence of the spin system given by

$$\frac{\partial s_i}{\partial t} = \frac{1}{2}\frac{\partial \sigma_i}{\partial t} = \frac{-i}{2\hbar}[\sigma_i, H] \tag{2.30}$$

We note that the Pauli matrices commute with functions of the momentum operator ($[\sigma_i, f(p)] = 0$), and recall the commutation relations for the Pauli matrices given by $[\sigma_i, \sigma_j] = 2i\sigma_k\epsilon_{ijk}$. In this case, the commutator becomes

$$[\sigma_i, H] = \sum_j \frac{g\mu_B B_j}{2}[\sigma_i, \sigma_j] = i\sum_{j,k} g\mu_B B_j \sigma_k \epsilon_{ijk}. \tag{2.31}$$

with $\epsilon_{ijk} = +(-)1$ for even (odd) permutations of indices and 0 for any repeated indices. Component-wise, Eq. 2.31 becomes

$$[\sigma_x, H] = ig\mu_B\left(B_y\sigma_z - B_z\sigma_y\right) \tag{2.32}$$

with the others given by an even permutation of indices. We recognize Eq. 2.32 as the general form for the cross product. With the definition of the Larmor precession frequency given by $\Omega_i = g\mu_B B_i/\hbar$, the time dependence of the spin operator is described by

$$\frac{\partial \vec{S}}{\partial t} = \vec{\Omega} \times \vec{S}. \tag{2.33}$$

Using the vectorial nature of spin, it is common to describe the spin polarization of the electron system, be it a single spin or an ensemble, by using the Bloch sphere depicted in Fig 2.2. In this case, the axis of energy quantization is taken along the $\hat{z}$ axis with

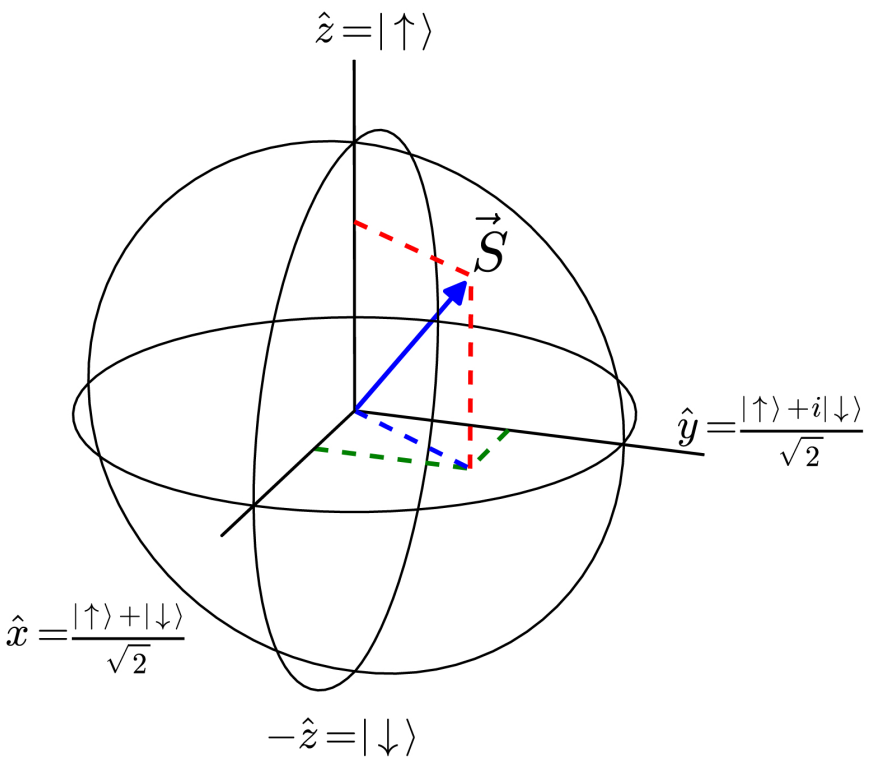


**Figure 2.2: Bloch sphere representation of spin polarization:** Spin polarization $\vec{S}$ is depicted on the Bloch sphere. Energy is quantized along the $\hat{z}$ axis, with the splitting between up and down spins described by Eq. 2.10. Spin alignment in the $xy$ plane is constructed from a linear superposition of up and down spin states.

eigenvalues of $\pm 1$ for eigenstates $|\uparrow\rangle$ and $|\downarrow\rangle$ respectively. The phase of the spin is described by the orientation of the $\vec{S}$ in the $xy$ plane. The unit vectors $\hat{x}$ and $\hat{y}$ are linear superpositions of $|\uparrow\rangle$ and $|\downarrow\rangle$ and are unit eigenvectors of the $\sigma_x$ and $\sigma_y$ Pauli matrices respectively.

Eq. 2.33 describes the time dependence of a single electron spin in the presence of a magnetic field in which the projection of the spin along the magnetic field is constant. In other words, energy is conserved. If the electron-magnetic field system were truly isolated and energy was never allowed to leave, this equation would be sufficient. In general, however, scattering processes will occur that allow the electron to lose or gain energy and therefore a diagonal component is necessary. This is most easily understood in the context of ensembles of electron spins. We consider the net spin polarization along the axis of quantization given

by $S_z = n_\uparrow - n_\downarrow$, with $n_{\uparrow(\downarrow)}$ the fractional occupation of up (down) spins. The time dependence of the up spins is described by [56]

$$\frac{\partial n_\uparrow}{\partial t} = -\frac{n_\uparrow}{2T_1} + \frac{n_\downarrow}{2T_1} \tag{2.34}$$

where $1/2T_1$ is the transition rate between up and down spins, assumed to be spin-independent. To understand this form, we consider the first term on the right as the transition of up to down spins weighted by the fractional occupation of up spins, $n_\uparrow$. The second term on the right conversely describes the transition of down to up spins with the appropriate weighting factor $n_\downarrow$. Here it is assumed the equilibrium state is such that $n_\uparrow = n_\downarrow$. Conservation of spins in this picture requires the following.

$$\frac{\partial n_\downarrow}{\partial t} = -\frac{\partial n_\uparrow}{\partial t}. \tag{2.35}$$

Finally, we phenomenologically allow the equilibrium spin polarization to reach a value $S_{eq}$ which is, in general, not zero in the presence of a magnetic field. In this case, the time dependent spin polarization along the quantization (magnetic field) axis is

$$\frac{\partial S_z}{\partial t} = -\frac{1}{T_1}\left(S_z - S_{eq}\right). \tag{2.36}$$

Here, we have taken explicitly that $\Omega_x = \Omega_y = 0$. The solution to this equation is an exponential decay, where $T_1$ is defined as the longitudinal spin relaxation time and defines the characteristic time scale over which the energy of the system relaxes to the equilibrium value.

In addition to the longitudinal relaxation time, there is a characteristic time scale over which an electron spin will lose its phase, or coherence information. To understand this concept, consider a single spin initially polarized in the $xy$ plane, such that $S_z = 0$ in the presence of an external magnetic field $\vec{B} = B\hat{z}$. In this case, the "in-plane" (i.e. perpendicular to $\hat{z}$)

components of the spin are given by

$$S_x(t) = S_{x0}\cos(\Omega t) - S_{y0}\sin(\Omega t) \tag{2.37}$$

$$S_y(t) = S_{x0}\sin(\Omega t) + S_{y0}\cos(\Omega t) \tag{2.38}$$

We can apply a unitary rotation $R$ on the basis in the $xy$ plane, which is equivalent to a rotation of the spin vector in the opposite direction. Denoting the rotated basis with a *prime* notation, and choosing the basis to rotate at the Larmor precession frequency, we achieve the following definition of the spin polarization:

$$\begin{pmatrix} S_{x'}(t) \\ S_{y'}(t) \\ S_{z'}(t) \end{pmatrix} = R^T \begin{pmatrix} S_x(t) \\ Sy(t) \\ 0 \end{pmatrix} = \begin{pmatrix} \cos(\Omega t) & \sin(\Omega t) & 0 \\ -\sin(\Omega t) & \cos(\Omega t) & 0 \\ 0 & 0 & 1 \end{pmatrix} \begin{pmatrix} S_{x0}\cos(\Omega t) - S_{y0}\sin(\Omega t) \\ S_{x0}\sin(\Omega t) + S_{y0}\cos(\Omega t) \\ 0 \end{pmatrix} \tag{2.39}$$

The solution in the rotating frame is

$$\begin{pmatrix} S_{x'}(t) \\ S_{y'}(t) \\ S_{z'}(t) \end{pmatrix} = \begin{pmatrix} S_{x0} \\ S_{y0} \\ 0 \end{pmatrix}. \tag{2.40}$$

This isn't a particularly surprising result. For a spin initially polarized in the $xy$ plane, in a basis rotating at the Larmor precession frequency, the spin appears motionless. In the same sense that the longitudinal spin relaxation time $T_1$ describes the characteristic time over which the spin system will relax to its equilibrium state, we now define a transverse spin coherence time $T_2$ that describes the rate at which a spin will lose its particular phase information, that is, the rate at which a spin will no longer be pointing along its original

direction in the rotating frame. In this system, we make the simplifying assumption that $T_2$ is the same for the $\hat{x}$ and $\hat{y}$ directions, in which case the time dependence of the in-plane spin polarization is given by

$$\frac{\partial S_{x'(y')}}{\partial t} = -\frac{1}{T_2} S_{x'(y')}. \tag{2.41}$$

An added complication in the transverse coherence time is the inclusion of inhomogeneity in the spin system. For example, for an ensemble of spins, there is, in general, an inhomogeneity in the electron g-factor centered around the average value. While each spin may appear stationary in its own rotating frame, because of the inhomogeneous g-factor in the Larmor precession frequency, each spin will have a different rotating frame, and the measured transverse coherence time will be reduced. This time scale is known as the inhomogeneous transverse spin coherence time, or the inhomogeneous spin dephasing time $T_2^*$. The inhomogeneous transverse coherence time is necessarily less than the transverse coherence time (i.e. $T_2^* < T_2$) and is, in general, the quantity that is experimentally measured. To determine the transverse spin coherence time $T_2$, one would usually employ a method to rephase an ensemble of spins, such as a Hahn echo [57].

The Bloch equation, rotated back to the stationary basis, is given in matrix form by

$$\frac{\partial}{\partial t}\begin{pmatrix} S_x \\ S_y \\ S_z \end{pmatrix} = \begin{pmatrix} -\frac{1}{T_2^*} & -\Omega & 0 \\ \Omega & -\frac{1}{T_2^*} & 0 \\ 0 & 0 & -\frac{1}{T_1} \end{pmatrix} \begin{pmatrix} S_x \\ S_y \\ S_z \end{pmatrix} + \begin{pmatrix} 0 \\ 0 \\ \frac{1}{T_1} S_{eq} \end{pmatrix} \tag{2.42}$$

where again we explicitly take $\Omega_x = \Omega_y = 0$. This is in a slightly limiting form, though it can be generalized to the following vector form

$$\frac{\partial \vec{S}}{\partial t} = -\overleftrightarrow{\Gamma} \cdot \vec{S} + \vec{\Omega} \times \vec{S} + \Gamma_{eff} \vec{S}_{eq} \tag{2.43}$$

where now we allow $\vec{\Omega}$ to have components along all axes. This is particularly useful for situations in which it is no longer appropriate to take the axis of quantization along the direction of an external magnetic field, as we will see in Ch. 6. Furthermore, it will be shown that the inhomogeneous transverse spin coherence time $T_2^*$ will not necessarily be isotropic, in which case we define $\overleftrightarrow{\Gamma}$ as the spin relaxation rate tensor (behaving like $\Gamma \sim T^{-1}$) that, in general, has three orthogonal eigenvectors with unique eigenvalues. We finally describe the equilibrium spin polarization as a vector $\vec{S}_{eq}$, with effective relaxation rate $\Gamma_{eff}$, which we point out need not be along an eigenvector of the spin relaxation rate. Eq. 2.43 will be the form of the Bloch equation used throughout this work.

## 2.3 GaAs band structure

The semiconductor on which measurements are taken is InGaAs, having the same zincblende structure as GaAs in which the gallium and arsenic structures form two interpenetrating face-centered cubic lattices separated by $a\sqrt{3}/4$ along the [111] crystal axis, where $a$ is the lattice parameter. It has the same structure as the diamond lattice (e.g. silicon), forming tetrahedral bonds, except with alternating gallium and arsenic atoms, as shown in Fig. 2.3(a). It is a member of the $T_d$ point group and is a common crystal structure for III-V semiconductors.

Fig. 2.3(b) depicts the first Brillouin zone in reciprocal ($k$) space [58]. The conduction band exhibits local minima at the center of the Bruiloiun zone ($\Gamma$ point) for which $\vec{k} = 0$, and along its edges at points of high symmetry ($L$ and $X$ points). There are other local band minima, but these are sufficient for our purposes. For direct band gap semiconductors, such as GaAs, the minimum of the conduction band is located at the $\Gamma$ point for which the band is spherically symmetric. That is, the energy is the same for $\vec{k}$ along $\hat{x}$, $\hat{y}$, and $\hat{z}$ very near $k = 0$. For the indirect band gap semiconductors silicon and germanium, the conduction band minima are located at the $X$ and $L$ points respectively and have ellipsoidal constant

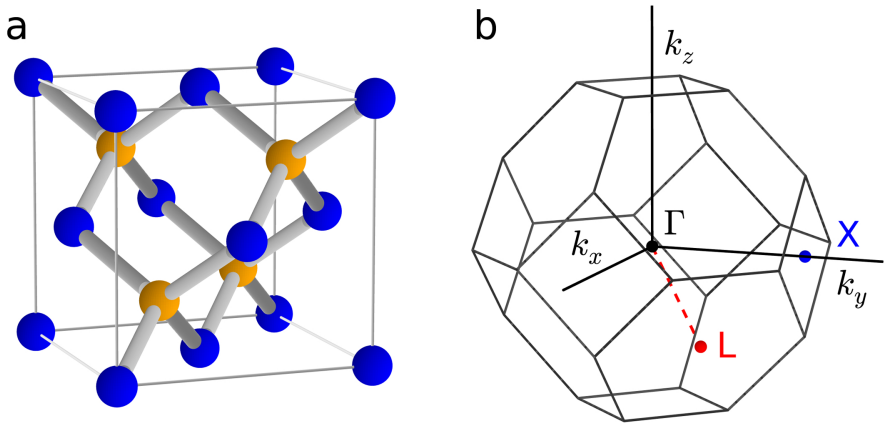


**Figure 2.3: Zincblende structure and first Brilloiun zone:** (a) Zincblende structure for GaAs. Gallium and arsenic (maize and blue spheres respectively) alternate in a tetrahedral bond. (b) First Bruilloiun zone for tetrahedral crystals. Γ valley is spherically symmetric and centered at $k = 0$. Eight identical $L$ valleys (red) and six identical $X$ valleys (blue) are centered at the edge of the Bruilloiun zone and are, in general, ellipsoidal.

energy surfaces. An advantage to zincblende semiconductors over silicon and germanium is that they have a direct band gap at the Γ point and are therefore optically accessible without the need of phonon assisted transitions, as will be discussed in Sec. 4.1.3.

### 2.3.1 The Γ point

The valence electron configurations for gallium and arsenic are $4s^2 4p$ and $4s^2 4p^3$. For the isolated atoms, the $s$ orbitals have lower energy than the $p$ orbitals. With tetrahedral bonding, however, we observe a hybridized $4s4p^3$ shell for each [59], in which case each the $s$ and $p$ orbitals are split into bonding and antibonding states. The bonding states typically have lower energy than the antibonding, and we see the bonding $p$ orbital pushed down to a lower energy than the raised antibonding $s$ orbital. The result is that the valence electrons occupy the bonding $s$ and $p$ orbitals in a polar bond, while the antibonding $s$ orbital is held above the bonding $p$ orbital by an energy splitting defined as the band gap ($E_g$). The representation of the $s$ and $p$ orbitals at the Γ point are given by the $\Gamma_6$ and $\Gamma_{15}$ double

groups, respectively [60], where the irreducible representation $\Gamma_6$ is two-fold degenerate, and $\Gamma_{15}$ can be separated into the irreducible representations $\Gamma_7$ and $\Gamma_8$, which are two- and four-fold degenerate, respectively. $\Gamma_8$ corresponds to the heavy-hole and light-hole states, which split in energy away from the $\Gamma$ point, and $\Gamma_7$ corresponds to the split-off band, which is separated in energy from $\Gamma_8$ by the valence band spin-orbit splitting $\Delta_0$. One typically refers to the bonding $p$ orbital described by $\Gamma_{15}$ as the valence band and the antibonding $s$ orbital described by $\Gamma_6$ as the conduction band. We point out that the antibonding $p$ and bonding $s$ orbitals at the Gamma point are far separated above and below the conduction and valence bands, respectively. For more information about the double and single group symmetries, see Ref. [61].

From the Bloch theorem, for an electron in a periodic potential, we can define the electron wave function as having the form [62]

$$\psi_{n,\vec{k}}\left(\vec{r}\right) = e^{i\vec{k}\cdot\vec{r}} u_{n,\vec{k}}\left(\vec{r}\right) \tag{2.44}$$

where $u_{n,\vec{k}}(\vec{r})$ is a periodic wave function matching the periodicity of the crystal such that

$$u_{n,\vec{k}}(\vec{r}) = u_{n,\vec{k}}(\vec{r} + \vec{R}) \tag{2.45}$$

with $\vec{R}$ a vector pointing between identical points in two different unit cells of the lattice. That is $\vec{R} = \sum_{i=1}^{3} m_i \vec{a}_i$, where $m_i$ are integers and $\vec{a}_i$ the three primitive vectors of the Bravais lattice. For cubic semiconductors, such as diamond and zincblende, the $\vec{a}_i$ are all equal in magnitude and orthogonal with $a = |\vec{a}|$ the lattice parameter. The subscript $n$ denotes the particular state to which the wave function $u_{n,\vec{k}}$ refers. At the $\Gamma$ point, we take $\vec{k} = 0$, in which case the electron wave function is approximated by $\psi_{n,0}\left(\vec{r}\right) = u_{n,0}\left(\vec{r}\right)$ and matches the periodicity of the lattice. With our knowledge of the $s$-like behavior of the conduction band and the $p$-like behavior of the valence band, we choose three valence band

states (corresponding to $m_l = 0, \pm 1$), denoted by $|X\rangle$, $|Y\rangle$, and $|Z\rangle$ and one conduction band state (corresponding to $m_l = 0$), denoted by $|1\rangle$. The valence and conduction band states have the same symmetry as the $\Gamma_{15}$ and $\Gamma_6$ double groups (i.e. $T_1$ and $A_1$ point symmetries) respectively [61]. We will see that the states $|X\rangle$, $|Y\rangle$, and $|Z\rangle$ behave similarly to the corresponding spatial coordinate variables near the $\Gamma$ point, though we point out that they necessarily obey a cubic, rather than spherical symmetry.

Nonetheless, we find that such a suitable choice for the form of these states, namely the nearly free electron wave functions [60], allows us to build the familiar angular momentum eigenvalue equations:

$$\begin{array}{lcl} L_z|1\rangle = 0|1\rangle & , & L^2|1\rangle = 0|1\rangle \\ L_z|Z\rangle = 0|Z\rangle & , & L^2|Z\rangle = 2\hbar^2|Z\rangle \\ L_z|+\rangle = L_z\left(-\frac{|X\rangle+i|Y\rangle}{\sqrt{2}}\right) = \hbar|+\rangle & , & L^2|+\rangle = 2\hbar^2|+\rangle \\ L_z|-\rangle = L_z\left(\frac{|X\rangle-i|Y\rangle}{\sqrt{2}}\right) = -\hbar|-\rangle & , & L^2|-\rangle = 2\hbar^2|-\rangle \end{array}$$

I have made the definitions for $|+\rangle$ and $|-\rangle$ in accordance with Ref. [60]. In this case, the angular momentum operator $L$ is given by the form of the spin-orbit splitting Hamiltonian in Eq. 2.21, namely $H_{SO} = \lambda\vec{L}\cdot\vec{S}$ with $\vec{L} \propto \nabla V \times \vec{p}$. We can see from the above eigenvalue equations that these states map exactly to the angular momentum eigenstates described by $L_z|l, m_l\rangle = m_l\hbar|l, m_l\rangle$ and $L^2|l, m_l\rangle = l(l+1)\hbar^2|l, m_l\rangle$. In analogy to the spherically symmetric spin-orbit Hamiltonian, we can build our total angular momentum states $|j, m_j\rangle$ from linear superpositions of the states $|l, m_l\rangle \otimes |m_s\rangle$ where it is implied for the electron $s = 1/2$. The conduction band at the $\Gamma$ point is simple. As $l = 0$ (and therefore $m_l = 0$), there is no spin-orbit splitting and the $|j, m_j\rangle$ states are defined trivially as

$$|j = 1/2, m_j = \pm 1/2\rangle = |1\rangle \otimes |\uparrow (\downarrow)\rangle\,. \tag{2.46}$$

Here I have made the familiar definition $|m_s = \pm 1/2\rangle \equiv |\uparrow (\downarrow)\rangle$, and by inspection of the

eigenvalue equations above, $|1\rangle \Leftrightarrow |l = 0, m_l = 0\rangle$.

The valence band at the $\Gamma$ point can be built without much difficulty. Due to spin-orbit splitting, $j$ can be allowed integer values ranging between $j = l \pm s$, each with a discrete energy. With $l = 1$ and $s = 1/2$, we have $j = 1/2, 3/2$, with $j = 3/2$ the heavy-hole/light-hole band and $j = 1/2$ the split-off band. The energy splitting between the heavy-hole/light-hole and split-off bands is denoted by $\Delta_0$ and is commonly referred to as the valence band spin-orbit splitting.

We first build the heavy-hole/light-hole bands by noticing the lowest angular momentum state ($|j = 3/2, m_j = -3/2\rangle$) is as trivial as the conduction band and is given simply by

$$|j = 3/2, m_j = -3/2\rangle = |-\rangle \otimes |\downarrow\rangle \tag{2.47}$$

as this is the only combination that gives the proper angular momentum $m_j = -3/2$. Again, from inspection of the eigenvalue equations, I have made the relation $|-\rangle \Leftrightarrow |l = 1, m_l = -1\rangle$. The $m_j = -1/2$ state is built using the angular momentum raising operator:

$$J_+ |j = 3/2, m_j = -3/2\rangle = (L_+ + S_+) |-\rangle \otimes |\downarrow\rangle \tag{2.48}$$

$$\sqrt{3} |j = 3/2, m_j = -1/2\rangle = \sqrt{2} |Z\rangle \otimes |\downarrow\rangle + |-\rangle \otimes |\uparrow\rangle \tag{2.49}$$

$$|j = 3/2, m_j = -1/2\rangle = \frac{1}{\sqrt{3}} \left( \sqrt{2} |Z\rangle \otimes |\downarrow\rangle + |-\rangle \otimes |\uparrow\rangle \right) \tag{2.50}$$

where the raising operator is, in general, given by $J_+ |m_j\rangle = \sqrt{j(j+1) - m_j(m_j+1)}\, |m_j + 1\rangle$. For a derivation of the raising operator see [48]. We continue this procedure until we reach the highest angular momentum state in the heavy-hole/light-hole band. The final step is to determine the split-off band states. We note that the $|j = 1/2, m_j = -1/2\rangle$ state is built from a linear superposition of the same states as $|j = 3/2, m_j = -1/2\rangle$, as they give the same overall z-projection of the angular momentum. However, they have different eigenvalues of

the $J^2$ operator and must therefore be orthogonal, that is

$$\langle j = 1/2, m_j = -1/2 | j = 3/2, m_j = -1/2 \rangle = 0. \tag{2.51}$$

By inspection of Eq. 2.50, we can define the spin down split-off band state as

$$|j = 1/2, m_j = -1/2\rangle = \frac{1}{\sqrt{3}} \left( \sqrt{2} \, |-\rangle \otimes |\uparrow\rangle - |Z\rangle \otimes |\downarrow\rangle \right). \tag{2.52}$$

The coefficients are chosen in this way to satisfy orthonormality, while the state is defined up to an arbitrary overall phase factor. The angular momentum raising operator is used from here to determine the spin up split-off band state. Table 2.1 below summarizes the angular momentum states in terms of the Bloch states at the Γ point for GaAs. The coefficients will be used to build the optical selection rules in Ch. 4.

| | | | |
|---|---|---|---|
| Conduction Band ($\Gamma_6$) | $\lvert j = 1/2, m_j = 1/2\rangle$ | $\lvert 1\rangle \otimes \lvert\uparrow\rangle$ | $\sim {}^{l=0,m_l=0}_{s=1/2,m_s=1/2}$ |
| | $\lvert j = 1/2, m_j = -1/2\rangle$ | $\lvert 1\rangle \otimes \lvert\downarrow\rangle$ | $\sim {}^{l=0,m_l=0}_{s=1/2,m_s=-1/2}$ |
| HH Valence Band ($\Gamma_8$) | $\lvert j = 3/2, m_j = 3/2\rangle$ | $-\frac{1}{\sqrt{2}} \left( \lvert X\rangle + i \lvert Y\rangle \right) \otimes \lvert\uparrow\rangle$ | $\sim {}^{l=1,m_l=1}_{s=1/2,m_s=1/2}$ |
| | $\lvert j = 3/2, m_j = -3/2\rangle$ | $\frac{1}{\sqrt{2}} \left( \lvert X\rangle - i \lvert Y\rangle \right) \otimes \lvert\downarrow\rangle$ | $\sim {}^{l=1,m_l=-1}_{s=1/2,m_s=-1/2}$ |
| LH Valence Band ($\Gamma_8$) | $\lvert j = 3/2, m_j = 1/2\rangle$ | $\frac{1}{\sqrt{6}} \left[ 2 \lvert Z\rangle \otimes \lvert\uparrow\rangle - \left( \lvert X\rangle + i \lvert Y\rangle \right) \otimes \lvert\downarrow\rangle \right]$ | $\sim {}^{l=1,m_l=0,1}_{s=1/2,m_s=\pm 1/2}$ |
| | $\lvert j = 3/2, m_j = -1/2\rangle$ | $\frac{1}{\sqrt{6}} \left[ 2 \lvert Z\rangle \otimes \lvert\downarrow\rangle + \left( \lvert X\rangle - i \lvert Y\rangle \right) \otimes \lvert\uparrow\rangle \right]$ | $\sim {}^{l=1,m_l=0,-1}_{s=1/2,m_s=\mp 1/2}$ |
| SO Valence Band ($\Gamma_7$) | $\lvert j = 1/2, m_j = 1/2\rangle$ | $\frac{1}{\sqrt{3}} \left[ \left( \lvert X\rangle + i \lvert Y\rangle \right) \otimes \lvert\downarrow\rangle + \lvert Z\rangle \otimes \lvert\uparrow\rangle \right]$ | $\sim {}^{l=1,m_l=1,0}_{s=1/2,m_s=\mp 1/2}$ |
| | $\lvert j = 1/2, m_j = -1/2\rangle$ | $\frac{1}{\sqrt{3}} \left[ \left( \lvert X\rangle - i \lvert Y\rangle \right) \otimes \lvert\uparrow\rangle - \lvert Z\rangle \otimes \lvert\downarrow\rangle \right]$ | $\sim {}^{l=1,m_l=-1,0}_{s=1/2,m_s=\pm 1/2}$ |

**Table 2.1: Angular momentum states at the Γ point for GaAs:** The left center column lists the total angular momentum states, while the right center column lists their constructions from the orthonormal Bloch states. The right column lists the analogous spin and orbital angular momentum states for a spherically symmetric potential.

### 2.3.2 Parabolic bands and effective mass

The band diagram near the Γ point, but with $\vec{k} \neq 0$, can be built using $\vec{k} \cdot \vec{p}$ theory. Going back to the Bloch wave function (Eq. 2.44), Schrödinger's equation for the states $u_{n,\vec{k}}(\vec{r})$ near the Γ point becomes

$$\left( \frac{p^2}{2m} + \frac{\hbar \vec{k} \cdot \vec{p}}{m} + \frac{\hbar^2 k^2}{2m} + V(\vec{r}) \right) u_{n,\vec{k}}(\vec{r}) = \varepsilon_{n,\vec{k}} u_{n,\vec{k}}(\vec{r}) \tag{2.53}$$

where it is understood that $V(\vec{r})$ represents the periodic lattice potential and the $u_{n,\vec{k}}(\vec{r})$ obey the periodicity described by Eq. 2.45. The solutions to $\varepsilon_{n,0}$ and $u_{n,0}(\vec{r})$ give the energies and Bloch states at the Γ point (for which $\vec{k} = 0$). Assuming the states and energies are known, expansion around this point is achieved using perturbation theory, treating the components involving $\vec{k}$ as small perturbations. For the conduction band, this is straightforward as nondegenerate perturbation theory applies. We take a local minimum in the conduction band to occur at the Γ point, for which the energy is expanded to second order as [60]

$$\varepsilon_{c,k} = \varepsilon_{c,0} + \frac{\hbar^2 k^2}{2m} + \frac{\hbar^2}{m^2} \sum_{n \neq c} \frac{\left| \langle u_{n,0} | \, \vec{k} \cdot \vec{p} \, | u_{c,0} \rangle \right|^2}{\varepsilon_c - \varepsilon_n} \tag{2.54}$$

$$\varepsilon_{c,k} = \varepsilon_{c,0} + \frac{\hbar^2 k^2}{2m^*} \tag{2.55}$$

where the conduction band electron effective mass has been defined as

$$\frac{1}{m^*} = \frac{1}{m} + \frac{2}{m^2 k^2} \sum_{n \neq c} \frac{\left| \langle u_{n,0} | \, \vec{k} \cdot \vec{p} \, | u_{c,0} \rangle \right|^2}{\varepsilon_c - \varepsilon_n} \tag{2.56}$$

Fig. 2.4(left) shows a schematic of the band diagram near the Γ point. As this is the point at which optical transitions occur, and doping levels for the samples studied are relatively

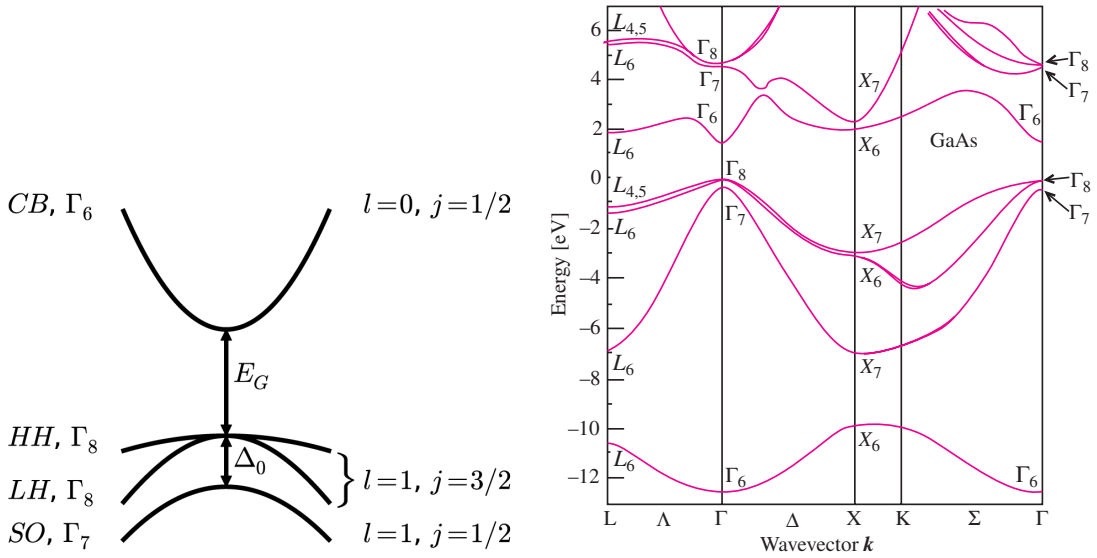


**Figure 2.4: GaAs band diagram:** (left) Band diagram near the Γ point shows a nearly parabolic band energy dispersion. The split off band (SO) separation is increased in the figure for clarity. (right) Full band diagram for GaAs along directions of high symmetry using the pseudopotential method. The figure is reproduced from Ref. [60] with permission from Springer-Verlag under License No. 3374190701099.

low ($10^{16}$ - $10^{17}$ cm$^{-3}$), we treat conduction band electrons to be well described as free with an effective mass.

The effective masses for the valence bands are found in a similar form, though degenerate perturbation theory must be used. We notice that the effective masses in the valence band are negative, in which case the energy is maximized for $\vec{k} = 0$. In this case, when a single electron is removed from the valence band, the gap left, which is typically called a hole, will move to the Γ point at the top of the valence band. As such, we will refer to a valence band effective mass as a hole effective mass. We note that the light-hole band has a steeper band dispersion than that of the heavy-hole, corresponding to a lighter hole effective mass (hence the heavy-hole/light-hole nomenclature). The difference in effective masses for these states stems from the values of the matrix elements $\langle u_{n',\vec{k}} | \, \vec{k} \cdot \vec{p} \, | u_{n,\vec{k}} \rangle$.

It was determined both numerically and experimentally that for ternary compounds, such as $In_xGa_{1-x}As$, the effective masses, as well as relevant energy splittings, can be approxi-

| Parameter | GaAs | InAs | $C$ | $In_{0.04}Ga_{0.96}As$ |
|---|---|---|---|---|
| $E_g$ | 1.519 | 0.417 | 0.477 | 1.457 |
| $\Delta_0$ | 0.341 | 0.39 | 0.15 | 0.34 |
| $m^*$ | 0.067 | 0.026 | 0.0091 | 0.065 |
| $m^*_{HH}$ | 0.35 | 0.33 | -0.145 | 0.35 |
| $m^*_{LH}$ | 0.090 | 0.027 | 0.0202 | 0.087 |
| $m^*_{SO}$ | 0.172 | 0.14 | 0 | 0.17 |

**Table 2.2: InGaAs material parameters:** Band structure parameters near the Γ point for GaAs, InAs, and $In_{0.04}Ga_{0.96}As$ as well as relevant bowing parameters. Energies $E_g$ and $\Delta_0$ are in units of eV, while effective masses $m^*$ are in units of the free electron mass $m_0$.

mated as a linear interpolation of such a parameter for each of the pure binary compounds, with a bowing parameter [63]. In this way the effective mass can be described in quadratic form using the formula

$$m^*\left(\mathrm{In}_x\mathrm{Ga}_{1-x}\mathrm{As}\right) = xm^*\left(\mathrm{InAs}\right) + \left(1-x\right)m^*\left(\mathrm{GaAs}\right) - Cx\left(1-x\right) \tag{2.57}$$

where $C$ is the bowing parameter determined both numerically and from experiment, and $m^*(...)$ represents the effective mass of the structure in parentheses. Table 2.2 shows the band gap ($E_g$), valence band spin-orbit splitting ($\Delta_0$), and the conduction and valence band effective masses, as well the corresponding bowing parameters ($C$) for InAs, GaAs, and $In_{0.04}Ga_{0.96}As$ as this is the structure on which measurements are taken. These parameters are approximated for low temperature.

The band diagram away from the Γ point can be achieved using the pseudopotential technique [64] and is shown for GaAs in Fig. 2.4(right). In this case, the bands are neither parabolic nor spherically symmetric. In fact, we point out that the parabolicity of the light-hole valence band is lost very rapidly as a function of $k$. This is a result of mixing between the light-hole and split-off band states [65]. Finally, we also point out that while the conduction band is spherically symmetric near the Γ point, the valence band obeys an obvious and strong cubic symmetry, with band dispersion differing even for momentum along different

points of high symmetry (i.e. $\vec{k} \parallel [100]$, [110], and [111]). While it is sometimes suitable to take an average of the hole effective masses over all $\vec{k}$ directions as an approximation very near the $\Gamma$ point [60], it is necessary to point out that the heavy-hole/light-hole valence band effective masses have a directional dependence which can be described by the Kohn-Luttinger parameters [66]. In table 2.2, the valence band effective masses are shown only for $\vec{k} \parallel [100]$.

## 2.4 Spin-orbit splitting in the conduction band

Our applications involve $n$-type doped InGaAs in which both equilibrium and transient behavior is measured on electron spins in the conduction band. As such, it is necessary to discuss how spatial inversion symmetry breaking leads to a spin splitting in the conduction band. While this effect also occurs in the valence band, leading to a splitting away from the $\Gamma$ point, we treat this additional interaction as negligible for the time being. As before, we treat the spin-orbit interaction as having the form

$$H_{SO} = \frac{\hbar^2}{4m^{*2}c^2}\left(\nabla V \times \vec{k}\right) \cdot \vec{\sigma} \tag{2.58}$$

in which case we will treat $\vec{k}$ as the electron momentum described by $\vec{p} = \hbar\vec{k}$, and $\vec{\sigma}$ as describing the vector electron spin.

### 2.4.1 Bychov-Rashba spin-orbit field

The Bychov-Rashba spin-orbit splitting (frequently called simply the Rashba spin-orbit splitting) arises from the inherent nonzero potential gradient present in heterostructures along the growth axis. Consider the transition from material $A$ to material $B$ (Fig. 2.5(a)) where the interface represents a location of spatial inversion symmetry breaking along the growth axis, resulting in lifted degeneracy in the spin state as discussed in Sec. 2.2.3. This type

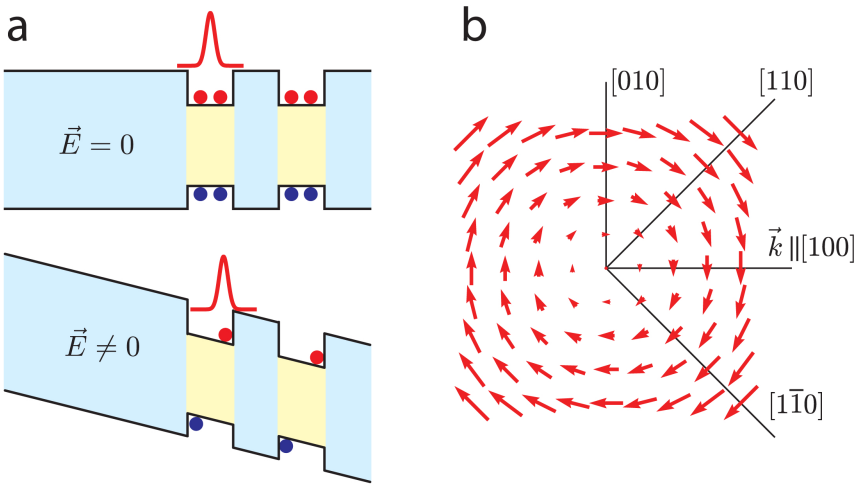


**Figure 2.5: Rashba spin-orbit effective magnetic field:** (a) Heterostructure stacking results in structural inversion asymmetry (SIA). Internal or external electric fields can be used to generate two-dimensional electron gases at the interfaces. (b) Rashba spin-orbit effective magnetic field is isotropic and perpendicular to momentum in the plane orthogonal to the growth axis.

of spin-orbit splitting is typically referred to as structural inversion asymmetry (SIA). The resulting spin-orbit Hamiltonian is traditionally given by [10]

$$H_R = \alpha \left( \vec{\sigma} \times \vec{k} \right) \cdot \hat{n} \tag{2.59}$$

where $\hat{n}$ is the unit vector along the axis of broken symmetry and $\alpha$ is the Rashba coefficient, proportional to the gradient in the electric potential, i.e. the electric field, at the band interface.

To intuitively understand the Rashba spin-orbit Hamiltonian, consider an electron in a potential well at the heterostructure interface confined to travel in the plane perpendicular to the growth axis. From the rest frame of the electron, the electric field contained in the Rashba coefficient $\alpha$ will give rise to an in-plane effective magnetic field transverse to the electron momentum. With the analogy of a Zeeman-type spin Hamiltonian given by $H_Z = g\mu_B \vec{\sigma} \cdot \vec{B}_{eff}$, we can then define a Rashba spin-orbit effective magnetic field as

$$\vec{B}_R = \frac{\alpha}{g\mu_B} \left( k_y \hat{x} - k_x \hat{y} \right). \tag{2.60}$$

Fig. 2.5(b) depicts the Rashba spin-orbit effective magnetic field as a function of electron momentum $\vec{k}$; it is found to be linear in momentum, isotropic, and is always perpendicular to $\vec{k}$.

One might argue that a bound electron should observe no net electric field. In truth, as pointed out in Ref. [67], the electric field experienced by the electron along the growth direction averages to very nearly zero, and predicts a spin-orbit splitting in the conduction band orders of magnitude smaller than that measured experimentally. A sufficient model explained this effect by expanding the $2 \times 2$ conduction band Hamiltonian to include interactions with not only the $\Gamma_7$ and $\Gamma_8$ valence bands, but also with the higher energy $\Gamma_7$ and $\Gamma_8$ antibonding $p$ orbitals above the conduction band. This $14 \times 14$ Hamiltonian was treated in a five-level degenerate perturbation theory using the $\vec{k} \cdot \vec{p}$ approach. The theoretical framework was in good agreement with previously observed experimental results.

It was finally pointed out that inclusion of an external electric field, in the form of a top gate as in Ref. [68], does not actually serve to increase the electric field experienced by the electron, which still must be near zero for the bound state. Rather, the top gate serves to distort the symmetry of the electron wave function in the quantum well, thereby causing an enhancement of the effect. It was found that while the Rashba effect is strong at heterostructure interfaces, it falls off very rapidly for electrons that are not near the interface and is therefore expected to be the dominant effect only in tightly confined geometries such as quantum wells and two-dimensional electron gases (2DEGs). It plays less of a role in bulk semiconductors.

### 2.4.2 Dresselhaus spin-orbit field

The Dresselhaus spin-orbit splitting is a result of bulk inversion asymmetry in zincblende semiconductors. At the center point between gallium and arsenic atoms (Fig. 2.6(a)), there is a nonzero potential gradient pointing between the two atoms. Each atom is surrounded by four such points of broken inversion symmetry in a tetrahedral bond. While the Dresselhaus spin-orbit splitting can be derived using the $T_d$ group basis functions [9], it can be useful to directly investigate the symmetry from a geometric standpoint.

From the $\nabla V \times \vec{k}$ term in the spin-orbit splitting, we know that momentum along or against the direction of the potential gradient results in a vanishing spin splitting. In Fig. 2.6(a) this corresponds to 8 directions for which the Dresselhaus spin-orbit splitting vanishes given by permutations of $\pm 1$ along each of the principal crystal axes. Furthermore, we know that for $\vec{k}$ along a particular direction of symmetry perpendicular to the potential gradient, an effective magnetic field perpendicular to both $\nabla V$ and $\vec{k}$ must result.

We can examine these conditions in turn. Consider $\vec{k}$ from the center gallium atom (maize) to the front arsenic atom (blue) in the figure to be defined as $\vec{k}_{\parallel} = -k(\hat{x}+\hat{y}+\hat{z})/\sqrt{3}$ (with $\hat{x} \parallel [100]$, $\hat{y} \parallel [010]$, and $\hat{z} \parallel [001]$) such that $\vec{k}$ is along the bond (i.e. $\vec{k}_{\parallel} \parallel \nabla V$). By the definition of the spin-orbit field we require $\vec{B}_D(\vec{k}_{\parallel}) = 0$. The same is true for $\vec{k} = -\vec{k}_{\parallel}$. Now consider $\vec{k} \perp \nabla V$. By the three-fold rotational symmetry of the tetrahedral bond we can choose one of three identical such momentum vectors. We will choose $\vec{k}_{\perp} = k(\hat{x}+\hat{y}-2\hat{z})/\sqrt{6}$. Again from the definition of the spin-orbit field, we require $\vec{B}_D(\vec{k}_{\perp})$ to be nonzero and perpendicular to both $\vec{k}_{\perp}$ and $\nabla V$. In this case that would give $\vec{B}_D(\vec{k}_{\perp}) \propto \hat{x} - \hat{y}$. There are two additional definitions of $\vec{k}_{\perp}$ that will satisfy this condition and are given by rotations of $\pm 120^{\circ}$ from $\vec{k}_{\perp}$ along the [111] axis. In passing, such a rotational symmetry is said to belong to the $8C_3$ class of symmetry operations. Table 2.3 displays the conditions for the one parallel and three perpendicular momentum vectors with respect to $\nabla V$ and the requirements on

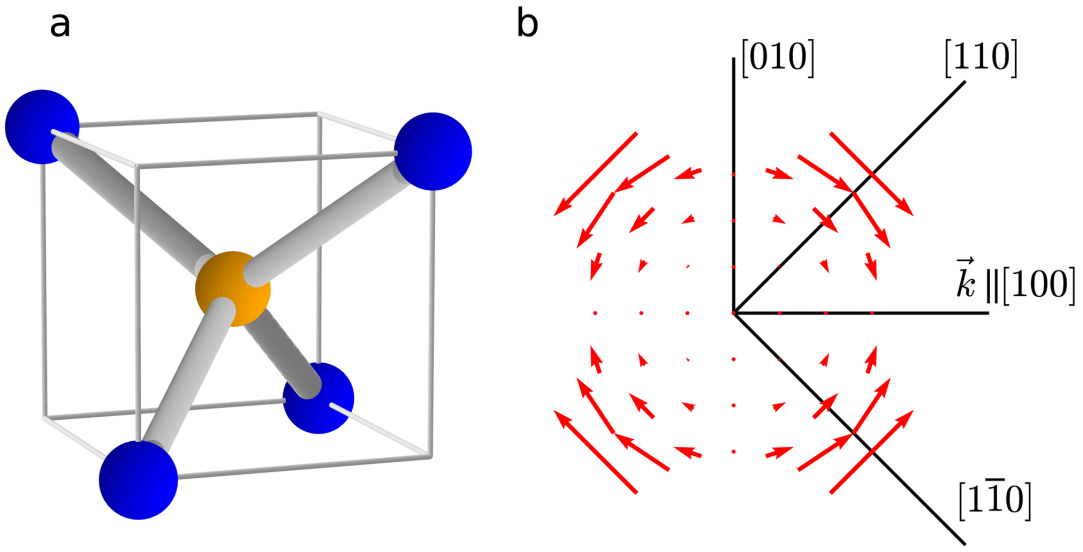


**Figure 2.6: Dresselhaus spin-orbit field:** (a) Gallium (maize sphere) atom surrounded by arsenic (blue sphere) atoms in a tetrahedral bond (same as methane $CH_4$ molecule). The center point of each bond (gray cylinder) represents a point of spatial inversion symmetry breaking along the bond axis. (b) Resulting Dresselhaus spin-orbit effective magnetic field for $\vec{k}$ confined in the (001) plane.

the spin-orbit fields they must generate for the bond along the [111] axis.

The definitions for $\vec{k}_{\parallel}$ and $\vec{k}_{\perp}$ is repeated for each of the other three bonds and a form for the Dresselhaus spin-orbit field is established. The field that satisfies Table 2.3 for each of the four bonds is, to lowest order,

$$\vec{B}_D \propto \gamma \left[ k_x \left( k_y^2 - k_z^2 \right) \hat{x} + k_y \left( k_z^2 - k_x^2 \right) \hat{y} + k_z \left( k_x^2 - k_y^2 \right) \hat{z} \right] \tag{2.61}$$

where $\gamma$ is the cubic Dresselhaus coefficient and is a material specific parameter. It may be obvious that Eq. 2.61 is not the only form for $\vec{B}_D$. Indeed there are many definitions to increasingly higher order in momentum that will satisfy the symmetry of the zincblende structure. This represents the lowest order which will dominate in cases of small $\vec{k}$ which is usually the case. One may notice that the form of Eq. 2.61 obeys the exact same symmetry as the basis function for the three dimensional irreducible representation $T_1$ of the $T_d$ point

| | $\vec{k} \propto$ | $\vec{B}_D \propto$ |
|---|---|---|
| $\vec{k}_{\parallel}$ | $(1,1,1)$ | $(0,0,0)$ |
| $\vec{k}_{\perp,1}$ | $(1,1,-2)$ | $(1,-1,0)$ |
| $\vec{k}_{\perp,2}$ | $(-2,1,1)$ | $(0,1,-1)$ |
| $\vec{k}_{\perp,3}$ | $(1,-2,1)$ | $(-1,0,1)$ |

**Table 2.3: Dresselhaus spin-orbit field constraints:** Constraints on the directionality of the Dresselhaus spin-orbit field for different directions of $\vec{k}$ parallel and perpendicular to $\nabla V$, with $\nabla V \parallel [111]$. These requirements stem from the form of $\vec{B} \propto \nabla V \times \vec{k}$ and the symmetry of the tetrahedral crystal structure.

group, and in particular of the $\Gamma_5$ irreducible representation of the $T_1 \otimes D_{1/2}$ double group of which the zincblende structure is a member. This is not a coincidence, and in fact is required due to the invariant nature of the Hamiltonian under certain symmetry operations. For more detail consult Ref. [69].

In situations for which the average momentum along $\hat{z}$ goes to zero, such as epilayers and quantum wells, Eq. 2.61 reduces to the two dimensional form

$$\vec{B}_{D,(001)} \propto \gamma \left[ k_x \left( k_y^2 - \langle k_z^2 \rangle \right) \hat{x} + k_y \left( \langle k_z^2 \rangle - k_x^2 \right) \hat{y} \right]. \tag{2.62}$$

The term $\langle k_z^2 \rangle$ represents the confinement along the $z$ axis which increases as the confinement becomes stronger (i.e. the well thickness decreases). For epilayers, which approach the bulk regime, the confinement term is typically neglected, though it is important to point out that in such cases it is possible to have a localized nonzero $k_z$, even if averaged over the entire structure it is zero. The Dresselhaus field in the (001) plane is depicted in Fig. 2.6(b). We can see that it is neither isotropic, nor does its magnitude depend only on the magnitude of $\vec{k}$; it is cubic in $|\vec{k}|$ for $\vec{k} \parallel [110]$, $[1\bar{1}0]$, and vanishes for $\vec{k} \parallel [100]$, $[010]$ when the confinement term is negligibly small.

It is finally worth noting a few more interesting cases for the Dresselhaus field. For confinement in the (111) plane (i.e. a quantum well perpendicular to [111]), the Dresselhaus

field takes on a two dimensional symmetry equal to that of the Rashba field [18], and for confinement along the [111] axis, such as with a quantum wire, the Dresselhaus field vanishes entirely. These conditions are particularly useful for situations in which one desires to minimize the spin-orbit interaction, such as to increase the spin coherence time (Sec. 3.4.1).

### 2.4.3 Strain-induced spin-orbit fields

Due to heterostructure stacking, strain is necessarily present in non lattice-matched materials, as is the case for $In_{0.04}Ga_{0.96}As$ grown on a (001) GaAs substrate. The mismatch in the lattice parameters causes compressive strain of the InGaAs epilayer in the plane perpendicular to the growth axis and tensile strain along the growth axis. Furthermore, anisotropic strain relaxation throughout the epilayer can give rise to a shear strain equivalent to that of a uniaxial strain applied in the plane perpendicular to the growth axis. These strain components give rise to an additional source of spatial inversion symmetry breaking and will result in a spin splitting in the conduction band as well.

This splitting will be characterized by a perturbation of the Hamiltonian in the presence of strain and is given by [61]

$$H_{\epsilon}^{\alpha\beta} = \sum_{i,j} D_{ij}^{\alpha\beta} \epsilon_{ij} \tag{2.63}$$

where $\epsilon_{ij}$ are the elements of the strain tensor, $D_{ij}$ is the deformation potential operator and $\alpha$ and $\beta$ represent the states of the unperturbed Hamiltonian given in Table 2.1. The strain tensor elements are built in the symmetric form according to [61]

$$\epsilon_{ij} = \frac{1}{2}\left(\frac{\partial u_i}{\partial x_j} + \frac{\partial u_j}{\partial x_i}\right) \tag{2.64}$$

where $u_i$ represents the displacement field of the structure from the equilibrium position and $x_i$ represents the coordinate basis in the unstrained Bravais lattice.

In general, the form of the deformation potential will satisfy a set of symmetry constraints to which the crystal is subject. We introduced the concept of symmetry operations in the last section, with the $C_3$ rotation around the axes of the tetrahedral bond. For zincblende structures, there are five such classes of symmetry operations, formed from different magnitudes and orientations of rotations and reflections relative to the tetrahedral molecule. These form 24 total and distinct symmetry operations (for diamond structures, an additional reflection symmetry exists for each bond and the total number of distinct symmetry operations becomes 48). The $T_d$ point group can be broken into a set of irreducible representations that build basis functions which behave according to this set of symmetry operations. The table that relates the irreducible representations to the symmetry class is called the character table for the group [61]. We saw earlier that the symmetry class $C_3$ gave rise to the basis functions of the $\Gamma_5$ irreducible representation which is how the Dresselhaus spin-orbit field is defined. Another common three-dimensional irreducible representation is $\Gamma_4$ and has basis functions that are vectorial in nature, i.e. of the form $\{x, y, z\}$. The electron momentum $\vec{k}$ falls into the $\Gamma_4$ irreducible representation. As was pointed out in the previous section, the invariant nature of the Hamiltonian must obey a particular set of symmetry operations; for the spin-orbit Hamiltonian of the form $H_{SO} \propto \vec{B} \cdot \vec{\sigma}$, this requires that $\vec{B}$ must belong to the $\Gamma_5$ irreducible representation. We can build the form of the strain-induced spin-orbit Hamiltonians to meet the requirements of the symmetry operations. The details can be found in Ref. [60]. We present them here as

$$H_{biaxial} = D\left[\left(\epsilon_{yy} - \epsilon_{zz}\right) k_x \sigma_x + \left(\epsilon_{zz} - \epsilon_{xx}\right) k_y \sigma_y + \left(\epsilon_{xx} - \epsilon_{yy}\right) k_z \sigma_z\right] \tag{2.65}$$

$$H_{uniaxial} = \frac{C_3}{2}\left[\left(\epsilon_{zx} k_z - \epsilon_{xy} k_y\right) \sigma_x + \left(\epsilon_{xy} k_x - \epsilon_{yz} k_z\right) \sigma_y + \left(\epsilon_{yz} k_y - \epsilon_{zx} k_z\right) \sigma_x\right] \tag{2.66}$$

where $C_3$ and $D$ are material parameters and are related to the matrix elements mixing the

conduction and valence band states [11]. As with the case of the Dresselhaus spin-orbit field, we confine carriers in the plane perpendicular to $\hat{z}$. In this case, with the Hamiltonian given by the form $H_{SO} \propto \vec{B}_{SO} \cdot \vec{\sigma}$, we can define strain-induced spin-orbit effective magnetic fields to have the form

$$\vec{B}_{biaxial} \propto D\left(\epsilon_{zz} - \epsilon_{xx}\right)\left(k_x\hat{x} - k_y\hat{y}\right) \tag{2.67}$$

$$\vec{B}_{uniaxial} \propto \frac{C_3\epsilon_{xy}}{2}\left(k_y\hat{x} - k_x\hat{y}\right). \tag{2.68}$$

The biaxial and uniaxial strain-induced spin-orbit effective magnetic fields are displayed in Fig. 2.7(a) and (b) respectively. We can see that the uniaxial strain-induced field is linear in $\vec{k}$, is isotropic, and in fact maps exactly to the Rashba spin-orbit effective magnetic field, up to a potential minus sign, depending on the sign of $\epsilon_{xy}$. On the other hand, the biaxial strain-induced field is linear in $\vec{k}$, but is no longer anisotropic, and maps to the directionality of the Dresselhaus spin-orbit field.

### 2.4.4 Anisotropic spin-orbit fields

The total spin-orbit effective magnetic field experienced by the electron will be the sum of the effects discussed in the previous sections. We pull symmetric terms together and get the following form for the spin-orbit field:

$$\vec{B}_{SO} = \left(\alpha k_y + \beta k_x + \gamma k_x k_y^2\right)\hat{x} - \left(\alpha k_x + \beta k_y + \gamma k_y k_x^2\right)\hat{y} \tag{2.69}$$

where the term $\alpha$ contains both the Rashba and uniaxial strain-induced spin-orbit fields, $\beta$ contains both the linear Dresselhaus and biaxial strain-induced spin-orbit fields, and $\gamma$ contains only the cubic Dresselhaus term. We note that the form of Eq. 2.69 is anisotropic

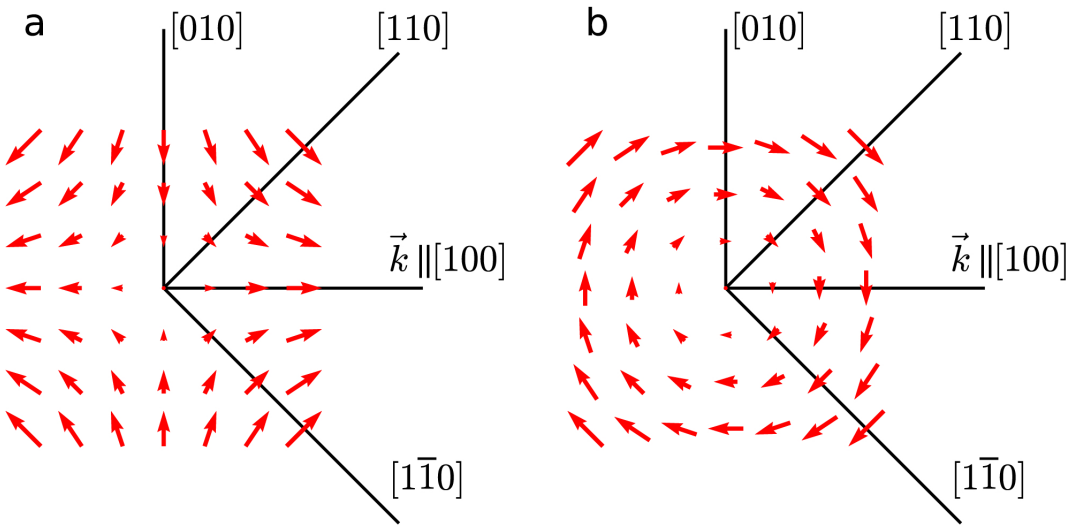


**Figure 2.7: Strain-induced spin-orbit field:** Biaxial strain (a) is a result of lattice mismatch and obeys the same symmetry as the linear Dresselhaus SO field. Uniaxial strain (b) is a result of anisotropic strain relaxation throughout the epilayer and obeys the same symmetry as the Rashba SO field.

in momentum, and for small $\gamma$ exhibits a set of extremum for $k_x = \pm k_y$. For $\alpha > 0$, the minimum occurs for $k_x = -k_y$ corresponding to $\vec{k} \parallel [1\bar{1}0]$. By including the Dresselhaus term, $\gamma$ we find that the minimum is shifted symmetrically to either side of the $[1\bar{1}0]$ direction, with the magnitude of the deviation given by

$$\theta = \frac{\pi}{4} - \cos^{-1}\left[\frac{1}{2} + \frac{1}{2}\sqrt{1 - \frac{2\alpha\left(2\beta + \gamma k^2\right)}{\gamma^4 k^2 \left(4\beta + \gamma^2 k^2\right)^2}}\right]. \tag{2.70}$$

For a specific set of spin-orbit field parameters, this deviation is only defined for $k$ greater than some minimum value for which the second term in the square root is equal to one. As we do not observe a deviation in the minimum spin-orbit field, and as no cubic behavior is observed for $\vec{k} \parallel [110], [1\bar{1}0]$, we take the cubic Dresselhaus term to be negligibly small for electron momentum $k$ in the range of our measurements. The spin-orbit field in this case is described by

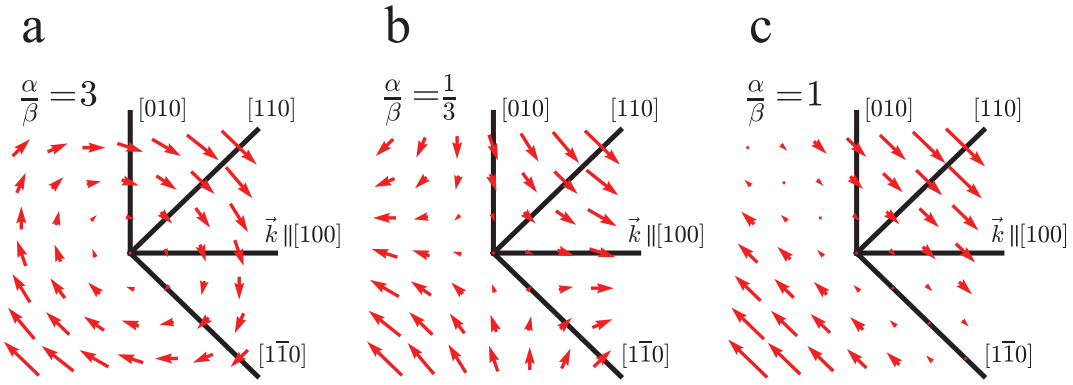


**Figure 2.8: Anisotropic spin-orbit field:** Mapped for uniaxially dominated (a), biaxially dominated (b), and matched (c) strain-induced spin-orbit terms.

$$\vec{B}_{SO} = (\alpha k_y + \beta k_x)\,\hat{x} - (\alpha k_x + \beta k_y)\,\hat{y}. \tag{2.71}$$

This is the form of the in-plane spin-orbit field that will be used throughout this work. Fig. 2.8 displays the resulting anisotropic spin-orbit field for various choices of the ratio $\alpha/\beta$. As we do not expect the Rashba spin-orbit field to play a significant role in bulk semiconductors, and the linear Dresselhaus field, which is proportional to the confinement along the growth axis, is expected to be small for bulk semiconductors, we expect the terms $\alpha$ and $\beta$ to be dominated by the uniaxial and biaxial strain-induced fields, respectively. We notice an interesting case, that when $\alpha = \beta$ the system enters a spin helix state [44] in which the spin-orbit effective magnetic field points along one of two opposing directions for all $\vec{k}$. Such a state is particularly useful in helping to minimize inhomogeneous dephasing due to scattering according to the D'yakonov-Perel dephasing mechanism, as will be discussed in Sec. 3.4.1.

# Chapter 3

# Carrier Scattering and Spin Relaxation

## 3.1 Introduction

In the previous chapter, we built the framework for the electron spin and its interactions in the conduction band of the GaAs band structure. We discussed the behavior of the spin in the Bloch sphere representation and built the time dependence of the spin polarization in Eq. 2.43. This chapter will expand on the time dependence by addressing the nature of the spin relaxation mechanism. It will be organized as follows. In Sec. 3.2, the mechanisms giving rise to electron scattering in the conduction band will be introduced, from which the momentum and energy relaxation times will be found. Sec. 3.3 will introduce the electron transport in low field conditions, building the mobility and distribution functions. Finally, in Sec. 3.4, the relevant spin relaxation mechanisms will be discussed, and the spin relaxation rate tensor will be developed.

## 3.2 Carrier scattering

Quantum mechanically, we treat scattering as an approximation that, over an infinitesimal time scale, a particle changes its momentum from some initial state $\vec{k}$ to a final state $\vec{k}'$. The mechanism that causes the scattering and the available initial and final momenta will depend on the situation. We can envision scattering as a "black box" and define the rate at which the scattering takes place to be $S(\vec{k}, \vec{k}')$ where the *prime* notation will be used throughout this chapter to denote the final state, and the *unprimed* notation will denote the initial state. This process is depicted in Fig. 3.1.

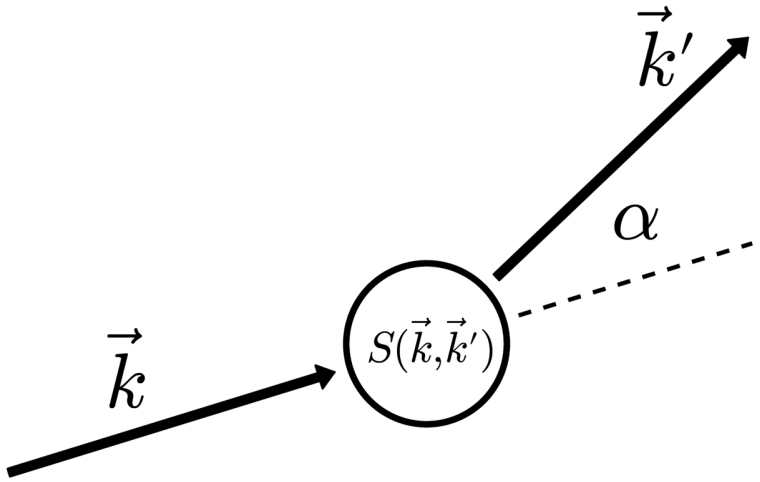


**Figure 3.1: Momentum scattering diagram:** Carrier scatters from initial momentum state $\vec{k}$ to final state $\vec{k}'$ at a rate $S(\vec{k}, \vec{k}')$.

The scattering rate can be calculated using Fermi's golden rule [70, 71]. We start with a Hamiltonian of the form $H = H_0 + H_1$ where $H_0$ is the unperturbed Hamiltonian and $H_1$ is a small perturbation that results in scattering. The solutions to $H_0$ are presumed to be known, and are given by

$$H_0 \left|\psi_{\vec{k}}^0\left(\vec{r}\right)\right\rangle = \varepsilon_{\vec{k}} \left|\psi_{\vec{k}}^0\left(\vec{r}\right)\right\rangle \tag{3.1}$$

$$\left|\psi_{\vec{k}}^0\left(\vec{r},t\right)\right\rangle = e^{-i\varepsilon_{\vec{k}}t/\hbar} \left|\psi_{\vec{k}}^0\left(\vec{r}\right)\right\rangle \tag{3.2}$$

where $\vec{r}=0$ represents the location of the scattering event. The unperturbed wave function is typically taken to be that of the free electron (i.e. a plane wave). We begin by assuming that the electron is in the state $|\psi_{\vec{k}}^0\rangle$ at time $t=0$ and in the state $|\psi_{\vec{k}'}^0\rangle$ as $t\to\infty$. In this case, the transition matrix element $H_{\vec{k}',\vec{k}}$ is approximated in terms of the unperturbed wave function as

$$H_{\vec{k}',\vec{k}}\left(t\right) = \left\langle\psi_{\vec{k}'}^0\left(\vec{r}\right)\right| H_1\left(\vec{r},t\right)\left|\psi_{\vec{k}}^0\left(\vec{r}\right)\right\rangle. \tag{3.3}$$

Suppose the perturbation causing scattering has an oscillatory time dependence, such as an oscillating field or lattice. We can represent this by taking the time dependence of the matrix element to have the form

$$H_{\vec{k}',\vec{k}}\left(t\right) = H_{\vec{k}',\vec{k}}^{a,e} e^{\pm i\omega t}. \tag{3.4}$$

Then the scattering rate from an initial momentum state $\vec{k}$ to a final state $\vec{k}'$ is expressed as (see Ref. [51] for details)

$$S\left(\vec{k},\vec{k}'\right) = \frac{2\pi}{\hbar}\left[\left|H_{\vec{k}',\vec{k}}^{a}\right|^2 \delta\left(\varepsilon_{\vec{k}'}-\varepsilon_{\vec{k}}-\hbar\omega\right) + \left|H_{\vec{k}',\vec{k}}^{e}\right|^2 \delta\left(\varepsilon_{\vec{k}'}-\varepsilon_{\vec{k}}+\hbar\omega\right)\right]. \tag{3.5}$$

Eq. 3.5 is the statement of Fermi's golden rule for determining the scattering rate between two momentum states $\vec{k}$ and $\vec{k}'$. The dirac-$\delta$ functions serve to indicate conservation of energy. Essentially it states that the energy of the final state must equal the energy of the initial state plus or minus a quanta of energy that was absorbed or emitted respectively.

This quanta of energy is usually a phonon or a photon (a quanta of acoustic wave or light energy respectively). If no energy is absorbed or emitted upon a scattering event, indicating that the perturbation is a constant in time, then Eq. 3.5 reduces to

$$S\left(\vec{k},\vec{k}'\right) = \frac{2\pi}{\hbar}\left|H_{\vec{k}',\vec{k}}\right|^2 \delta\left(\varepsilon_{\vec{k}'} - \varepsilon_{\vec{k}}\right). \tag{3.6}$$

The rest of this section will be devoted to building characteristic times for different scattering mechanisms in GaAs.

### 3.2.1 Scattering rate: momentum and energy relaxation times

We have a general form for the scattering rate for elastic (Eq. 3.6) and inelastic (Eq. 3.5) scattering mechanisms in terms of the initial and final momentum states $\vec{k}$ and $\vec{k}'$, respectively. To get the relaxation rate for a particular momentum state $\vec{k}$, then, we must sum the scattering rate over all final momenta $\vec{k}'$, weighted by the probability that the final state is unoccupied. We saw in Sec. 2.2.1 this sum takes the form

$$\frac{1}{\tilde{\tau}\left(\vec{k}\right)} = \sum_{\vec{k}'} S\left(\vec{k},\vec{k}'\right)\left[1 - f\left(\vec{k}'\right)\right]. \tag{3.7}$$

With $f(\vec{k}')$ the distribution function, then $1 - f(\vec{k}')$ is just the probability that the state $\vec{k}'$ is unoccupied. That the state $\vec{k}'$ must be unoccupied for the scattering event to occur is a result of the Pauli exclusion principle [6]. The term $\tilde{\tau}$ in Eq. 3.7 is called the carrier relaxation time and gives the characteristic time scale between scattering events. The $\sim$ accent indicates that it is the relaxation time for a particular momentum $\vec{k}$. The final carrier relaxation time will be achieved by summing over all momenta with appropriate weightings.

The momentum relaxation time is a measure of the time it takes for the momentum of a carrier to become randomized. In many semiconductors, the momentum relaxation time

is significantly longer than the carrier relaxation time, as it is the scattering rate for each momentum weighted by the fractional change in the momentum direction. The momentum relaxation time is given by

$$\frac{1}{\tilde{\tau}_m\left(\vec{k}\right)} = \sum_{\vec{k}'} S\left(\vec{k},\vec{k}'\right)\left[1 - f\left(\vec{k}'\right)\right]\left[1 - \frac{k'}{k}\cos\alpha\right] \tag{3.8}$$

where $\alpha$ is the angle between $\vec{k}$ and $\vec{k}'$ (Fig. 3.1).

Similar to the momentum relaxation time, the energy relaxation time is a measure of the time it takes for the energy of a carrier to become randomized. It is built from the carrier relaxation time with a similar weighting factor and is given by

$$\frac{1}{\tilde{\tau}_\varepsilon\left(\vec{k}\right)} = \sum_{\vec{k}'} S\left(\vec{k},\vec{k}'\right)\left[1 - f\left(\vec{k}'\right)\right]\left[1 - \frac{\varepsilon_{\vec{k}'}}{\varepsilon_{\vec{k}}}\right]. \tag{3.9}$$

Notice that the energy relaxation time is necessarily only important for inelastic scattering events. Each of the sums in Eqs. 3.7, 3.8, and 3.9 are converted to integrals with the prescription (assuming spin conserving scattering mechanisms)

$$\sum_{\vec{k}'} g\left(\vec{k}'\right) \rightarrow \frac{1}{8\pi^3}\int_{\vec{k}'} g\left(\vec{k}'\right) d\vec{k}'. \tag{3.10}$$

For electrons in thermal equilibrium, $f(\vec{k}')$ is the Fermi-Dirac distribution function given by

$$f\left(\vec{k}\right) = \frac{1}{1 + \exp\left[\left(\varepsilon_k - \mu\right)/k_B T\right]} \tag{3.11}$$

with $\mu$ the chemical potential defined as the Fermi energy at temperature $T = 0$. For semiconductors with a parabolic conduction band in the absence of any additional potential energy terms, the energy is $\varepsilon_k = \varepsilon_C + \hbar^2 k^2/(2m^*)$, with $\varepsilon_C$ the energy of the bottom of the

conduction band. We will use the Joyce-Dixon approximation [72] for the chemical potential

$$\frac{\mu - \varepsilon_C}{k_B T} \equiv \eta \cong \ln\left(\frac{n}{N_C}\right) + \frac{n}{N_C\sqrt{8}}. \tag{3.12}$$

with $n$ the free carrier concentration and $N_C$ the effective density of states. In the case of parabolic bands it is given by

$$N_C = 2\left(\frac{m^* k_B T}{2\pi\hbar^2}\right)^{3/2}. \tag{3.13}$$

The free carrier concentration in the conduction band is evaluated by taking the overlap integral of the Fermi distribution and the density of states.

$$n = \int_0^\infty d\varepsilon \left[D\left(\varepsilon\right) f\left(\varepsilon\right)\right] = N_C \mathscr{F}_{1/2}\left(\eta\right) \tag{3.14}$$

$\mathscr{F}_{1/2}$ is the Fermi-Dirac integral of order 1/2 and the density of states in three dimensions is $D(\varepsilon) = m^*\sqrt{2m^*\varepsilon}/(\pi^2\hbar^3)$. In this definition of the density of states, as well as in Eq. 3.14, I have taken $\varepsilon$ to be just the kinetic energy component of the electron energy, namely $\varepsilon = \hbar^2 k^2/(2m^*)$. In the sections to follow, we will evaluate the relaxation times for the degenerate semiconductor using the Fermi distribution function.

### 3.2.2 Ionized-impurity scattering

For doped semiconductors that give up an electron ($n$-type), the ionized impurity acts as the perturbing potential discussed in the previous section. For GaAs, a common $n$-type dopant is silicon (Si). For the samples in this study, the Si dopant concentration is $n = 3 \times 10^{16}$ cm$^{-3}$. To evaluate the scattering matrix element, we must first determine the form of the perturbation potential created by the ionized impurity. We can start by assuming, for a lone electron, that this is simply the Coulomb potential energy

$$H_1'(r) = \frac{e^2}{4\pi\epsilon r} \tag{3.15}$$

where $\epsilon$ is the dielectric constant in the material, $e$ is the electron charge, and $r$ is the radial distance between the electron and the ion. Notice that the perturbing Hamiltonian is time independent, indicating that ionized impurity scattering of this form is elastic, and the scattering rate is given by Eq. 3.6. When the electron concentration is high enough, we have to account for the attraction of electrons to the ion which effectively screen the Coulomb potential. The simplest model is to assume a uniform density of unequal positive and negative charge distributions around the ion. Poisson's equation in this form is

$$\nabla^2 V(r) = \frac{e}{\epsilon}(n - n_d) \tag{3.16}$$

where $V(r)$ is the electric potential, $n_d$ is the ionized impurity density, and $n$ is the electron density given by

$$n = N_C \mathscr{F}_{1/2}\left(\frac{\mu - \varepsilon_C + eV(r)}{k_B T}\right). \tag{3.17}$$

The fluctuation of $n$ around equilibrium is described in terms of the perturbation of the potential $\delta V$ by

$$\delta n = \frac{\partial n}{\partial V}\delta V. \tag{3.18}$$

Using the familiar relation for Fermi-Dirac integrals $\partial \mathscr{F}_n(\eta)/\partial\eta = \mathscr{F}_{n-1}(\eta)$, we have the following form for the perturbation Hamiltonian:

$$H_{1,II}(r) = \frac{e^2}{4\pi\epsilon r}\exp\left(-\frac{r}{L_D}\right) \tag{3.19}$$

where $L_D$ is the Debye screening length given for degenerate semiconductors by

$$L_D = \sqrt{\frac{\epsilon k_B T}{e^2 n_0}} \sqrt{\frac{\mathscr{F}_{1/2}(\eta)}{\mathscr{F}_{-1/2}(\eta)}} \tag{3.20}$$

and $n_0$ is the equilibrium carrier concentration. The matrix element for the perturbation Hamiltonian is evaluated according to Eq. 3.3 and the scattering rate from Eq. 3.6. The result after taking the integral is

$$H_{\vec{k}',\vec{k},II} = \frac{e^2}{\epsilon\left[4k^2\sin^2(\alpha/2) + 1/L_D^2\right]} \tag{3.21}$$

$$S_{II}\left(\vec{k},\vec{k}'\right) = \frac{\pi n_d e^4}{\hbar\epsilon^2} \frac{\delta\left(\varepsilon_{\vec{k}'} - \varepsilon_{\vec{k}}\right)}{\left[4k^2\sin^2(\alpha/2) + 1/L_D^2\right]^2}. \tag{3.22}$$

As in Fig. 3.1, $\alpha$ is the scattering angle. The factor $n_d$ in the second line is just a multiplicative factor taking into account the scattering rate for all of the ionized impurities, in which case $n_d$ represents the ionized impurity density. In this form, we take scattering events to be independent. We can define the incoming electron momentum along $\hat{z}$, in which case $\alpha$ is equivalent to the polar angle $\theta$. We use Eq. 3.7 to determine the relaxation rate as a function of electron energy:

$$\frac{1}{\tilde{\tau}_{II}(\varepsilon)} = \frac{\sqrt{\pi}e^4 N_C n_d}{\hbar\epsilon^2 (k_B T)^{3/2}} \int_0^{\pi} d\theta \int_0^{\infty} d\varepsilon' \left[\frac{\sin\theta\sqrt{\varepsilon'}\delta(\varepsilon' - \varepsilon)}{\left(\frac{8m^*}{\hbar^2}\varepsilon'\sin^2\frac{\theta}{2} + \frac{1}{L_D^2}\right)^2}\right]. \tag{3.23}$$

By using the substitution $x = 1 - \cos\theta$ and making the following definition

$$\gamma^2 = \frac{8m^* L_D^2 \varepsilon}{\hbar^2} \tag{3.24}$$

the relaxation rate becomes

$$\frac{1}{\tilde{\tau}_{II}(\varepsilon)} = \frac{\sqrt{\pi}e^4 N_C n_d L_D^4}{\hbar\epsilon^2 (k_B T)^{3/2}} \sqrt{\varepsilon}\,(1 - f(\varepsilon)) \int_0^2 \frac{dx}{[1 + (\gamma^2/2)\,x]^2}. \tag{3.25}$$

The integral is solvable, and we get for the carrier relaxation rate due to ionized impurity scattering

$$\frac{1}{\tilde{\tau}_{II}(\varepsilon)} = \frac{2\sqrt{\pi}e^4 N_C n_d L_D^4}{\hbar\epsilon^2 (k_B T)^{3/2}} \frac{\sqrt{\varepsilon}\,(1 - f(\varepsilon))}{1 + \gamma(\varepsilon)^2}. \tag{3.26}$$

The momentum relaxation time simply requires that we include a factor of $1 - \cos(\theta)$ before integration. Again, the integral is solvable, and we get the momentum relaxation rate due to ionized impurity scattering

$$\frac{1}{\tilde{\tau}_{m,II}(\varepsilon)} = \frac{4\sqrt{\pi}e^4 N_C n_d L_D^4}{\hbar\epsilon^2 (k_B T)^{3/2}} \frac{\sqrt{\varepsilon}\,(1 - f(\varepsilon))}{\gamma(\varepsilon)^4} \left[\ln\left(1 + \gamma(\varepsilon)^2\right) - \frac{\gamma(\varepsilon)^2}{1 + \gamma(\varepsilon)^2}\right]. \tag{3.27}$$

The relaxation time and momentum relaxation time for $In_{0.04}Ga_{0.96}As$ at $T = 10$ K with a doping concentration of $n = 3 \times 10^{16}$ cm$^{-3}$ is shown in Fig. 3.2. Recall that for purely elastic scattering, the energy relaxation time diverges. We can illustrate the behavior of the relaxation times in a more convenient form using some approximations. For the above analysis, we find a numerical evaluation of $\gamma \cong 25.4\ \text{eV}^{-1/2}\sqrt{\varepsilon}$. In this case, except for small energy, we can make the approximation $1 + \gamma^2 \approx \gamma^2$. The carrier relaxation time and momentum scattering time are then approximately given in power law form by

$$\tilde{\tau}_{II}(\varepsilon) \approx \tau_0 \sqrt{\frac{\varepsilon}{k_B T}} \tag{3.28}$$

$$\tilde{\tau}_{m,II}(\varepsilon) \approx \tau_{m,0} \left(\frac{\varepsilon}{k_B T}\right)^{3/2}. \tag{3.29}$$

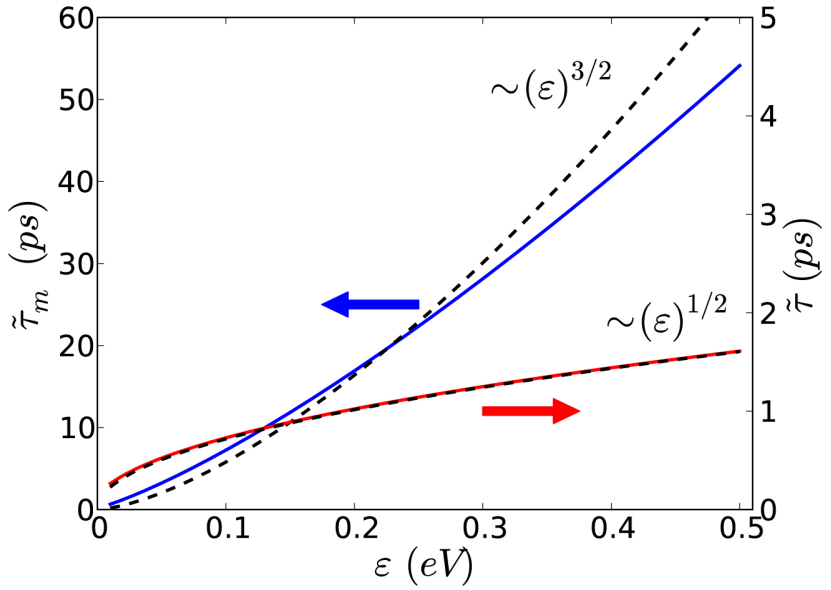


**Figure 3.2: Ionized impurity relaxation time:** Scattering time (red line, right axis) and momentum relaxation time (blue line, left axis) as a function of electron kinetic energy. Parabolic bands are assumed. Numerical evaluation is for $In_{0.04}Ga_{0.96}As$ at $T = 10$ K with a doping concentration of $n = 3 \times 10^{16}$ cm$^{-3}$. Dashed black lines represent scattering times having power law form.

The pre-factors are given by $\tau_0 = 1.96 \times 10^{-3}$ ps and $\tau_{m,0} = 0.0185\left(\ln\left(\gamma^2\right) - 1\right)^{-1}$ ps. The power law approximations are shown as the dotted black lines in Fig. 3.2. We can see that for sufficiently high energy the carrier relaxation time is in excellent agreement with the power law form of Eq. 3.28. The momentum relaxation time, however, involves a slowly varying function of the energy given by the $\ln(\gamma)$ term in Eq. 3.29. The dashed black line shows the power law form specifically for $\gamma$ evaluated at $\varepsilon = 0.225$ eV. We can see that the power law form for the momentum relaxation time due to ionized impurity scattering is only valid over a small energy range. In general, we will evaluate the relaxation times according to Eqs. 3.26 and 3.27.

### 3.2.3 Deformation potential scattering

The term phonon is used to describe a quanta of lattice vibration energy and obeys much of the same statistics and physical laws as a photon. For example, both obey Bose-Einstein statistics [3]. Phonons, however, can be classified into a broader set of groups each obeying its own distinct set of physical properties, particularly the $\varepsilon$ vs. $\vec{k}$ dispersion. A phonon can be thought of as a displacement wave traveling down a lattice. This displacement can be allowed three orthogonal directions that are linearly independent. For longitudinal waves, the displacement is along the direction of propagation, while for transverse waves, there are two orthogonal displacement directions. The longitudinal and transverse waves are depicted in the left and right columns, respectively, of Fig. 3.3.

In addition to the displacement direction, we can also classify a phonon by its mode. In the lowest order vibrational mode, each atom moves in the same direction as its neighboring atom, with the separation in phase described by the wave velocity. This is similar, in concept, to the first harmonic of a guitar string (with the exception that a guitar string is a standing wave). The next order mode consists of neighboring atoms moving in opposite directions, so we can think of a virtual node located at the halfway point between two adjacent atoms in the standing wave analogy. We typically call the lowest order mode an acoustic phonon, since this is the mode by which sound waves travel. All higher order modes are called optical phonons, though it is typical to refer to the optical phonon as just the mode directly above the acoustic mode in which neighboring atoms move in opposite directions. The acoustic and optical phonons are depicted in the top and bottom rows, respectively of Fig. 3.3.

To determine the scattering rate, we must first determine the perturbing Hamiltonian due to the lattice displacement induced by the phonon. The perturbations are due to the change in the conduction and valence band edges as a function of the change in the lattice parameter and are characterized by the deformation potentials. Consider in one dimension

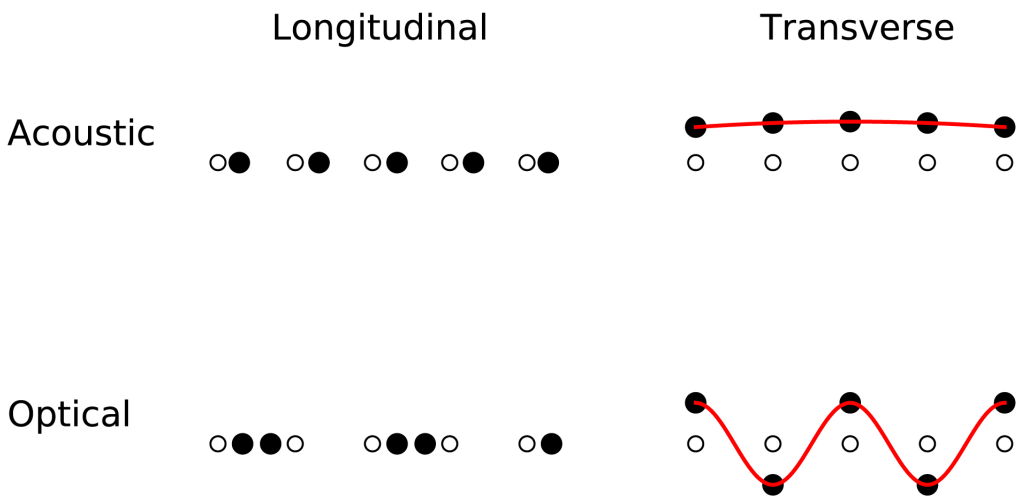


**Figure 3.3: Phonons in 1D lattice:** Atom (filled circle) is displaced from its equilibrium position (open circle) by a traveling displacement wave. Longitudinal and transverse phonons are depicted in the left and right columns, respectively, while acoustic and optical phonons are depicted in the top and bottom rows, respectively.

an acoustic wave of the form

$$u\left(x,t\right)=u_{0}e^{i(\beta x-\omega t)}+u_{0}^{*}e^{-i(\beta x-\omega t)} \tag{3.30}$$

where $u$ is taken to be a dimensionless displacement normalized to the lattice parameter $a$. It is common to use the Greek letter $\vec{\beta}$ to represent the phonon momentum (analogous to $\vec{k}$ for electrons). For an acoustic wave, the difference in displacement for adjacent atoms, that is, $u(x,t)-u(x+a,t)$, can be approximated by the derivative

$$\delta u_{A}\approx\frac{\partial u}{\partial x}a \tag{3.31}$$

This approximation is valid when the phonon wavelength is long compared to the lattice

parameter, as is expected for acoustic phonons involved in intravalley scattering [51]. For optical waves, the derivative approach is no longer valid as the wavelength is necessarily on the order of the lattice parameter. However, we note that the displacement between two adjacent atoms is just described by the sum of their respective displacements. Noting that their displacements are roughly equal and opposite, the difference in displacement for adjacent atoms is given by

$$\delta u_O \approx u \tag{3.32}$$

For acoustic and optical phonons, we have our perturbing potentials of the form

$$H_{1,A}\left(\vec{r},t\right) = D_A \nabla u\left(\vec{r},t\right) \tag{3.33}$$

$$H_{1,O}\left(\vec{r},t\right) = D_O u\left(\vec{r},t\right) \tag{3.34}$$

We have made the generalization to three dimensions, and have assumed a spherical band. For semiconductors having conduction band minima at the $L$ and $X$ points (such as germanium and silicon respectively) the band has elliptical constant energy surfaces. Furthermore, for a $p$-type valence band orbital, the band has a symmetry that is more cubic than spherical, as discussed in Sec. 2.3.1. In these cases, the deformation potential constants $D_A$ and $D_O$ will have a directional dependence. For the conduction band of GaAs, the spherical band approximation will be used and these parameters are constant. We finally point out that the difference between longitudinal and transverse waves is contained in the form of $u(\vec{r},t)$ and in the $\varepsilon$ vs. $\vec{\beta}$ dispersions.

For a full treatment of phonon dispersion, consult Ref. [73]. I will point out a few details here. The phonon band is built in much the same way as the band structure for the crystal and is reduced to the first Brillouin zone, ranging over $\pm\pi/a$. The acoustic mode is the

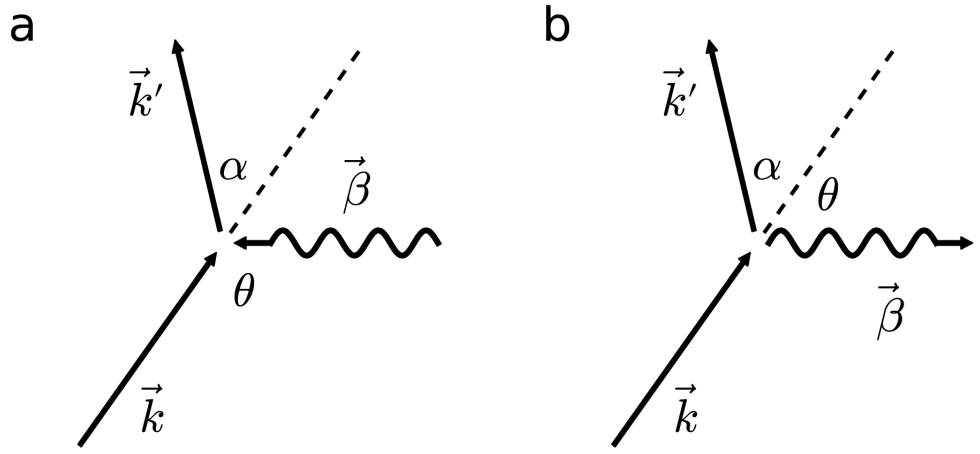


**Figure 3.4: Phonon scattering:** Electron scatters from initial momentum state $\vec{k}$ to final state $\vec{k}'$ by absorption (a) or emission (b) of a phonon with momentum state $\vec{\beta}$. $\theta$ is the angle between the initial electron and phonon momenta, and $\alpha$ is the angle between initial and final electron momenta.

lowest energy and obeys the relation $\lim_{\beta\to 0}\varepsilon_A(\beta) = 0$, with $\varepsilon_A \propto \beta$ near $\beta = 0$. The optical mode, however, necessarily has a nonzero energy as the wave vector goes to zero. This is understood in that a minimum threshold energy must be achieved to induce the creation of an optical phonon. The optical phonon is roughly constant near $\beta = 0$. For electron-phonon scattering, the wave vectors for electrons and phonons are on the same order of magnitude ($k \sim \beta$). For electrons near the $\Gamma$ point then, for which $\vec{k} = 0$, we will make the following approximations for acoustic and optical phonons:

$$\omega_A(\beta) = \upsilon_s\beta \quad , \quad \omega_O(\beta) = \omega_o \tag{3.35}$$

with $\upsilon_s$ the sound velocity of acoustic waves.

We build interactions of electrons with phonons first by requiring conservation of both energy and momentum. From Fig. 3.4, this can be expressed in terms of the initial electron, final electron, and phonon momentum states $\vec{k}$, $\vec{k}'$, and $\vec{\beta}$ respectively by

$$\frac{\hbar^2 k'^2}{2m^*} = \frac{\hbar^2 k^2}{2m^*} \pm \hbar\omega(\beta) \tag{3.36}$$

$$\vec{k}' = \vec{k} \pm \vec{\beta} \tag{3.37}$$

where the plus and minus refer to absorption and emission of a phonon by the electron, respectively. These equations together imply that the magnitude of the phonon momentum can be expressed as

$$\beta = \mp 2k\cos\theta \pm \frac{2m^*}{\hbar\beta}\omega(\beta). \tag{3.38}$$

In this expression, $\theta$ is the angle between the phonon and the incoming electron momenta. By inspection of Eq. 3.38, we notice that there is a maximum value allowed for $\beta$ as a result of simultaneous energy and momentum conservation. This is given by

$$\beta_{max} = 2k\left(1 \pm \frac{m^*}{\hbar k}\frac{\omega}{\beta_{max}}\right) \tag{3.39}$$

For phonon absorption or emission, we notice the maximum phonon momentum occurs when $\theta = \pi$ or 0, respectively. This corresponds to a phonon "hitting" the electron head on, or the electron imparting as much of its linear momentum as possible into the creation of a phonon, respectively.

We will start with the acoustic deformation potential. Using Eq. 3.33 and the periodic form for $u(\vec{r}, t)$, the perturbation potential is

$$H_{1,ADP}(\vec{r}, t) = i\beta D_A u(\vec{r}, t). \tag{3.40}$$

The scattering matrix element and rate, given by Eqs. 3.3 and 3.5 respectively, are

$$H_{\vec{k}',\vec{k},ADP} = \beta D_A u_0 \delta_{\vec{k}',\vec{k}\pm\vec{\beta}} \tag{3.41}$$

$$S_{ADP}\left(\vec{k},\vec{k}'\right) = \frac{\pi m^* D_A^2}{\hbar^2 k \rho \upsilon_s}\left(N_\beta + \frac{1}{2} \mp \frac{1}{2}\right)\delta\left(\pm\cos\theta + \frac{\beta}{2k} \mp \frac{m^*\upsilon_s}{\hbar k}\right) \tag{3.42}$$

with $\rho$ the mass density. The form of the prefactor has to do with the correct treatment of our wave amplitude $u_0$ and the quantum mechanical energy of an oscillator given by $\varepsilon = (N_\beta + 1/2)\omega$. For a detailed discussion, see Ref. [51]. The sign along the top or bottom in Eq. 3.42 is due to absorption or emission of a phonon upon the scattering event, respectively. The prefactor implies that for absorption to occur, we must have $N_\beta \neq 0$. To get the carrier relaxation rate, we integrate Eq. 3.42 according to Eq. 3.7, which gives

$$\frac{1}{\tilde{\tau}_{ADP}\left(\vec{k}\right)} = \frac{m^* D_A^2}{8\pi^2\hbar^2 k\rho\upsilon_s}\times \int_{\vec{\beta}}\left(N_\beta + \frac{1}{2} \mp \frac{1}{2}\right)\left[1 - f\left(k^2+\beta^2 \pm 2k\beta\cos\theta\right)\right]\delta\left(\pm\cos\theta + \frac{\beta}{2k} \mp \frac{m^*\upsilon_s}{\hbar k}\right)d\vec{\beta}. \tag{3.43}$$

As there is a one-to-one mapping between $\vec{k}'$ and $\vec{\beta}$, we have the liberty of integrating over $\vec{\beta}$ space instead of $\vec{k}'$ space. The delta function in the integral over $\cos\theta$ sets the value of $\cos\theta$ in the Fermi distribution, and allows us to restrict our integral in $\beta$ to the range $0 \leq \beta \leq \beta_{max}$. For acoustic phonons we use the dispersion relation $\omega = \upsilon_s\beta$ to get $\beta_{max} = 2k[1 - m^*\upsilon_s/(\hbar k)]$. In this case, the relaxation rate is

$$\frac{1}{\tilde{\tau}_{ADP}\left(\vec{k}\right)} = \frac{m^* D_A^2}{4\pi\hbar^2 k\rho\upsilon_s}\int_0^{\beta_{max}} d\beta\left\{\beta^2\left(N_\beta + \frac{1}{2} \mp \frac{1}{2}\right)\left[1 - f\left(k^2 \pm \frac{2\beta m^*\upsilon_s}{\hbar}\right)\right]\right\}. \tag{3.44}$$

As phonons are bosons, $N_\beta$ is given by the Bose-Einstein distribution function

$$N_\beta = \frac{1}{\exp\left[\frac{\hbar \upsilon_s \beta}{k_B T}\right] - 1}. \tag{3.45}$$

Eq. 3.44 does not have an analytical solution, in general, and must be solved numerically. The energy relaxation time is a trivial extension. We must simply include a factor of

$$1 - \frac{k'^2}{k^2} = \mp \frac{2m^* \upsilon_s \beta}{\hbar k^2}$$

in the integral over $\beta$. This gives the energy relaxation rate due to acoustic deformation potential scattering

$$\frac{1}{\tilde{\tau}_{\varepsilon,ADP}\left(\vec{k}\right)} = \frac{m^{*2} D_A^2}{2\pi\hbar^3 k^3 \rho} \int_0^{\beta_{max}} d\beta \left\{ \mp\beta^3 \left( N_\beta + \frac{1}{2} \mp \frac{1}{2} \right) \left[ 1 - f\left( k^2 \pm \frac{2\beta m^* \upsilon_s}{\hbar} \right) \right] \right\}. \tag{3.46}$$

The overall negative sign for absorption just indicates that an absorption event serves to counteract the energy relaxation due to an emission event. For acoustic deformation potential scattering in most semiconductors, even at low temperatures, these events happen at a similar rate, and therefore energy relaxation times can be extremely long. As such, this is usually ignored as a source of energy relaxation. In fact, in the high temperature limit, we can approximate $N_\beta + 1 \approx N_\beta$ and $1 - f(k') \approx 1$, in which case the energy relaxation rate goes to zero and acoustic deformation potential scattering becomes an elastic process.

To calculate the momentum relaxation rate, we introduce a factor of $1 - k' \cos\alpha / k$ in the integral over $\beta$. Using the definition $\vec{\beta} = \pm(\vec{k'} - \vec{k})$ and conservation of energy, we have the expression

$$1 - \frac{k'}{k}\cos\alpha = \frac{\beta}{k^2}\left( \frac{\beta}{2} \mp \frac{m^* \upsilon_s}{\hbar} \right).$$

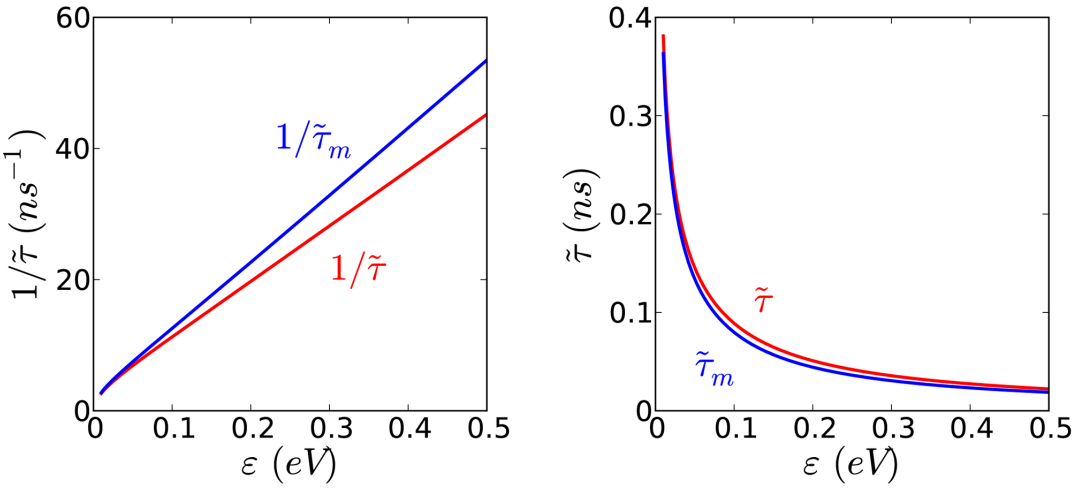


**Figure 3.5: Acoustic deformation potential relaxation time:** Relaxation rate (left) and time (right) as a function of electron kinetic energy. Parabolic bands are assumed. Numerical evaluation is for $In_{0.04}Ga_{0.96}As$ at $T = 10$ K with a doping concentration of $n = 3 \times 10^{16}$ cm$^{-3}$. For low temperature, the scattering rate is roughly linear and several orders of magnitude weaker than ionized impurity scattering.

The momentum relaxation rate due to acoustic deformation potential scattering is

$$\frac{1}{\tilde{\tau}_{m,ADP}\left(\vec{k}\right)} = \frac{m^* D_A^2}{4\pi\hbar^2 k^3 \rho \upsilon_s} \times \int_0^{\beta_{max}} d\beta \left\{ \beta^3 \left( \frac{\beta}{2} \mp \frac{m^* \upsilon_s}{\hbar} \right) \left( N_\beta + \frac{1}{2} \mp \frac{1}{2} \right) \left[ 1 - f\left( k^2 \pm \frac{2\beta m^* \upsilon_s}{\hbar} \right) \right] \right\}. \tag{3.47}$$

Fig. 3.5 shows the carrier and momentum relaxation rates and times as a function of electron kinetic energy for $In_{0.04}Ga_{0.96}As$ at a temperature of $T = 10$ K with a doping density of $n = 3 \times 10^{16}$ cm$^{-3}$. We see that the scattering rate is roughly a linear function of the electron energy, in contrast to the room temperature behavior obeying a $\sqrt{\varepsilon}$ dependence. We also notice that the relaxation time and momentum relaxation time are nearly equal. This implies that the scattering due to acoustic deformation potential phonons is nearly

isotropic. In the high temperature limit of elastic scattering and equipartition, we find that the functional forms of the relaxation time and momentum relaxation time are exactly the same. We finally notice that the relaxation time is several orders of magnitude longer than that of ionized impurities. We will see in Sec. 3.2.6 that this implies that relaxation due to acoustic deformation potential scattering is a non-dominant effect.

The optical deformation potential scattering term is found in a similar way, where now we use the approximate form of the optical phonon dispersion given by $\omega = \omega_o$. The perturbation Hamiltonian, given by Eq. 3.34, gives us a matrix element and scattering rate of

$$H_{\vec{k}',\vec{k},ODP} = D_o u_0 \delta_{\vec{k}',\vec{k}\pm\delta} \tag{3.48}$$

$$S_{ODP}\left(\vec{k},\vec{k}'\right) = \frac{\pi m^* D_o^2}{\hbar^2 k \rho \omega_o \beta}\left(N_\beta + \frac{1}{2} \mp \frac{1}{2}\right)\delta\left(\pm\cos\theta + \frac{\beta}{2k} \mp \frac{m^*\omega_o}{\hbar k\beta}\right). \tag{3.49}$$

The scattering rate is achieved by substituting $D_A \to D_o/\beta$ and $\upsilon_s \to \omega_o/\beta$ in Eq. 3.42. We can figure out the scattering rate using Fermi's golden rule, as before. We must first, however, determine both the maximum and minimum allowed phonon momenta $\beta$ from conservation of energy and momentum. For acoustic phonons, we could have arbitrarily small $\beta$ as $\omega_\beta \to 0$. For optical phonons, however, we take $\omega(\beta) = \omega_o = const.$ For absorption (emission), we substitute $\theta = 0$ ($\pi$) and $\pi$ (0) into Eq. 3.38 to get $\beta_{min}$ ($\beta_{max}$) and $\beta_{max}$ ($\beta_{min}$) respectively. This gives

$$\beta_{max,ODP} = k\left(1 + \sqrt{1 \pm \frac{2m^*\omega_o}{\hbar k^2}}\right) \quad , \quad \beta_{min,ODP} = k\left(\mp 1 \pm \sqrt{1 \pm \frac{2m^*\omega_o}{\hbar k^2}}\right). \tag{3.50}$$

Notice that for absorption, all electron momenta $k$ are allowed. For emission to occur, however, the term in the square root must be positive, implying that $\hbar^2 k^2/(2m^*) \geq \hbar\omega_o$.

This makes sense, as this just requires that for an electron to emit an optical phonon in a scattering event, the initial electron energy must be greater than or equal to the optical phonon energy that it emits.

As with the acoustic deformation potential, we can take the integral over $\vec{\beta}$ space and find that the carrier relaxation rate is

$$\frac{1}{\tilde{\tau}_{ODP}\left(\vec{k}\right)} = \frac{m^* D_o^2}{4\pi\hbar^2 k\rho\omega_o}\int_{\beta_{min}}^{\beta_{max}} d\beta\left\{\beta\left(N_\beta + \frac{1}{2} \mp \frac{1}{2}\right)\left[1 - f\left(k^2 \pm \frac{2m^*\omega_o}{\hbar}\right)\right]\right\} \tag{3.51}$$

We notice that when the optical phonon dispersion can be treated as roughly constant with respect to $\beta$, then $N_\beta = N_{\omega_o} = 1/[\exp(\hbar\omega_o/k_BT) - 1]$. This term, as well as the term involving the Fermi distribution function, comes out of the integral, and, substituting for $\beta_{min}$ and $\beta_{max}$, we have the carrier relaxation rate due to optical deformation potential phonons as

$$\frac{1}{\tilde{\tau}_{ODP}\left(\varepsilon\right)} = \frac{\left(2m^*\right)^{3/2} D_o^2}{4\pi\hbar^3\rho\omega_o}\left(N_{\omega_o} + \frac{1}{2} \mp \frac{1}{2}\right)\left[1 - f\left(\varepsilon \pm \hbar\omega_o\right)\right]\sqrt{\varepsilon \pm \hbar\omega_o} \tag{3.52}$$

where I have substituted the electron kinetic energy $\varepsilon = \hbar^2k^2/(2m^*)$. We see that, in the approximation of a parabolic, spherical conduction band having a constant optical phonon dispersion, the optical deformation potential relaxation rate has a $\sqrt{\varepsilon}$ dependence. To calculate the energy relaxation, we include the term $1 - \varepsilon'/\varepsilon$ in the integrand, where the final electron energy is $\varepsilon' = \varepsilon \pm \hbar\omega_o$ for absorption and emission, respectively. This is a constant term and comes out of the integral. The energy relaxation rate due to optical deformation potential scattering is

$$\frac{1}{\tilde{\tau}_{\varepsilon,ODP}\left(\varepsilon\right)} = \mp\frac{\hbar\omega_o}{\varepsilon}\frac{1}{\tilde{\tau}_{ODP}\left(\varepsilon\right)}. \tag{3.53}$$

The momentum relaxation rate is deceptively simple. As before we must include a term $1-(k'\cos\alpha)/k = \beta^2/(2k^2) \mp m^*\omega_o/(\hbar k^2)$ in the integrand. After evaluating the integral we have the term

$$\frac{\beta^4}{8k^2} \mp \frac{m*\omega_o\beta^2}{2\hbar k^2}\Bigg|_{\beta_{min}}^{\beta_{max}} = 2k^2\sqrt{1 \mp \frac{2m^*\omega_o}{\hbar k^2}}.$$

We notice that this is equal to $(\beta_{max}^2 - \beta_{min}^2)/2$, which was the result of the integral of the relaxation rate. The result for the momentum relaxation rate is

$$\frac{1}{\tilde{\tau}_{m,ODP}(\varepsilon)} = \frac{1}{\tilde{\tau}_{ODP}(\varepsilon)} \tag{3.54}$$

This implies that scattering due to optical deformation potential phonons is isotropic. There is a caveat. If we look closely at Eq. 3.38, we realize that very near $k = 0$ there is no solution when $\omega$ is a constant. As such, optical deformation potential scattering does not have an effect at the $\Gamma$ point. Perturbations in the electric field produced by optical phonons, however, do have an effect that can become very strong at high temperatures, as we will see in Sec. 3.2.5.

### 3.2.4 Piezoelectric scattering

Piezoelectric scattering can be a common feature in polar semiconductors in which the neighboring atoms are partially ionized. When an acoustic phonon travels through the crystal, in addition to inducing a perturbation due to the deformation of the lattice, there is an additional perturbation due to the electric dipole wave generated by the phonon. The absorption and emission of an acoustic wave obeys the same physics as in the previous section, we just need to amend the form of the perturbation potential. In the same way that the acoustic phonon perturbed the lattice spacing by the form $\delta a \propto \partial u/\partial x$, we can characterize local fluctuations in the electric dipole moment by the relation

$$\epsilon E = -e_{pz}\frac{\partial u\left(x,t\right)}{\partial x} \tag{3.55}$$

where $E$ is the electric field, $e_{pz}$ is a material constant, $\epsilon$ is the permittivity of the material, and $u(x,t)$ is the form of the phonon wave function. Using the familiar relation $H = qV = q\int dx[E(x))]$, we get that the perturbation potential is

$$H_{1,PZ}\left(\vec{r},t\right) = -\frac{ee_{pz}u\left(\vec{r},t\right)}{\epsilon}. \tag{3.56}$$

The matrix element and scattering rate are

$$H_{\vec{k}',\vec{k},PZ} = \frac{ee_{pz}u_0}{\epsilon}\delta_{\vec{k}',\vec{k}\pm\vec{\beta}} \tag{3.57}$$

$$S_{PZ}\left(\vec{k},\vec{k}'\right) = \frac{\pi m^* e^2 e_{pz}^2}{\hbar^2 k\epsilon^2\rho\upsilon_s\beta^2}\left(N_\beta + \frac{1}{2} \mp \frac{1}{2}\right)\delta\left(\pm\cos\theta + \frac{\beta}{2k} \mp \frac{m^*\upsilon_s}{\hbar k}\right). \tag{3.58}$$

The scattering rate obeys a very similar form to that of the acoustic deformation potential in Eq. 3.42, with the functional dependence differing only by a factor of $1/\beta^2$. We can build the carrier relaxation time in much the same way, and we get

$$\frac{1}{\tilde{\tau}_{PZ}\left(\vec{k}\right)} = \frac{m^* e^2 e_{pz}^2}{4\pi\hbar^2 k\epsilon^2\rho\upsilon_s}\int_0^{\beta_{max}} d\beta\left\{\left(N_\beta + \frac{1}{2} \mp \frac{1}{2}\right)\left[1 - f\left(k^2 \pm \frac{2\beta m^*\upsilon_s}{\hbar}\right)\right]\right\}. \tag{3.59}$$

Similarly the energy and momentum relaxation times are given by

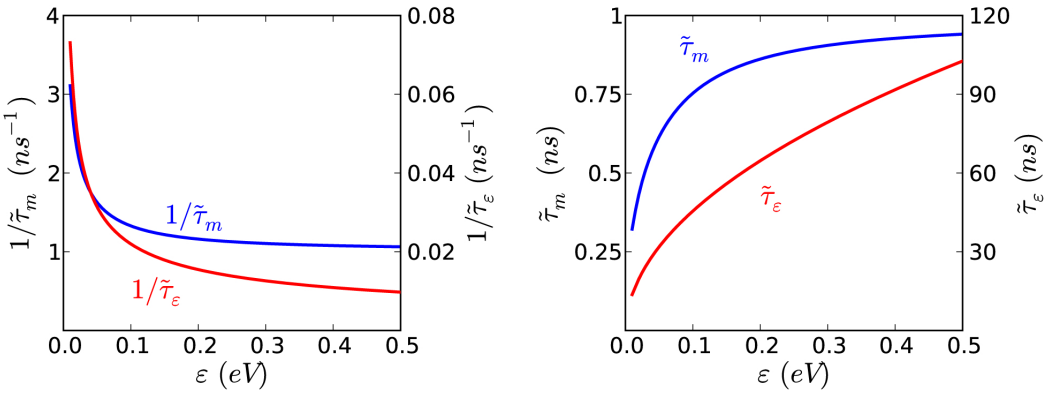


**Figure 3.6: Piezoelectric relaxation time:** Relaxation rates (left) and times (right) as a function of electron kinetic energy. Momentum and energy relaxation times are shown. Parabolic bands are assumed. Numerical evaluation is for $In_{0.04}Ga_{0.96}As$ at $T = 10$ K with a doping concentration of $n = 3 \times 10^{16}$ cm$^{-3}$. Momentum scattering rate is an order of magnitude weaker than ionized impurity scattering.

$$\frac{1}{\tilde{\tau}_{\varepsilon,PZ}\left(\vec{k}\right)} = \frac{m^{*2}e^2e_{pz}^2}{2\pi\hbar^3k^3\epsilon^2\rho}\int_0^{\beta_{max}} d\beta \left\{\mp\beta\left(N_\beta + \frac{1}{2} \mp \frac{1}{2}\right)\left[1 - f\left(k^2 \pm \frac{2\beta m^* v_s}{\hbar}\right)\right]\right\} \quad (3.60)$$

$$\frac{1}{\tilde{\tau}_{m,PZ}\left(\vec{k}\right)} = \frac{m^*e^2e_{pz}^2}{4\pi\hbar^2k^3\epsilon^2\rho v_s}\times \int_0^{\beta_{max}} d\beta \left\{\beta\left(\frac{\beta}{2} \mp \frac{m^* v_s}{\hbar}\right)\left(N_\beta + \frac{1}{2} \mp \frac{1}{2}\right)\left[1 - f\left(k^2 \pm \frac{2\beta m^* v_s}{\hbar}\right)\right]\right\}. \quad (3.61)$$

The momentum and energy relaxation times due to piezoelectric scattering are depicted in Fig. 3.6 for $In_{0.04}Ga_{0.96}As$ at $T = 10$ K with a doping concentration of $3 \times 10^{16}$ cm$^{-3}$. The scattering rate at high temperature is characterized by roughly a $1/\sqrt{\varepsilon}$ dependence. At low temperature such a form is not accurate and the value is achieved through direct integration of Eqs. 3.59- 3.61. We finally make a note that the integral in Eq. 3.59 diverges as $\beta \to 0$. Such is true for the form presented in this section, however, to more accurately treat piezoelectric scattering for low $\beta$ (and low energy, for that matter), it is necessary to

include a screening term as in Ref. [74]. Piezoelectric scattering is not expected to dominate in this case [75], however, so we will will forego such rigorous analysis.

### 3.2.5 Fröhlich scattering

In the same sense that piezoelectric scattering was caused by polar acoustic phonons, Fröhlich scattering (sometimes called longitudinal optical (LO) phonon or polar optical phonon scattering) is a result of the polarization wave generated by polar optical phonons. We build it in a similar way as we did for piezoelectric scattering. In the case of optical phonons, we can characterize local fluctuations in the electric field normalized to the unit cell by

$$\epsilon_0 E = -q' u\left(x,t\right) \tag{3.62}$$

where $q'$ represents a fraction of the electron charge $e$ that participates in the polar bond. The perturbation Hamiltonian is given by $H_1 = -eV = e\int dx(E)$. With the form of the LO phonon wave, this gives

$$H_{1,FR}\left(\vec{r},t\right) = \frac{ieq'}{\beta\epsilon_0} u\left(\vec{r},t\right) \tag{3.63}$$

The transition matrix element is evaluated as for the optical deformation potential phonon, and we have

$$H_{\vec{k}',\vec{k},FR} = \frac{ieq'u_0}{\beta\epsilon} \tag{3.64}$$

$$S_{FR} = \frac{\pi m^* e^2 q'^2}{\hbar^2 k\rho\omega_o\epsilon_0^2\beta^3}\left(N_{\omega_o}+\frac{1}{2}\mp\frac{1}{2}\right)\delta\left(\pm\cos\theta+\frac{\beta}{2k}\mp\frac{m^*\omega_o}{\hbar k\beta}\right). \tag{3.65}$$

We can evaluate the fractional charge participating in the polar bond according to the dielectric constant of the material at zero frequency and for $\beta\to\infty$. Details can be found

in Ref. [74]. We present the results here, with the definition of the dielectric constant as $\epsilon = \kappa\epsilon_0$:

$$\frac{q'^2}{\rho\omega_o} = \epsilon_0\omega_o\left(\frac{1}{\kappa_\infty} - \frac{1}{\kappa_0}\right) \tag{3.66}$$

where $\kappa_0$ and $\kappa_\infty$ represent the dielectric constant at zero and infinite frequency respectively.

The integral over $\beta$ space to determine the carrier relaxation rate is achieved in the usual fashion, where the $\delta$-function again puts restrictions on the range of the integral over $\beta$. The carrier relaxation rate is

$$\frac{1}{\tilde{\tau}_{FR}(k)} = \frac{m^* e^2\omega_o}{4\pi\hbar^2\epsilon_0 k}\left(\frac{1}{\kappa_\infty} - \frac{1}{\kappa_0}\right)\left(N_{\omega_o} + \frac{1}{2} \mp \frac{1}{2}\right)\left[1 - f\left(k^2 \pm \frac{2m^*\omega_o}{\hbar}\right)\right]\int_{\beta_{min}}^{\beta_{max}} \frac{d\beta}{\beta}. \tag{3.67}$$

The integral becomes $\ln(\beta_{max}/\beta_{min})$. With $\beta_{max}$ and $\beta_{min}$ given for optical phonons in Eq. 3.50, we have the carrier relaxation rate for Frölich scattering:

$$\frac{1}{\tilde{\tau}_{FR}(\varepsilon)} = \frac{m^* e^2\omega_o}{4\pi\hbar\epsilon_0\sqrt{2m^*\varepsilon}}\left(\frac{1}{k_\infty} - \frac{1}{k_0}\right)\left[1 - f\left(\varepsilon \pm \hbar\omega_o\right)\right]\left(N_{\omega_o} + \frac{1}{2} \mp \frac{1}{2}\right) \times \ln\left(\frac{1 + \sqrt{1 \pm \hbar\omega_o/\varepsilon}}{\mp 1 \pm \sqrt{1 \pm \hbar\omega_o/\varepsilon}}\right) \tag{3.68}$$

where again for emission we only evaluate the rate when $\varepsilon \geq \hbar\omega_o$. To evaluate the momentum and energy relaxation times, we proceed in the same fashion as with the optical deformation potential scattering, including the terms $1-(k'\cos\alpha)/k$ and $1-\varepsilon'/\varepsilon$ respectively. The results are

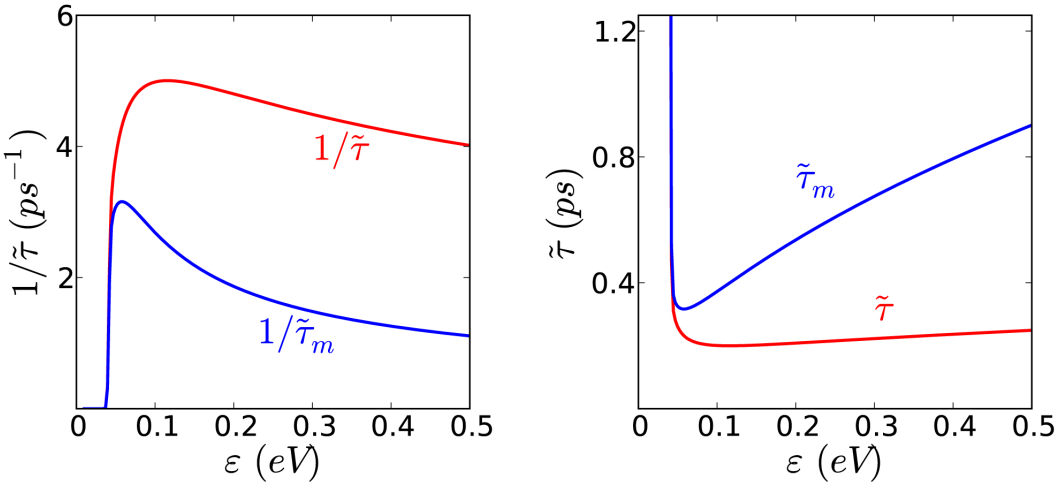


**Figure 3.7: Fröhlich relaxation time:** Scattering and momentum relaxation rates (left) and times (right) as a function of electron kinetic energy. Parabolic bands are assumed. Numerical evaluation is for $In_{0.04}Ga_{0.96}As$ at $T = 10$ K with a doping concentration of $n = 3 \times 10^{16}$ cm$^{-3}$.

$$\frac{1}{\tilde{\tau}_{m,FR}(\varepsilon)} = \frac{m^* e^2 \omega_o}{4\pi\hbar\epsilon_0\sqrt{2m^*\varepsilon}} \left(\frac{1}{k_\infty} - \frac{1}{k_0}\right) [1 - f(\varepsilon \pm \hbar\omega_o)] \left(N_{\omega_o} + \frac{1}{2} \mp \frac{1}{2}\right) \times \left[\sqrt{1 \pm \frac{\hbar\omega_o}{\varepsilon}} \mp \frac{\hbar\omega_o}{2\varepsilon} \ln\left(\frac{1 + \sqrt{1 \pm \hbar\omega_o/\varepsilon}}{\mp 1 \pm \sqrt{1 \pm \hbar\omega_o/\varepsilon}}\right)\right] \tag{3.69}$$

$$\frac{1}{\tilde{\tau}_{\varepsilon,FR}(\varepsilon)} = \mp \frac{\hbar\omega_o}{\varepsilon} \frac{1}{\tilde{\tau}_{FR}(\varepsilon)}. \tag{3.70}$$

Fig. 3.7 shows the carrier and momentum relaxation times due to Fröhlich scattering for $In_{0.04}Ga_{0.96}As$ at $T = 10$ K with a doping concentration of $n = 3 \times 10^{16}$ cm$^{-3}$. Note that the relaxation rate increases by many orders of magnitude once phonon emission is allowed. One may notice that the Fröhlich relaxation rate appears to dominate over ionized impurities, which is true at very high electron energies. However, we point out that, at low temperatures, the Fermi distribution function goes to nearly zero at energies well below that required for phonon emission. At high temperatures, however, Fröhlich scattering can play an important,

and usually dominant, role as the relaxation rate due to phonon absorption increases by many orders of magnitude and is on the order of that due to emission. Furthermore, the high energy tail of the Fermi distribution extends further at high temperature as well. This will be discussed in more detail in the following section.

### 3.2.6 Other scattering effects and the total scattering time

There are other scattering effects that are worth mentioning, even if they do not contribute significantly to the relaxation rates for GaAs at our temperatures and doping concentrations of interest. One of these is intervalley scattering, in which a phonon of sufficient momentum is absorbed or emitted such that the electron undergoes a transition to a neighboring valley. For GaAs, this most commonly occurs at high doping concentrations, in extremely high fields or temperatures [76] such that an electron in the $\Gamma$ valley can move to one of the eight neighboring $L$ valleys or six neighboring $X$ valleys. It is also common in indirect band gap semiconductors such as silicon or germanium. In these cases, we can have transitions between different types of valleys (i.e. $L \leftrightarrow X$), or between the same type of valley (i.e. $L \leftrightarrow L$ and $X \leftrightarrow X$) as there are multiple instances of these valleys.

Neutral impurity scattering can play an influential role [77] as well, particularly at extremely low temperatures such that the donor electrons (or acceptor holes) are "frozen out." It also occurs in situations where a dilute neutral substitutional atom is introduced. Using $\vec{k} \cdot \vec{p}$ theory (Sec. 2.3.2), we found that we can treat an electron in a pure, infinite semiconductor with parabolic, isotropic bands as a free electron with an effective mass different from that of the free electron mass. In the simplest view, then, the ionized impurity can be treated as a Hydrogen atom, causing scattering from either polarization effects or through exchange interactions. For doping impurities, it is only expected when the dopant electrons are donor bound. For our purposes, we are beyond the metal to insulator transition for GaAs [78], and we treat the silicon impurities as ionized.

Electrons can also scatter off other electrons in semiconductors for which the free carrier level is beyond a certain threshold. This can be treated as a binary process, which is similar in principle to the process of scattering due to ionized impurities with the exception that the scattering center is no longer stationary. This requires a rather rigorous treatment to determine the distribution function of the "target" electron. Scattering can also occur between an electron and local oscillations in the electron density. Such oscillations occur at the plasma frequency. As long as the scattering rate does not exceed the oscillation frequency, these oscillations are sustained and can contribute significantly to scattering. This frequency is called the plasmon frequency and is used to classically describe the frequency dependence of the dielectric constant

$$\epsilon(\omega) = 1 - \frac{\omega_p^2}{\omega^2}.$$

For GaAs, plasmon scattering is not expected to contribute significantly for doping concentrations below $1 \times 10^{17}$ cm$^{-3}$ [79], which is an order of magnitude above our doping concentrations of interest. As such, we will ignore the effects of electron-plasmon scattering, as well as electron-electron scattering.

We are now in a position to evaluate the total scattering rate due to the mechanisms described in the previous sections. As is common with time dependent differential equations, we treat the time derivative of a certain function $f$ as a sum of the individual influences $\Gamma$ on $f$ (assuming these influences are noninteracting). As a simple analogy to classical mechanics, consider the total force $(d\vec{p}/dt)$ acting on an object is given by the sum of the forces. In this sense, we can build the total scattering rate from the sum of the scattering rates due to all processes, given by

$$\tilde{\Gamma} \equiv \frac{1}{\tilde{\tau}} = \frac{1}{\tilde{\tau}_{II}} + \frac{1}{\tilde{\tau}_{ADP}} + \frac{1}{\tilde{\tau}_{ODP}} + \frac{1}{\tilde{\tau}_{PZ}} + \frac{1}{\tilde{\tau}_{FR}} + ... \tag{3.71}$$

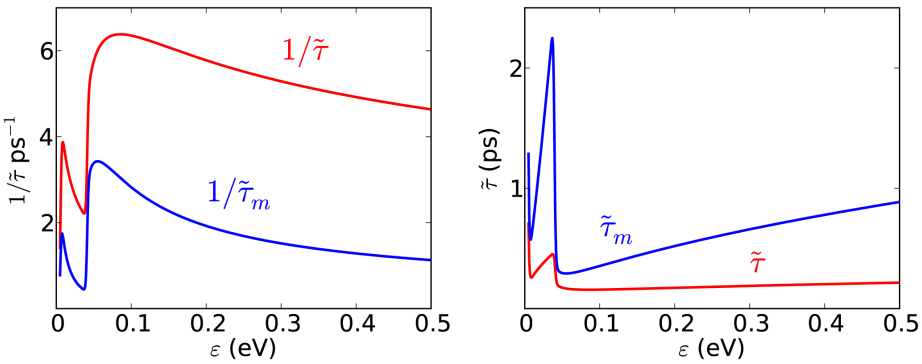


**Figure 3.8: Total relaxation rate and time:** Relaxation rate (left) and time (right) determined from Eq. 3.71. It is dominated almost entirely by ionized impurity and Fröhlich scattering. Numerical evaluation is for $In_{0.04}Ga_{0.96}As$ at $T = 10$ K with a doping concentration of $n = 3 \times 10^{16}$ cm$^{-3}$.

where I have introduced the Greek letter $\Gamma$ to represent the scattering rate. From the form of Eq. 3.71, it is apparent that those mechanisms having the shortest relaxation times will contribute most strongly to scattering. The same form applies to the momentum and energy relaxation times. Fig. 3.8 shows the total carrier and momentum relaxation rate (left) and time (right) due to the mechanisms worked out in this chapter. Comparison to the previous plots shows that relaxation is dominated almost entirely by ionized impurity scattering at low electron kinetic energy, and by the combined effect of ionized impurity and Fröhlich scattering beyond the threshold for optical phonon emission. These calculations are evaluated for $In_{0.04}Ga_{0.96}As$ at $T = 10$ K at a doping concentration of $3 \times 10^{16}$ cm$^{-3}$.

## 3.3 Low field transport

The above methods were used to describe electron scattering, particularly with an emphasis on the momentum relaxation rate, describing the rate at which an ensemble of electrons with a particular initial momentum $\vec{k}$ will become randomized. But the distribution function we used was isotropic in $\vec{k}$, which suggests that no net momentum can exist. We can see this by taking the average momentum, defined by

$$\langle \vec{k} \rangle \equiv \frac{\int_{\vec{k}} \vec{k} f\left(\vec{k}\right) d\vec{k}}{\int_{\vec{k}} f\left(\vec{k}\right) d\vec{k}} = 0$$

To treat the distribution function properly, we must go out of equilibrium. To do this, we will use the Boltzmann transport equation. We will see that at low electric fields, and therefore low electron velocities, we can describe the electrons as being in near equilibrium, and we will use a modified form of the Fermi-Dirac distribution function. For a detailed discussion, consult Ref. [80].

### 3.3.1 Boltzmann transport equation

Our goal is to build the time dependence of the electron distribution function in near equilibrium conditions. Obviously, in equilibrium, $df/dt = 0$. In carrier transport, it is common to assume that the distribution function is characterized by three variables: position, momentum, and time. In this case, the time dependent distribution function is given by

$$\frac{df}{dt} = \frac{\partial f}{\partial t} + \frac{\partial f}{\partial \vec{p}} \cdot \frac{d\vec{p}}{dt} + \frac{\partial f}{\partial \vec{r}} \cdot \frac{d\vec{r}}{dt} \tag{3.72}$$

where it is understood that $\partial f/\partial \vec{r} = \nabla_r f$, and similarly for $\vec{p}$. It is common to use the definitions $d\vec{p}/dt = \vec{F}$ and $d\vec{r}/dt = \vec{v}$, where $\vec{F}$ and $\vec{v}$ are the force and velocity respectively, in which case we have

$$\frac{df}{dt} = \frac{\partial f}{\partial t} + \vec{F} \cdot \nabla_p f + \vec{v} \cdot \nabla_r f. \tag{3.73}$$

The next step is to evaluate what physical phenomena give rise to the transient behavior of the distribution function. We saw that the scattering mechanisms presented in the previous section were one such case, and this is the case that we will focus on. We will also include terms that allow for generation and decay of carriers as well. This could be, for example, due

to optical generation and recombination of electron-hole pairs, which will be characterized by the terms $G$ and $R$ respectively. Plugging these terms into the left side of Eq. 3.73, we have

$$\left.\frac{df}{dt}\right|_{scatt} + G - R = \frac{\partial f}{\partial t} + \vec{F} \cdot \nabla_p f + \vec{v} \cdot \nabla_r f. \tag{3.74}$$

Eq. 3.74 is the Boltzmann transport equation [81]. It is typically solved for $\partial f/\partial t$ to determine the functional time dependence of the distribution function. We point out that $f$ could depend on any number of variables, in which case we must include additional partial derivatives on the right. For the moment, we will take $G = R$, such that carrier generation and recombination is in equilibrium. Our last remaining goal is to evaluate the scattering derivative on the left. We can evaluate this, for a particular momentum, based on the scattering rate determined in the previous section (Eq. 3.71). To treat this for all momenta, we then simply need to integrate over $\vec{k}$ space with the appropriate weighting function. This is given by

$$\left.\frac{df}{dt}\right|_{scatt,out} = -\frac{1}{8\pi^3}\int_{\vec{k}} \frac{1}{\tilde{\tau}_{\vec{k}}} f\left(\vec{k}\right) d\vec{k} = -\frac{1}{\left(8\pi^3\right)^2}\int_{\vec{k}} d\vec{k} \int_{\vec{k}'} d\vec{k}' \left\{ S\left(\vec{k},\vec{k}'\right) f\left(\vec{k}\right)\left[1 - f\left(\vec{k}'\right)\right]\right\} \tag{3.75}$$

where in the last step I substituted in the integral form of Eq. 3.7. Eq. 3.75 represents the rate at which carriers scatter "out" (hence the overall minus sign) from a particular momentum $\vec{k}$ to $\vec{k}'$ summed over all $\vec{k}$ and $\vec{k}'$. However, to conserve carrier numbers, for every "out" scattering event, we must consider that this corresponds to an "in" scatter into a different momentum. Including both in- and out-scattering, the total scattering derivative becomes

$$\left.\frac{df}{dt}\right|_{scatt} = \frac{1}{(8\pi^3)^2}\int_{\vec{k}} d\vec{k}\int_{\vec{k}'} d\vec{k}'\left\{S\left(\vec{k}',\vec{k}\right)f\left(\vec{k}'\right)\left[1-f\left(\vec{k}\right)\right]-S\left(\vec{k},\vec{k}'\right)f\left(\vec{k}\right)\left[1-f\left(\vec{k}'\right)\right]\right\} \tag{3.76}$$

Eq. 3.76 is used to determine the distribution function in the Boltzmann transport equation when scattering processes are present. We finally point out that this was demonstrated by defining a state according to its momentum, however this can be achieved using any definition of the electron state, as long as the appropriate weighting function is used.

### 3.3.2 Mobility calculations

As was pointed out previously, in equilibrium the distribution function is given by the Fermi-Dirac form, which is isotropic in momentum and, as such, implies no net current flow. In the relaxation time approximation [51], we can approximate that the distribution function can be described almost entirely by the equilibrium distribution plus a small anisotropic perturbation, namely

$$f\left(\vec{k},t\right) = f_{\mu^*}\left(\vec{k}\right) + f_A\left(\vec{k},t\right). \tag{3.77}$$

The term $\mu^*$ is the quasi-chemical potential [62], with a deviation from the chemical potential described by the material and conditions giving rise to scattering. We make the approximation, under low field conditions, that $f_{\mu^*}$ does not contribute to the scattering derivative [51], which can be seen by taking the integral in Eq. 3.76 using the Fermi-Dirac distribution function. In this case, the scattering derivative is given by

$$\left.\frac{df\left(\vec{k},t\right)}{dt}\right|_{scatt} = \left.\frac{df_A\left(\vec{k},t\right)}{dt}\right|_{scatt} = -\frac{f_A\left(\vec{k},t\right)}{\tilde{\tau}_m\left(\vec{k}\right)} \tag{3.78}$$

where the last step is the relaxation time approximation, with $\tilde{\tau}_m$ the momentum relaxation time. It is valid under low field conditions when the scattering mechanism is either elastic or isotropic. Using the Boltzmann transport equation in the presence of a weak electric field ($\vec{E}$), assuming no temporal or spatial dependence in the distribution function, the asymmetric part of the distribution function is given by

$$f_A\left(\vec{k}\right) = e\tilde{\tau}_m \vec{E} \cdot \nabla_p f\left(\vec{k}\right). \tag{3.79}$$

We can make the approximation in the low field limit that $\nabla_p f \approx -\upsilon f/(k_B T)$. Using some foresight, we know that an electric field gives rise to a nonzero average velocity of carriers, and we can evaluate this velocity by integrating over momentum:

$$\langle \upsilon \rangle = \frac{1}{m^*} \frac{\int_{\vec{k}} d\vec{k}\,[pf\,(p)]}{\int_{\vec{k}} d\vec{k}\,[f\,(k)]} \tag{3.80}$$

where I used the substitution $p = m^*\upsilon$. Noting that $\int [pf_{\mu'}(p)]dp = 0$, as was discussed previously, and recognizing that the mobility ($\mu$) is defined for electrons by the relation $\langle \vec{v} \rangle = -\mu \vec{E}$, we can solve Eq. 3.80 to get

$$\mu = \frac{e}{m^*} \frac{\langle \varepsilon \tau_m\,(\varepsilon) \rangle}{\langle \varepsilon \rangle} \tag{3.81}$$

where here $\mu$ is defined to be the carrier mobility, not to be confused with the chemical potential. We can use the momentum relaxation times from the previous section to solve for the carrier mobility. This is shown, as a function of temperature for $In_{0.04}Ga_{0.96}As$ at a doping concentration of $n = 3 \times 10^{16}$ cm$^{-3}$ in Fig. 3.9. The blue line is the calculated mobility using the total momentum relaxation time described by Eq. 3.71, while the dashed red and green lines represent the mobility calculated using only the ionized impurity and Fröhlich momentum relaxation times. Blue circles are measurements of the mobility for a

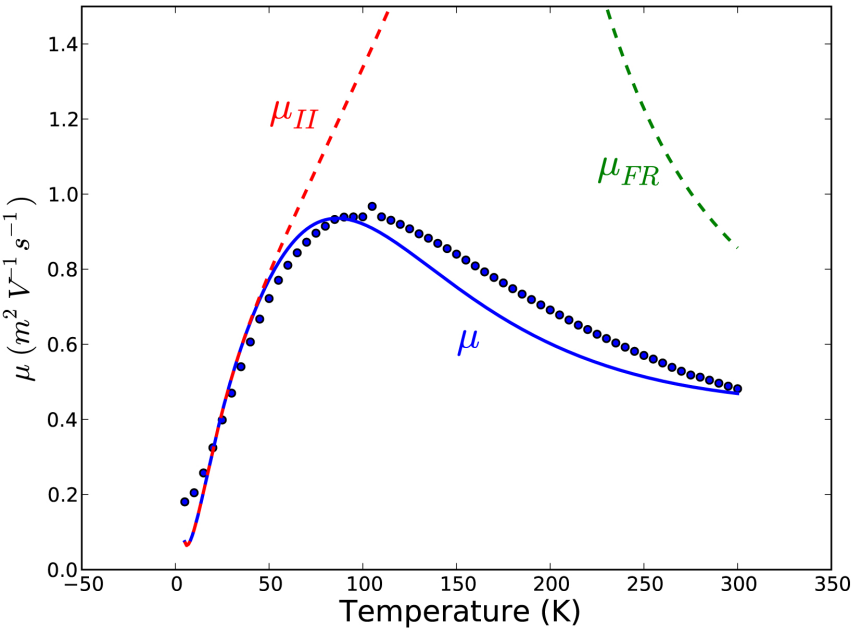


**Figure 3.9: Electron mobility:** Depicted for $In_{0.04}Ga_{0.96}As$ as a function of temperature at a doping concentration of $3 \times 10^{16}$ cm$^{-3}$. Blue line is numerical calculation according to Eq. 3.81, while blue circles are data taken from van der Pauw measurements [82]. Dashed red and green lines display mobility expected due to only ionized impurity and Fröhlich scattering mechanisms respectively.

sample having the given parameters using the four-contact van der Pauw technique [82]. We can see that the calculated mobility is in agreement with the measurements.

## 3.4 Spin relaxation mechanisms

In the two previous sections we calculated the relaxation times and mobility for electrons assuming spin conserving scattering mechanisms. Now we are in a position to address spin relaxation, both by allowing spin coupling while undergoing ballistic transport, and by allowing scattering that is accompanied by a spin flip. This will be addressed in terms of the common spin relaxation mechanisms for GaAs, but is in no way an exhaustive treatment. For a more complete enumeration of spin relaxation in semiconductors, consult Ref. [83].

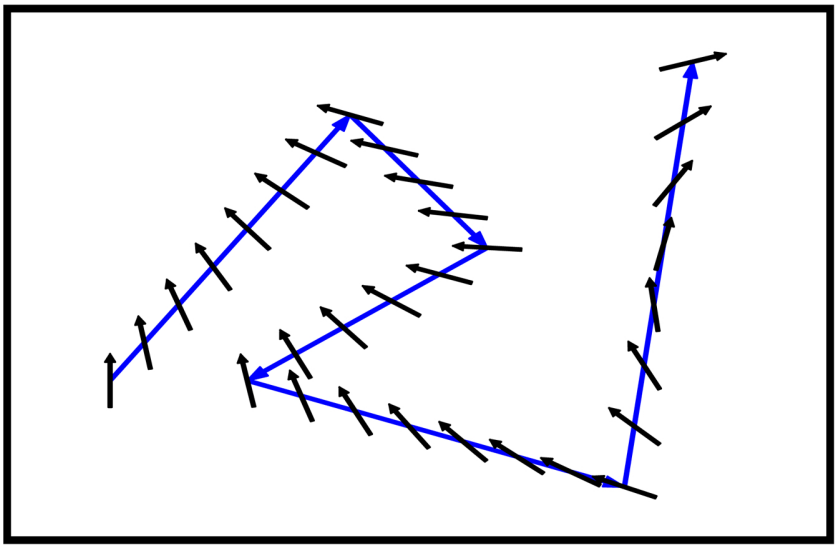

**Figure 3.10: D'yakonov-Perel spin relaxation mechanism:** Electron momentum depicted by blue arrow and spin depicted by black arrow. After each scattering event the electron experiences a new spin-orbit effective magnetic field, causing a change in the spin precession direction and rate. Adapted from Ref. [83].

### 3.4.1 D'yakanov-Perel

We saw in the previous chapter that spatial inversion symmetry breaking in semiconductors gives rise to a momentum dependent spin splitting that can be characterized by a spin-orbit effective magnetic field $\vec{B}_{SO}$. This field was found to be linear in momentum and anisotropic in the (001) crystal plane (see Fig. 2.8). We also found in Sec. 2.2.4 that the presence of a magnetic field, be it external or spin-orbit induced, serves to couple the initial electron spin to the direction orthogonal to the magnetic field via spin precession, as described by Eq. 2.33. For a ballistic electron, the momentum direction does not change, and so too does the spin direction remain the same in the frame rotating at the precession frequency. However each scattering event changes the electron momentum direction, which in turn changes the spin-orbit field magnitude and direction experienced by the electron, as depicted in Fig. 3.10.

For an ensemble of electrons with a spread in velocities centered around the drift veloc-

ity, this effect will serve to randomize the electron spins. Such an effect was proposed by D'yakonov and Perel [12] in 1971 and is termed the D'yakonov-Perel spin relaxation mechanism. We present the general form of the spin relaxation rate. For a detailed discussion, consult Ref. [11]. The spin relaxation rate is, in general, a tensor with matrix elements given by

$$\frac{1}{\tilde{\tau}_{s,ii}\left(\vec{k}\right)} = \gamma_l \left(\overline{\Omega^2} - \overline{\Omega_i^2}\right) \tilde{\tau}_m \left(\vec{k}\right) \tag{3.82}$$

$$\frac{1}{\tilde{\tau}_{s,ij}\left(\vec{k}\right)} = \gamma_l \left(\overline{\Omega_i \Omega_j}\right) \tilde{\tau}_m \left(\vec{k}\right) \tag{3.83}$$

where $\tilde{\tau}_m$ is the momentum relaxation time determined in Sec. 3.2. $\gamma_l$ is a term involving the expansion of the Hamiltonian in spherical harmonics. The choice of subscript $l$ depends on the symmetry of the function $\vec{\Omega}(\vec{k})$. For our purposes, it will suffice to say that $l = 1$ and $\gamma_l = 1$ [11]. The term $\overline{\Omega_i \Omega_j}$ is the product of Larmor precession frequencies along directions $\hat{e}_i$ and $\hat{e}_j$ averaged over the solid angle in $k$ space. This is given by

$$\overline{\Omega_i \Omega_j} = \frac{1}{4\pi} \int_0^{2\pi} d\phi \int_0^{\pi} d\left(\cos\theta\right) \left\{\Omega_i\left(k,\theta,\phi\right) \Omega_j\left(k,\theta,\phi\right)\right\}. \tag{3.84}$$

We now build a form for the spin relaxation rate tensor in the presence of an anistropic spin-orbit effective magnetic field. From Eq. 2.71, we can address the spin-orbit field component-wise as

$$\Omega_x = k\left(\alpha' \sin\theta \sin\phi + \beta' \sin\theta \cos\phi\right) \tag{3.85}$$

$$\Omega_y = -k\left(\alpha' \sin\theta \cos\phi + \beta' \sin\theta \sin\phi\right) \tag{3.86}$$

$$\Omega_z = 0 \tag{3.87}$$

with $\hat{x}$, $\hat{y}$, and $\hat{z}$ along the [100], [010], and [001] crystal axes respectively, and $\theta$ and $\phi$ are the usual polar and azimuthal angles in spherical coordinates, respectively. We used the *prime* notation to relate the coefficients for the field with those of the precession frequency, namely

$$\alpha' = \frac{g\mu_B}{\hbar}\alpha$$

and similarly for $\beta$. The components of the spin relaxation tensor are then

$$\overline{\Omega_x\Omega_x} = \frac{k^2}{4\pi}\int_0^{2\pi} d\phi \left(\alpha'^2 \sin^2\phi + \beta'^2 \cos^2\phi + 2\alpha'\beta' \sin\phi\cos\phi\right) \int_0^{\pi} d\theta \left(\sin^3\theta\right) \tag{3.88}$$

$$\overline{\Omega_y\Omega_y} = \frac{k^2}{4\pi}\int_0^{2\pi} d\phi \left(\alpha'^2 \cos^2\phi + \beta'^2 \sin^2\phi + 2\alpha'\beta' \sin\phi\cos\phi\right) \int_0^{\pi} d\theta \left(\sin^3\theta\right) \tag{3.89}$$

$$\overline{\Omega_x\Omega_y} = \overline{\Omega_y\Omega_x} = \frac{k^2}{4\pi}\times \int_0^{2\pi} d\phi \left(\alpha'^2 \sin\phi\cos\phi + \beta'^2 \sin\phi\cos\phi + \alpha'\beta'\left[\sin^2\phi + \cos^2\right]\phi\right) \int_0^{\pi} d\theta \left(\sin^3\theta\right) \tag{3.90}$$

$$\overline{\Omega_z\Omega_z} = \overline{\Omega_x\Omega_z} = \overline{\Omega_z\Omega_x} = \overline{\Omega_y\Omega_z} = \overline{\Omega_z\Omega_y} = 0 \tag{3.91}$$

Using Eqs. 3.82 and 3.83, and taking the integrals, the spin relaxation tensor is

$$\frac{1}{\tilde{\tau}_s\left(\vec{k}\right)} = \frac{k^2\tilde{\tau}_m\left(\vec{k}\right)}{3}\begin{pmatrix} \alpha'^2+\beta'^2 & 2\alpha'\beta' & 0 \\ 2\alpha'\beta' & \alpha'^2+\beta'^2 & 0 \\ 0 & 0 & 2\left(\alpha'^2+\beta'^2\right) \end{pmatrix} \tag{3.92}$$

With the assignment $r = \alpha'/\beta' = \alpha/\beta$, and $\tilde{\Gamma}_0(\vec{k}) = (g\mu_B\beta)^2k^2\tilde{\tau}_m(\vec{k})/(3\hbar^2)$, the spin relaxation tensor is

$$\frac{1}{\tilde{\tau}_s\left(\vec{k}\right)} = \tilde{\Gamma}_0\left(\vec{k}\right)\begin{pmatrix} 1+r^2 & 2r & 0 \\ 2r & 1+r^2 & 0 \\ 0 & 0 & 2\left(1+r^2\right) \end{pmatrix} \tag{3.93}$$

We finally recognize that this matrix can be diagonalized by rotating the basis by $\pi/4$, and we have, in the $[1\bar{1}0]$, [110], [001] crystal axis basis, the spin relaxation tensor:

$$\frac{1}{\tau_s\left(\upsilon_d\right)} = \Gamma_0\left(\upsilon_d\right)\begin{pmatrix} \left(1+r\right)^2 & 0 & 0 \\ 0 & \left(1-r\right)^2 & 0 \\ 0 & 0 & 2\left(1+r^2\right) \end{pmatrix} \tag{3.94}$$

In the last step, we integrated $\tilde{\tau}_m(\vec{k})$ over $k$ space with the distribution function centered at the drift velocity (given by $\vec{\upsilon}_d = \mu\vec{E}$). In general, we will allow $\Gamma_0$ to be a fit parameter for comparisons with measurements, as will be discussed in Ch. 6. We note finally that the spin relaxation rate can be minimized by minimizing the spin-orbit effective magnetic field. Clever sample design can be used to minimize the Dresselhaus spin-orbit coupling inherent to zincblende structures, as has been seen with (001) [17] and (111) [18] GaAs quantum wells. In both cases, a sizable increase in the spin relaxation time was observed. For example, the increase was up to two orders of magnitude for (111) quantum wells [18].

### 3.4.2 Elliott-Yafet

Whereas the D'yakonov-Perel spin relaxation mechanism involves relaxation between scattering events, the Elliott-Yafet mechanism involves spin relaxation due to spin flips at scattering events. It was proposed by Elliott [13] in 1954, and its temperature dependence was characterized by Yafet [14] in 1963. It is a result of the fact that the Bloch states examined in Sec. 2.3.1 are not eigenstates of the spin basis. As such, there is an non-diagonal component that allows for spin mixing between the conduction and valence bands. We treat this by expanding the transition Hamiltonian to include a spin interaction.

The matrix element is given by

$$H_{s'k',sk} = \sum_m \frac{H_{s'k',mk'} H_{mk',mk} H_{mk,sk}}{(\varepsilon_{s'} - \varepsilon_m)(\varepsilon_s - \varepsilon_m)} \tag{3.95}$$

where $s$ and $s'$ are the initial and final conduction band electron spin states, $k$ and $k'$ are the corresponding initial and final momentum states, and $m$ is the valence band spin state mediating the interaction. The interaction Hamiltonian $H_{mk',mk}$ is one of the spin conserving scattering mechanisms discussed in Sec. 3.2. The terms $\varepsilon_{m,s,s'}$ represent the energies of the spin-split bands. As this treatment describes an interaction between the conduction and valence band states, we expect $\varepsilon_s - \varepsilon_m \sim \varepsilon_g, \varepsilon_g + \Delta_0$ with $\varepsilon_g$ the band gap and $\Delta_0$ the energy separation of the split-off band. It is worth pointing out that a similar treatment for just the conduction band states was examined by Boguslawski [84] in 1980, specifically for electron-electron scattering. As we do not expect this to be a significant source of scattering, however, it will not be addressed here.

As with the carrier relaxation rates discussed in Sec. 3.2, we can represent the spin relaxation rate according to the same prescription:

$$\frac{1}{\tilde{\tau}_s\left(\vec{k}\right)} = \frac{4\pi}{\hbar}\sum_{\vec{k}'}\left|H_{s'k',sk}\right|^2\delta\left(\varepsilon_{k'} - \varepsilon_k + \Delta_\varepsilon\right) \tag{3.96}$$

where $\Delta_\varepsilon = \pm\hbar\omega, 0$ for phonon interactions and ionized impurity scattering respectively. The extra factor of two accounts for both spin states. The matrix elements in Eq. 3.95 can be evaluated using the Kane $8\times 8$ matrix (see Ref. [11] for details). If we assume that the contribution of the spin-orbit splitting in the conduction band is negligible compared to the band gap and split-off band energies, then the matrix element is given by

$$H_{s'k',sk} = H_{k',k}\frac{2i\varepsilon_k\eta\sin\theta\left(1-\eta/2\right)}{3\varepsilon_g\left(1-\eta/3\right)} \tag{3.97}$$

where $\eta = \Delta_0/(\Delta_0+\varepsilon_g)$, $\varepsilon_k$ is the electron kinetic energy, and $\theta$ is the angle between $\vec{k}$ and $\vec{k}'$. In this treatment, we have approximated the scattering process to be elastic. As the dominant scattering mechanism at low temperatures is ionized-impurity scattering (as in Fig. 3.9), we will take this to be a valid approximation. The spin relaxation rate becomes

$$\frac{1}{\tilde{\tau}_s\left(\vec{k}\right)} = \frac{8}{9}\left(\frac{\varepsilon_k}{\varepsilon_g}\right)^2\left[\frac{\eta\left(1-\eta/2\right)}{1-\eta/3}\right]^2\left\{\frac{2\pi}{\hbar}\sum_{\vec{k}'}\left|H_{k',k}\right|^2\sin^2\theta\delta\left(\varepsilon_{k'} - \varepsilon_k + \Delta_\varepsilon\right)\right\} \tag{3.98}$$

It is typical to cast the term in curly braces in terms of the momentum scattering rate. To do so, we must introduce a factor $\tilde{\Phi}(k)$ given by

$$\tilde{\Phi}\left(k\right) = \frac{\int_{-1}^{1} d\left(\cos\theta\right)\left[\left|H_{k',k}\right|^2\left(1-\cos^2\theta\right)\right]}{\int_{-1}^{1} d\left(\cos\theta\right)\left[\left|H_{k',k}\right|^2\left(1-\cos\theta\right)\right]} \tag{3.99}$$

In doing so, the spin relaxation rate due to the Elliott-Yafet mechanism is

$$\frac{1}{\tau_s\left(\upsilon_d\right)} = \frac{8}{9}\left(\frac{\langle\varepsilon_k\rangle}{\varepsilon_g}\right)^2\left[\frac{\eta\left(1-\eta/2\right)}{1-\eta/3}\right]^2\frac{\Phi\left(\upsilon_d\right)}{\tau_m\left(\upsilon_d\right)} \tag{3.100}$$

where again, in the last step, we integrate over $k$ space weighted by the distribution function centered at the drift velocity.

There are a few comparisons to make between the Elliott-Yafet and D'yakonov-Perel spin relaxation rates. The first is that the Elliott-Yafet mechanism was found to be a scalar function described by Eq. 3.100, while the D'yakonov-Perel mechanism is, in general, a tensor with a specific eigenbasis described by Eq. 3.94. Furthermore, the Elliott-Yafet spin relaxation rate is proportional to the momentum relaxation rate. This is understood, as a higher rate of electron scattering increases the overall probability of a spin-flip (which is presumed roughly constant for each scattering event at a particular momentum). The D'yakonov-Perel spin relaxation rate, however, is proportional to the inverse of the momentum relaxation rate ($\tau_m$ is contained in the definition of $\Gamma_0$). This is also understood because a very high rate of momentum scattering will not allow for appreciable spin precession, and therefore dephasing, between scattering events.

As the mobility is proportional to the momentum relaxation time, averaged over $k$ space, we then expect samples with high mobility to be dominated by the D'yakonov-Perel dephasing mechanism, while samples with low mobility are dominated by the Elliott-Yafet mechanism. For GaAs, the turning point occurs at a doping density of $n \sim 2 \times 10^{16}$ cm$^{-3}$ [78]. The samples in this study have a doping concentration of $n = 3 \times 10^{16}$ cm$^{-3}$, and therefore the D'yakonov-Perel spin relaxation is expected to dominate. Indeed, we will see in Chs. 4 and 6 that the measured spin relaxation is anisotropic, having a tensor form. However we point out that the Elliott-Yafet mechanism, though not dominant, may still play an influential role in spin relaxation.

### 3.4.3 Bir-Aronov-Pikus

We conclude spin relaxation by mentioning the Bir-Aronov-Pikus mechanism, which involves the exchange interaction between electron and hole spins [15]. It can be described in a similar

form as the D'yakonov-Perel relaxation mechanism, with electron spins precessing around the effective magnetic field generated by the hole spin. It has the added complication of allowing holes to have a spread in velocities and their own set of scattering mechanisms. As was pointed out by Fabian and Sarma [83], it is only expected to be a significant source of spin relaxation in semiconductors having a sizable overlap between the electron and hole wave functions. For $n$-doped semiconductors, it is not expected to contribute.

# Chapter 4

# Equipment and Data Collection

In the previous chapters we built a framework to describe the physical behavior of carriers and spins in the conduction band of III-V semiconductors, namely $In_{0.04}Ga_{0.96}As$. This chapter will be devoted to introducing the measurement techniques and associated equipment used throughout this research. It will be organized as follows. In Sec. 4.1, I will discuss optical spin generation techniques, including the pulsed Ti:Sapphire laser and photoelastic modulator used to excite carriers, and address the optical selection rules that give rise to a spin polarization. Sec. 4.2 will introduce the concept of Faraday/Kerr rotation used to measure the spin polarization, as well as the equipment and signal processing techniques to isolate signal from noise.

The optical setup and measurements of the time evolution of spin polarization will then be discussed in Sec. 4.3. This is where the pump-probe measurement scheme will be introduced in Sec. 4.3.1. I will conclude the chapter with a discussion of steady-state spin polarization in Sec. 4.4, introducing the concept of Hanle measurements. This chapter will serve to build the framework for the measurements presented in the chapters to come.

## 4.1 Optical spin generation

This section will go through the fundamental principles of optically generating spin polarization. This will be seen to be an important procedure for measurements of material parameters presented in this chapter as well as the spin-orbit splitting presented in Ch. 5.

### 4.1.1 Pulsed titanium-sapphire laser

Optical measurements throughout this work are performed using a mode-locked MIRA 900 titanium sapphire laser that is pumped by a 532 nm beam from the Verdi V-10, both of which are Coherent products.

The Verdi is a diode-pumped solid state (DPSS) [85] laser system separated into a power supply and a laser head [86]. The power supply drives current to a laser diode array, in addition to controlling temperature and optical servo loops. The diode array output is sent to the laser head [87] by use of an optical fiber and umbilical. Once in the head, light passes through a unidirectional resonating ring cavity [88] in which the gain medium is a neodymium vanadate crystal [89] lasing at 1064 nm. Finally a non-linear, phase matched lithium triborate (LBO) crystal is used as a frequency doubler to generate the output 532 nm green light which is used to pump the MIRA 900.

The MIRA 900 is a bidirectional laser cavity with a broad band titanium-doped sapphire crystal (Ti:Sapphire) as the active gain medium and is wavelength tunable in the range 700-1000 nm, and is controlled by temperature and optical servo loops [90]. The wavelength is tunable by rotating a birefringent filter in the beam path. The MIRA 900 is designed specifically to produce coherent light pulses (in the time domain) through a procedure known as mode-locking. The term "mode" refers to the longitudinal modes for standing waves that are allowed in the cavity (note the sum of all non-standing waves will destructively interfere and do not contribute to lasing). When some appreciable number of these modes are in

phase, the laser is said to be mode-locked. The MIRA 900 can operate in either femtosecond mode or picosecond mode. In the former, a larger range of cavity modes (corresponding to a larger bandwidth) is phase-matched and the pulse duration is shorter. In the latter, a more narrow range of cavity modes is locked and therefore the pulse duration is longer. For most of our applications, the picosecond mode provides sufficiently short pulses and offers a much narrower bandwidth than the femtosecond mode. For this reason, we typically operate in picosecond mode.

The MIRA 900 uses a passive mode-locking method known as Kerr lens mode-locking (KLM), in which an optically active medium focuses high intensity light to a narrower focus than lower intensity light due to the field produced in the material by the electromagnetic radiation. The Ti:Sapphire crystal is such a material. An aperture placed in the beam path blocks low intensity light while allowing narrowly focused high intensity laser pulses through. In principle, the mode-locking can be self starting, where even slight vibrations can be sufficient to initialize phase matching. In the MIRA 900, however, this is achieved more efficiently by a Brewster window mounted to a galvo motor, the oscillations of which seed mode-locking. The Brewster window also serves the purpose of polarizing the light in the cavity.

The ends of the cavity are the output coupler and a Gires-Tournois Interferometer (GTI, only available in picosecond mode), the latter of which monitors and adjusts the group velocity dispersion in a process known as $\beta$-lock. Our typical operation uses $\beta$-lock, although it is often not necessary to achieve and maintain mode-locking. The temporal spacing between successive optical pulses, referred to as the laser repetition rate, is determined by the length of the optical cavity. The repetition of our MIRA 900 is $t_{rep} = 13.16$ ns. This number can vary slightly between different lasers, and can also vary slightly based on temperature and humidity. To avoid humidity problems, the cavity is continuously purged with nitrogen gas. Care must be taken with the nitrogen flow, as too high of a flow rate can generate significant

vibrations that interfere with the ability to achieve mode-lock. Finally, an adjustable slit (two razor blades that may be horizontally traversed and variably spaced) just before the output coupler can be used to filter out any remaining continuous wave (CW) component.

### 4.1.2 Photoelastic modulator

To optically excite spin-polarized carriers, we must first convert the linearly polarized output light from the laser into circularly polarized light (Sec. 4.1.3). While this may be done using a quarter wave plate, it is beneficial to use a method that rapidly oscillates the light between left and right circular polarizations. This is useful as it modulates the measurement signal and allows for lock-in detection (Sec. 4.2.3). The photoelastic modulator (PEM) is a device that provides such a method.

PEM operation is based on the photoelasticity of an optically transparent material. For the Hinds Model I/FS50, this material is a fused silica bar, which is made to vibrate at a natural resonance frequency of 50 kHz by a quartz piezoelectric transducer. This corresponds to periodic compressive and tensile strain along the modulation axis at a rate of 50 kHz. When the bar is compressed, the component of light polarized along the compression axis will travel faster through the material and lead the polarization perpendicular to the axis of compression. Likewise, when the fused silica bar is stretched, the component along the modulation axis will lag. The phase difference (in length units) between the two polarization components is given by

$$\theta = d\,(n_x - n_y) \tag{4.1}$$

where $d$ is the thickness of the material, and $n_x$ and $n_y$ are the indices of refraction along and perpendicular to the modulation axis, respectively. The Hinds PEM-100 controller sets the amplitude of oscillation to vary the indices of refraction based on the wavelength of light and

the desired retardation [91]. It has two modes, operating with a peak retardation at either $\lambda/2$ or $\lambda/4$, corresponding to a half or quarter wave plate respectively. The controller works most efficiently when the incoming linear light polarization is at a 45° angle with respect to the modulation axis. In half wave plate mode, the modulation will be between linear polarization parallel and perpendicular to the original polarization direction. In quarter wave plate mode, the output light will modulate between left and right circular polarizations.

### 4.1.3 Optical selection rules in GaAs

Right or left circularly polarized light from the pump beam, tuned to the band gap energy, is used to excite electrons from the light-hole/heavy-hole valence bands into the conduction band. The laser line width is sufficiently narrow to avoid simultaneous excitation from the split-off valence band. To build the optical transition strengths for each subband, we make use of the angular momentum state definitions for these bands presented in Table. 2.1 to address the transition matrix elements directly.

We will use the dipole approximation [92], in which we can treat the field induced by the light as directly exciting dipole oscillations. This approximation is valid as the photon dispersion is extremely strong compared to that of the crystal [93] ($\omega = \upsilon_c k$ with $\upsilon_c$ the speed of light in the material). As such, we treat dipole transitions as being nearly vertical and, when tuned to the band gap, occurring near the $\Gamma$ point. We further treat the field-induced dipole oscillations as having an orthonormal basis analogous to that of the cubic Bloch states in the valence band. Defining $\hat{D}$ as the dipole moment operator, it then follows that [11]

$$\langle 1| D_i |X_j\rangle = |D| \delta_{ij} \tag{4.2}$$

where $|X_j\rangle$ is one of the $p$-like valence band states $|X\rangle$, $|Y\rangle$, $|Z\rangle$ discussed in Sec. 2.3.1, and $|1\rangle$ is the $s$-like conduction band state. Eq. 4.2 makes sense from a conservation of

momentum standpoint. A dipole oscillation along $\hat{x}$ should not affect the $|Y\rangle$ state in the $p$-like valence band. We will take the transition matrix to have the form $\langle\psi_f|\,\hat{D}\,|\psi_i\rangle$ with $f$ and $i$ representing the final and initial state respectively. We have defined $|D|$ as the magnitude of the matrix element. Due to the cubic symmetry of the crystal, it is expected to be the same for each of the orthogonal basis vectors. As we are concerned only with the ratio of transition matrix elements, we will not directly evaluate the integral.

We will now build the transition matrix elements from the valence band states to the spin up conduction band state with the laser axis along the axis of quantization $|Z\rangle$. In this case, we take the dipole operator for right and left circularly polarized light as

$$D^- = \frac{1}{\sqrt{2}}\left(D_x - iD_y\right), \qquad D^+ = -\frac{1}{\sqrt{2}}\left(D_x + iD_y\right) \tag{4.3}$$

respectively. Consider first the transition from the $m_j = +3/2$ heavy-hole valence band state. For right circularly polarized light we have

$$\langle {}^{j=1/2}_{m_j=1/2}|\, D^- \,|^{j=3/2}_{m_j=3/2}\rangle = -\frac{1}{2}\langle 1|\left(D_x - iD_y\right)\left(|X\rangle + i\,|Y\rangle\right). \tag{4.4}$$

Here I have used the orthonormality of spin states, namely $\langle\uparrow\,|\,\uparrow\rangle = 1$, and the definition of the spin $+3/2$ heavy-hole valence band state $|j = 3/2, m_j = 3/2\rangle$ from Table 2.1. Using Eq. 4.2 this gives

$$\langle {}^{j=1/2}_{m_j=1/2}|\, D^- \,|^{j=3/2}_{m_j=3/2}\rangle = -\,|D| \tag{4.5}$$

Notice that if we perform the same transition using left circularly polarized light, we get $\langle j = 1/2, m_j = 1/2|\, D^+\,|j = 3/2, m_j = 3/2\rangle = 0$. Keeping in mind that the orthonormality of spin states requires that $\langle\uparrow\,|\,\downarrow\rangle = 0$, we immediately see that a transition from the $m_j = -3/2$ valence band state to the $m_j = +1/2$ conduction band state is not allowed.

We can similarly build the transition matrix element from the $|j = 3/2, m_j = -1/2\rangle$

valence band state using left circularly polarized light to get

$$\begin{aligned}\left\langle {}^{j=1/2}_{m_j=1/2}\right| D^+ \left|{}^{j=3/2}_{m_j=-1/2}\right\rangle &= \frac{1}{\sqrt{12}} \langle 1| \left(D_x + iD_y\right) \left(|X\rangle - i\,|Y\rangle\right) \\ &= -\frac{1}{\sqrt{3}} |D| \,. \end{aligned} \tag{4.6}$$

From Fermi's golden rule, the transition rate is proportional to the square of the transition matrix element. We find the ratio of transition strengths is:

$$\frac{\left|\left\langle {}^{j=1/2}_{m_j=1/2}\right| D^- \left|{}^{j=3/2}_{m_j=-1/2}\right\rangle\right|^2}{\left|\left\langle {}^{j=1/2}_{m_j=1/2}\right| D^+ \left|{}^{j=3/2}_{m_j=3/2}\right\rangle\right|^2} = \frac{1}{3}. \tag{4.7}$$

We build a similar set of relative transition strengths for each valence to conduction band transition. The results are shown in Fig. 4.1. We see that by pumping with left circularly polarized light ($\sigma^+$), we create three times as many spin down carriers as spin up. The spin polarization induced in the conduction band is

$$P = \left|\frac{n_\uparrow - n_\downarrow}{n_\uparrow + n_\downarrow}\right| = \frac{3-1}{3+1} = \frac{1}{2}. \tag{4.8}$$

We point out that the allowed transitions represent conservation of angular momentum. The transition ratios for carrier recombination are the same, and, as such, polarized photoluminescence can be used to measure the spin polarization of electrons in the conduction band [94] or holes in the valence band [95].

Note that for these transition strengths we used only circularly polarized light along the axis of spin quantization. If we allow the light polarization to be orthogonal to the axis of quantization (such that $D^+ \propto |Y\rangle \pm i\,|Z\rangle$, for example), then a vertical transition is also allowed (with $\Delta m_j = 0$), having a relative strength of two compared to the transition strengths

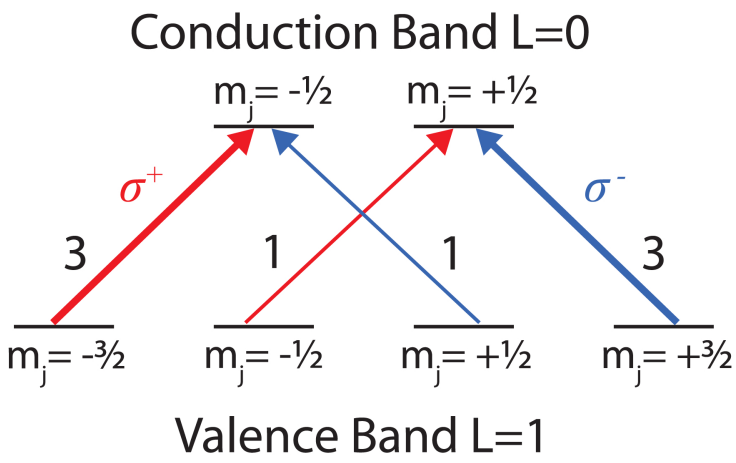


**Figure 4.1: Optical selection rules:** Shown for right ($\sigma^-$) and left ($\sigma^+$) circularly polarized light absorption in GaAs. For each handedness, heavy-hole to conduction band transitions occur at a rate three times greater than light-hole to conduction band transitions.

in Fig. 4.1. Such would be an important transition if the spin measurement axis were perpendicular to the optically-induced spin polarization axis. As we will see in Sec. 4.3.1, we choose these axes to be parallel and such a transition is not considered.

We finally point out that the transition ratios depicted in Fig. 4.1 assume equal numbers of available conduction and valence band states for each transition. This is, in general, not the case, and the transition rates will need to be weighted by the joint density of states [73] for the transition as the deviation from the $\Gamma$ point increases. Furthermore, in cases for which the semiconductor structure does not obey cubic symmetry, such as with a strain axis or quantum confinement, or when the light-hole/heavy-hole degeneracy at the $\Gamma$ point is lifted, these transition ratios will no longer be valid.

## 4.2 Optical spin detection

We mentioned in the previous section that spin polarization measurements have been conducted using polarized photoluminescence. Such a method, however, requires measurement of the light produced from electron-hole recombination. For this reason, it is not an effec-

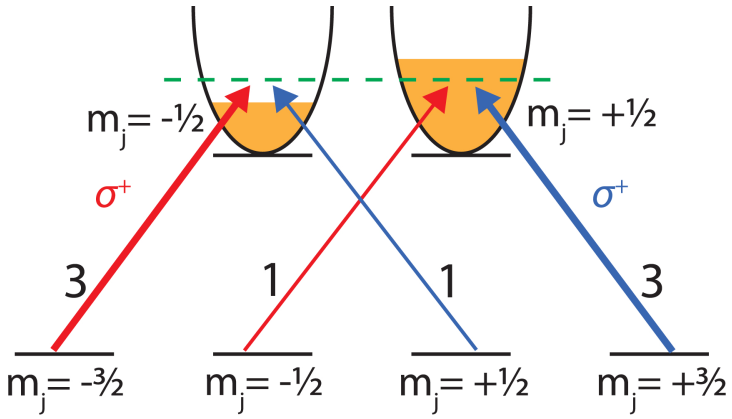


**Figure 4.2: Faraday rotation optical selection rules:** Optical selection rules give rise to a circular birefringence for samples with a spin polarization in the conduction band.

tive method for measuring the conduction band spin population after carrier recombination has occurred. For this task, Faraday and Kerr rotation are an effective and extremely high resolution method of measuring spin polarization.

### 4.2.1 Faraday/Kerr rotation

Faraday rotation is defined as the rotation of linearly polarized light upon transmission through an optically active material. The Faraday effect was first discovered by Michael Faraday in 1846 in a piece of glass in a magnetic field [96]. It can also be described in the context of a spin-polarized conduction band in GaAs (or other such materials with spin polarization generating optical selection rules). An unequal population of up and down spins in the conduction band (Fig. 4.2) results in a shift in the absorption curves for left and right circularly polarized light (Fig. 4.3), known as circular birefringence. In the figure, the spin up conduction band has a higher carrier density than spin down. For the energy transition depicted at the dashed green line, then, only optical absorption into the spin down state is allowed. We see that, due to the optical selection rules, this occurs at a ratio of 3:1 for left and right circularly polarized light, respectively.

Fig. 4.3(a) depicts the shift in absorption curves for left and right circularly polarized

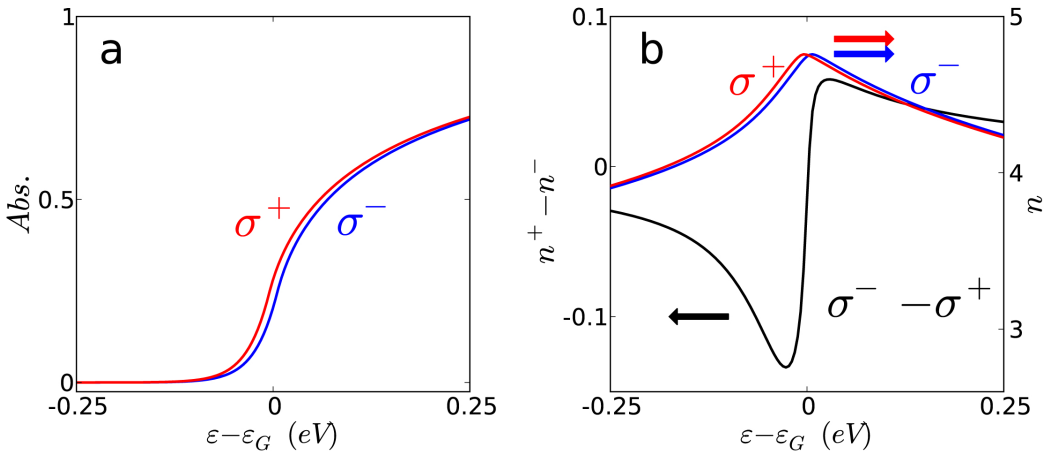


**Figure 4.3: Circular birefringence:** (a) Spin polarization in the conduction band gives rise to a shift in the absorption edge for left and right circularly polarized light. (b) Through the Kramers-Kronig relations this translates to a difference in refractive indices. Principal value of the integral was obtained using the Python quadrature integration package (in the SciPy library) with a Cauchy weighting.

light. These are treated as being proportional to $\sqrt{\varepsilon - \varepsilon_g}$ with a saturation at high energy, in accordance with three dimensional semiconductors. An exponentially decaying Urbach tail below the band gap [97] has been added to more accurately depict the observed behavior. The absorption is described by the imaginary component of the complex index of refraction. Using the Kramers-Kronig relations [73], this corresponds to a shift in the real part of the indices of refraction for left and right circularly polarized light, depicted in Fig. 4.3(b). The difference in indices of refraction contains extrema of opposing sign on either side of the band gap.

To see how this difference in index of refraction gives rise to a rotation of linearly polarized light, consider that we can decompose linearly polarized light into a superposition of left and right circularly polarized light. Using the standard Jones matrix notation for light polarization [98], we can represent the incident horizontally polarized light as

$$\vec{E}_i = E_0 \begin{pmatrix} 1 \\ 0 \end{pmatrix} e^{i(kz-\omega t)} = \frac{E_0}{2} \left[ \begin{pmatrix} 1 \\ i \end{pmatrix} + \begin{pmatrix} 1 \\ -i \end{pmatrix} \right] e^{i(kz-\omega t)} \tag{4.9}$$

For light of a particular polarization transmitting through a material with index of refraction $n$ and thickness $d$, the light will experience a shift in phase given by $\Delta\phi = nkd$ [99]. We assume, for simplicity, normal incidence. Letting $n_r$ and $n_l$ correspond to the index of refraction for right and left circularly polarized light respectively, then the light polarization after transmission through a material of thickness $d$ is given by

$$\begin{aligned}\vec{E}_t &= \frac{E_0}{2}\left[\begin{pmatrix}1\\ i\end{pmatrix}e^{i(n_r kd-\omega t)} + \begin{pmatrix}1\\ -i\end{pmatrix}e^{i(n_l kd-\omega t)}\right] \\ &= \frac{E_0}{2}\exp\left[i\left(\frac{n_r+n_l}{2}kd-\omega t\right)\right]\left[\begin{pmatrix}1\\ i\end{pmatrix}e^{\Delta nkd/2} + \begin{pmatrix}1\\ -i\end{pmatrix}e^{-\Delta nkd/2}\right] \end{aligned} \tag{4.10}$$

where in the last line I made the substitution $\Delta n = n_r - n_l$. We ignore the overall phase factor as the intensity of light will go as the square of the polarization. Using the definition $\theta = \Delta nkd/2$, the final light polarization is

$$E_f = E_0\left[\begin{pmatrix}1\\ 0\end{pmatrix}\cos\theta - \begin{pmatrix}0\\ 1\end{pmatrix}\sin\theta\right] = E_0\begin{pmatrix}\cos\theta & \sin\theta\\ -\sin\theta & \cos\theta\end{pmatrix}\begin{pmatrix}1\\ 0\end{pmatrix}. \tag{4.11}$$

We see that a circular birefringence has the effect of rotating the polarization of linearly polarized light upon passing through the material. The angle of rotation is called the Faraday rotation angle (or Kerr rotation angle for rotation of linearly polarized light upon reflection). In Sec. 4.2.2 we will describe how this angle is measured. It is found that for small polarizations, the angle of Faraday/Kerr rotation is proportional to the component of the spin polarization along the direction of laser propagation [11].

Fig. 4.4 displays the measured Kerr rotation amplitude due to optically oriented electron spin polarization for an $In_{0.03}Ga_{0.97}As$ semiconductor sample as a function of probe wave-

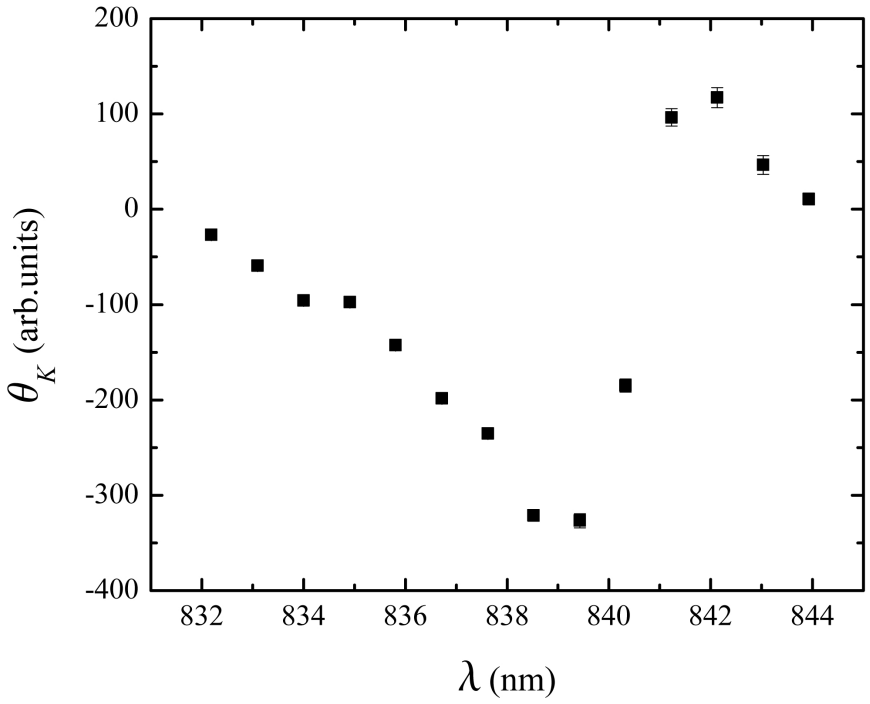


**Figure 4.4: Kerr rotation vs. laser wavelength:** Kerr rotation amplitude measured as a function of laser wavelength for $In_{0.03}Ga_{0.97}As$ at $T = 10$ K. We see rotation extrema occur in opposite directions on either side of the band gap.

length. We can see that as we tune through the band gap energy, we sweep from a Kerr rotation minimum to a maximum. We will discuss in Chs. 5 and 6 the advantages to taking measurements at the low or high energy Kerr rotation peaks.

### 4.2.2 Photodiode bridge

The spin polarization is obtained by measuring the angle of Faraday/Kerr rotation of light intensity upon transmission through or reflection off of the sample. This is achieved by using a balanced photodiode bridge. Light is split into horizontal and vertical components using a Wollaston prism, with each component fiber-coupled to a photodiode circuit. The circuit diagram is shown in Fig. 4.5(a). Three Texas Instruments A128JM low noise operational amplifiers magnify the difference current between the two photodiodes, as well as the two

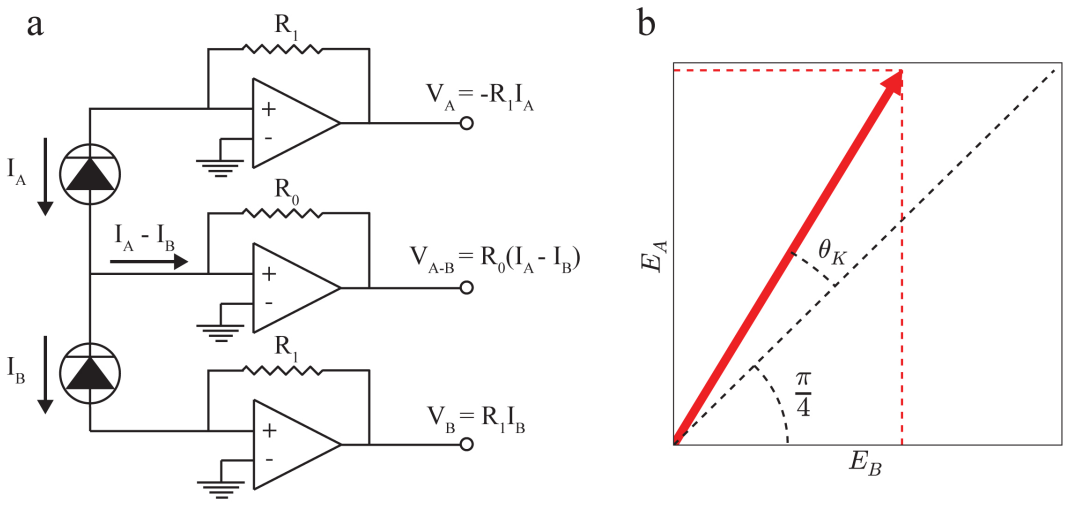


**Figure 4.5: Photodiode bridge and Faraday rotation:** (a) Photodiode bridge circuit diagram (adapted from Ref. [100]). (b) Faraday rotation angle extracted from light polarization intensities.

reference currents. We label each reference voltage $A$ and $B$ and the difference voltage $A-B$. The $A-B$ output is proportional to the difference in light intensities for horizontally and vertically polarized light, while $A$ and $B$ are proportional to each of the individual intensities.

Fig. 4.5(b) shows the Kerr rotation angle and how it is extracted from measurements of the light polarization intensities. A half wave plate is placed in front of the Wollaston prism to match the polarization intensities for the unrotated signal. In such a situation the photodiode bridge is said to be balanced. When the polarization is rotated by an angle $\theta$ we can write the polarization components as

$$E_A = E \sin\left(\theta + \frac{\pi}{4}\right) \tag{4.12}$$

$$E_B = E \cos\left(\theta + \frac{\pi}{4}\right) \tag{4.13}$$

where $E_{A,B}$ represents the light electric field for horizontal ($A$) and vertical ($B$) light. Keeping in mind that the light intensity goes as the square of the electric field (for which the polarization is defined) we have the polarization intensities

$$I_A = I\sin^2\left(\theta+\frac{\pi}{4}\right) = \frac{I}{2}\left[1-\cos\left(2\theta+\frac{\pi}{2}\right)\right] = \frac{I}{2}\left[1+\sin\left(2\theta\right)\right] \tag{4.14}$$

$$I_B = I\cos^2\left(\theta+\frac{\pi}{4}\right) = \frac{I}{2}\left[1+\cos\left(2\theta+\frac{\pi}{2}\right)\right] = \frac{I}{2}\left[1-\sin\left(2\theta\right)\right] \tag{4.15}$$

where $I = I_A + I_B = E_A^2 + E_B^2$. I used the trigonometric identity $\cos(\alpha+\pi/2) = -\sin(\alpha)$. Using Eqs. 4.14 and 4.15, we can represent the Faraday/Kerr rotation angle in terms of the ratio of difference and sum intensities as

$$\sin\left(2\theta\right) \approx 2\theta = \frac{I_A - I_B}{I_A + I_B} \tag{4.16}$$

where the approximation holds in the paraxial approximation (i.e. for small angles). The photodiode current, which is proportional to these intensities, is amplified and sent from the photodiode bridge output to a lock-in amplifier.

One practical consideration is that the $A-B$ voltage is amplified by a factor of two greater than each of the $A$ and $B$ voltages ($R_0 = 2R_1$). As such, we must divide Eq. 4.16 by an additional factor of two to get the correct rotation angle.

### 4.2.3 Digital signal processing and lock-in detection

As discussed in Sec. 4.1.2, the photoelastic modulator (PEM) modulates the pump beam between left and right circular polarizations according to a sine wave at 50 kHz. Due to the symmetry of the optical selection rules, we expect the photo-induced conduction band spin polarization to oscillate between spin up and down at the same frequency, ultimately resulting in oscillations of the measured Faraday/Kerr rotation angle.

The Signal Recovery Model 7265 DSP Lock-in Amplifier [101] is designed to isolate such measurements occurring at a known frequency from noise (which is presumed to have a

frequency distribution). The measurement signal is coupled from the photodiode bridge to the lock-in input using an impedance-matched 50 Ω BNC cable. Meanwhile, a reference signal from the PEM (also a sinusoid oscillating at the PEM frequency) is BNC coupled to the reference input on the lock-in.

The measurement signal is passed through an input amplifier to a line frequency rejection filter centered at 60 and 120 Hz designed to reject signal induced by the American standard AC electrical line frequency. This signal then passes through an AC gain and antialiasing filter into the main analog to digital converter (ADC), which has a sampling rate of 166 kHz. The now digital signal is sent to two digital signal processors (DSPs), which measure the in-phase and quadrature components relative to the reference signal. Meanwhile, the reference signal goes through its own ADC and is converted into a pair of sine and cosine waves. The cosine and sine components are sent to the in-phase and quadrature DSPs, respectively.

The DSP digitally multiplies the measurement signal by the reference signal. We will examine this for the in-phase component. Consider measurement ($V_m$) and reference ($V_r$) signals of the form

$$V_m = \sum_i V_i \cos(\omega_i t + \delta) = \sum_i V_i \left[\cos(\omega_i t)\cos(\delta) - \sin(\omega_i t)\sin(\delta)\right] \tag{4.17}$$

$$V_r = \cos(\omega_r t) \tag{4.18}$$

where the measurement signal is presumed to be an infinite sum of appropriately weighted frequency components. These are composed of a DC offset, low and high frequency noise, and the desired measurement signal oscillating at the PEM frequency $\omega_r$, with a corresponding amplitude $V_0$. Other than the DC offset, we expect the component oscillating at the reference frequency to strongly dominate over other individual components, though we point out that the infinite sum, which represents the noise, may be several orders of magnitude larger than

the desired measurement signal. The digital signal processor multiplies signals $V_m$ by $V_r$, resulting in (with some trigonometric identities)

$$V = \frac{1}{2}\sum_i V_i \{\cos\delta\left(\cos\left[\left(\omega_i - \omega_r\right)t\right] + \cos\left[\left(\omega_i + \omega_r\right)t\right]\right) - \\ \sin\delta\left(\sin\left[\left(\omega_i - \omega_r\right)t\right] + \sin\left[\left(\omega_i + \omega_r\right)t\right]\right)\} \tag{4.19}$$

The signal given in Eq. 4.19 is sent to a low pass digital filter with cutoff frequency set by the time constant. In practice, the filtration efficiency has a frequency dependence that is usually given in decibels (dB), where 6 dB corresponds to a signal attenuation by a factor of roughly 2. The lock-in has up to 4 stage filtration, each of which has an attenuation slope of 6 dB per octave (where an octave corresponds to a factor of 2 increase in the frequency). As such, the available output filters are 6, 12, 18, and 24 dB per octave. Consider in Eq. 4.19, we expect the largest signal to be that occurring at $\omega_i = \omega_r$, corresponding to the desired measurement signal, as well as a DC offset for which $\omega_i = 0$. Keeping these terms, we have

$$V = \frac{V_0}{2}\cos\delta + V_{DC}\cos\delta\cos\left(\omega_r t\right) + \frac{V_0}{2}\cos\left(2\omega_r t + \delta\right) \tag{4.20}$$

We desire only the first term to survive filtration as it is $V_0$ that we wish to measure. As such, we need a low pass filtration slope that attenuates the signal sufficiently well below a frequency of $\omega_r$. The low pass digital filtration is achieved using a discrete Fourier transform method [102], and has an attenuation equivalent to that of a Butterworth filter, expressed in terms of the frequency, in decibels, by

$$G(\omega) = -10\log\left[1 + \left(\frac{\omega}{\omega_c}\right)^{2n}\right] \tag{4.21}$$

where $n$ is the stage of filtration, given by $n = 1, 2, 3, 4$ for a slope of 6, 12, 18, 24 dB per

octave, respectively. $\omega_c$ is the cutoff frequency defined as $\mathrm{TC}^{-1}$ with TC the time constant of the lock-in which is selectable by the user. With the PEM operating at a frequency of 50 kHz, we select a time constant of $\mathrm{TC} = 160\ \mu s$. According to Eq. 4.21, this would correspond to an attenuation of 68 dB and 80 dB at a frequency of $\omega_r$ and $2\omega_r$ respectively, which is sufficient to filter out the DC offset and double frequency component given by the second and third terms in Eq. 4.20.

The resulting filtered signal given by

$$V_X = \frac{V_0}{2}\cos\delta \tag{4.22}$$

is half the amplitude of the component of the measurement signal oscillating at the PEM frequency, weighted by $\cos\delta$, where $\delta$ is the phase difference between the signal and reference waves. $V_X$ is the in-phase component of the processed signal. There is also a quadrature component $V_Y$ that has a $\sin\delta$ weighting factor which is achieved by multiplying the measurement signal by $\sin(\omega_r t)$. The Signal Recovery Model 7265 Lock-in Amplifier has an autophase feature, which, when applied on the $X$ and $Y$ signals, attempts to set the phase $\delta$ to 0 and $\pi/2$, respectively.

A practical consideration to note here is that the output processor of the lock-in amplifier multiplies the output signal by an additional factor of $\sqrt{2}$, such that the output signal is $V_X = (V_0\cos\delta)/\sqrt{2}$, that is, the root mean square (RMS) voltage. This is simply because RMS voltage is the commonly reported unit for AC electronics applications. We point out that when the input measurement signal has a square wave form, instead of sinusoidal, only the first harmonic of the square wave survives the digital signal processing and filtration. This is a factor of 0.6365 times the peak to peak square wave voltage, which, when multiplied by the factor of $1/\sqrt{2}$ from the DSP and output processor, results in an output voltage of 0.45 times the peak to peak square wave voltage, or 90% of the signal amplitude.

After the first stage of low pass filtration, but before the output processor, the lock-in amplifier also sends the signals through digital to analog converters (DACs) to the FAST X and FAST Y outputs. This allows for a cascaded lock-in procedure. As discussed earlier, a PEM in the pump path results in modulation of the handedness of the circularly polarized light and, thus, the sign of the spin polarization and resulting Faraday rotation. We can perform an additional stage of lock-in amplification and noise filtration by including an optical chopper in the probe path, as it is the probe polarization intensities that are measured by the photodiode bridge. The FAST X output of the first lock-in, modulated by the PEM at 50 kHz, is sent to a second lock-in input, which is modulated by the optical chopper at a frequency of 1370 Hz. This cascaded lock-in procedure greatly increases the signal to noise ratio.

There are some practical considerations to address when performing cascaded lock-in detection. The desired measurement signal will now be described by a product of cosinusoidal functions modulating at the PEM ($\omega_1$) and optical chopper ($\omega_2$) frequencies, given by

$$V_m = V_0 \cos(\omega_1 t + \delta_1) \cos(\omega_2 t + \delta_2) \tag{4.23}$$

where I have ignored the infinite sum of frequency components representing noise for simplicity. When multiplied by the PEM reference signal, modulated at frequency $\omega_1$, the resulting digital signal is

$$V = V_1 \left[\cos\delta \cos(\omega_2 t + \delta_2) - \cos(2\omega_r t + \delta_1) \cos(\omega_2 t + \delta_2)\right]. \tag{4.24}$$

This is the signal that is sent through the FAST X output of the first lock-in into the input of the second. We note that filtration, as described earlier, is used to remove the second term; however, the first term is also time dependent. As such, we must choose an appropriate time constant such that the first term is not filtered out. We also see that this implies $\omega_2 < 2\omega_r$,

and $\omega_r \gg \omega_2$ such that efficient filtration can occur.

It is typical to consider an attenuation of 3 dB ($\sim 1/\sqrt{2}$ decrease is signal strength) as the signal rolloff point. To have the FAST X output of the first lock-in retain the signal up to the 3 dB point, from Eq. 4.21, we require the cutoff frequency to be no less than

$$\omega_c \geq \frac{\omega_2}{\left(10^{0.3}-1\right)^{2n}} \tag{4.25}$$

For a slope of 12 dB per octave, and $\omega_2 = 2\pi \times 1370$ Hz $= 8608$ rad/s, this corresponds to a time constant no greater than TC$= 116$ $\mu$s. Our nearest options allowed by the lock-in are 80 $\mu$s and 160 $\mu$s. To obtain a cleaner signal, we are willing to sacrifice some signal magnitude for greater noise filtration and chose the latter option, with a time constant of TC$= 160$ $\mu$s. However, when the full signal is required, it is recommended, at these frequency settings, to decrease the time constant to 80 $\mu$s. For further noise filtration, the 24 dB per octave option can be used in this case.

One final point to notice about the cascaded lock-in procedure is that the FAST X output on the first lock-in has not yet gone through output signal processing. As such, the magnitude of the signal, which has gone through a series of amplifications based on the gain settings and sensitivity, as well as loss due to filtration, is not a well defined measurement parameter. While the FAST X output will be proportional to the desired measurement signal, the proportionality constant is not known. For this reason, the amplitude read from the second lock-in cannot be used to measure the absolute Faraday rotation. When this angle is needed, the value should be read from the first lock-in. Another option instead of using a cascaded lock-in procedure is to design a circuit that produces a reference frequency that is a sum of the two modulation frequencies. As long as this can be matched to the frequencies of the individual devices (for example, to account for frequency jitter), the resulting sum frequency can be sent to the lock-in reference, and the signal can be measured using only a

single lock-in amplifier.

## 4.3 Time-resolved spin polarization measurements

This section is devoted to presenting the temporal dynamics of conduction band electron spins and how measurements are conducted in both the time and frequency domains.

### 4.3.1 Pump-probe measurement scheme

The optical setup is shown in Fig. 4.6. The output horizontally polarized light from the Ti:Sapph laser is sent through a pair of collimating lenses, and then split into pump and probe pulses using a 50:50 cube beam splitter. The pump is then sent through a polarizing beam splitter (which transmits horizontally polarized light and reflects vertically polarized light) into the mechanical delay line.

The mechanical delay line is a retroreflector mirror attached to a cart on a track, the position of which is set by a computer-controlled stepper motor. After one pass down the delay line, the pump beam goes through a quarter wave plate, converting it to left circularly polarized light, then reflects off a mirror at normal incidence, converting it to right circularly polarized light, and finally through the quarter wave plate, again converting the initially horizontally polarized light to vertically polarized. The light then continues on its reflection path back through the delay line. As such, this is called a "double-pass" delay line, and has a range of $\sim 8$ ns. An advantage to using a double-pass delay line over a single-pass is that one can achieve the same temporal separation range in half the space.

On the return path, the now vertically polarized light reflects off of the polarizing beam splitter rather than transmitting through. This serves a dual purpose. The first, and obvious, is that more of the pump light gets to the sample than if a 50:50 beam splitter were used. The less obvious, but even more important reason, is to prevent light from coupling back

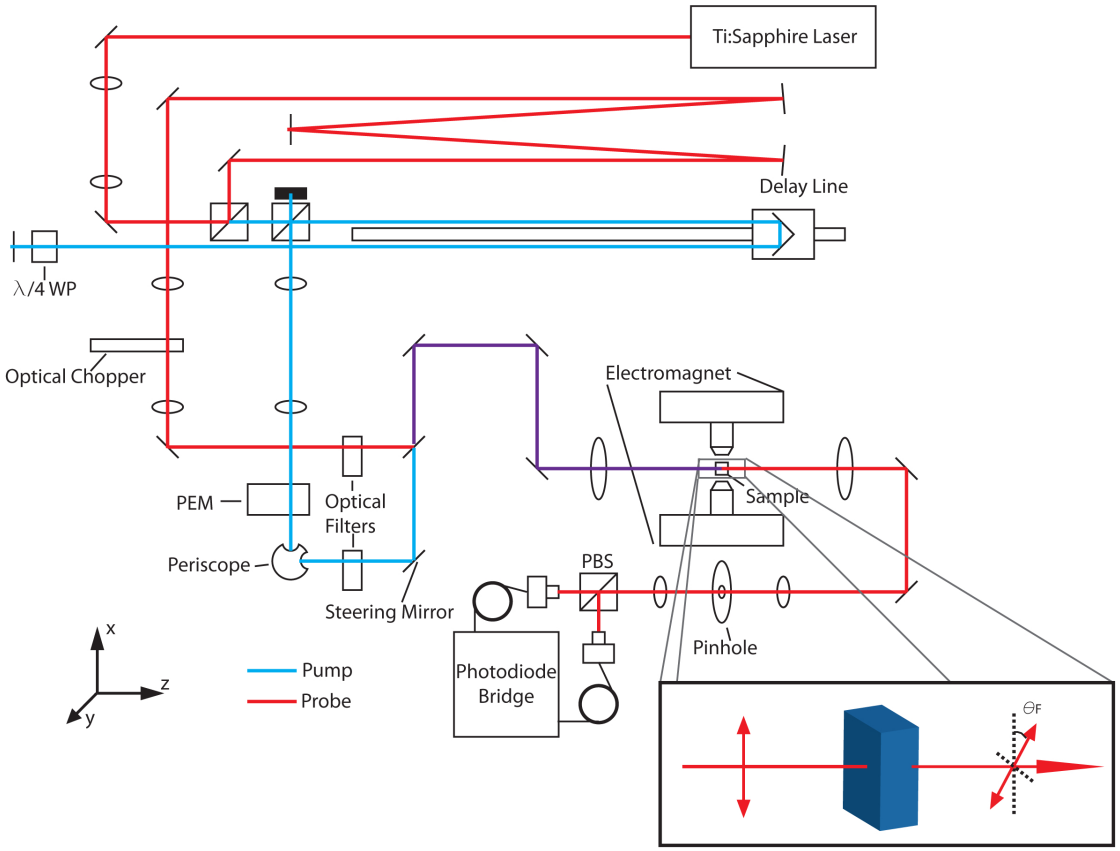


**Figure 4.6: Pump-probe experimental setup:** Pump (blue) is temporally separated from probe (red) using a mechanical delay line. A steering mirror in the pump path allows for spatial positioning of the pump relative to the probe. A PEM is used to optically excite spin polarization with the pump. The probe measures spin polarization through Faraday (Kerr) rotation upon transmission through (reflection off of) the sample. The rotation angle is measured using a balanced photodiode bridge.

into the laser, as this dramatically decreases the ability to achieve mode-lock. Note that this requirement is a feature of using a double-pass delay line; coupling light back into the laser is not an issue for a single-pass delay line. For a perfectly aligned delay line, there is no way to isolate the return beam from the outgoing beam without using polarization optics. After going through the delay line, the pump beam passes through another collimating lens pair that doubles the pump spot size, and into the photoelastic modulator (PEM) which modulates the beam between left and right circular polarization at a frequency of 50 kHz used for lock-in detection. The pump beam then passes through a vertical periscope and

variable neutral density filter wheel, to a steering mirror and finally continues on to the focusing lens to the sample. The steering mirror is used to allow for two-dimensional spatial positioning of the pump spot on the sample.

Meanwhile, the probe beam goes through a fixed delay path that is equal in length to the pump delay line when it is set to zero delay (near the far right end of the track in the figure). It then passes through a collimating lens pair that doubles the probe spot size. An optical chopper is placed at the focus of the lens pair, modulating at a frequency of 1.370 kHz and is also used for lock-in detection. The probe beam then goes through a variable neutral density filter wheel to the focusing lens to the sample.

The neutral density filter wheels are used to adjust the power of the pump and probe beams. Typical measurements are taken with a pump power of $\sim 800$ $\mu$W and a probe power of $\sim 150$ $\mu$W. On the approach to the final focusing lens, the pump and probe beams are vertically offset from one another and parallel, with the probe going through the center of the lens and the pump offset by $\sim 1$ cm. As such, a two inch diameter lens is used to avoid spherical aberrations. When the beams are parallel, the pump and probe spots should focus to the same location on the sample. The overlap can be adjusted using the pump beam steering mirror and an overlap scan. The pump is deflected vertically upon reflection off of or transmission through the sample and is then blocked.

The sample is mounted onto the cold finger of a liquid Helium flow cryostat. For transmission, the Janis Model ST-300 cryostat is used, while, for reflection, the ST-500 is used. The cryostat is, in turn, mounted to a three dimensional translation stage, which allows for the position of the sample relative to optics to be adjusted, including the focus. In addition, when Kerr rotation in reflection is used, the cryostat is mounted to a rotatable stage, which allows the sample to be rotated along the laser axis as well. This is particularly useful when one wishes to take measurements along different crystal axes without having to warm up the cryostat and remount the sample. This option is not available for the transmission cryostat,

and, as such, the bulk of the measurements in this work are taken using Kerr rotation.

The cryostat cold finger is held between two poles of an external electromagnet, with a field range of $\sim \pm 300$ mT at a pole spacing that allows for the cryostat to have a reasonable amount of translational and rotational flexibility. The maximum field can be increased, if desired, by reducing the pole spacing, or using chilled water flow to allow for a higher current. The magnet, run by the Kepco Power Supply, has a failsafe procedure that shuts off the current if the temperature gets too high. Without chilling, for a pole spacing of $\sim 2.8$ cm, a field of 250 mT running for $\sim 30$ minutes will trigger the failsafe.

The linearly polarized probe beam continues through, or reflects off of, the sample undergoing Faraday or Kerr rotation, respectively, and on to the collection path. In transmission the sample can be oriented such that the laser is at normal incidence. For reflection, however, to allow the probe beam to be picked off in the collection path, a slight angle must be introduced. For our purposes, the cryostat is angled $\sim 5^\circ$ from normal incidence. We keep this angle at a minimum so that we may still use the optical selection rules for normal incidence. In Fig. 4.6, only the transmission diagram is shown. In the collection path, an additional collimating lens pair is used to reduce the laser spot size. At the focal point of this lens pair, a pinhole is used to cut out as much scattered light from the pump beam as possible. The probe beam then passes through a quarter wave plate and the Wollaston prism, splitting into horizontal and vertical polarizations, and finally to the fibers coupling the light to the photodiode bridge.

### 4.3.2 Time domain measurements

Time-domain measurements are conducted by fixing the strength of the external magnetic field, and varying the pump-probe time delay ($\Delta t$). By making the pump delay line shorter, we are causing the pump beam to be incident on the sample at an earlier time, and therefore increasing the delay time between the pump and probe. By measuring the Kerr rotation

at each time delay, we can examine the temporal behavior of the conduction band spin polarization induced by the pump. We take the polarization of spins by the pump to occur on a near instantaneous time scale compared to the free evolution of spins thereafter. As such, we model the time-dependent spin polarization according to the form presented in Sec. 2.2.4, and given here as

$$\frac{\partial \vec{S}}{\partial t} = -\overleftrightarrow{\Gamma} \cdot \vec{S} + \vec{\Omega} \times \vec{S} \tag{4.26}$$

where $\vec{\Omega} = g\mu_B \vec{B}_{ext}/\hbar$ is the Larmor precession frequency, with $g$ the electron g-factor, $\mu_B$ the Bohr magneton, $\hbar$ the reduced Planck constant, and $\vec{B}_{ext}$ the external magnetic field vector, taken to be in-plane in the Voigt geometry with $\vec{B}_{ext} = B_{ext}\hat{x}$. Here I have neglected spin-orbit effective magnetic field contributions to $\vec{\Omega}$. $\overleftrightarrow{\Gamma}$ is the anisotropic spin relaxation rate, and I have taken the equilibrium spin polarization to be zero. In the $[1\bar{1}0]$, [110], [001] crystal axis basis Eq. 4.26 is given in matrix form as

$$\frac{\partial \vec{S}}{\partial t} = \begin{pmatrix} -\Gamma_x & 0 & 0 \\ 0 & -\Gamma_y & -\Omega \\ 0 & \Omega & -\Gamma_z \end{pmatrix} \begin{pmatrix} S_x \\ S_y \\ S_z \end{pmatrix} \tag{4.27}$$

where I have dropped the subscript on the precession frequency for notational simplicity. The pump initially polarizes spins along the $\hat{z}$ direction, so we will take $S_x(0) = S_y(0) = 0$, and $S_z(0) = S_0$. We see that Eq. 4.27 represents a pair of coupled differential equations in the $\hat{y}$ and $\hat{z}$ directions. These can be decoupled to arrive at a second order differential equation in the $\hat{z}$ (measured) component of the spin polarization:

$$\partial_t^2 S_z + (\Gamma_y + \Gamma_z)\, \partial_t S_z + \left(\Omega^2 + \Gamma_y \Gamma_z\right) S_z = 0. \tag{4.28}$$

In the limit that $\Omega \gg \Gamma_y, \Gamma_z$, this has solutions of the form

$$S_z(\Delta t) = S_0 \exp\left(-\frac{\Delta t}{\tau}\right)\cos(\omega \Delta t) \tag{4.29}$$

with the following definitions:

$$\tau = 2\left(\Gamma_x + \Gamma_y\right)^{-1} \tag{4.30}$$

$$\omega = \sqrt{\Omega^2 - 1/4\left(\Gamma_z - \Gamma_y\right)^2}. \tag{4.31}$$

We note that this solution is only defined for $\Omega \geq |\Gamma_z - \Gamma_y|/2$. Fig. 4.7(a) shows a set of time-resolved Kerr rotation measurements of the free evolution of conduction band spin polarization. The pump initializes spins at a time delay of $\Delta t = 0$. Measurements are conducted with an external magnetic field strength of 100 (black), 200 (red), and 300 (blue) mT. Lines are fits to Eq. 4.29. From the fit function we can extract the average spin relaxation time and the Larmor precession frequency. A linear fit of the Larmor precession frequency (Fig. 4.7(b)) gives the conduction band electron g-factor. Here we have taken the anisotropy in the spin relaxation rate to be negligibly small compared to the precession frequency, namely $(\Gamma_z - \Gamma_y)^2/(8\Omega^2) \ll 1$, in which case we make the approximation $\Omega \approx \omega$. This approximation is valid when the precession frequency is proportional to the external magnetic field. For small $B_{ext}$, we see that the linear behavior breaks down due to the spin relaxation rate anisotropy.

The Lakeshore Model 331 temperature controller allows for temperature tuning using a resistive heater and thermocouple. Calibration curves are specific to each cryostat. By controlling the liquid helium flow and PID settings of the temperature controller, the temperature of the cryostat can be maintained in a range from $\sim 5$ K up to room temperature. Time resolved Kerr rotation measurements are taken at a variety of temperatures, the results of which are displayed in Fig. 4.8. Panel (a) displays the measured Kerr rotation peak

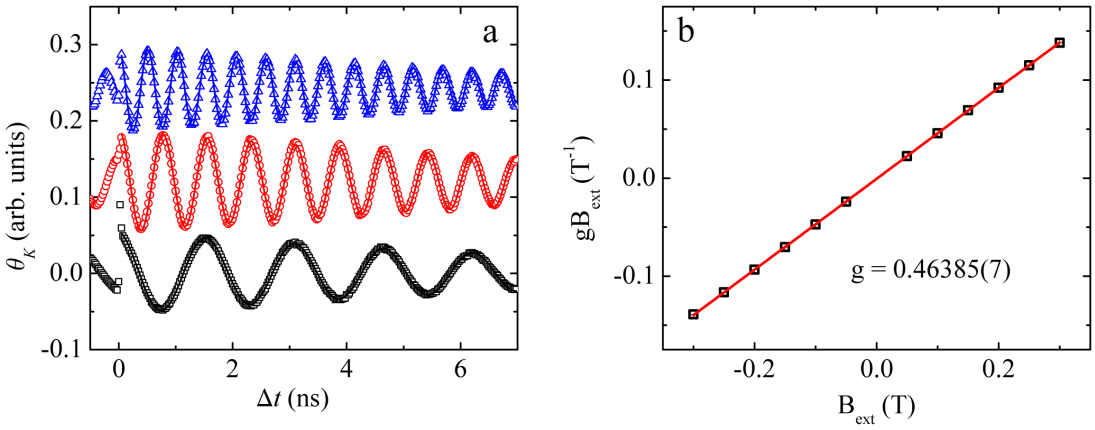


**Figure 4.7: Time-resolved Kerr rotation:** (a) Time-resolved Kerr rotation signal for an external voltage of 100 mT (black squares), 200 mT (red circles), and 300 mT (blue triangles). Lines are fits to Eq. 4.29. (b) The precession frequency is proportional to the external magnetic field; the constant of proportionality is the electron g-factor. Measurements are taken on $In_{0.03}Ga_{0.97}As$ at a temperature of $T = 30$ K and a wavelength of $\lambda = 839.4$ nm.

wavelength. This is in excellent qualitative agreement with the measured and theoretical behavior of the band gap energy for GaAs [103]. Panel (b) shows the Kerr rotation amplitude as a function of temperature. As we expect the optically generated spin polarization to be independent of temperature [11], the decrease in amplitude is a result of the temperature dependence of the optical activity of the material. The measured conduction band electron g-factor is displayed in panel (c) and is also in qualitative agreement with the measured and theoretical behavior for GaAs [103, 104, 105, 106]. The spin relaxation time extracted from the fits is shown in panel (d). A log-log plot (inset) shows that, for a temperature of $T = 50$ K and above, the spin relaxation time obeys a $T^{-2.2}$ dependence, in precise accordance with the measured [16] and theoretical [107] temperature behavior above $\sim 70$ K when spin relaxation is dominated by the D'yakonov-Perel spin relaxation mechanism. This is due to the high temperature behavior of the spin relaxation rate in which the non-degenerate limit may be used and the principle of energy equipartition applies, namely $\tau_s^{-1} \propto \tau_m T^3$, with $T$ the temperature and $\tau_m$ the momentum relaxation time. Here polar optical phonon scattering dominates. We can use measurements of the mobility to estimate the temperature

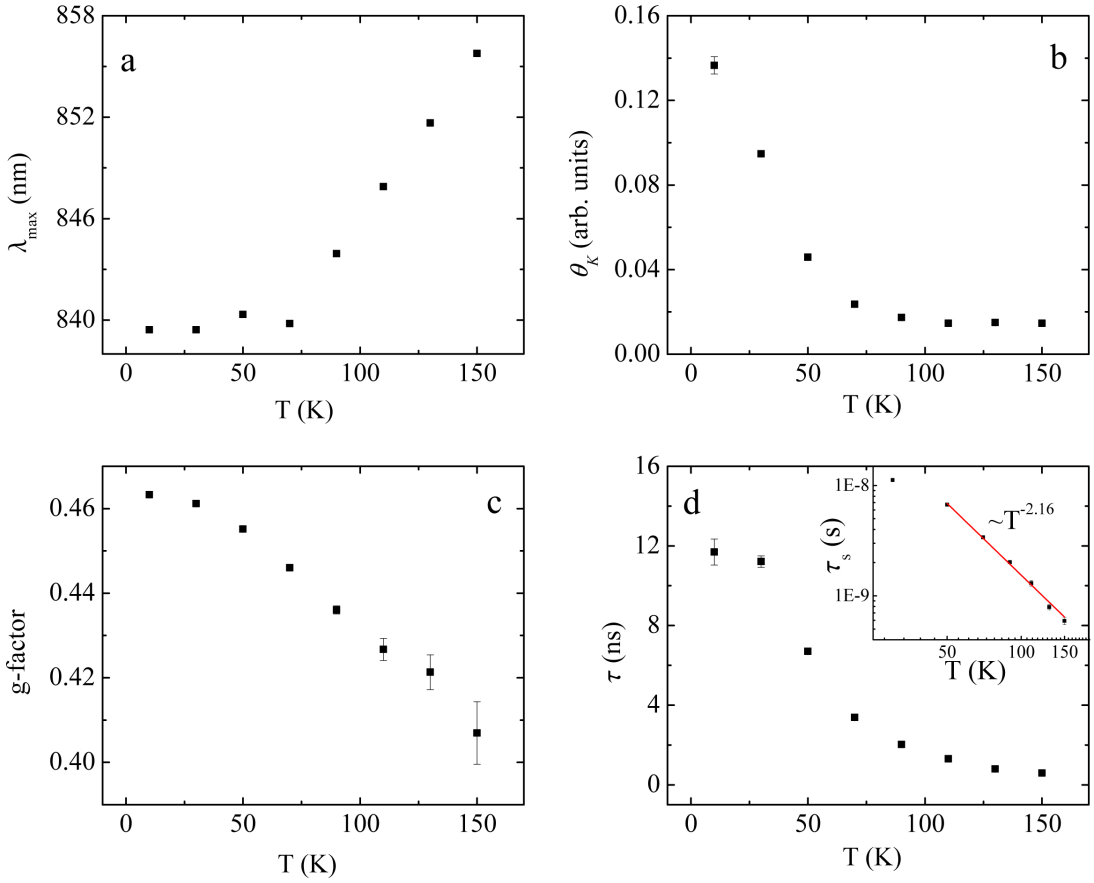


**Figure 4.8: Kerr rotation vs. temperature:** (a) and (b) Peak Kerr rotation wavelength and amplitude, respectively. (c) and (d) Electron g-factor and spin relaxation time, respectively, extracted from fits to Eq. 4.29. Inset of (d) log-log plot shows spin relaxation time power law dependence of $\sim T^{-2.2}$

dependence of $\tau_m$, from which we get $\tau_m \propto T^{0.8}$, and hence $\tau_s \propto T^{-2.2}$. The low temperature behavior is more complicated as the degenerate case must be used and equipartition no longer applies. Ref. [107] attributes a weak temperature and doping dependence of the spin relaxation time to an incomplete thermalization of carriers. In this case the spin relaxation time is expected to obey a $\sim T^{-1/2}$ dependence, also due to the D'yakonov-Perel mechanism, with scattering dominated by ionized impurities.

### 4.3.3 Frequency domain measurements

In addition to fixing the frequency and measuring the time evolution of spins by varying the pump-probe time delay, it is also possible to vary the precession frequency while maintaining the pump and probe at a fixed time delay. In the absence of a net drift of spins, when the spin relaxation time is sufficiently long, that is, on the order of the laser repetition rate, we must account for the spin polarization induced by a series of pump pulses occurring at the laser repetition rate. In this case, the time dependent spin polarization in Eq. 4.29 must be modified to

$$S_z(\omega) = S_0 \sum_{n=0}^{\infty} \Theta(\Delta t + n t_{rep}) \exp\left(-\frac{\Delta t + n t_{rep}}{\tau}\right) \cos\left[\omega(\Delta t + n t_{rep})\right]. \tag{4.32}$$

where $t_{rep}$ is the laser repetition time taken to be $t_{rep} = 13.16$ ns and $\Theta(\Delta t + n t_{rep})$ is the Heaviside function, defined to be zero when its argument is negative and one when its argument is positive. It serves the purpose of allowing us to account for an instantaneous spin polarization generated during each pump pulse. Eq. 4.32 reduces to Eq. 4.29 when only the $n = 0$ term in the sum is considered. In this case, at a fixed time delay, the spin polarization is described by a cosine function in the precession frequency $\omega$. By including previous pump pulses, we are including terms of higher order in frequency weighted by exponentially decaying amplitudes. The result, shown in Fig. 4.9(a), is a cosine wave with "sharpened" peaks, which correspond to the frequency for which all pulses have rephased at the given time delay. This phenomenon is known as resonant spin amplification (RSA) [16].

When the spin relaxation time is significantly longer than the laser repetition time ($\tau \gg t_{rep}$), each individual peak can be approximated as a Lorentzian function, the width of which can be used to determine the relaxation rate for each magnetic field about which the

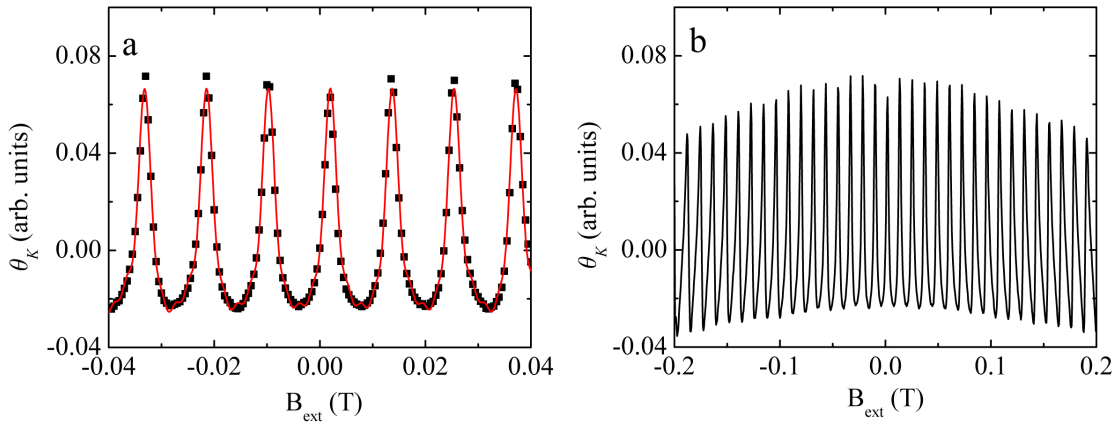


**Figure 4.9: Resonant spin amplification:** Measurements are shown over a narrow (a) and broad (b) external magnetic field range. Depression of center peak is due to anisotropic spin relaxation time. Line in (a) is fit to Eq. 4.32, from which the average relaxation time and g factor are extracted.

Lorentzian is centered [108]. We are not in a regime where such an approximation is valid. Instead, we fit the data in Fig. 4.9(a) to Eq. 4.32, from which the overall spin relaxation time and g-factor are determined. Only the first four terms in the sum are used.

Notice that the center peak is depressed compared to the surrounding peaks. This is a result of the anisotropic spin relaxation rate. Recall the solutions given in Eqs. 4.29 and 4.32 are only valid when the precession rate is sufficiently large compared to the spin relaxation rate. In the case in which the precession frequency is zero (i.e. $B_{ext} = 0$), then the spin relaxation is no longer given by the average of the rates along the $\hat{y}$ and $\hat{z}$ directions, but is rather described only by $\Gamma_z$. Recall from the D'yakonov-Perel spin relaxation mechanism, we expect $\Gamma_z = 2\Gamma_y$ (Sec. 3.4.1). The spin relaxation time, then, is reduced at $B_{ext} = 0$, and, as a result, the center peak is diminished. The ratio in heights of the center peak compared to the surrounding peaks is given by [108]

$$\frac{h_{center}}{h_{side}} = \frac{\exp\left(t_{rep}\Gamma\right) - 1}{\exp\left(t_{rep}\Gamma_z\right) - 1} \tag{4.33}$$

Taking the height ratio to be $\sim 0.9$, and assuming a spin relaxation time of $\tau \approx 3t_{rep}/2$

(determined from the fit), we get that $\Gamma_z \approx 1.2\Gamma_y$. Notice that this is less than the expected anisotropy in the spin relaxation rate due to the D'yakonov-Perel relaxation mechanism alone, and suggests that an additional spin relaxation mechanism is present. We expect this to be due to inhomogeneous relaxation and the Elliott-Yafet mechanism [78].

We finally note that the side peaks are expected to have constant amplitude as a function of $B_{ext}$ only when the time delay is equal to the laser repetition time ($\Delta t = t_{rep}$). If this is not the case, then there is an overall cosinuoidal envelope function with a frequency increasing with $\Delta t - t_{rep}$ [16]. This behavior is shown in Fig. 4.9(b), for which the fixed time delay is $\Delta t = 13$ ns.

### 4.3.4 Spatial separation of pump and probe

One final practical measurement consideration to discuss is the drift of electrons under action of an applied current, as is the case in many of the experiments conducted and discussed in this work. A "packet" of electron spins, induced by the pump, is Gaussian distributed at the pump spot at time $\Delta t = 0$. However when a current is applied the electron spin packet will have a net drift velocity given by the mobility. The probe is incident on the sample at time $\Delta t > 0$, for which the spatial separation between the pump and the spin packet will be $\Delta x = v_d \Delta t$. To measure the spin polarization at the spin packet center, it is then necessary to provide a spatial separation between the pump and probe. This scenario is depicted in Fig. 4.10.

The pump-probe spatial separation is achieved by including a two dimensional steering mirror in the pump path, which is chosen over the probe path to avoid having to continuously realign the collection path. The steering mirror is composed of a high precision two-axis kinematic mount (Newport Part No. U100-G) with motorized actuators (Newport Model No. TRA12PP) which are servo-controlled by a Newport Model ESP301 Motion Controller. The mirror steers the pump beam prior to the focusing lens and allows variable positioning

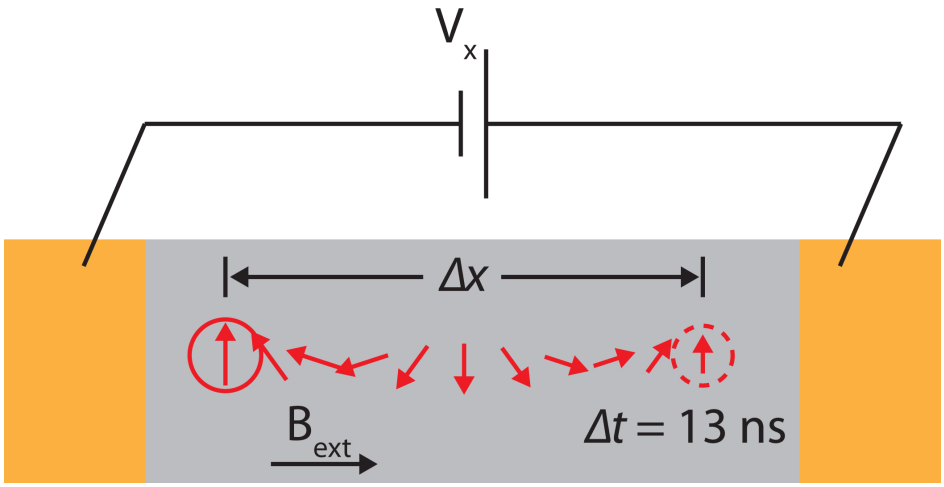


**Figure 4.10: Pump-probe spatial separation:** Pump (solid circle) and probe (dashed circle) spots are spatially separated on sample to provide maximum overlap of probe spot with pump-induced spin packet.

of the pump beam on the sample. The angle change is extremely small and as such we take the pump beam to be normal to the sample over the range of motion of interest. Linear behavior is confirmed. The actuators have submicron resolution, which translates to an angular resolution depending on the separation of the mirror from the lens and the focal length of the lens. For our applications, this translates to a submicron resolution of the position of the pump on the sample. The actuators have a backlash of $\sim 15\mu$m, which must be overcome when the direction is reversed.

The steering mirror is calibrated by traversing the pump beam across a 150 $\mu$m optical slit (Thorlabs Part No. S150R, with width tolerance of $\pm 4\mu$m) and measuring the power of the transmitted beam using a photodiode detector. An optical chopper is included in the pump path for these measurements alone to allow for lock-in detection. We treat the edge of the slit as a Heaviside step function and the pump beam as having a Gaussian power distribution from the center, with Gaussian widths that are different along the lab vertical and horizontal. The laser power transmitted is a convolution of the Gaussian distribution with the Heaviside function, which we recognize as the error function given by [93]

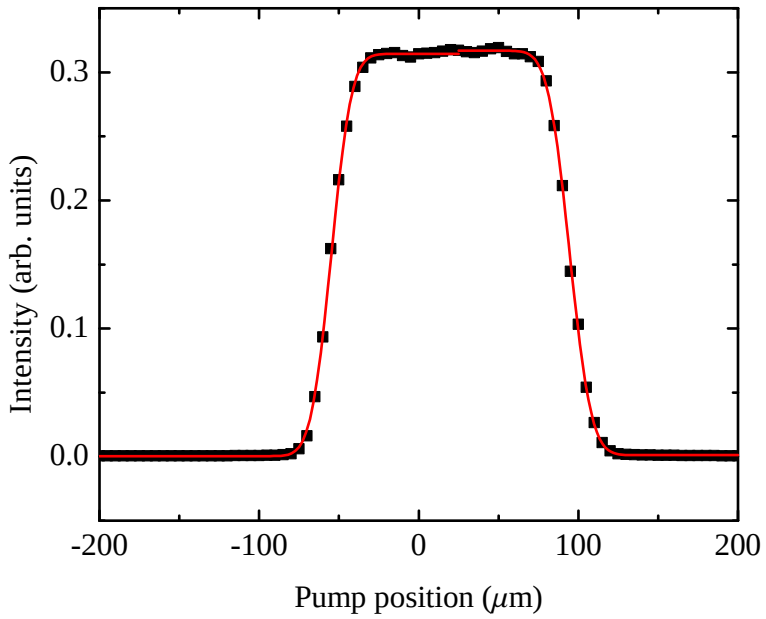


**Figure 4.11: Steering mirror calibration:** Pump is traversed across a 150 $\mu$m slit and transmitted power is measured. Each edge is fit to an error function. The separation between the error functions corresponding to opposite edges of the slit are used to calibrate the mirror actuators. The width of each error function gives the pump spot size. The procedure is performed for both the vertical and horizontal axes.

$$\mathrm{erf}\,(x) = \int_0^x \exp\left(-z^2\right) dz. \tag{4.34}$$

We calibrate the vertical and horizontal actuators by traversing the pump across the slit in the horizontal and vertical directions respectively and measuring the distance between the resulting centers of the error function fits. From the width of the error function fit, we can also determine the vertical and horizontal pump widths. An example of the calibrated pump-slit overlap curve, with error function fits at each edge, is shown in Fig. 4.11.

To determine the probe spot size, we perform a pump-probe overlap scan on the sample. The resulting measurement is a convolution of two Gaussians, which is also a Gaussian, with width given by $\sigma = \sqrt{\sigma_{pump}^2 + \sigma_{probe}^2}$. With $\sigma_{pump}$ determined from the mirror calibration,

| | Horizontal ($\mu$m) | Vertical ($\mu$m) |
|---|---|---|
| Pump | 12.8 | 9.5 |
| Probe | 6.7 | 17.5 |

**Table 4.1: Pump and probe spot sizes:** Horizontal and vertical Gaussian widths ($\sigma$) of pump and probe spots at the focal point.

and $\sigma$ measured from the pump-probe overlap, we can extract $\sigma_{probe}$. Table 4.1 shows the pump and probe spot sizes at the focal point using a 150 mm focal length lens. These are presented as the Gaussian width ($\sigma$) defined by

$$f(x) = \exp\left(-\frac{x^2}{2\sigma^2}\right). \tag{4.35}$$

It is related to the full width at half max by FWHM $= (2\sqrt{2\ln 2})\sigma$.

## 4.4 Steady-state spin polarization measurements

We finally briefly mention steady-state measurements of the spin polarization, in which case spins are being continuously polarized by some mechanism. This can be done electrically, as will be discussed in detail in Ch. 6. In this case, the optical pump is blocked. The equation describing the time dependence of the spin polarization given by Eq. 4.27 will be amended to include the source of spin polarization and will have the form

$$\frac{\partial \vec{S}}{\partial t} = \begin{pmatrix} -\Gamma & 0 & 0 \\ 0 & -\Gamma & -\Omega \\ 0 & \Omega & -\Gamma \end{pmatrix} \begin{pmatrix} S_x \\ S_y \\ S_z \end{pmatrix} + \begin{pmatrix} 0 \\ \gamma_y \\ \gamma_z \end{pmatrix} \tag{4.36}$$

The directions for $\vec{\Omega}$ and $\vec{\gamma}$, as well as the isotropy of the relaxation rate $\Gamma = \tau^{-1}$, are chosen to simplify the discussion. The general form will be addressed in Ch. 6. In the steady-state,

we take $\partial\vec{S}/\partial t = 0$, in which case we have the steady state component of the spin polarization along the $\hat{z}$ axis of

$$S_z = \gamma_y \tau \frac{\Omega\tau}{1 + (\Omega\tau)^2} + \gamma_z \tau \frac{1}{1 + (\Omega\tau)^2} \tag{4.37}$$

The first term has an odd Lorentzian form, while the second is an even Lorentzian (typically the "even" qualifier is left off) in the precession frequency $\Omega$. The amplitude for each term is given by the expected steady state value in the absence of precession (i.e. $\gamma\tau$). A typical Hanle measurement [109] will use circularly polarized light to continuously excite spins along the $\hat{z}$ direction and measure the polarized photoluminescence. This can by done using continuous wave excitation. In this case $\gamma_y = 0$ and the resulting measurement follows an even Lorentzian curve. On the other hand, a typical current-induced spin polarization measurement [29] uses electrical current to continuously align spins along the $\hat{y}$ direction (in which case $\gamma_z = 0$) and the resulting measurement is an odd Lorentzian.

# Chapter 5

# Spin-Orbit Field Measurements

## 5.1 Introduction

The polarization and coherent manipulation of electron spins is of key importance for spintronics applications [110]. While this can be accomplished by local magnetic fields either externally or using on chip magnetic materials [111], all-electrical manipulation of electron spins can be desirable as it offers significantly faster switching times and highly localizable patterning.

Using the spin-orbit (SO) effects described in Sec. 2.4, the motion of electrons under current translates to an effective magnetic field. The spin analog of the field effect transistor (FET) presented by Datta and Das [68] proposes that electrical control of magnetism through the use of spin-orbit effects can be potentially useful as a spin selective device for spintronics applications.

Electrical spin manipulation using the Rashba spin-orbit interaction has been observed in quantum wells [112, 113] and two-dimensional electron gasses (2DEGs) [114]. In bulk materials, strain-induced fields have been observed to manipulate electron spins in the ab-

sence of any external magnetic field sources and without use of magnetic materials [26]. Mechanical strain has also been used as a method of manipulating spins by allowing variable control of the spin-orbit interaction strength [24, 115]. Such strain-induced spin manipulation has been spatially mapped for electrons under drift and diffusion [116]. Anisotropic spin-orbit interactions have also been observed and mapped as a function of current direction in GaAs/InGaAs quantum wells [117] and bulk InGaAs epilayers [118, 119].

In addition to spin manipulation, control of spin coherence is also possible using spin-orbit effects. This was observed in ZnO, in which application of an in-plane electric field was found to nearly double the transverse spin coherence time [120]. More recently, spin-orbit interactions have been tuned using electric fields in (111) GaAs quantum wells to increase spin relaxation times by up to two orders of magnitude [18]. A similar effect was shown previously in (001) GaAs quantum wells [17] using strain to manipulate spin-orbit interactions. In both cases, the spin-orbit interactions were minimized in an effort to reduce the effect of the dominant D'yakonov-Perel spin relaxation mechanism (Sec. 3.4.1).

This chapter will focus on III-V semiconductor heterostructures for which the momentum $\vec{k}$- linear Bychov-Rashba [10] and $\vec{k}$-cubic Dresselhaus [9] spin-orbit interactions are present. Furthermore the samples are grown in an epilayer in which strain and strain relaxation are present, giving rise to $\vec{k}$-linear biaxial and uniaxial strain-induced spin-orbit interactions as well [121]. These spin-orbit interactions and their corresponding effective magnetic fields are described in more detail in Sec. 2.4. The Rashba spin-orbit magnetic field, due to structural inversion asymmetry (SIA), and the unixial strain-induced field obey they same $\vec{k}$-dependent symmetry (up to a potential minus sign), and can therefore be combined into a single SIA-like spin-orbit field. Similarly the linear Dresselhaus, due to bulk inversion asymmetry (BIA), and biaxial strain-induced fields can be combined into a single BIA-like spin-orbit field. Combining the linear components of the in-plane spin-orbit interaction, the spin-orbit effective magnetic field is generalized to

$$\vec{B}_{SO} = (\alpha k_y + \beta k_x)\,\hat{x} - (\alpha k_x + \beta k_y)\,\hat{y}, \tag{5.1}$$

where $k$ represents the magnitude of the electron momentum, $x$ and $y$ the [100] and [010] crystal axes, respectively, and $\alpha$ and $\beta$ represent the SIA and BIA spin-orbit field components, respectively. The resulting anisotropic spin-orbit field map was presented in Fig. 2.8. Notice the special case, that when $\alpha = \beta$, Eq. 5.1 becomes

$$\vec{B}_{SO,matched} = \alpha\,(k_x + k_y)\,(\hat{x} - \hat{y}) \tag{5.2}$$

In this case, the sample exhibits a spin-helix state for which the spin-orbit effective magnetic field is always along one of two opposing directions, despite the direction of the in-plane electron momentum. This is particularly useful as it provides a means of significantly reducing spin dephasing for drift electrons [44].

In this chapter, we present an optical means of measuring the spin-orbit effective magnetic field, showing that the strength of the spin-orbit field components vary for different samples taken across the same wafer. We use this method to measure the carrier velocity as a function of applied electric field and show that the spin-orbit field strength is proportional to the electron velocity. Using a four-contact geometry, we present the anisotropy of the spin-orbit effective magnetic field for a single location in a sample. By varying the direction of the electrical current, we will show that we can vary the strength of the spin-orbit effective magnetic field. This will ultimately be used to compare the magnitude of current-induced spin polarization with the strength of the spin-orbit field in Ch. 6.

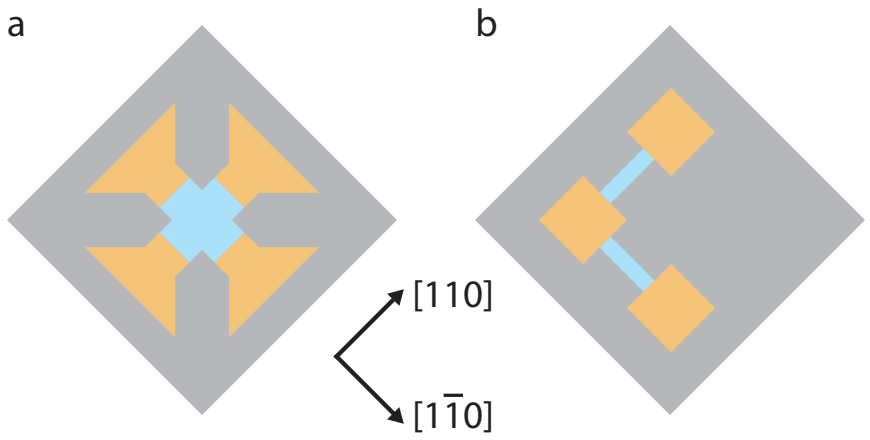


**Figure 5.1: Sample designs:** Schematic for cross (a) and L-shaped (b) sample patterns. InGaAs epilayer is depicted in blue, ohmic contacts in orange, and the substrate in gray. Chip size is not to scale.

## 5.2 Sample design

The samples are 500 nm epilayers of $In_{0.04}Ga_{0.96}As$ grown on a (001) GaAs substrate and capped with a 100 nm GaAs layer. The epilayer is n-doped (Si) at $3 \times 10^{16}$ cm$^{-3}$. Biaxial strain results from the lattice mismatch between the epilayer and substrate. The InGaAs epilayer has a larger lattice constant than the GaAs substrate, and therefore compressive strain of the InGaAs epilayer results in plane, and tensile strain out of plane. Because the epilayer is grown beyond the critical thickness [122], anisotropic and inhomogeneous strain relaxation occurs resulting in non-uniform uniaxial strain as well.

Samples are patterned into one of two geometries, each of which are in the plane of the (001) growth axis. Sample fabrication is performed using photolithography and a chemical wet etch. The L-shaped pattern (Fig. 5.1(b)) has two orthogonal channels oriented in the plane of the sample. The cross pattern (Fig. 5.1(a)) has a four-contact planar geometry allowing arbitrary tuning of the strength and direction of the in-plane electric field.

### 5.2.1 L-shaped pattern

The original sample design has discrete channels through which uniform electrical conduction occurs. The sample dimensions are chosen to provide a large region of uniformity while still keeping power dissipation at a minimum. The L-shape pattern gives two orthogonal channels in the (001) plane. Fig. 5.2 displays the sample and experimental schematic with spin-orbit field components. Samples were fabricated with channels along [110] and $[1\bar{1}0]$ or along [100] and [010].

For channels along [110] and $[1\bar{1}0]$, the SIA and BIA components of the spin-orbit field are either parallel or antiparallel, corresponding to a spin-orbit field maximum or minimum. In this case, both components of the spin-orbit field are perpendicular to electrical conduction (Sec. 2.4). For channels along [100] and [010], the spin-orbit field components are orthogonal, with the SIA component perpendicular to electrical conduction, and the BIA component either parallel or antiparallel. In this case, the spin-orbit effective magnetic field components can be measured independently. If the total spin-orbit field is well-described by Eq. 5.1, then we expect the following set of relations to hold true.

$$\left|\vec{B}_{[110]}\right| = |B_{SIA} + B_{BIA}| \tag{5.3}$$

$$\left|\vec{B}_{[1\bar{1}0]}\right| = |B_{SIA} - B_{BIA}| \tag{5.4}$$

As in Sec. 2.4, $B_{BIA}$ is taken to be positive and the sign of $B_{SIA}$ depends on the uniaxial strain component. With the two-channel geometry, however, it is impossible to compare the spin-orbit field extrema with the SIA and BIA components on any one sample and especially for a specific location on this sample. This is particularly necessary because many samples taken from the same wafer exhibit differing strengths of spin-orbit field components due to

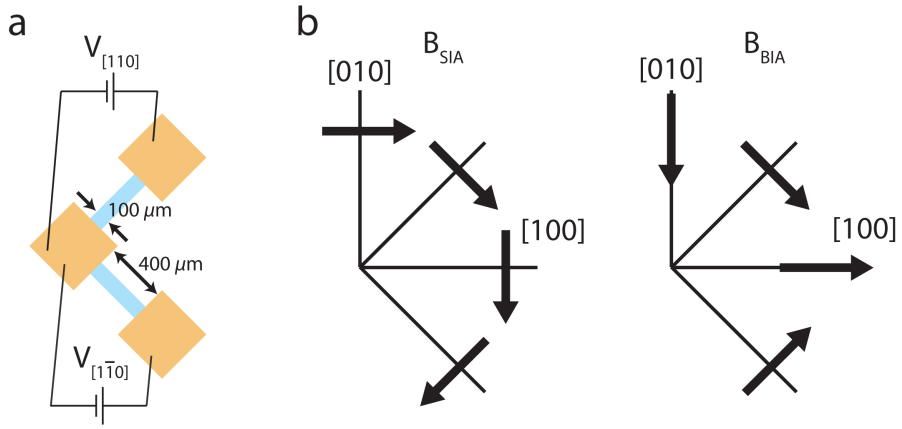


**Figure 5.2: L-shaped sample schematic:** (a) Epilayers are etched into two orthogonal conductive channels with electrical contacts at either end. An external voltage is applied to the contacts to provide electrical conduction parallel to or perpendicular to the external magnetic field. (b) SIA and BIA spin orbit field components for electron momentum along [110], [1$\bar{1}$0], [100], and [010]. For $\vec{k}$ along [110] or [1$\bar{1}$0], $\vec{B}_{int}$ is a maximum or minimum and is perpendicular to electron momentum. For $\vec{k}$ along [100] or [010], the SIA and BIA spin-orbit field components are orthogonal, with SIA perpendicular to momentum and BIA either parallel or antiparallel.

inhomogeneous strain relaxation.

### 5.2.2 Cross pattern

The four contact geometry was used to measure the magnitude of the spin-orbit effective magnetic field for electron momentum ($\vec{k}$) along any direction in the (001) plane at a single location on the sample. Fig. 5.3(a) depicts the sample schematic. The dimensions are again chosen to maximize the region of electric field uniformity while minimizing the power dissipation. When electron momentum ($\vec{k}$) is oriented along the external magnetic field, the components of the spin-orbit effective magnetic field can be used to determine the spin-orbit field orientation $\xi$ with respect to electron momentum (Fig. 5.3(b)). This will be discussed in detail in the following section.

Relaxation calculations to Poisson's equation [123] are performed numerically to map the electric potential and electric field throughout the cross region of the sample (Fig. 5.3(c) and (d)). This is described in Appendix A. The orientation and magnitude of the electric field

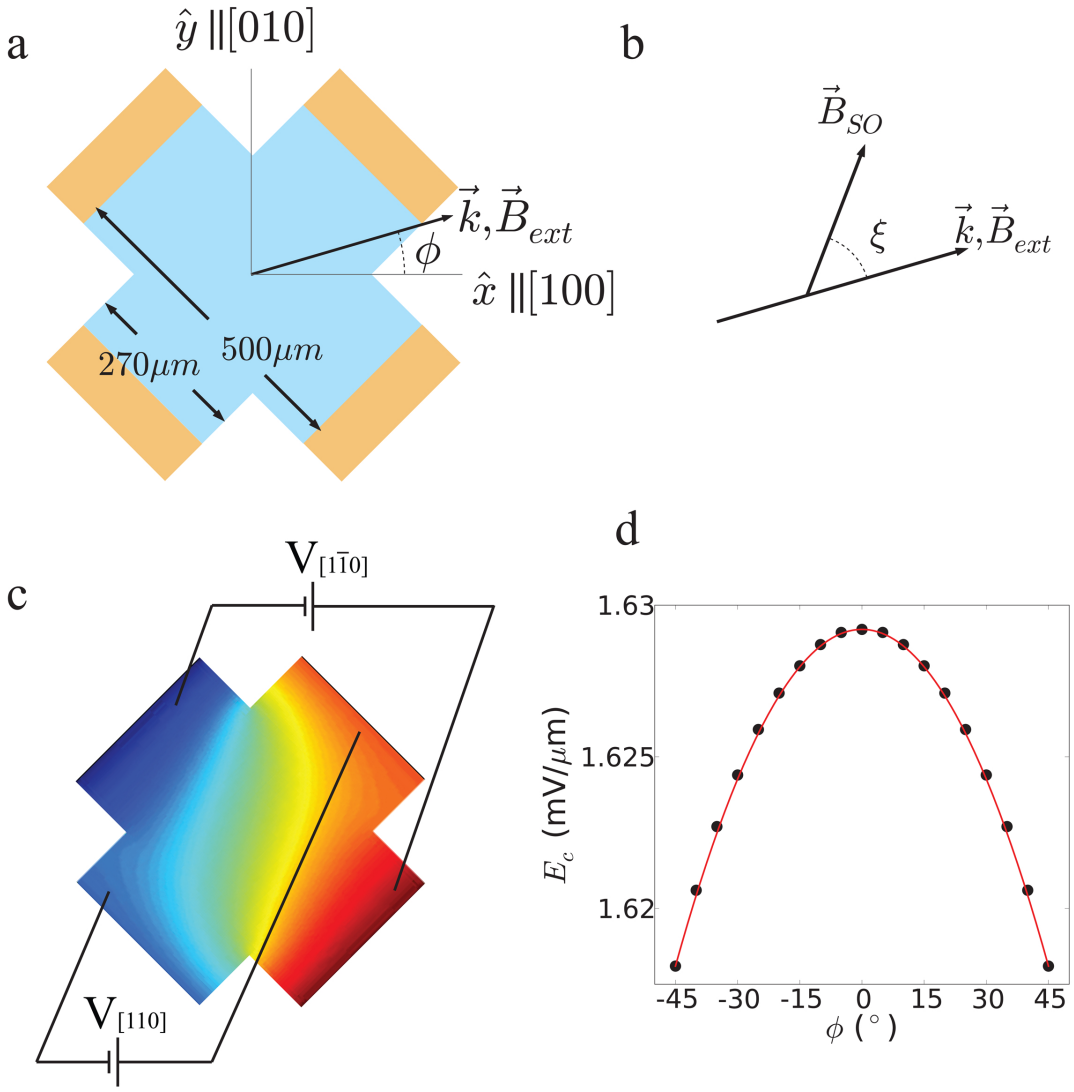


**Figure 5.3: Cross-patterned sample schematic:** (a) Cross sample schematic and experimental geometry. (b) Spin-orbit field orientation (c) Relaxation calculations of the electric potential for $\phi = -15°$. (d) Electric field mapping at the sample center from relaxation calculations, fit to a parabolic curve (red line). The relative strengths of electrical bias applied to opposite contacts is used to set the electron momentum direction $\phi$.

at the center is described by the following relations:

$$\tan\left(\phi + \pi/4\right) = \frac{V_{[110]}}{V_{[1\bar{1}0]}} \tag{5.5}$$

$$\left|\vec{E}_c\right| = E_{max} - a\phi^2. \tag{5.6}$$

The parameters $E_{max}$ and $a$ are determined using relaxation methods (Appendix A). The angle $\phi$ with respect to the [100] crystal axis is used to describe the electron momentum direction. Using the form of the spin-orbit Hamiltonian described in Eq. 5.1, the spin-orbit effective magnetic field is given by

$$\vec{B}_{SO} = k\left[\left(\alpha\sin\phi + \beta\cos\phi\right)\hat{x} - \left(\alpha\cos\phi + \beta\sin\phi\right)\hat{y}\right]. \tag{5.7}$$

It has proven useful to define the in-plane angle $\xi$ (Fig. 5.3(b)) that the spin-orbit effective magnetic field makes with the electron momentum $\vec{k}$ as a function of the momentum direction $\phi$. In this case, the magnitude and orientation of the spin-orbit field can be described by the following set of relations:

$$\left|\vec{B}_{SO}\right| = \frac{k}{g\mu_B}\sqrt{\alpha^2 + \beta^2 + 2\alpha\beta\sin\left(2\phi\right)} \tag{5.8}$$

$$\xi = -\tan^{-1}\left(\frac{{}^{\alpha}\!/_{\beta} + \sin\left(2\phi\right)}{\cos\left(2\phi\right)}\right) \tag{5.9}$$

.

## 5.3 Experimental setup

To map the spin-orbit effective magnetic field, we measure the modulated spin precession of electron spins subject to current in the semiconductor samples. This is done optically in the pump-probe scheme described in Sec. 4.3.1. Measurements are taken in a liquid helium flow cryostat at either 10 K or 30 K. The pump and probe beams are temporally separated at a fixed time delay of 13 ns. This is done by setting the pump delay line to -160 ps (the laser pulse period being 13.16 ns). The pump pulse rapidly induces a spin polarization in the conduction band according to the optical selection rules that outlasts the carrier recombination time (Sec. 4.1.3). This is approximated to occur on a time scale that is considered instantaneous compared to the free evolution of the electron spins. The time evolution (Sec. 2.2.4) is described by the Bloch equation

$$\frac{\partial \vec{S}}{\partial t} = -\frac{1}{T_2^*}\vec{S} + \vec{\Omega}_L \times \vec{S} \tag{5.10}$$

where $\vec{S}$ represents the electron spin density, $T_2^*$ the transverse spin coherence time, and $\vec{\Omega}_L$ the Larmor precession frequency given by $\vec{\Omega}_L = g\mu_B(\vec{B}_{ext} + \vec{B}_{int})/\hbar$. The coherence time of interest is taken to be the transverse, rather than longitudinal, ($T_2$ rather than $T_1$) because spins will precess in the plane perpendicular to the external magnetic field axis, along which energy quantization is defined. In the form given by Eq. 5.10, we made the approximation that $1/T_2^*$ is given by the average of the in plane and out of plane spin relaxation rates, as discussed in Sec. 4.3.2.

Experimental measurements are taken in the Voigt geometry, with an external magnetic field in the plane of the epilayer and the laser axis along the growth direction, and perpendicular to the external magnetic field. The time-dependent $\hat{z}$ component of the electron spin polarization is measured by Faraday or Kerr rotation of the linearly polarized probe

beam (Sec. 4.2.1). Faraday rotation refers to rotation of the probe beam upon transmission through the sample, whereas Kerr rotation refers to reflection.

### 5.3.1 External magnetic field measurements

The time-dependent behavior of the electron spin density is described by Eq. 5.10. As the external and spin-orbit magnetic fields lie in the plane of the sample, we can simplify the differential equation by taking $\Omega_z = 0$. In this case, Eq. 5.10 becomes

$$\frac{\partial}{\partial t}\begin{pmatrix} S_x \\ S_y \\ S_z \end{pmatrix} = \begin{pmatrix} -1/T_1 & 0 & \Omega_y \\ 0 & -1/T_2^* & -\Omega_x \\ -\Omega_y & \Omega_x & -1/T_2^* \end{pmatrix}\begin{pmatrix} S_x \\ S_y \\ S_z \end{pmatrix}. \tag{5.11}$$

Using a simple rotation matrix about the $\hat{z}$ axis,

$$R_z(\theta) = \begin{pmatrix} \cos\theta & -\sin\theta & 0 \\ \sin\theta & \cos\theta & 0 \\ 0 & 0 & 1 \end{pmatrix},$$

and choosing $\tan\theta = \Omega_y/\Omega_x$, Eq. 5.11 can be cast as

$$\frac{\partial}{\partial t}\begin{pmatrix} S_{x'} \\ S_{y'} \\ S_z \end{pmatrix} = \begin{pmatrix} -1/\tilde{T}_1 & 0 & 0 \\ 0 & -1/\tilde{T}_2^* & -\Omega_{tot} \\ 0 & \Omega_{tot} & -1/\tilde{T}_2^* \end{pmatrix}\begin{pmatrix} S_{x'} \\ S_{y'} \\ S_z \end{pmatrix}. \tag{5.12}$$

with $\Omega_{tot} = \sqrt{\Omega_{x'}^2 + \Omega_{y'}^2}$. The *prime* notation represents the rotated basis, with $\hat{z}' = \hat{z}$. The longitudinal and transverse spin relaxation times will, in general, be rotated as well, however we approximate this deviation will be small when $\Omega_y \gg \Omega_x$, as is usually the case, in which case we take $\tilde{T} \approx T$. Notice that Eq. 5.12 has nearly the same form as Eq. 4.27 in Sec. 4.3.2,

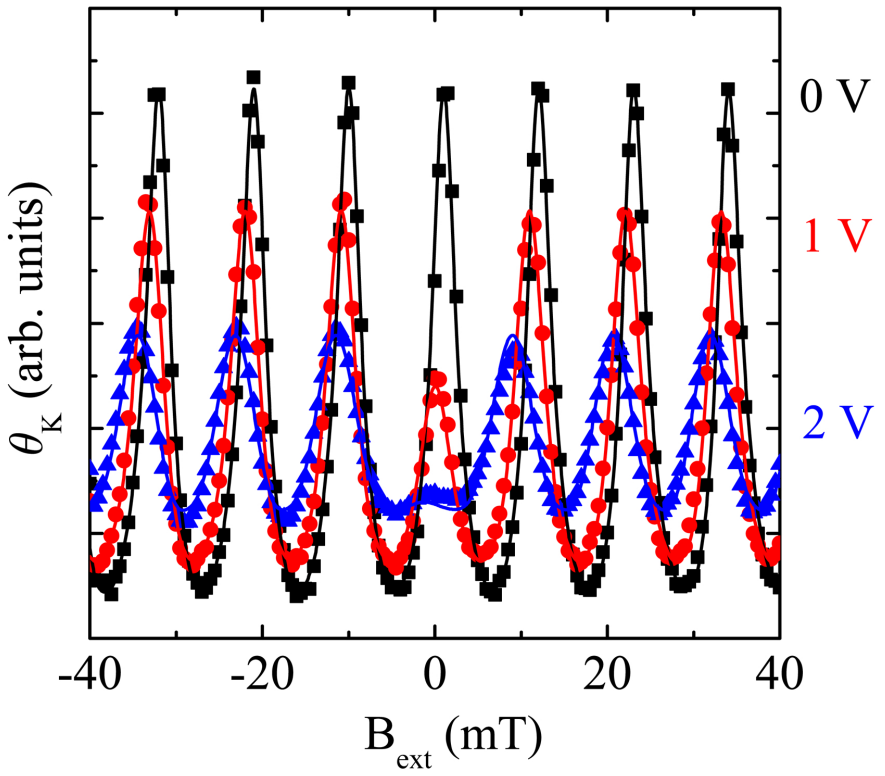


**Figure 5.4: Spin-orbit field measurements:** Optical Kerr rotation as a function of $B_{ext}$ at a fixed time delay of $\Delta t = 13$ ns for external voltages of 0 V (black squares), 1 V (red circles), and 2 V (blue triangles). The component of the spin-orbit effective magnetic field parallel to $B_{ext}$ shifts the phase while the perpendicular component modifies the height of the center peak. Fits to Eq. 5.13 (solid lines) are used to extract these components.

with a corresponding solution to the $\hat{z}$-component of the spin polarization

$$S_z = S_{z,0} e^{-\Delta t/T_2^*} \cos\left[\frac{g\mu_B \Delta t}{\hbar}\sqrt{\left(B_{ext} + B_{\parallel}\right)^2 + B_{\perp}^2}\right]. \tag{5.13}$$

$B_{\perp}$ and $B_{\parallel}$ represent the components of the spin-orbit effective magnetic field perpendicular to and parallel to the external magnetic field, respectively. From optical pumping, we approximate at time zero that spin polarization is aligned only along the laser ($\hat{z}$) axis. $\Delta t$ is the pump-probe delay time.

At a fixed pump-probe time delay of $\Delta t = 13$ ns, sweeps in the external magnetic field from -40 to 40 mT are conducted and the $\hat{z}$-component of the spin polarization measured.

In the absence of spin-orbit interactions, Eq. 5.13 reduces to a simple cosine function in $B_{ext}$. This function is modified by inclusion of the spin-orbit field terms. Fig. 5.4 shows Kerr rotation measurements for various voltages. The component of the spin-orbit field parallel to the external magnetic field shifts the phase of the cosine wave, while the perpendicular component modifies the height of the center peak. We see that the strength of the spin-orbit field increases as the electron current increases. This is expected; from Eq. 5.7 the spin-orbit field is expected to be proportional to the electron velocity.

### 5.3.2 Spatial overlap

When the potential difference between contacts is nonzero, there will be a net drift velocity experienced by the pump-induced electron spin packet. After the 13 ns pump-probe delay time, this will correspond to a spatial migration which depends on the strength of the electric current. In order to measure the spin polarization using the probe beam, it is therefore necessary to control the pump-probe spatial separation as well. This is done by including a two-axis steering mirror in the pump path prior to reaching the focusing optics (Sec. 4.3.4). The pump mirror is steered rather than the probe to avoid having to realign the probe collection path for each spatial separation.

The approximate pump-probe spatial separation for each external voltage is estimated from the mobility in the samples. This separation is given by

$$\Delta x = \mu E \Delta t \tag{5.14}$$

where $\mu$ is the electron mobility, $E$ the applied electric field, and $\Delta t$ the pump-probe time delay. For the L-shaped channels, the applied electric field is homogeneous and is given by the familiar expression $E = V/d$, where $V$ and $d$ are the potential difference and physical separation between the contacts, respectively. In the case of the cross sample, the electric

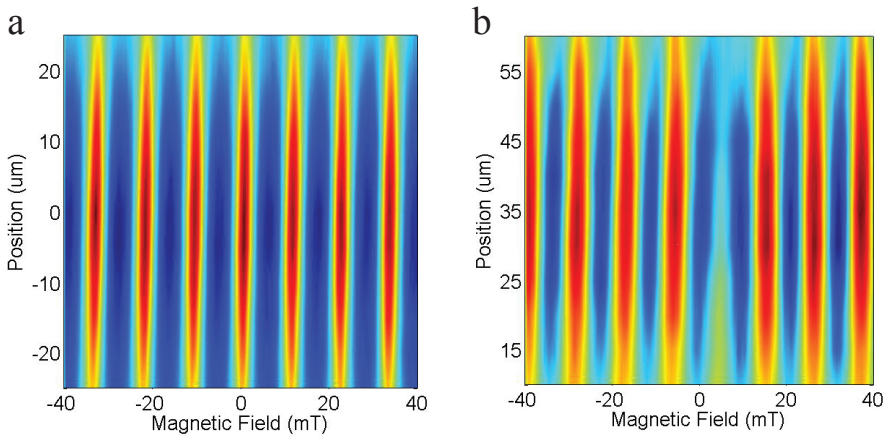


**Figure 5.5: Spin-orbit field measurements vs. $B_{ext}$, $\Delta_x$:** Kerr rotation measurements of the $\hat{z}$-component of the spin polarization used to extract spin-orbit magnetic field for an external bias of 0 V (a) and 2 V (b). For each pump-probe spatial separation (vertical axis), a magnetic field scan is taken (horizontal axis) which is evaluated by Eq. 5.13. The phase shift and center peak depression corresponding to the parallel and perpendicular spin-orbit field components, respectively, is clear for the high external bias (b). It is present, but not pronounced, for zero bias (a) due purely to electron diffusion.

field is estimated numerically. This electric field is taken to be approximately homogeneous in the region of interest.

At each external voltage, spatial separation scans are taken at 5 $\mu$m intervals over a 50 $\mu$m range centered at the expected pump-probe spatial separation. For each spatial separation, an external magnetic field scan is performed. Fig. 5.5 shows Kerr rotation measurements of the $\hat{z}$-component of the spin-polarization as a function of external magnetic field (horizontal axis) and pump-probe spatial separation (vertical axis) for various voltages. The spin-orbit field measurements as in Fiq. 5.4 represent horizontal cross-cuts. Fits to the amplitude in Eq. 5.13 give the $\hat{z}$-component of the spin polarization density (Fig. 5.6(a)).

The laser has a Gaussian beam profile, and, as such, the probe beam and pump-induced spin packet both have a Gaussian spatial profile as well. By scanning the pump beam, we are, in effect, scanning the pump-induced spin packet across the probe beam profile, and a convolution of the two Gaussian profiles is measured, which is itself Gaussian. Fig. 5.6(a)

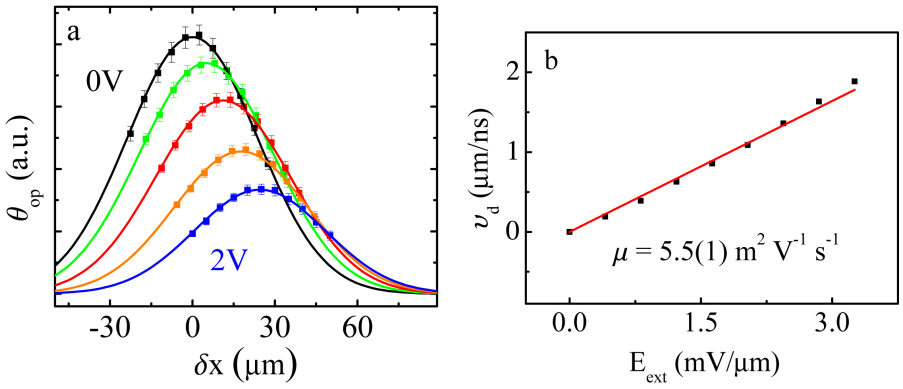


**Figure 5.6: Spin packet velocity measurements:** (a) Spin polarization amplitude as a function of pump-probe spatial separation for 0 V (black), 0.5 V (green), 1.0 V (red), 1.5 V (orange), and 2.0 V (blue). The center of the Gaussian distribution is used to determine the location of the spin packet center, from which the electron velocity (b) and spin-orbit field components are calculated.

shows this Gaussian distribution for several voltages. The Gaussian amplitude, given by $S_{z,0}\exp\left(-\Delta t/T_2^*\right)$ in Eq. 5.13, decreases for increasing electric field, indicating that the spatial spin polarization density decreases with increasing voltage. This can be due either to electric field-dependent spin dephasing or diffusion. As the spin packet width for each voltage is approximately the same and does not show any trend, diffusion is not expected to cause the decrease in spin polarization observed. As described in Sec. 3.4.1, spin relaxation has a strong electric field dependence, and therefore the decreased spin polarization at higher voltages is a result of the increased spin relaxation rate.

### 5.3.3 External electric field dependence

The center of each Gaussian fit in Fig. 5.6(a) is used to determine the electron drift velocity, given by $\upsilon_d = x_d/\Delta t$ and shown in Fig. 5.6(b). For each spatial separation, a fit of the external magnetic field scan to Eq. 5.13 is used to determine the components of the spin-orbit effective magnetic field perpendicular to and parallel to the external magnetic field. Fig. 5.9(a-b) shows these components as a function of pump-probe spatial separation.

The pump-induced electron spin packet has a spatial distribution analogous to a displaced

Maxwellian velocity distribution and can, in general, be described by

$$f_s(\delta x) \propto \exp\left[-\frac{(\delta x - x_d)^2}{2\sigma_d^2}\right] \tag{5.15}$$

with $x_d$ the center of the electron spin packet, given by $x_d = \upsilon_d \Delta t$ and $\sigma_d$ the spatial width of the electron spin packet. The subscript $d$ denotes the drift-induced spin packet. $x_d$ is expected to be proportional to the electric field for low field transport [51]. Eq. 5.15 describes the spatial distribution of electrons, which in turn describes their velocity distribution. Those electrons at the leading edge of the spin packet have moved faster than those at the trailing edge. The probe beam, therefore, takes an average measurement over some finite range for which the velocity distribution is not symmetric. As shown in Fig. 5.7, this means that the average velocity over the probe range is not equal to the velocity given by the probe center position.

The probe beam has a Gaussian spatial distribution similar to that of the electron spin packet:

$$f_p(\delta x) \propto \exp\left[-\frac{(\delta x - x_p)^2}{2\sigma_p^2}\right] \tag{5.16}$$

with the subscript $p$ denoting the probe beam spatial distribution. To determine the measured spin-orbit effective magnetic field ($B_{SO,meas}$) at a particular probe beam location, we take a convolution of $B_{SO}$ weighted by the spatial distribution of electron spins with the probe beam. This is described by

$$B_{SO,meas}(x_p) = \frac{\int_{-\infty}^{\infty} d\delta x \left\{ B_{SO}(\delta x) \exp\left[-\frac{(\delta x - x_d)^2}{2\sigma_d^2}\right] \exp\left[-\frac{(\delta x - x_p)^2}{2\sigma_p^2}\right] \right\}}{\int_{-\infty}^{\infty} d\delta x \left\{ \exp\left[-\frac{(\delta x - x_d)^2}{2\sigma_d^2}\right] \exp\left[-\frac{(\delta x - x_p)^2}{2\sigma_p^2}\right] \right\}}. \tag{5.17}$$

From Eq. 5.7, to first order, the spin-orbit effective magnetic field is proportional to the electron velocity, which is, in turn, proportional to the electric field. We approximate the

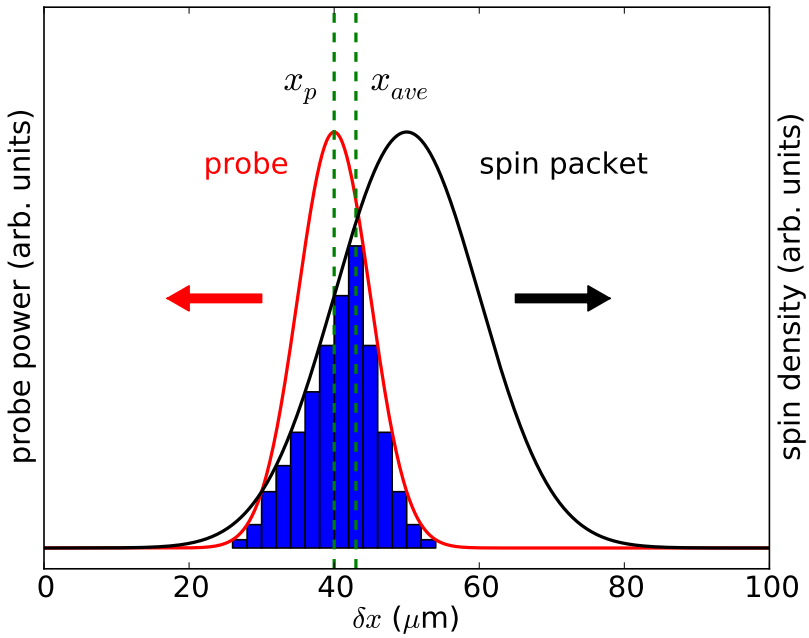


**Figure 5.7: Spatial overlap of probe beam and spin packet:** When the probe beam is separated from the center of the pump-induced spin packet, the average velocity of measured electrons is shifted from the velocity of the electrons at the center of the probe beam, due to the asymmetric distribution of electrons.

electric field to be uniform and therefore $B_{SO} \propto \delta x$. Using this definition, the solution to Eq. 5.17 is

$$B_{SO,meas}\left(x_p\right) = \frac{B_{int}\left(x_p\right)\sigma_d^2 + B_{int}\left(x_d\right)\sigma_p^2}{\sigma_d^2 + \sigma_p^2}. \tag{5.18}$$

Eq. 5.18 represents the spin-orbit effective magnetic field measured by the probe beam at a particular pump-probe spatial separation $x_p$, with an average electron drift velocity given by $v_d = x_d/\Delta t$. As shown in Fig. 5.7, when the probe is on the trailing edge of the spin packet, the average velocity is greater than that of the probe beam center, and therefore a larger spin-orbit field is measured. Similarly, when the probe beam is on the leading edge of the spin packet, a smaller spin-orbit field is measured. The end result is that as the probe traverses across the spin packet, the measured spin-orbit field obeys a linear relationship

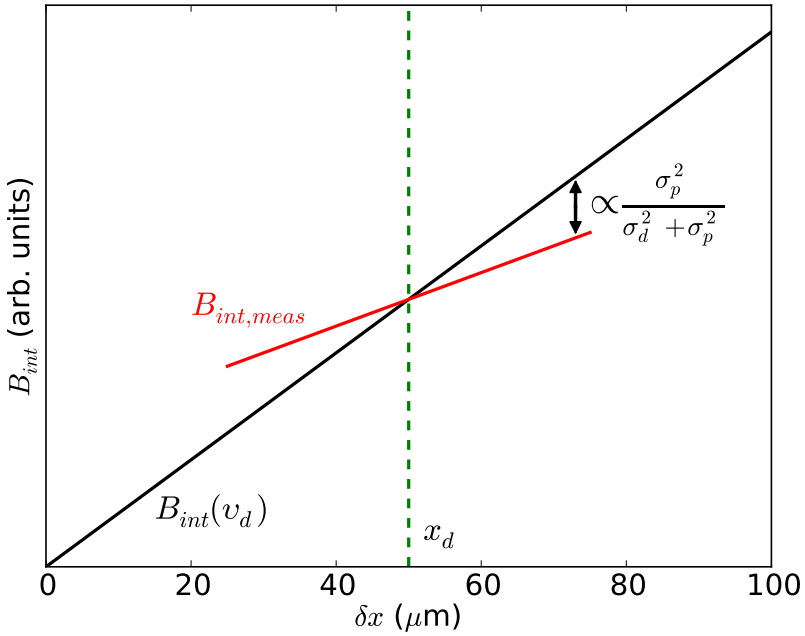


**Figure 5.8: Measured spin-orbit field:** The measured spin-orbit field at a particular probe location is deviated from the actual spin-orbit field due to the finite size of the probe beam. The deviation increases as the probe spot size ($\sigma_p$) increases compared to the electron spin packet ($\sigma_d$), and goes to zero when the probe overlap with the spin packet is maximized (i.e. when $x_p = x_d$).

described by Eq. 5.18, but with a slope less steep than given by Eq. 5.7. This is shown in Fig. 5.8.

The spin-orbit field as a function of drift velocity and the measured spin-orbit field intersect at the spin packet center. Taking a linear fit of the measured spin-orbit field as a function of pump-probe spatial separation (Fig. 5.9(a-b)) and evaluating at the spin packet center as determined in Fig. 5.6(a), we can get the spin-orbit field as a function of electron drift velocity. This is shown in Fig. 5.9(c). The components of the spin-orbit effective magnetic field are found to be proportional to the electron drift velocity, as expected from Eq. 5.7, and the proportionality constant $\kappa$ is used to characterize its strength. The spin-orbit field magnitude is given by

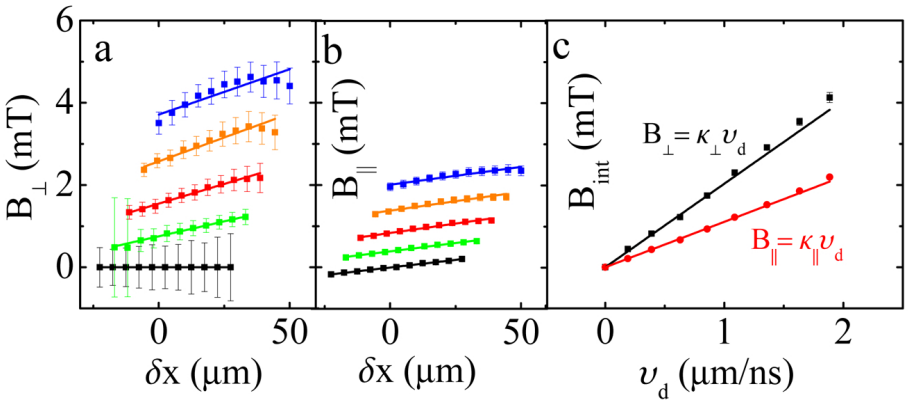


**Figure 5.9: Spin-orbit field components:** Components perpendicular to (a) and parallel to (b) the external magnetic field. The total spin-orbit field is determined from the vector sum of these components. (c) The spin-orbit field components evaluated at the spin packet center are plotted as a function of velocity. The proportionality constant $\kappa$ is used to represent the strength of the spin-orbit effective magnetic field.

$$\left|\vec{B}_{SO}(\phi)\right| = \kappa(\phi)\,\upsilon_d = \upsilon_d\sqrt{\kappa_\perp(\phi)^2 + \kappa_\parallel(\phi)^2}. \tag{5.19}$$

## 5.4 Spin-orbit field vs. carrier velocity

The L-shaped and cross patterned samples are designed to provide an approximately uniform electric field, and therefore electron velocity, from which the spin-orbit effective magnetic field components are calculated. Samples presented here are all taken from the same wafer of InGaAs. For the L-shaped channel samples, we extract the spin-orbit field components, and show that several samples from the same wafer do not exhibit the same strength of spin-orbit interaction. In fact, it is found that samples can even have the opposite sign of the SIA spin-orbit field.

| Sample | $[1\bar{1}0]$ | [110] | [100] | [001] |
|---|---|---|---|---|
| A | 0.11(1) | 1.80(9) | 1.33(4) | - |
| B | 1.36(4) | 3.40(4) | 3.27(6) | - |
| C | 3.92(15) | 0.496(96) | - | - |
| D | 1.72(5) | 4.97(18) | - | - |
| E | 0.901(63) | 4.89(36) | - | - |
| F | - | - | 3.04 | 3.94 |
| G | - | - | 3.91(28) | 3.35(2) |

**Table 5.1: Spin-orbit field proportionality constant $\kappa$:** Proportionality constant $\kappa$ with respect to electron drift velocity in units of $\mathrm{mT{\cdot}ns{\cdot}}\mu\mathrm{m}^{-1}$ for seven samples taken from the same wafer.

### 5.4.1 Spin-orbit splitting components

Table 5.1 shows the spin-orbit field coefficient components extracted from several samples taken from the same wafer. We clearly see that, not only do the spin-orbit field components not add up according to Eq. 5.3, but that the individual SIA and BIA components vary for different samples across the wafer. Fig. 5.10 shows a diagram of the wafer indicating the sample locations before cleaving. There does not appear to be any trend relating the spin-orbit splitting to the location of the sample on the wafer. We consider the spin-orbit inhomogeneity to be due to strain relaxation as the epilayer is grown beyond the critical thickness.

### 5.4.2 Mapping spin-orbit splitting

The spin-orbit field anisotropy is mapped as a function of electron momentum direction $\phi$ in two cross patterned samples (samples A and B). Each data point represents a set of spin-orbit field measurements as a function of electron velocity as presented in the previous section. As the spin-orbit field is found to be proportional to the electron velocity, we use

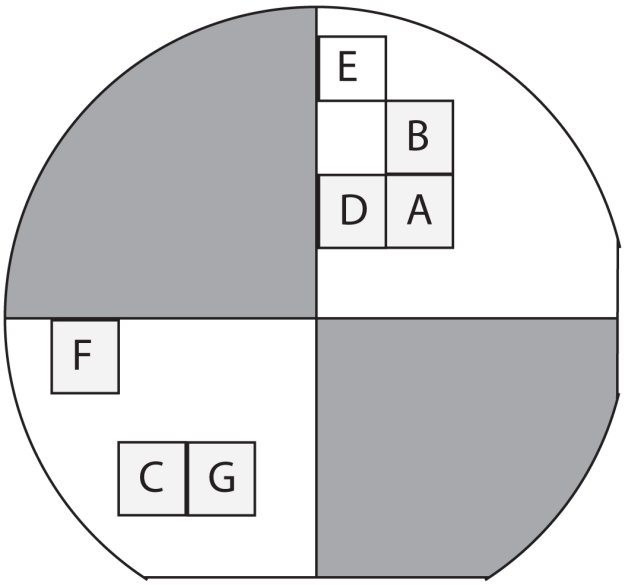


**Figure 5.10: Wafer diagram:** Locations of the seven samples presented in Table 5.1.

the proportionality constant $\kappa$ to characterize its strength. Fig. 5.11 shows the spin orbit field magnitude ($\kappa$) and orientation ($\xi$) with respect to the electron momentum direction as a function of $\phi$. The magnitude and orientation are fit to Eqs. 5.8 and 5.9 respectively.

In both samples, the spin-orbit field is oriented perpendicular to electron momentum for $\vec{k} \parallel [110], [1\bar{1}0]$ ($\phi = 45°, -45°$ respectively), which is expected from the form of the spin-orbit effective magnetic field equation (see [110] and $[1\bar{1}0]$ crystal directions in Fig. 5.2(b)). However the orientations are opposite for $\phi = -45°$. This is because for sample A, the BIA spin-orbit field dominates, and the spin-orbit field points along [110]. For sample B, on the other hand, the SIA spin-orbit field dominates and the spin-orbit field points in the opposite direction ($[\bar{1}\bar{1}0]$). This behavior is displayed in the spin-orbit field maps in Fig. 2.8(a) and (b). The relative strength of the SIA and BIA spin-orbit field components can be determined from fits to the data in Fig. 5.11.

From the form of Eq. 5.7, the spin-orbit field is expected to be maximized or minimized for $\vec{k} \parallel [110], [1\bar{1}0]$. While the minimum in both samples does occur for $\vec{k} \parallel [1\bar{1}0]$, the maximum does not occur for $\vec{k} \parallel [110]$ in either sample. This behavior is not well understood, but

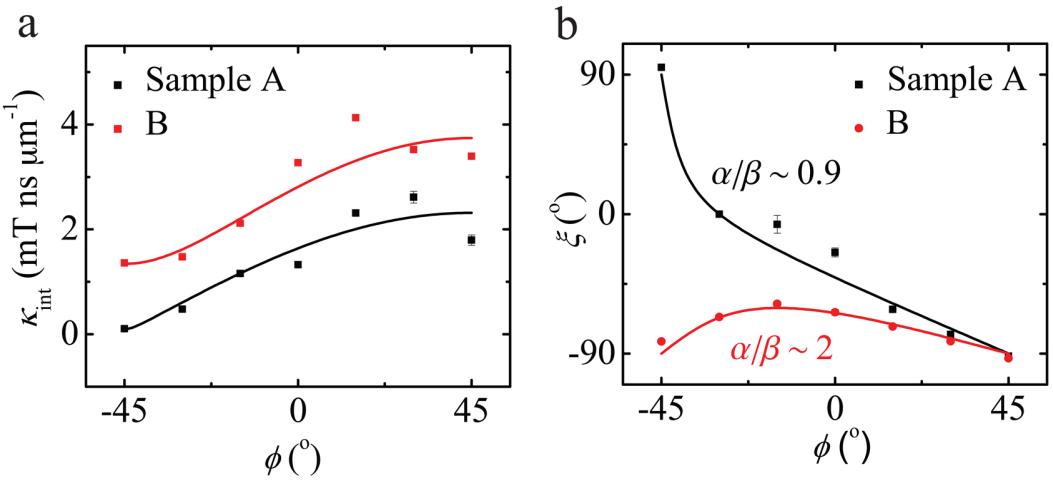


**Figure 5.11: Spin-orbit field map:** Spin-orbit effective magnetic field as a function of electron momentum direction $\phi$ for two cross patterned samples taken from the same wafer. (a) Magnitude of the spin-orbit field proportionality constant $\kappa$ with velocity. Solid lines are fits to Eq. 5.8. Deviations from the expected field strength are apparent and stress the importance of measuring the spin-orbit field directly. (b) In-plane angle $\xi$ of the spin-orbit field with respect to the electron momentum direction $\phi$. Solid lines are fits to Eq. 5.9.

is most likely due to the inclusion of an additional strain axis due to growth beyond the critical thickness, anisotropic strain relaxation, and sample mounting. It is important to stress, however, that the spin-orbit field cannot be mapped by simply taking measurements for $\vec{k} \parallel [110], [1\bar{1}0]$ and extrapolating to all $\phi$ according to Eq. 5.7, as has been done in the past [26]. The spin-orbit field must be directly measured for each electron momentum direction of interest for comparison with the current-induced spin polarization magnitude, as will be discussed in Ch. 6.

# Chapter 6

# Current-Induced Spin Polarization Measurements

## 6.1 Introduction

Current-induced spin polarization (CISP) is a general term used to describe the preferential orientation of carrier spins under the action of an electrical bias. It has the potential to be useful for spintronics applications such as spin-based information processing [124], the electrical control of magnetization [125], and as a method of electrically generating a net spin polarization [110]. As an all-electrical phenomenon, it avoids conductivity mismatch problems observed in semiconductor-to-ferromagnet interfaces [126]. Furthermore, it is compatible with the current state of the art in semiconductor wafer processing and therefore allows for a high level of on-chip localizability and fast tunability.

That carrier spins can be oriented using all electrical means was first proposed by Ivchenko and Pikus [37], in which the inverse effect, a photogalvanic current induced by absorption of circularly polarized light, was calculated for a hole current in tellurium. The rotation of

linearly polarized light upon application of a current was subsequently measured in tellurium by Vorob'ev *et. al.* [38]. It was found that the rotation angle of light was proportional to the magnitude of the current, and changed sign with a reverse in direction of the current. This was deemed the electrical analog of the Faraday effect [127], and describes a Faraday rotation that is, for small polarizations, proportional to the spin polarization of free carriers. As such, the measurements conducted by Vorob'ev *et. al.* are the first to observe a current-induced spin polarization.

It was proposed by Aranov and Lyanda-Geller [39] that such a spin polarization should be observable in semiconductors that exhibit a spin-splitting in the carrier band which is proportional to the carrier momentum, such as with strain. It was suggested that this effect could be detected through the use of either polarization-dependent photoluminescence or nuclear resonance with an oscillating electric field. The effect was ultimately measured using Faraday/Kerr rotation techniques in strained bulk InGaAs [29]. It was further spatially imaged along with the spin Hall effect in two-dimensional electron gases confined in AlGaAs quantum wells [40]. Further work in InGaAs/InAlAs two-dimensional electron gases [128] presented a unified picture of current-induced spin polarization, spin photocurrent, and the Rashba spin-orbit effective magnetic field through measurements of Shubnikov-de Hass oscillations. In this work, it was found that, along a particular crystal direction, the magnitude of the electrically generated spin polarization was proportional to the spin-orbit splitting in that both were proportional to the electrical current.

Current-induced spin polarization was soon after shown in the absence of an external magnetic field by measuring the polarized photoluminescence from the in-plane edge of InGaN/GaN superlattice samples [129], indicating that current-induced spin polarization is a purely electrical phenomenon. It has been observed in bulk GaN crystals (wurtzite phase) having a weak spin-orbit splitting [41] and in ZnSe (II-VI) having no measurable spin-orbit splitting [42]. The former measured a spin polarization at temperatures up to 200K, while

the latter was able to measure room temperature current-induced spin polarization. Time-resolved measurements indicate that electron spins orient along the spin-orbit field within picoseconds and then precess about the vector sum of the external and spin-orbit magnetic fields [29, 130].

Aronov *et. al.* [131] attributed polarization of spins by current to two dominant mechanisms: the equilibrium orientation of spins along the spin-orbit effective magnetic field, and a non-equilibrium state filling for electrons that undergo scattering accompanied by a spin flip. Engel *et. al.* [132] explained the observed out-of-plane spin polarization by using a model that requires anisotropic scattering and nonparabolic bands. In each of these studies, as well as the theories presented in the above cited papers, it was predicted that the strength of the electrically generated spin polarization should be proportional to the strength of the spin-orbit splitting, yet no clear trend has yet been observed experimentally [29]. Thus, the mechanism that gives rise to current-induced spin polarization remains an open question.

This chapter is devoted to presenting our measurements and establishing a trend between current-induced spin polarization and spin-orbit fields in n-type InGaAs. It will be organized as follows. Sec. 6.2 will present the experimental design and sample geometry. Sec. 6.3 will phenomenologically present the set of time evolution equations used to describe current-induced spin polarization, with the time-dependent and steady-state behavior presented in Secs. 6.4 and 6.5, respectively. Finally Sec. 6.6 will present our experimental findings, with an emphasis on the relationship between the measured steady-state current-induced spin polarization and the magnitude and orientation of the spin-orbit effective magnetic field.

We find that, contrary to previous theories, the strength of the current-induced spin polarization is not proportional to the strength of the spin-orbit splitting, but in fact, the two obey a negative differential relationship. That is, in crystals having an anisotropic spin-orbit splitting (Sec. 2.4.4), those crystal directions having the weakest spin-orbit splitting have the strongest current-induced spin polarization and vice versa. In fact, a strong current-induced

spin polarization is even measured along a sample orientation for which the spin-orbit field is nearly immeasurable. Furthermore, we find that the steady-state in-plane spin polarization, even in the absence of an external precession mechanism, is shifted from the direction of the spin-orbit effective magnetic field. A phenomenological model is used to explain the former effect, while we present a new model to describe the latter in terms of an anisotropic spin relaxation rate.

## 6.2 Experimental setup

Measurements of the electrically generated spin polarization are taken using optical Kerr rotation (Fig. 6.1(a)) in a similar fashion as with the spin-orbit field, though without the use of an optical pump. The conduction band electron spins are oriented electrically using AC square wave generators modulated for lock-in detection at 1167 Hz. Measurements are taken in a liquid helium flow cryostat with optical access out-of-plane. As spins are oriented initially in-plane (Sec. 6.4.2), they must be rotated out-of-plane using an external magnetic field in the Voigt geometry.

For cross-patterned samples, two phase matched square wave sources applied across opposite contacts at varying relative strengths determine the orientation ($\phi$) of the in-plane electron momentum $\vec{k}$ (Fig. 6.1(b)). By mounting the cryostat on a rotation stage, we can vary the direction of the in-plane external magnetic field relative to the [100] crystal axis. Throughout this chapter, we will use $\hat{x}$ to denoted the [100] crystal axis, and a rotated (*prime*) basis in plane with $\hat{x}'$ along the external magnetic field.

As shown in Ch. 5, the spin-orbit effective magnetic field magnitude and orientation will depend on the electron momentum direction. We assume that the current-induced spin polarization alignment vector $\vec{\gamma}$ is aligned along the spin-orbit magnetic field $\vec{B}_{SO}$. Throughout this chapter, we define $\xi$ as the angle $\vec{\gamma}$ and $\vec{B}_{SO}$ make with the external magnetic

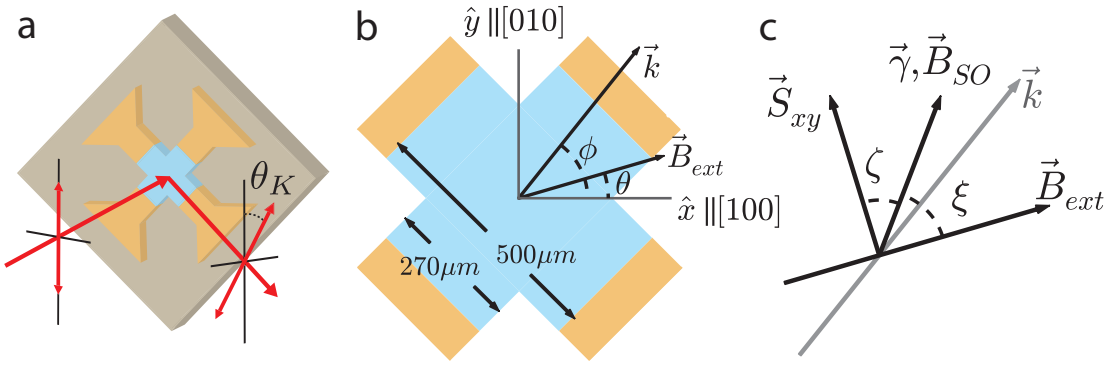


**Figure 6.1: Experimental geometry for CISP measurements:** (a) Kerr rotation in reflection is used to measure the out-of-plane component of spin polarization. (b) Sample is patterned into a four-contact geometry so that arbitrary in-plane momentum direction can be produced. (c) CISP alignment vector $\vec{\gamma}$ is along the spin-orbit effective magnetic field, at an angle $\xi$ with respect to the external magnetic field. Steady-state in-plane polarization $\vec{S}_{xy}$ is shifted from gamma by an angle $\zeta$.

field $\vec{B}_{ext}$. The steady-state in-plane spin polarization $\vec{S}_{xy}$ is shifted from the spin polarization alignment vector $\vec{\gamma}$ by an angle $\zeta$. In this chapter, our goal is to characterize $\gamma$ and $\zeta$.

## 6.3 Spin polarization evolution equation

As the mechanism that gives rise to current-induced spin polarization is not well understood and experimental measurements do not follow trends expected from theory, we will begin by describing CISP phenomenologically assuming a spin-dependent relaxation rate:

$$\Gamma_{\downarrow(\uparrow)} = \Gamma + (-)\,\gamma \tag{6.1}$$

In the limit of small polarizations, $\Gamma$ represents the average spin relaxation rate, and is defined by $\Gamma = (\Gamma_\uparrow + \Gamma_\downarrow)/2$. On the other hand, $\gamma$ represents half the difference in scattering rates between up and down spins, defined by $\gamma = (\Gamma_\downarrow - \Gamma_\uparrow)/2$. The scattering rates describe both spin-conserving and spin-flip scattering mechanisms. In the definition above, taking $\gamma$ to be positive, down spins will scatter at a higher rate than up spins, where "spin up" is

taken to mean orientation along the spin-orbit field $\vec{B}_{int}$.

### 6.3.1 Spins polarized along SO field

To understand how Eq. 6.1 gives rise to a current-induced spin polarization, we can investigate spin-conserving and spin-flip scattering mechanisms in turn. For those scattering mechanisms that conserve spin, such as the D'yakonov-Perel mechanism (Sec. 3.4.1), down spins will scatter, and therefore dephase, at a rate faster than up spins. In the steady-state limit, this gives rise to a net spin polarization with the majority spin up carriers. For scattering mechanisms that flip spin, such as the Elliot-Yafet and Bir-Aronov-Pikus mechanisms (Secs. 3.4.2 and 3.4.3), $\Gamma_{\downarrow(\uparrow)}$ represents the rate at which down (up) spins flip to up (down) spins. Thus, a spin dependent scattering rate as in Eq. 6.1 gives rise to a net spin polarization for spin flip mechanisms by preferentially driving spins towards a particular direction.

To see how a net spin polarization arises, consider the time dependent behavior of each spin species in the absence of all interactions except relaxation according to Eq. 6.1:

$$\frac{\partial n_{\uparrow}}{\partial t} = -\Gamma_{\uparrow} n_{\uparrow} = -\left(\Gamma - \gamma\right) n_{\uparrow} \tag{6.2}$$

$$\frac{\partial n_{\downarrow}}{\partial t} = -\Gamma_{\downarrow} n_{\downarrow} = -\left(\Gamma + \gamma\right) n_{\downarrow} \tag{6.3}$$

where $n_{\uparrow(\downarrow)}$ represents the density of up (down) spin carriers and the total carrier density is $n = n_{\uparrow} + n_{\downarrow}$. In the simplest context of electrically generating spin polarization, the carrier density $n$ is independent of position and time. Eqs. 6.2 and 6.3 represent exponential decay. The definition of the spin polarization is $S = (n_{\uparrow} - n_{\downarrow})/n$. Subtracting Eq. 6.3 from Eq. 6.2 and dividing by $n$ we arrive at the time dependence of the spin polarization.

$$\frac{\partial S}{\partial t} = \frac{-\Gamma\left(n_{\uparrow} - n_{\downarrow}\right) + \gamma\left(n_{\uparrow} + n_{\downarrow}\right)}{n} \tag{6.4}$$

$$\frac{\partial S}{\partial t} = -\Gamma S + \gamma \tag{6.5}$$

From Eq. 6.5, we immediately see that in addition to the decay term $\Gamma$ there is also a spin polarization driving term $\gamma$. The solution to the differential equation is

$$S\left(t\right) = \frac{\gamma}{\Gamma}\left(1 - e^{-\Gamma t}\right) \tag{6.6}$$

in which case the steady-state spin polarization as $t \to \infty$ is $S = \gamma\tau$ with the definition of the spin relaxation time $\tau = \Gamma^{-1}$. Eq. 6.6 gives a steady-state spin polarization proportional to the spin-dependent scattering term $\gamma$ defined in Eq. 6.1. As the spin-degeneracy is lifted due to the spin-orbit interaction, we will begin with the assumption that $\vec{\gamma}$ aligns along the spin-orbit effective magnetic field $\vec{B}_{int}$. The goal is to characterize current-induced spin polarization by characterizing the spin generation term $\gamma$.

### 6.3.2 Anisotropic spin relaxation

The samples measured in this study are Si-doped $In_{0.04}Ga_{0.96}As$ epilayers exhibiting an anisotropic spin-orbit field (Sec. 2.4.4 and Fig. 5.11) with a doping concentration of $n = 3 \times 10^{16}$ cm$^{-3}$. For GaAs, a doping concentration beyond approximately $2 \times 10^{16}$ cm$^{-3}$ is on the metal side of the metal to insulator transition (MIT) for which the D'yakonov-Perel (DP) spin relaxation mechanism is expected to dominate [78]. The spin relaxation tensor according to the DP mechanism (see Sec. 3.4.1 for more detail) is given by [11]

$$\overleftrightarrow{\Gamma} = \frac{1}{\tau_0\left(\upsilon_d\right)} \begin{pmatrix} (1+r)^2 & 0 & 0 \\ 0 & (1-r)^2 & 0 \\ 0 & 0 & 2\left(1+r^2\right) \end{pmatrix} \tag{6.7}$$

where $\tau_0$ is the electron drift velocity-dependent spin relaxation time in the absence of in-plane anisotropy (i.e. $r = 0$) and $2r$ represents the unitless difference between the SO field magnitudes for spins oriented along [110] and $[1\bar{1}0]$. If the D'yakonov-Perel relaxation mechanism is the only one present, or strongly dominates all other spin relaxation mechanisms, then $r$ is defined as the ratio of the structural inversion asymmetry (SIA)- to bulk inversion asymmetry (BIA)-like SO splitting terms ($r = \alpha/\beta$). In Eq. 6.7, the eigenbasis states are defined by:

$$[1\bar{1}0] = \begin{pmatrix} 1 \\ 0 \\ 0 \end{pmatrix} \quad , \qquad [110] = \begin{pmatrix} 0 \\ 1 \\ 0 \end{pmatrix} \quad , \qquad [001] = \begin{pmatrix} 0 \\ 0 \\ 1 \end{pmatrix}$$

Note square brackets are used to represent the crystal axes and parentheses are used for matrices and column vectors.

With an anisotropic dephasing rate, the spin polarization components can become coupled, and we must, therefore, describe the spin polarization as a vector quantity. Eq. 6.5 becomes

$$\frac{\partial \vec{S}}{\partial t} = -\overleftrightarrow{\Gamma} \cdot \vec{S} + \vec{\gamma} \tag{6.8}$$

where the vector $\vec{\gamma}$ represents the spin alignment per unit time and is oriented along the spin-orbit field. When $\vec{\gamma}$ is along an eigenbasis state of the spin relaxation tensor, the spin polarization direction remains along the eigenvector, and the time-dependent solution is analogous to Eq. 6.6. This is component-wise given by

$$S_i(t) = \frac{\gamma_i}{\Gamma_{ii}}\left(1 - e^{-\Gamma_{ii}t}\right) \tag{6.9}$$

with corresponding steady-state solutions $S_i(t \to \infty) = \gamma_i \tau_i$ and $\tau_i = \Gamma_{ii}^{-1}$.

## 6.4 Time-dependent behavior

Due to the direction of the spin-orbit effective magnetic field in the plane of the sample, it is expected and observed that $\vec{\gamma}$ has no out-of-plane component. A quick analysis of the spin polarization components given by Eq. 6.9 shows that for $\gamma_z = 0$, $S_z(t) = 0$. As Faraday and Kerr rotation only measures the component of the spin polarization along the laser ($\hat{z}$) axis, it is necessary to couple the spin polarization components. This is done in a controlled way by the application of an in-plane external magnetic field. The time-dependence of the spin-polarization in this case is given by:

$$\frac{\partial \vec{S}}{\partial t} = -\overleftrightarrow{\Gamma} \cdot \vec{S} + \vec{\Omega} \times \vec{S} + \vec{\gamma} \tag{6.10}$$

In certain simplified cases, Eq. 6.10 has a well-defined analytical solution. In general, however, numerical techniques must be used. Throughout this section, when a numerical solution is required, it will be achieved by using the Runge-Kutta method for solving ordinary differential equations. This procedure is discussed in Appendix A. This section will be devoted to simulating the time dependence of electrical generation of spin polarization for comparison with measured steady-state behavior.

### 6.4.1 Time-dependent spin polarization without precession

In the absence of spin precession, the time dependence of the spin polarization is described component-wise by Eq. 6.9, where the basis states $i$ are defined to be the eigenbasis states

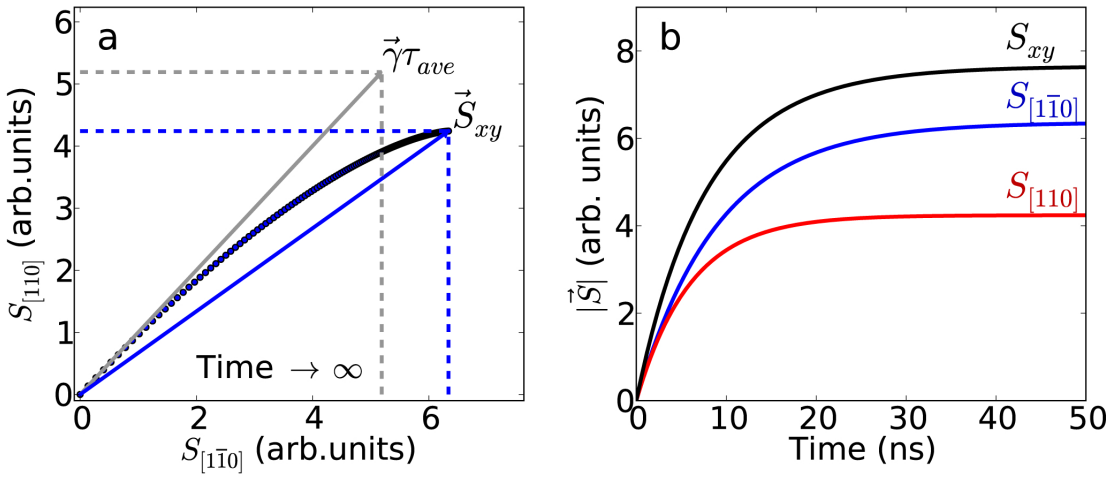


**Figure 6.2: Time-dependent spin polarization without precession:** (a) As time increases, the spin polarization increasingly deviates from the direction of the spin generation vector $\vec{\gamma}$. (b) The components of the spin polarization along the eigenbasis states of the spin relaxation tensor relax to their steady-state values at their respective rates, as described in Eq. 6.9.

of the spin relaxation tensor, i.e. $[1\bar{1}0]$, [110], and [001]. The in-plane spin polarization is plotted in Fig. 6.2(a). Blue filled circles represent the spin polarization at equally spaced time steps of approximately 0.2 ns, $\vec{S}_{xy}$ represents the in-plane spin polarization as $t \to \infty$, and $\vec{\gamma}\tau_{ave}$ represents the in-plane spin polarization in the case that spin dephasing is isotropic and described by $\tau_{ave}^{-1} = (\tau_{[1\bar{1}0]}^{-1} + \tau_{[110]}^{-1})/2$. In the figure, $\tau_{[1\bar{1}0]} = 9$ ns and $\tau_{[110]} = 6$ ns. In the case that $\vec{\gamma}$ is constant, the in-plane spin polarization relaxes to the steady-state value $\vec{S}_{xy}$ on a time scale given by the relaxation time components. Fig. 6.2(b) shows the time dependence of the spin polarization components. In these plots, we set $\gamma_{[1\bar{1}0]} = \gamma_{[110]}$. In other words, the polarization is generated equally along the $[1\bar{1}0]$ and [110] crystal axes. Yet as time increases, the in-plane spin polarization increasingly deviates from alignment along $\vec{\gamma}$. This is understood as spins that align along [110] dephase more rapidly than spins aligned along $[1\bar{1}0]$. This deviation will be quantified in Sec. 6.5.1.

### 6.4.2 Time-dependent spin polarization with precession

With precession, spin polarization generated in-plane along $\vec{\gamma}$ is rotated out-of-plane at the Larmor precession frequency ($\vec{\Omega}$) and decays component-wise according to the spin relaxation tensor. The precession frequency is a vector sum of the external magnetic field ($\vec{B}_{ext}$) and the spin-orbit effective magnetic field ($\vec{B}_{SO}$) as in Ch. 5, given by $|\vec{\Omega}| = |\vec{\Omega}_{ext} + \vec{\Omega}_{SO}| = \sqrt{\Omega_{[1\bar{1}0]}^2 + \Omega_{[110]}^2}$. Taking $\vec{\gamma}$ to have only in-plane components, the matrix form of Eq. 6.10 is

$$\frac{\partial}{\partial t}\begin{pmatrix} S_{[1\bar{1}0]} \\ S_{[110]} \\ S_{[001]} \end{pmatrix} = \begin{pmatrix} -1/\tau_{[1\bar{1}0]} & 0 & \Omega_{[110]} \\ 0 & -1/\tau_{[110]} & -\Omega_{[1\bar{1}0]} \\ -\Omega_{[110]} & \Omega_{[1\bar{1}0]} & -1/\tau_{[001]} \end{pmatrix}\begin{pmatrix} S_{[1\bar{1}0]} \\ S_{[110]} \\ S_{[001]} \end{pmatrix} + \begin{pmatrix} \gamma_{[1\bar{1}0]} \\ \gamma_{[110]} \\ 0 \end{pmatrix}. \tag{6.11}$$

Eq. 6.11 is a set of coupled first order differential equations in time with source terms and, in general, must be solved numerically. This is achieved by using the fourth order Runge Kutta method for solving ordinary differential equations as outlined in Appendix A. In this section, time-dependent solutions are simulated for various choices of parameters, and the steady-state behavior is extrapolated.

In the simplest case, we assume that $\vec{\gamma}$ is constant for $t > 0$ and zero for $t < 0$. Time zero can then be thought of as an instantaneous switching on of the current-induced spin polarization. This approximately simulates the experiment with the assumption that an AC square wave can instantaneously turn on the current to a constant high value. The time dependence of the spin polarization components for several choices of external magnetic field strength is show in Fig. 6.3. The steady-state spin polarization is reached within 50 ns. Notice that at low external magnetic fields the in-plane spin polarization component dominates. As the field is increased, the out-of-plane component then dominates, and both diminish with increasing field. We will show in Sec. 6.6 that the former corresponds to an

even Lorentzian lineshape while the latter corresponds to an odd Lorentzian dependence on the magnetic field.

In this simulation, we take $\vec{\gamma} \propto \hat{e}_{[1\bar{1}0]} + \hat{e}_{[110]}$, $\vec{\Omega}_{ext} \propto \hat{e}_{[1\bar{1}0]} - \hat{e}_{[110]}$, and $\vec{\Omega}_{SO} \parallel \vec{\gamma}$. This configuration is consistent with the commonly used measurement geometry. By orienting the external magnetic field perpendicular to the spin-orbit field direction, the maximum out-of-plane spin precession can be achieved. For all magnetic fields, the in-plane ($\vec{S}_{xy}$) and out-of-plane ($\vec{S}_z$) components of the spin polarization oscillate according to the total magnetic field strength, while relaxing to the steady state value. This relaxation occurs on a time scale much shorter than the modulation period of the AC square wave used to generate current-induced spin polarization ($f = 1167$ Hz), and we can therefore treat the square wave as though it is modulating between two steady-state conditions. In all simulations, the spin-orbit field is $\Omega_{SO} = \pi/32$ ns$^{-1}$, corresponding to an internal field of $B_{SO} \sim 5$ mT. This is in accordance with the measurements in Ch. 5.

The pulsed probe has the effect of inducing carriers at a repetition rate equal to that of the laser. As the probe pulse is linearly polarized, the optically-induced carriers will have no net polarization according to the optical selection rules for GaAs (Sec. 4.1.3). The photo-induced carriers, however, will have higher energy depending on the light energy used to excite electrons from the valence band, which will contribute to the current-induced spin polarization. Taking the laser pulse to be roughly square and lasting a duration of $t_p = 10$ ps, and assuming an intraband relaxation time of $\tau_p = 1$ ps, the time dependence of the polarization alignment $\gamma$ can be described by:

$$\frac{\partial \gamma}{\partial t} = \begin{cases} \frac{1}{\tau_p}(\gamma_p + \gamma_c) - \frac{1}{\tau_p}\gamma & for \;\; 0 < t \leq t_p \\ \frac{1}{\tau_p}\gamma_c - \frac{1}{\tau_p}\gamma & for \;\; t \geq t_p \end{cases} \tag{6.12}$$

where $\gamma_c$ is the spin alignment term from current-induced spin polarization alone, $\gamma_p$ is the additional spin alignment due to the optically-induced carriers, and $\gamma$ is used to describe

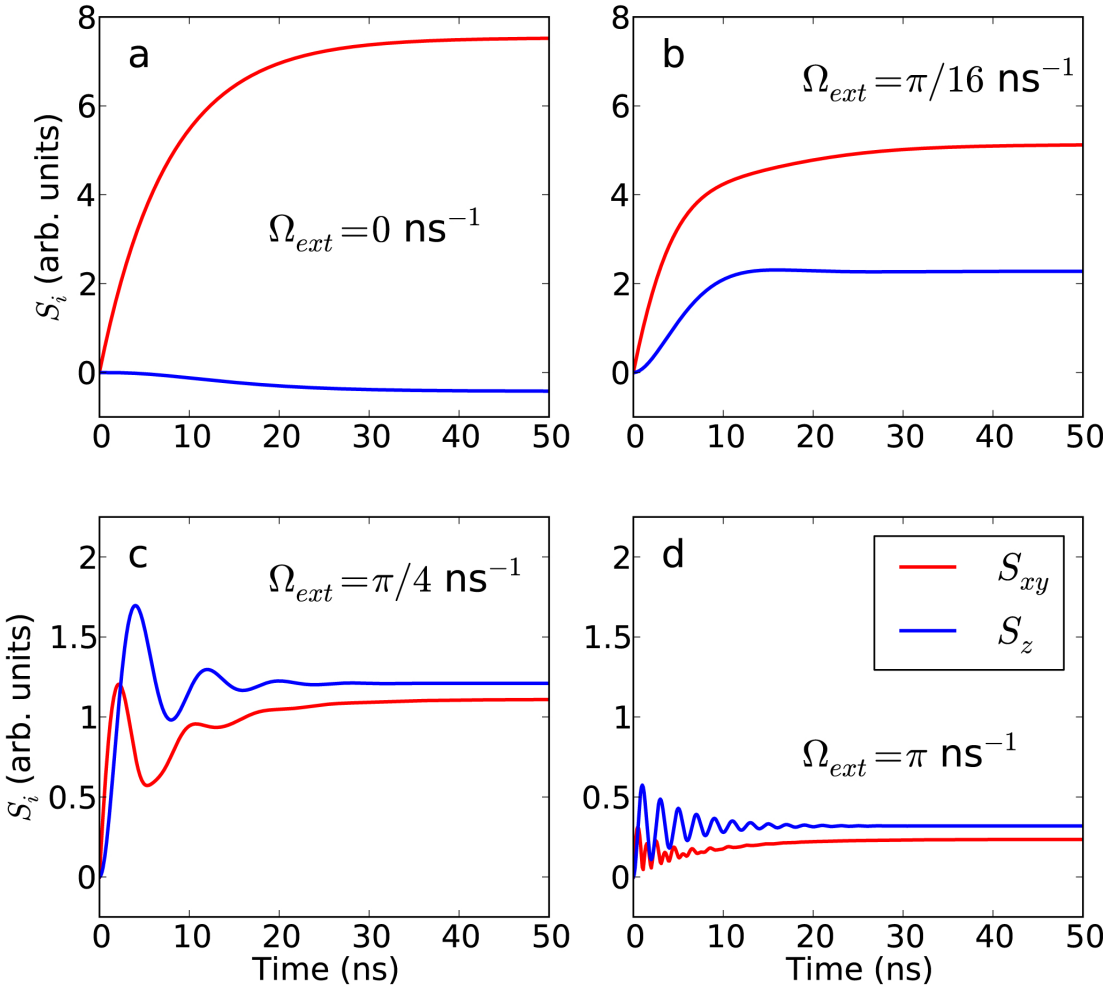


**Figure 6.3: Time-dependent spin polarization - sharp square wave:** In-plane (red line) and out-of-plane (blue line) components of spin polarization for an external magnetic field precession frequency of 0 (a), $\pi/16$ (b), $\pi/4$ (c) and $\pi$ (d) ns$^{-1}$. Spin polarization is initially zero and then relaxes to the steady-state value according to the relaxation rate tensor. Steady-state spin polarization is reached within 50 ns. In all simulations, $\vec{\gamma} \propto \hat{e}_{[1\bar{1}0]} + \hat{e}_{[110]}$, $\vec{\Omega}_{ext} \propto \hat{e}_{[1\bar{1}0]} - \hat{e}_{[110]}$, and $\vec{\Omega}_{SO} = (\pi/32)(\hat{e}_{[1\bar{1}0]} + \hat{e}_{[110]})/\sqrt{2}$.

the combined spin alignment per unit time. We assume $\gamma_p$ and $\gamma_c$ are constant in time and proportional to the external electrical bias. The proportionality between $\gamma_p$ and $\gamma_c$ is expected to depend on the laser pulse energy. In this case, the solution to Eq. 6.12 is found analytically. Requiring that $\lim_{\epsilon\to 0}[\gamma(t_p-\epsilon)-\gamma(t_p+\epsilon)]=0$ and $\gamma(t=0)=\gamma_c$, the solution is

$$\gamma(t)=\begin{cases}\gamma_c & for\ \ t\le 0\\ \gamma_p\left(1-e^{[-t/\tau_p]}\right)+\gamma_c & for\ \ 0\le t\le t_p\\ \gamma_p\left(e^{[-(t-t_p)/\tau_p]}-e^{[-t/\tau_p]}\right)+\gamma_c & for\ \ t\ge t_p\end{cases}. \tag{6.13}$$

The time dependence of $\gamma$ and the $\hat{z}$ component of the spin polarization are shown in Fig. 6.4(a) and (b) respectively. The pulse sequence in (a) depicts a spin alignment term prior to time zero that is due to current-induced spin polarization alone. At time zero, the laser pulse increases the spin alignment by a factor given by the excitation energy. Throughout the 10 ps pulse, the spin alignment has a constant source term described by the sum of the steady-state and laser-enhanced current-induced spin polarization as well as a decay term governed by the 1 ps intraband relaxation time. After the laser pulse is turned off, $\gamma$ undergoes free decay to the steady-state value.

The resulting $\hat{z}$ component of the spin polarization is shown in Fig. 6.4(b). This is calculated numerically using the Runge-Kutta method. In this simulation, $\vec{\gamma} \parallel \vec{B}_{SO}$, as before, and $\vec{B}_{ext} \perp \vec{B}_{SO}$. The current is "switched on" at a large negative time such that the semi-steady-state spin polarization is reached. Oscillations around the steady state occur according to the combined oscillation frequency $\vec{\Omega}=\vec{\Omega}_{ext}+\vec{\Omega}_{SO}$ and are triggered by the pulse sequence depicted in Fig. 6.4(a). The pulses are repeated at the laser repetition rate of 13.16 ns. The oscillations around the steady state value prior to time zero are a result of the previous pulse. Notice that both the offset and oscillation amplitude increase linearly with the applied voltage (i.e. $\gamma$), and the oscillation frequency changes slightly due to the

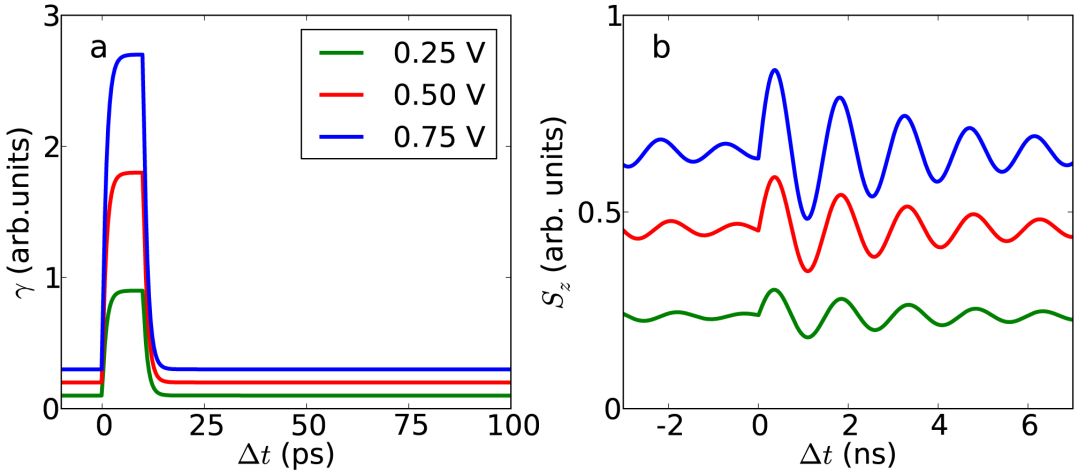


**Figure 6.4: Time-dependent spin polarization - single pulse with background:** (a) Pulsed current-induced spin polarization term ($\gamma$) due to the probe laser. Pulse duration is 10 ps and intraband relaxation time is 1 ps. Background is due to current-induced spin polarization in the absence of the laser pulse. (b) Resulting $\hat{z}$ component of the spin polarization as a function of time. Background and oscillating amplitude are proportional to electric current. The oscillation frequency shifts slightly with external voltage due to the spin-orbit effective magnetic field. The same color labeling is used in (a) and (b).

electric field dependent spin-orbit effective magnetic field. In this simulation, $\Omega_{ext} = 4\pi/3$ ns$^{-1}$ and $\Omega_{SO} = \pi/8 \times V$ ns$^{-1}$ where $V$ is the electrical bias providing current. The same spin relaxation times are used as in Fig. 6.2.

The time-dependent current-induced spin polarization described in Fig. 6.4 can be measured using a linearly polarized pump and probe setup. These measurements are shown for various voltages in Fig. 6.5. Using the same setup as in the time-resolved Kerr rotation measurements in Sec. 4.3.2, the photoelastic modulator is removed from the pump path, resulting in the pump pulse maintaining its linear polarization. A mechanical delay line is used to temporally separate the pump and probe pulses. The laser wavelength is tuned to the high energy Faraday rotation peak to increase the strength of the laser-enhanced current-induced spin polarization. Without the use of the photoelastic modulator, we can use only single-stage lock-in detection. This is done by applying an AC square wave bias to supply

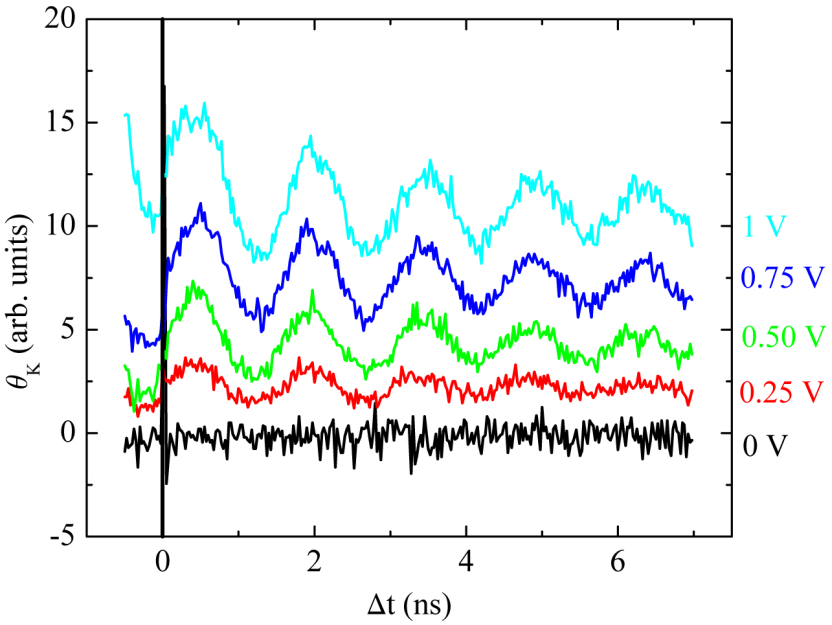


**Figure 6.5: Time-dependent spin polarization measurements:** Time-resolved current-induced spin polarization measurements for various voltages using a linearly polarized pump and probe scheme. Waveform is sinusoidal (odd) indicating initial polarization in-plane. Amplitude of oscillations is proportional to electrical bias. A linear background is added to each scan for clarity.

the electron current. As with the simulations, increasing the current increases the amplitude of oscillations. The wave obeys a sinusoidal dependence confirming that current-induced spin polarization is generated in the plane of the sample. A background is added to each scan for clarity.

## 6.5 Steady-state behavior

The bulk of the current-induced spin polarization measurements presented in this chapter are taken by measuring the out-of-plane, steady-state spin polarization. This section will therefore be devoted to describing the steady-state solutions to the spin polarization equations. In Sec. 6.5.1, there will be no spin precession mechanism, and the solution will remain in the plane of the epilayer. We will characterize the deviation of the steady-state spin polar-

ization direction from that of the spin-orbit effective magnetic field as a function of electron momentum. In Sec. 6.5.2, the precession term will be added and an approximation to the steady-state, out-of-plane spin polarization will be used to fit the experimental data.

### 6.5.1 In-plane without precession

The components of the spin polarization along the spin relaxation rate eigenvectors is described by Eq. 6.8. To see how the vector spin polarization $\vec{S}(t)$ behaves when the spin alignment term is not along an eigenvector of the relaxation tensor, we can choose $\vec{\gamma}$ having two or more non-zero eigenvector components. As we saw in Sec. 6.4.1, the ratio of the in-plane spin polarization components is

$$\frac{S_{[110]}(t)}{S_{[1\bar{1}0]}(t)} = \frac{\gamma_{[110]}\tau_{[110]}}{\gamma_{[1\bar{1}0]}\tau_{[1\bar{1}0]}}\left(\frac{1-e^{-t/\tau_{[110]}}}{1-e^{-t/\tau_{[1\bar{1}0]}}}\right) \tag{6.14}$$

The steady-state solution (denoted by dropping the time dependence) is

$$\frac{S_{[110]}}{S_{[1\bar{1}0]}} = \frac{\gamma_{[110]}\tau_{[110]}}{\gamma_{[1\bar{1}0]}\tau_{[1\bar{1}0]}} \tag{6.15}$$

It is immediately apparent that the ratio of spin components along $\hat{e}_{[110]}$ and $\hat{e}_{[1\bar{1}0]}$ is not equal to the ratio of the spin alignment components ($\gamma_{[110]}/\gamma_{[1\bar{1}0]}$) when the components for the spin relaxation tensor are not the same. It is more useful to quantify this deviation by rotating the relaxation time tensor by an angle of $\theta + 45°$ ($\theta$ is then the angle relative to the [100] crystal axis) in the growth plane of the sample.

$$\overleftrightarrow{\Gamma}' = \frac{1}{\tau_0(\upsilon_d)}\begin{pmatrix} 1+r^2-2r\sin 2\theta & 2r\cos 2\theta & 0 \\ 2r\cos 2\theta & 1+r^2+2r\sin 2\theta & 0 \\ 0 & 0 & 2(1+r^2) \end{pmatrix} \tag{6.16}$$

With this definition, an angle of $\theta = -45^\circ$ recovers the diagonal form given in Eq. 6.7. The *prime* notation is used throughout to denote the rotated basis. The angle $\theta$ that defines the basis vectors can be arbitrarily chosen, though it will make the equations simpler by choosing $\theta$ such that $\vec{\gamma} \parallel \hat{y}'$. Taking $\vec{\gamma} \parallel \vec{B}_{int}$, and assuming that $\vec{B}_{int}$ is well characterized by Eq. 5.7, this angle is expressed in terms of the in-plane electron momentum direction $\phi$ by

$$\theta = \tan^{-1}\left(\frac{r\cos\phi + \sin\phi}{r\sin\phi + \cos\phi}\right) \tag{6.17}$$

where in this equation $r$ is explicitly taken to be the ratio of the SIA- and BIA-like spin-orbit field components ($r = \alpha/\beta$). Using this definition, we have $\gamma_{y'} = \gamma$ and $\gamma_{x'} = 0$. Dropping the $\hat{z}$ dependence, the steady state spin polarization is achieved by solving Eq. 6.8 in the *prime* basis in the limit that $\partial\vec{S}/\partial t \to 0$,

$$\begin{pmatrix} 1 + r^2 - 2r\sin 2\theta & 2r\cos 2\theta \\ 2r\cos 2\theta & 1 + r^2 + 2r\sin 2\theta \end{pmatrix} \begin{pmatrix} S_{x'} \\ S_{y'} \end{pmatrix} = \begin{pmatrix} 0 \\ \gamma\tau_0 \end{pmatrix} \tag{6.18}$$

which gives the steady-state, in-plane spin polarization components

$$S_{x'} = \frac{-\gamma\tau_0\,(2r\cos 2\theta)}{(1-r^2)^2} \tag{6.19}$$

$$S_{y'} = \frac{\gamma\tau_0\,(1 + r^2 - 2r\sin 2\theta)}{(1-r^2)^2} \tag{6.20}$$

The first thing to notice is that, while there is no spin alignment term along the $\hat{x}'$ direction ($\gamma_{x'} = 0$), there is a nonzero component of the steady-state spin polarization along this direction. The only exception is when $\theta = \pm 45^\circ$, which is expected as for these orientations $\vec{\gamma}$ is along an eigenbasis of the spin relaxation tensor and Eq. 6.9 applies. The angle that the

steady-state spin polarization makes with the CISP alignment vector $\vec{\gamma}$ is given by

$$\zeta = \tan^{-1}\left[\frac{-2r\cos(2\theta)}{1+r^2-2r\sin(2\theta)}\right] \tag{6.21}$$

Using the definition given for $\theta$ in Eq. 6.17 this can be expressed in terms of the electron momentum direction $\phi$.

$$\zeta = \tan^{-1}\left[\frac{2r\left(\sin^2\phi-\cos^2\phi\right)}{1-r^2}\right] \tag{6.22}$$

The magnitude of the steady-state, in-plane spin polarization $|\vec{S}_{xy}|$ can be described in the familiar fashion by introducing an effective relaxation time.

$$S_{xy} = \gamma\tau_{xy} \tag{6.23}$$

$$\tau_{xy} = \frac{\tau_0\sqrt{1+6r^2+r^4-4r\left(1+r^2\right)\sin 2\theta}}{\left(1-r^2\right)^2} \tag{6.24}$$

Fig. 6.6 shows the deviation $\zeta$ of the steady-state, in-plane spin polarization from the CISP alignment vector $\vec{\gamma}$ as a function of electron momentum direction $\phi$ for a few choices of $r$. Notice that when $r$ is greater (less) than one, $\zeta$ will be negative (positive) for $\phi$ in the range $-45^\circ < \phi < 45^\circ$. Positive is defined in the same way as the azimuthal angle. To understand this behavior, consider when $r > 1$, the SIA-like spin-orbit field dominates giving a maximum SO field for $\vec{k} \parallel [110]$ (for which $\vec{B}_{SO} \parallel [1\bar{1}0]$) and minimum for $\vec{k} \parallel [1\bar{1}0]$ (for which $\vec{B}_{SO} \parallel [110]$). According to the D'yakonov-Perel mechanism, the relaxation time will be longest for the component of spin polarization oriented along $[1\bar{1}0]$ and shortest for the component along [110]. As such, the [110] spin polarization component will dephase more quickly and the net spin polarization will rotate towards $[1\bar{1}0]$ ($\zeta < 0$). For $\phi = \pm 45^\circ$ (corresponding to $\vec{k} \parallel [110], [1\bar{1}0]$) the deviation is zero as $\vec{\gamma}$ is along an eigenvector of the

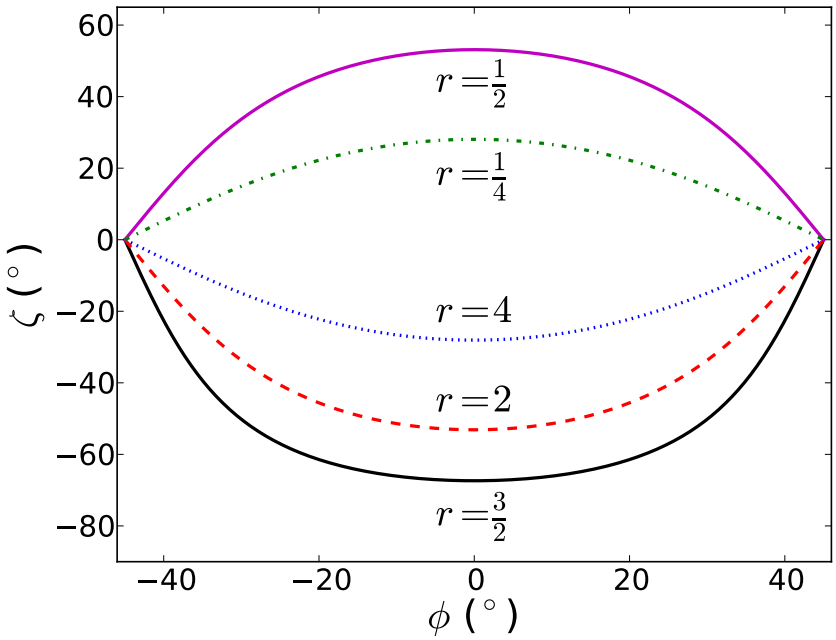


**Figure 6.6: Steady-state in-plane spin alignment:** Deviation ($\zeta$) of the steady-state, in-plane spin polarization ($\vec{S}_{xy}$) from the CISP alignment vector ($\vec{\gamma}$) as a function of the electron momentum direction ($\phi$) for various choices of spin-orbit field component ratios ($r$). Notice that for $r > 1$, deviation is in one direction and for $r < 1$ deviation is in the other. For all $r$ the magnitude of $\zeta$ is maximized at $\phi = 0$ (i.e. $\vec{k} \parallel [100]$) and goes to zero for $\phi = \pm 45°$ (i.e. $\vec{k} \parallel [110], [1\bar{1}0]$). For positive and negative $\zeta$, the deviation becomes larger as $r \to 1$.

spin relaxation tensor.

The magnitude of $\zeta$ reaches its maximum for all choices of $r$ when $\phi = 0$ (corresponding to $\vec{k} \parallel [100]$). In the limit as $r \to 1$ there will be a momentum direction for which the SIA- and BIA-like spin-orbit fields will exactly cancel. According to the D'yakonov-Perel mechanism alone, along such a direction the relaxation time will diverge and the system will become a spin-helix state [44]. In this case, for $\vec{\gamma}$ along any direction other than [110] and $[1\bar{1}0]$, $\zeta$ will be $\pm 90°$. Of course an infinite relaxation time cannot happen in practice as other relaxation mechanisms will then necessarily dominate.

In the case that other spin relaxation mechanisms play an important role, such as the Elliot-Yafet mechanism, it is necessary to determine the anisotropy factor $r$ directly from

the measured anisotropy in the spin relaxation rates. In this case we define the following set of relations:

$$r = \frac{\sqrt{\tau_{[110]}} - \sqrt{\tau_{[1\bar{1}0]}}}{\sqrt{\tau_{[110]}} + \sqrt{\tau_{[1\bar{1}0]}}} \tag{6.25}$$

$$\frac{1}{\sqrt{\tau_0}} = \frac{1}{2}\left(\frac{1}{\sqrt{\tau_{[110]}}} + \frac{1}{\sqrt{\tau_{[1\bar{1}0]}}}\right). \tag{6.26}$$

Out-of-plane measurements for $\vec{S} \parallel [1\bar{1}0]$ and [110] are taken by precessing spins around the axis perpendicular to both the steady-state in-plane spin polarization and the [001] crystal axis. The average relaxation rate (denoted by an overbar) is expressed in terms of the eigenvalues by

$$\overline{\Gamma}_{[1\bar{1}0]} = \frac{1}{2}\left(\Gamma_{[1\bar{1}0]} + \Gamma_{[001]}\right) \tag{6.27}$$

$$\overline{\Gamma}_{[110]} = \frac{1}{2}\left(\Gamma_{[110]} + \Gamma_{[001]}\right). \tag{6.28}$$

Using the relation that $\Gamma_{[001]} = \Gamma_{[1\bar{1}0]} + \Gamma_{[110]}$, the relaxation rate components $\Gamma_{[1\bar{1}0]}$ and $\Gamma_{[110]}$ are given by

$$\Gamma_{[1\bar{1}0]} = \frac{2}{3}\left(2\overline{\Gamma}_{[1\bar{1}0]} - \overline{\Gamma}_{[110]}\right) \tag{6.29}$$

$$\Gamma_{[110]} = \frac{2}{3}\left(2\overline{\Gamma}_{[110]} - \overline{\Gamma}_{[1\bar{1}0]}\right). \tag{6.30}$$

The values of $\overline{\Gamma}_{[1\bar{1}0]}$ and $\overline{\Gamma}_{[110]}$ are estimated from measurements of the current-induced spin polarization for spins polarized along these directions. These measurements will be presented in Sec. 6.6.

### 6.5.2 Out-of-plane with precession

The net spin polarization is measured along the optical axis using Faraday/Kerr rotation measurements. As such, to measure a spin polarization due to CISP, it is first necessary to rotate electron spins out of the plane of the sample into the optical axis, as discussed in Sec. 6.4. We seek solutions to Eq. 6.10 in the limit that $\partial\vec{S}/\partial t \to 0$. In the case of a constant spin alignment term $\vec{\gamma}$ (i.e. not taking the laser pulse into account) the steady-state spin polarization solution is

$$S_{[1\bar{1}0]} = \gamma_{[1\bar{1}0]}\tau_{[1\bar{1}0]}\left(1 + \frac{\Omega_{[110]}}{\gamma_{[1\bar{1}0]}}S_z\right) \tag{6.31}$$

$$S_{[110]} = \gamma_{[110]}\tau_{[110]}\left(1 - \frac{\Omega_{[1\bar{1}0]}}{\gamma_{[110]}}S_z\right) \tag{6.32}$$

$$S_z = \frac{\tau_z\left(\gamma_{[110]}\tau_{[110]}\Omega_{[1\bar{1}0]} - \gamma_{[1\bar{1}0]}\tau_{[1\bar{1}0]}\Omega_{[110]}\right)}{1 + \left(\Omega^2_{[1\bar{1}0]}\tau_{[110]} + \Omega^2_{[110]}\tau_{[1\bar{1}0]}\right)\tau_z} \tag{6.33}$$

Without knowing the functional form of $\vec{\gamma}$ and $\overleftrightarrow{\tau}$ (Sec. 6.6) this is as far as we can go with an exact solution. It is the goal to determine experimentally how $\vec{\gamma}$ and $\overleftrightarrow{\tau}$ behave as a function of the electron momentum direction $\phi$.

To this end, we approximate that spins polarize rapidly along the steady-state in-plane direction $\vec{S}_{xy}$ determined in Sec. 6.5.1, and then precess around the vector sum of the external and spin-orbit magnetic fields. We will choose a rotated basis such that the external magnetic field is along the $\hat{x}'$ direction, with $\hat{z}' = \hat{z}$. In this case the spin polarization can be described component-wise by

$$S_{x'} = \gamma_{x'}\tau_{xy}\left(1 + \frac{\Omega_{y'}}{\gamma_{x'}}S_z\right) \tag{6.34}$$

$$S_{y'} = \gamma_{y'}\tau_{xy}\left(1 - \frac{\Omega_{x'}}{\gamma_{y'}}S_z\right) \tag{6.35}$$

$$S_z = \frac{\tau_{eff}^2\left(\gamma_{y'}\Omega_{x'} - \gamma_{x'}\Omega_{y'}\right)}{1 + \left(\Omega_{tot}\tau_{eff}\right)^2} \tag{6.36}$$

with $\tau_{xy}$ given in Eq. 6.24, $\tau_{eff}$ the effective relaxation time given by $\tau_{eff} = \sqrt{\tau_{xy}\tau_z}$, and $\Omega_{tot}^2 = \Omega_{SO}^2 + \Omega_{ext}^2 + 2\Omega_{SO}\Omega_{ext}\cos(\xi)$. Using the following set of relations (Fig. 6.1(c))

$$\vec{\gamma} = \gamma\left(\phi\right)\left[\cos\left(\zeta + \xi\right)\hat{x}' + \sin\left(\zeta + \xi\right)\hat{y}'\right] \tag{6.37}$$

$$\vec{\Omega}_{SO} = \Omega_{SO}\left(\phi\right)\left[\cos\left(\xi\right)\hat{x}' + \sin\left(\xi\right)\hat{y}'\right] \tag{6.38}$$

in addition to our choice of $\vec{\Omega}_{ext} \parallel \hat{x}'$, the steady-state, out-of-plane spin polarization is given by

$$S_z = \gamma\tau\frac{\Omega_{ext}\tau\sin\left(\zeta + \xi\right) + \Omega_{SO}\tau\sin\left(\zeta\right)}{1 + \left(\Omega_{tot}\tau\right)^2}. \tag{6.39}$$

For notational simplicity I have relabeled $\tau_{eff}$ as $\tau$. Eq. 6.39 will be used to describe the measurements of the component of spin polarization along the optical axis in the following section. It is useful to define a measurement parameter $\theta_{el} = \gamma\tau\sin(\zeta + \xi)$ as the steady-state, out-of-plane, electrically generated spin polarization. This parameter is maximized when the steady-state in-plane polarization is perpendicular to the external magnetic field (i.e. when $\zeta + \xi = 90°$).

## 6.6 Experimental results

Initial measurements of the steady-state spin polarization are taken for $\vec{k}$ along [110] ($\phi = 45°$) or [1$\bar{1}$0] ($\phi = -45°$) as these directions typically correspond to the steady-state current-induced spin polarization extrema. In this case $\zeta = 0°$ (Fig. 6.6), $\xi = 90°$, and Eq. 6.39 reduces to

$$S_{z,\phi=\pm 45°} = \theta_{el} \frac{\Omega_{ext}\tau}{1 + (\Omega_{tot}\tau)^2} \tag{6.40}$$

with $\theta_{el} = \gamma\tau$. Eq. 6.40 resembles an odd Lorentzian, though with a modified denominator. Fig. 6.7(a) displays a measurement of the current-induced spin polarization as a function of external magnetic field for various external voltages with $\vec{k} \parallel [1\bar{1}0]$. The steady-state spin polarization $\theta_{el}$ and effective spin dephasing time $\tau$ are extracted from the amplitude and width of the curve respectively. These values are shown for several orientations of the electron momentum in Fig. 6.7(b) and (c).

The inset of panel (c) shows the effective spin relaxation time $\tau$ as a function of the spin-orbit magnetic field at an external voltage of 2 V. Each data point represents an individual electron momentum direction. The value of the spin-orbit effective magnetic field is obtained from the spin-orbit field measurements presented in Ch. 5. The red line represents a fit to the spin relaxation time which can be approximated by $\tau \sim \Omega_{SO}^{-2}$. We point out that while this relation is only exact for spin polarization along the relaxation tensor eigenvectors, the approximate behavior it represents is still useful. Namely, we see that the relaxation time decreases with increasing spin-orbit effective magnetic field. Furthermore, using the values of the effective spin relaxation time for spins polarized along [1$\bar{1}$0] and [110] we can extract the measured anisotropy in the spin relaxation rate described by the factor $r$. Using the values $\overline{\tau}_{[1\bar{1}0]} \sim 9$ ns and $\overline{\tau}_{[110]} \sim 6$ ns, we get a value of $r = 1/3$. We point out that this is

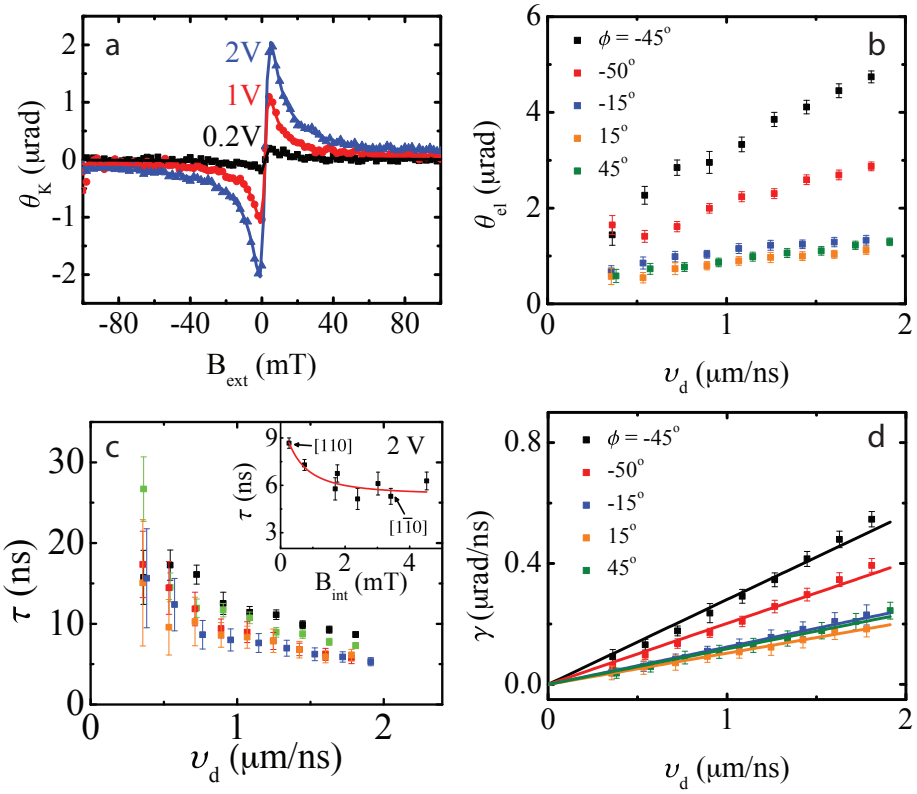


**Figure 6.7: Current-induced spin polarization measurement:** (a) Kerr rotation measurements of steady-state current-induced spin polarization as a function of external magnetic field for 0.2 V (black squares), 1 V (red circles), and 2 V (blue triangles). Electron momentum is along $[1\bar{1}0]$. The steady-state spin polarization amplitude $\theta_{el}$ (b) and effective spin relaxation time $\tau$ (c) are extracted from the amplitude and width of Eq. 6.39, respectively. (d) The spin polarization alignment vector $\gamma = \theta_{el}/\tau$ is extracted from the fit parameters. The proportionality constant $\eta$ is used to characterize the current-induced spin polarization strength. The same color scheme is used for (b)-(d). Measurements are taken at T = 10 K.

significantly lower than the measured anisotropy (maximized for $r = 1$) expected from the ratio of spin-orbit splitting components from this sample given by $\alpha/\beta = 0.89$, indicating that an additional spin relaxation mechanism other than the D'yakonov-Perel must play an important role.

The spin alignment term $\gamma$ is found from the effective relaxation time and steady-state spin polarization using the relation $\gamma = \theta_{el}/\tau$. In Fig. 6.7(d) we show that $\gamma$ is proportional to the electron velocity, verifying the assumption we made earlier in this chapter, and use the proportionality constant $\eta$ to represent the strength of the current-induced spin polarization. This procedure is repeated for all samples. For the cross patterned samples a range of electron momentum directions are used. For the L-shaped channel samples measurements are conducted on only two orthogonal momentum directions.

### 6.6.1 Pulsed laser

A difficulty with taking current-induced spin polarization measurements is that the pulsed probe beam induces unpolarized carriers as discussed in Sec. 6.4.2 and shown in Fig. 6.4. The Kerr rotation peak wavelength is necessarily tuned close to the band edge, and as such photoexcited carriers at this wavelength have an increased energy above the Fermi energy. Using the same pulse sequence as in Fig. 6.4 we can simulate the measured semi-steady-state spin polarization. The simulations are run for 150 ns, which is beyond the relaxation time required to reach steady-state. The time of measurement is taken to be in the center of a pulse. Fig. 6.8(a) displays the result of the simulation for varying levels of absorption as a function of external precession frequency. Strong oscillations, odd in the external field, are apparent and increase in amplitude with the level of light absorption.

Fig. 6.8(b) displays measurements as a function of external field for various probe wavelengths. The low energy Kerr rotation maximum occurs at $\lambda = 848$ nm, for which strong oscillations are present. These oscillations disrupt the ability to fit the parameters accu-

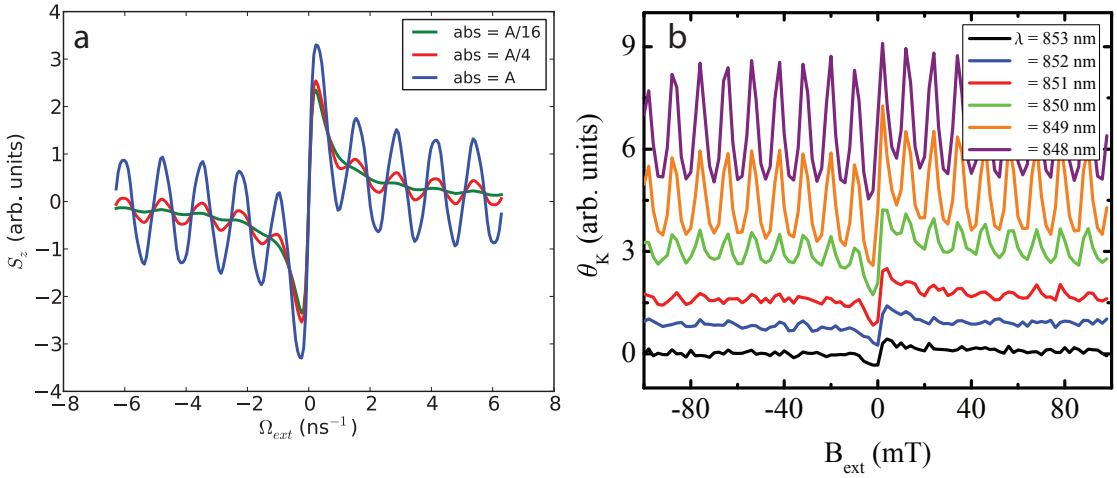


**Figure 6.8: Pulsed current-induced spin polarization:** (a) Simulations of steady-state current-induced spin polarization due to pulsed laser for various laser wavelengths. By decreasing the photoinduced carriers (absorption) the oscillations are suppressed. (b) Measurements showing the oscillations for various laser wavelengths. Oscillations are suppressed while still maintaining a sufficient signal to noise ratio for $\lambda = 851$ nm. Measurements are taken at T = 10 K.

rately from Eq. 6.40. By decreasing the probe energy (increasing wavelength) we can decrease the level of photoinduced carriers due to absorption, however, the measured Kerr rotation decreases as well. Finding an appropriate wavelength is a balancing act of reducing the oscillations while still maintaining a sufficient signal to noise ratio in the Kerr rotation measurements. For the wafer from which measurements are taken in Fig. 6.8(b) the chosen probe wavelength is $\lambda = 851$ nm. As the measured Kerr rotation depends strongly on the probe beam energy, it is necessary to ensure all measurements for a particular set of samples are conducted at the same wavelength, such that a comparison can be made.

### 6.6.2 Frequency and probe power dependence

The frequency of the AC square wave electric field used to supply the current, as well as the power of the probe laser are both experimental parameters used to conduct measurements, but are intended to have no influence on the magnitude of the measured spin polarization. Rather, the measurement statistics, namely the signal to noise ratio will depend on these

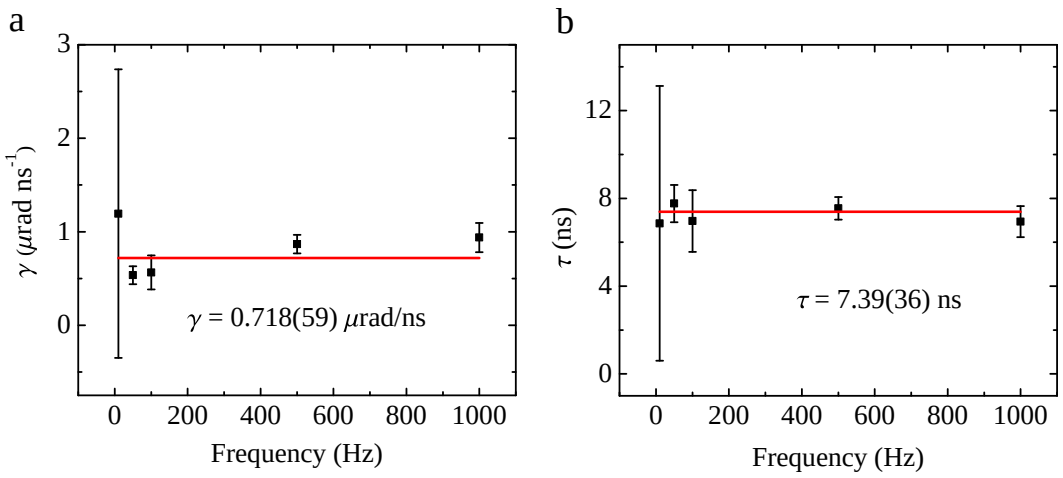


**Figure 6.9: Frequency dependent spin polarization:** Measured spin polarization per unit time $\gamma$ (a) and effective relaxation time $\tau$ (b) as a function of AC electric field modulation frequency. Measurements are taken for $\vec{k}$ along $[1\bar{1}0]$ at T = 10 K.

parameters. In this section I will present measurements of the spin alignment rate $\gamma$ and the effective dephasing time $\tau$ as a function of the electric field frequency and probe power, so that we can be assured that the these experimental parameters do not affect the measured spin-polarization values.

Fig. 6.9 displays the spin alignment rate $\gamma$ (a) and the effective spin relaxation time $\tau$ (b) as a function of electric field modulation frequency. We note the large error at low frequency. This is due to increased level of low frequency noise, as discussed in Sec. 4.2.3. In this case, the lock-in amplifier has a decreased ability to filter out the noise from the signal. Furthermore, the time constant for the lock-in at low frequencies must be extremely long. In general, we use a time constant of roughly $TC = 200 \times f^{-1}$ with $f$ the reference frequency. For the lowest frequency data point $f = 10$ Hz, requiring a time constant of 20 seconds. This is a long enough time scale such that the variations in the laser, detector, and other optoelectronic components will increase the statistical error in the measurements. We note that by going to higher frequencies, however, the values of $\gamma$ and $\tau$ remain constant. As the

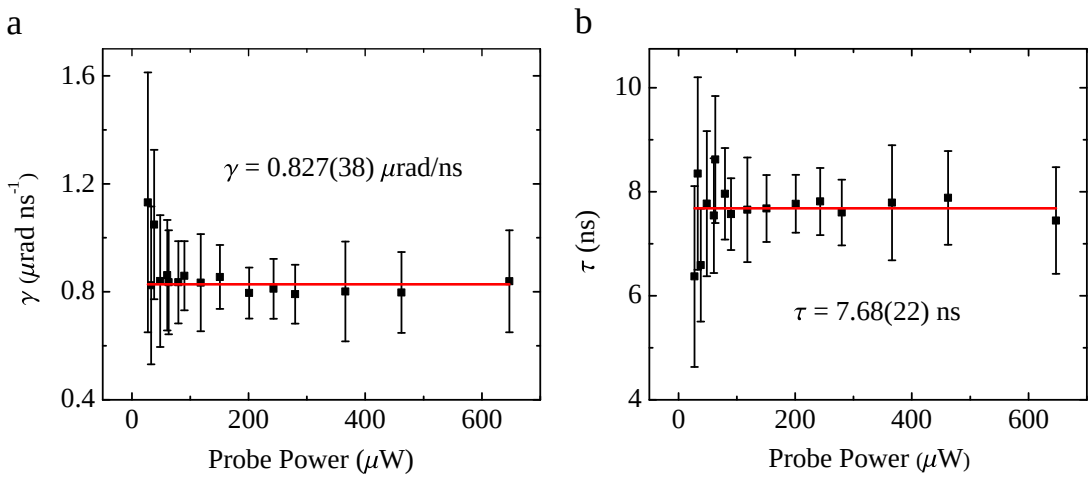


**Figure 6.10: Probe power dependent spin polarization:** Measured spin polarization per unit time $\gamma$ (a) and effective spin relaxation time $\tau$ (b) as a function of probe beam power. Measurements are taken for $\vec{k}$ along $[1\bar{1}0]$ at T = 10K.

spin polarization reaches a semi-steady state within 50 ns, we expect even high frequencies to be essentially DC compared to the time scale of the spin polarization dynamics. For all current-induced spin polarization measurements, an AC electric field modulation frequency of 1167 Hz is used.

Fig. 6.10 displays the spin alignment rate $\gamma$ (a) and the effective spin relaxation time $\tau$ (b) as a function of the probe laser power. Similar to the frequency-dependent measurements, there is an increasing error with decreasing probe power. This is again a result of increased statistical error due to the decrease in signal to noise ratio. Whereas with low frequency the error level is increased, a low laser power decreases the signal measured by the photodiode bridge. By increasing the laser power to a sufficiently high level ($\sim$ 75 $\mu$W) a threshold is passed in which the average error reaches a constant value. By increasing the power to too high of a level, however, the sample will begin to exhibit significant heating, as well as an increase in the oscillating signal due to photoexcited carriers, as shown in Fig. 6.8. For all current-induced spin polarization measurements, a probe laser power of $\sim$ 150 $\mu$W is used.

This is the same probe power as is used for the spin-orbit field measurements.

### 6.6.3 Current-induced spin polarization mapping

We showed in the previous section that the spin alignment per unit time $\gamma$ is proportional to the electron velocity, as is the spin-orbit effective magnetic field (Ch. 5), and used proportionality constants $\eta$ and $\kappa$ to characterize their strengths respectively. Furthermore, we showed in the previous chapter that the magnitude of the spin-orbit field does not closely follow the expected formula due to strain and a lack of inversion symmetry, pointing out the necessity to directly measure the spin-orbit field for each momentum direction individually. In this section, current-induced spin polarization measurements are conducted for electron momentum along the same directions as the spin-orbit field measurements so that a direct comparison between the two can be made. Measurements are conducted on two cross-patterned samples (A and B) and three L-shaped channel samples (C-E) all taken from the same InGaAs wafer. The results of these measurements are published in Ref. [119].

For each choice of the electron momentum direction $\phi$, we rotate the cryostat to scan the external magnetic field direction such that the measured out-of-plane spin polarization is maximized (i.e. when $\vec{S}_{xy} \perp \vec{B}_{ext}$). An odd-Lorenztian line shape is observed which is antisymmetric when $\vec{S}_{xy} \parallel \vec{\gamma} \perp \vec{B}_{ext}$. By rotating the cryostat, we can vary the angle ($\xi$) that $\vec{\gamma}$ makes with $\vec{B}_{ext}$. The resulting data sets for $\phi = -30°$ (sample A) are shown in Fig. 6.11. Fits to Eq. 6.39 are used to extract the steady-state electrically generated spin polarization $\theta_{el} = \gamma\tau \sin(\zeta + \xi)$ and the effective spin dephasing time $\tau$. The values for $B_{SO}$ and $\xi$ are obtained from the measurements in Ch. 5 and are fixed in the fits. We observe that the data is nearly antisymmetric in $B_{ext}$ when the spin-orbit and external fields are perpendicular (i.e. when $\xi = 90°$). As $\xi$ is decreased, the asymmetric behavior becomes increasingly noticeable and the measured out-of-plane spin polarization ($\theta_{el}$) gradually decreases, vanishing when $\zeta + \xi = 0$.

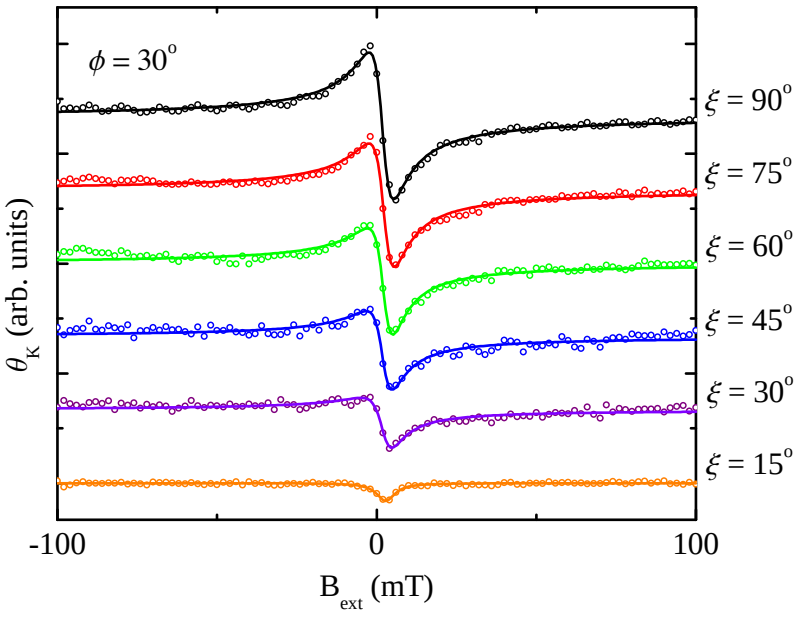


**Figure 6.11: Asymmetric spin polarization measurements:** Current-induced spin polarization measurements as a function of external magnetic field ($B_{ext}$) for various angles ($\xi$) of the spin-orbit effective magnetic field ($\vec{B}_{SO}$) with respect to $\vec{B}_{ext}$. When $\vec{B}_{SO} \perp \vec{B}_{ext}$, the data is nearly antisymmetric. As $\xi$ is decreased, an asymmetry begins to dominate. Lines are fits to Eq. 6.39.

Fig. 6.12(a) presents the out-of-plane electrically generated spin polarization ($\theta_{el}$) measured as a function of $\xi$ for $\phi = -45°$, $0°$, and $45°$ ($\vec{k} \parallel [1\bar{1}0]$, [100], and [110], respectively). For electron momentum along [110] and [1$\bar{1}$0], $\theta_{el}$ is largest when $\vec{\gamma} \perp \vec{B}_{ext}$, indicating that the in-plane spin polarization $\vec{S}_{xy}$ is along the current-induced spin polarization alignment vector $\vec{\gamma}$, as expected. However, for $\vec{k}$ along [100], $\vec{\gamma}$ is no longer along an eigenstate of the relaxation tensor and the in-plane spin polarization is shifted from $\vec{\gamma}$ by $\zeta \sim 37°$. We expect from Eq. 6.22 that $\zeta$ is maximized when $\vec{k}$ is along [100]. Fig. 6.12(b) displays $\zeta$ extracted from the measurements in (a) (red circles) and as determined from fits to Eq. 6.39 when $\vec{S}_{xy} \perp \vec{B}_{ext}$ (black squares) at an external voltage of 2 V. The behavior of $\zeta$ as a function of $\phi$ expected from our model is described by Eq. 6.22 (blue line). We point out that the curve is not a fit from the data, but rather the theoretical model taken from measurements

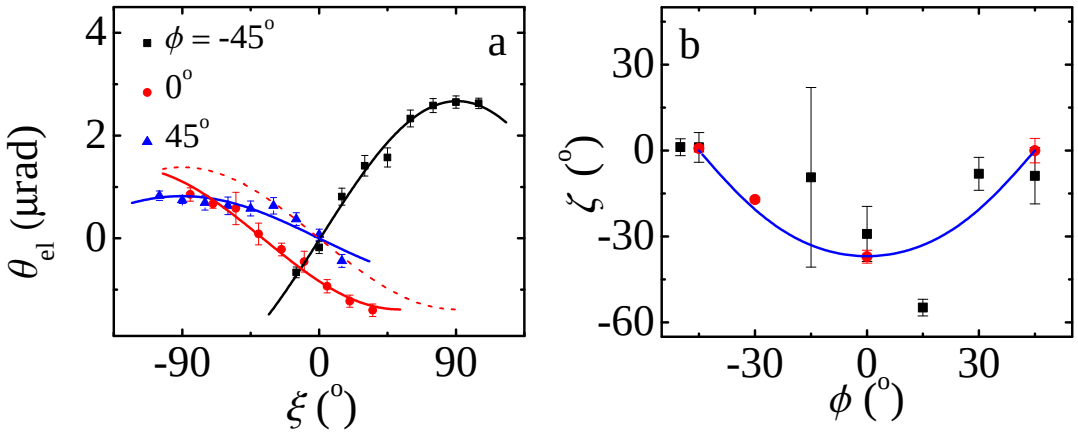


**Figure 6.12: Deviation of steady-state CISP from $\vec{B}_{SO}$:** (a) Steady-state spin polarization as a function of angle ($\xi$) between $\vec{B}_{SO}$ and $\vec{B}_{ext}$ for $\phi = -45°$ (black squares), 0° (red circles), and 45° (blue triangles) all taken at an external voltage of 2 V. Solid lines are fits to a sine curve. $\theta_{el}$ is maximized when $\vec{S}_{xy} \perp \vec{B}_{ext}$. The dashed red line is the expected curve for $\phi = 0°$ if $\vec{S}_{xy} \parallel \vec{\gamma}$; it is shifted from the experimental curve by $\sim 37°$. (b) Deviation ($\zeta$) of the in-plane spin polarization ($\vec{S}_{xy}$) from the spin alignment vector ($\vec{\gamma}$) extracted from measurements in (a) (red circles) and from fits to Eq. 6.39 (black squares). The blue line is a curve expected from the model given in Eq. 6.22

of the spin relaxation time anisotropy. We can see that the model and experimental data are consistent with each other.

### 6.6.4 CISP amplitude vs. spin-orbit field

Fig. 6.13 shows the current-induced spin polarization coefficient $\eta$ compared to the measured spin-orbit field coefficient $\kappa$ for the cross-patterned samples A and B (a) and the L-shaped patterned samples C-E having two orthogonal conductive channels along [110] and [1$\bar{1}$0] (b). All samples are taken from the same wafer. We can see that the electrically generated spin polarization obeys a negative differential relationship with the spin-orbit field; for $\vec{k}$ along the crystal direction having the weakest spin-orbit splitting, both the spin alignment rate $\gamma$ and the steady-state current-induced spin polarization are strongest. Furthermore, for each sample, there is a different ratio of the SIA- to BIA- like spin-orbit splitting terms ($\alpha/\beta$)

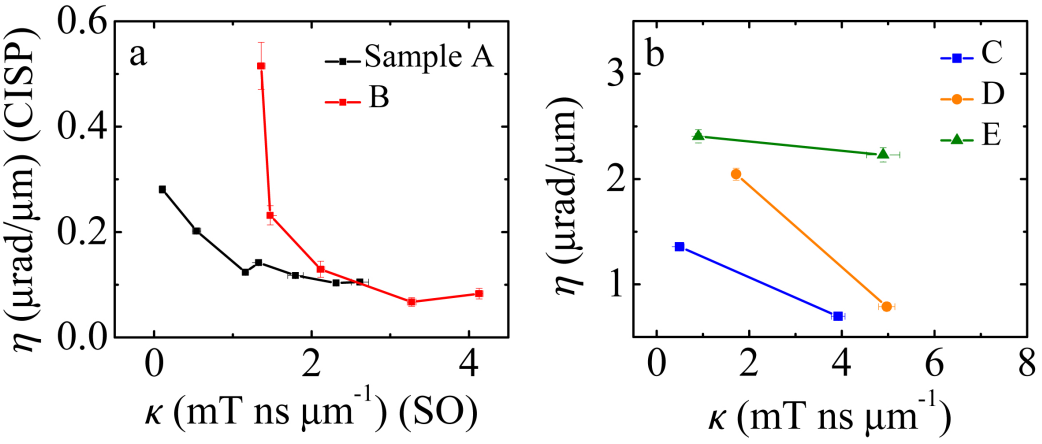


**Figure 6.13: Current-induced spin polarization vs. spin-orbit field:** (a) Current-induced spin polarization vs. spin-orbit field for various electron momentum directions ($\vec{k}$) in the cross-patterned samples. A negative differential relationship is observed. (b) The same negative differential relationship is observed in the L-shaped samples which have two channels patterned along [110] and [1$\bar{1}$0].

due to inhomogeneous strain in the wafer corresponding to a different curve on which the data points lie. From this it appears that current-induced spin polarization depends strongly on the anisotropy in the spin-orbit splitting, rather than on the magnitude for a particular crystal direction alone.

Fig. 6.14 displays the data presented in Ref. [29] taken on L-shaped samples having orthogonal channels patterned along [110] and [1$\bar{1}$0]. No clear relationship was established between the magnitudes of current-induced spin polarization and the spin-orbit splitting, however, we note that the two measurements taken from each individual sample (linked by a solid line) obey the same negative differential relationship we have established here.

Dynamic nuclear polarization measurements for these samples were conducted to confirm the sign of the alignment direction of the current-induced spin polarization, as shown in Fig. 6.15. This was performed by measuring the change in the Larmor precession frequency

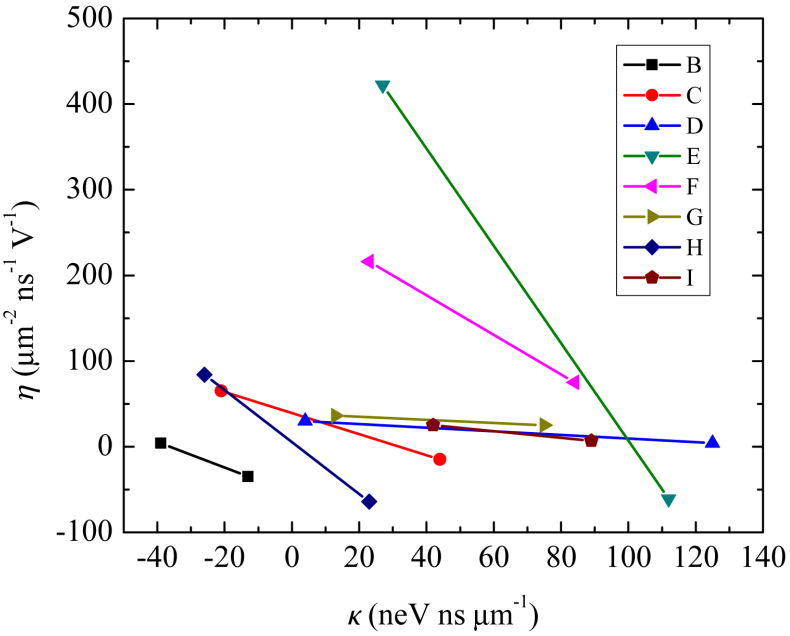


**Figure 6.14: CISP vs. SO from other sources:** Current-induced spin polarization vs. spin-orbit field for data taken from Ref. [29]. Two data points taken from each sample are linked by a solid line. The same negative differential relationship is observed for each individual sample.

upon application of an electric field using time-resolved Kerr rotation measurements, as in Sec. 4.3.2. The electric field was oriented such that $\vec{k} \parallel [110]$ or $[1\bar{1}0]$ with $\vec{B}_{int} \parallel \vec{B}_{ext}$. When the current is switched on (or changed from negative to positive), there is a rapid change in the precession frequency due to the spin-orbit effective magnetic field ($B_{SO}$ in figure). After several minutes the nuclear spin system will couple to the electron spin system according to the nuclear spin relaxation time (shown by $B_{nuc,sat}$ in the figure). This will be along the direction of the current-induced spin polarization. We see that the dynamic nuclear polarization is along the spin-orbit field direction, indicating that current-induced spin polarization in these samples at these temperatures is along the direction of the spin-orbit field as well. The strength of saturated nuclear spin polarization is consistent with the steady-state current-induced spin polarization. See Ref. [133] for more details on the dynamic nuclear polarization measurements.

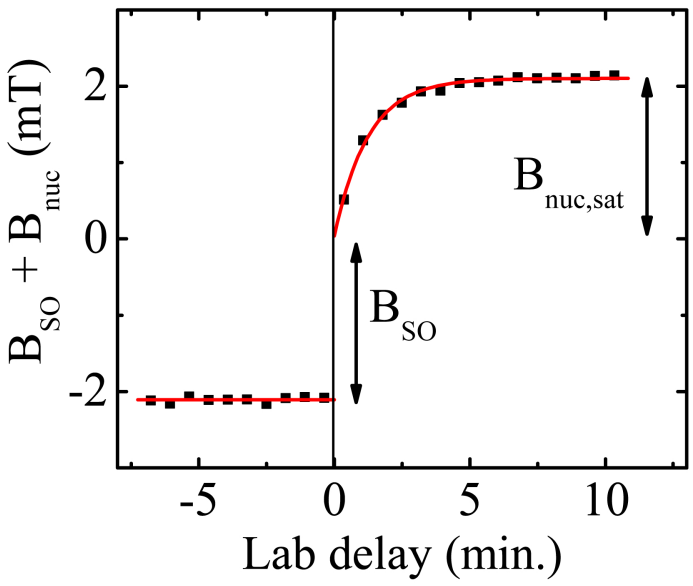


**Figure 6.15: Dynamic nuclear polarization:** Saturation of nuclear polarization along the spin-orbit effective magnetic field indicates current-induced spin polarization aligns along the spin-orbit field direction.

In summary, we have shown that the momentum directions that have the largest current-induced spin polarization also have the weakest spin-orbit field. It is clear from this relationship that electrically generated spin polarization cannot depend on the magnitude of the spin-orbit splitting alone, but that some other effects must contribute. We have further shown that the anisotropy in the spin relaxation rate is significantly reduced compared to what is expected from the D'yakonov-Perel spin relaxation mechanism and the measured spin-orbit splitting anisotropy, indicating that another scattering mechanism must be playing a significant role.

We found in these samples that the spin polarization is dynamically seeded along the spin-orbit field direction. While this may not seem like a surprising result, we point out that the g-factor for electrons in GaAs is negative, indicating that spin alignment against the spin-orbit field is the lower energy state. We observe electrons being "pumped" out of equilibrium into a higher energy state. This could be due to an Elliot-Yafet-type mechanism involving

scattering accompanied by a spin flip. It is unclear what gives rise to this effect and would require a thorough investigation of the transition matrix elements between the conduction band and nearby energy bands, with the relevant spin-dependent energy splittings taken into full account. Furthermore, it is not clear how this scattering mechanism would quantitatively depend on the spin-orbit splitting magnitude and anisotropy. Another possibility is spin-dependent scattering as a result of the extrinsic spin Hall effect dynamically seeding a current-induced spin polarization [134] proportional to the magnitude of the transverse spin-orbit field. This possibility will be investigated in future studies. With our phenomenological model presented in Sec. 6.3, we now have a qualitative understanding of the behavior of the spin polarization alignment per unit time $\vec{\gamma}$, which has been characterized in terms of the spin-orbit splitting in this chapter.

# Chapter 7

# Conclusions and Future Work

In this dissertation, we have investigated current-induced spin polarization, characterizing some unexpected phenomena, and ultimately shedding light on a process that is not well understood. Previously expected to be a result of spin-orbit interactions in the conduction band, this investigation focused on measuring both phenomena at a single location in a single sample for direct comparison. This work comprises the first study of its kind in which both spin-orbit interactions and current-induced spin polarization are directly compared as a function of electron momentum direction.

Measurements were conducted on the III-V semiconductor alloy, InGaAs, in which a strain-induced momentum linear spin-orbit interaction is present due to lattice mismatch between the InGaAs epilayer and the GaAs substrate. We found this spin-orbit interaction to be anisotropic with the electron momentum direction. Through the use of a four-contact geometry we were able to vary the direction of the in-plane momentum, and therefore the strength and direction of the spin-orbit effective magnetic field, at a single location in a sample. We furthermore found that the strength and anisotropy of the spin-orbit interaction varied for different samples taken from the same wafer. This allowed us the unique oppor-

tunity to have samples for which the spin-orbit interaction was varied while keeping other material parameters constant.

Current-induced spin polarization measurements were conducted on the same samples and for momentum along the same directions as the spin-orbit interactions, such that a direct comparison could be made. We found that the spin alignment is dynamically oriented along the spin-orbit effective magnetic field. While this may seem expected, we pointed out that the g-factor for GaAs is negative, and therefore from a simple Zeeman-type polarization perspective, one would expect spin alignment to be against the spin-orbit field. We presented a phenomenological model based on spin-dependent scattering accompanied by a spin-flip to describe this effect. This was characterized as a spin alignment per unit time, as well as the steady-state spin polarization, which was ultimately measured.

By allowing for anisotropic spin relaxation, as with the D'yakonov-Perel mechanism, we showed that spin polarization maintained its alignment along the spin-orbit field direction only when this alignment was along one of the relaxation tensor eigenvectors, namely the [110], [$1\bar{1}0$], and [001] crystal axes. We presented a new, quantitative model to describe this deviation, which was maximized for electron momentum along the [100] crystal axis. This model agrees with our experimental observations.

Finally, we presented an unexpected result, that the magnitude of current-induced spin polarization was maximized for those crystal directions having the weakest spin-orbit splitting, and vice versa. This was confirmed for several samples, and agrees with previous work in the field. From the perspective of an Elliott-Yafet-type spin-flip process, we attribute this result to a dynamic alignment of spins along the spin-orbit field direction (which is the higher energy state) that is more efficient when the spin-splitting in the conduction band is weaker. The quantitative analysis is not well understood at this time and a more rigorous treatment of the band structure at the $\Gamma$ point is required. To investigate this effect further, the following future work is proposed.

## 7.1 Investigation of electron and spin scattering by varying doping density

According to Ref. [78], the turning point between GaAs being treated as an insulator to being treated as a metal occurs at a doping density of $n = 2 \times 10^{16}$ cm$^{-3}$. Below this concentration, the donor electrons are more tightly bound and the lower mobility Elliot-Yafet spin relaxation rate (proportional to the inverse of the scattering time) is found to dominate. Above this concentration the higher mobility D'Yakonov-Perel spin relaxation rate (proportional to the momentum scattering time) is expected to dominate. The measured spin relaxation rate anisotropy, as well as the temperature dependence of the spin relaxation time presented in this work, indicates that our samples are dominated by the D'Yakonov-Perel spin relaxation mechanism. As our doping concentration is $n = 3 \times 10^{16}$ cm$^{-3}$, this is expected. We point out, however that as we are near the metal-to-insulator transition, we still expect the Elliott-Yafet mechanism to play an influential rule, even when it is not the dominant spin relaxation mechanism.

We suspect spin-dependent spin-flip scattering, described by the Elliott-Yafet mechanism, to be the phenomenon that gives rise to current-induced spin polarization. The natural next step to test this hypothesis is to investigate the strength of current-induced spin polarization for various doping concentrations around the metal to insulator transition. We expect that, for sufficiently high doping concentrations, spin-flip scattering becomes a less influential effect and current-induced spin polarization should be weak. On the other hand, for lower doping concentrations the spin-flip scattering rate should be increased, thereby increasing the rate of dynamic spin alignment term in the current-induced spin polarization model presented in this dissertation. As such, we have plans to have samples with doping concentrations of 1, 4, and 7 $\times 10^{16}$ cm$^{-3}$ to be grown in the near future.

## 7.2 Investigation of spin-orbit field anisotropy by varying indium concentration

It is also a natural next step to vary the indium substitutional percentage in the InGaAs epilayer. We expect an increase in the indium concentration to increase the strain in the epilayer, and, for a particular layer thickness, to also increase the spin-orbit field anisotropy due to strain relaxation. To test this effect we have already had $In_{0.03}Ga_{0.97}As$ samples grown for comparison with the 4% indium samples from which most of the measurements in this dissertation are conducted. Preliminary measurements indicate that the spin-orbit field anisotropy is reduced in the $In_{0.03}Ga_{0.97}As$ samples. This results in spin-orbit fields that are comparable for $\vec{k}$ along the [110] and [1$\bar{1}$0] rather than one crystal axis dominating significantly over the other.

We find the same negative differential relationship between current-induced spin polarization and the spin-orbit field in the 3% indium sample. The strength of the spin polarization, however, is weaker than in the 4% indium samples, roughly by a factor of 2-3 for the maximum CISP direction. We suspect that by increasing the strain, and also the spin-orbit field anisotropy, we can increase the current-induced spin polarization maximum. As such we have plans to have samples with higher indium concentration grown in the future.

## 7.3 Spin amplification and the spin Gunn effect

Amplification of spin polarization to levels near unity, at room temperature was proposed in Ref. [135] in an effect called the "spin Gunn effect." It is based on the charge Gunn effect which produces charge domains due to a negative differential resistance for $\Gamma - L$ valley transitions for conduction band electrons in GaAs. Such a domain is termed a "Gunn domain." Because electron scattering is energy dependent, as described in Sec. 3.2, a difference

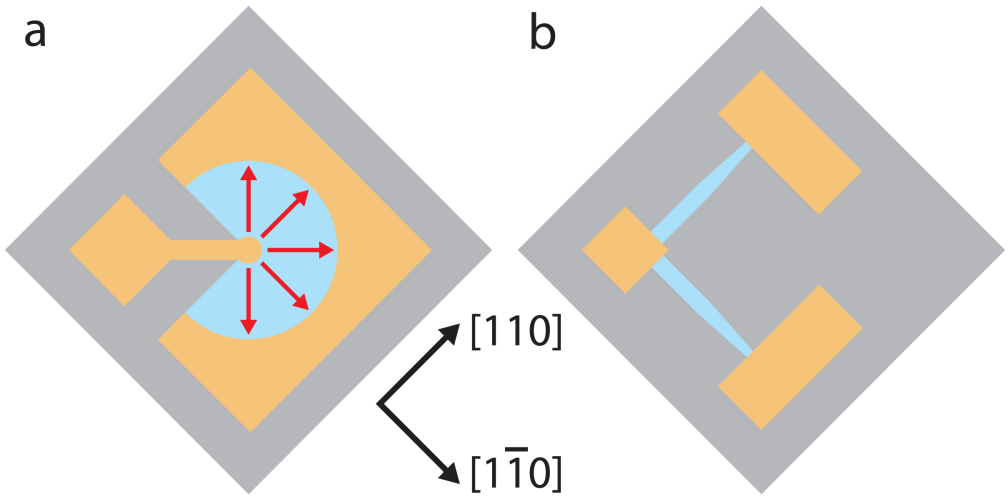


**Figure 7.1: E-field gradient sample design:** Concentric rings (a) and tapered channels along [110] and [1$\bar{1}$0] (b) create an electric field gradient along the direction of electron momentum. Electric field in (a) is shown by red arrows. InGaAs layer is depicted in blue, contacts in gold, and substrate in gray.

in energy levels for up and down spins will result in a spin-dependent scattering rate similar to that of the phenomenological model presented for current-induced spin polarization in this work.

It was shown in Ref. [135] that an amplification rate, to offset the spin relaxation rate, was proportional to the gradients in each the electric field, doping concentration, and mobility, and calculated to be, under certain conditions, greater than the relaxation rate such that a net spin polarization amplification, rather than decay, would result. To test this effect, we have fabricated samples in which an electric field gradient is present. Such a sample is shown in Fig. 7.1(a) and is composed of concentric ring contacts surrounding the InGaAs epilayer. We have also designed linear channels similar to the L-shaped samples presented in this work in which a gradient in the electric field is produced through a tapered width at one end of the channel, as shown in Fig. 7.1(b). The advantage to the first design is that it would allow for measurements along any crystal direction in the (001) plane. The advantage to the second is that it would allow us to compare current-induced spin polarization in a uniform

electric field to that in which there is an electric field gradient by the spatial position of the probe along the length of the channel. In each sample, an anisotropy in the steady-state spin polarization for momentum forward or backward (relative to the positive electric field gradient) would indicated some level of spin polarization amplification.

## 7.4 Spin generation and manipulation devices

For the purposes of technological advancement, it is necessary to keep in mind practical applications of a newly discovered effect. Previously, current-induced spin polarization has been shown to be an all-electrical method of generating spin polarization for potential spintronics applications. Furthermore, extensive work in spin manipulation has been conducted using spin-orbit fields. We have discovered an anomalous phenomenon in the samples studied in this dissertation, namely that the momentum direction corresponding to a current-induced spin polarization maximum is nearly orthogonal that which corresponds to a spin-orbit field maximum.

This effect has recently been exploited using timed electrical pulses [43]. A four-contact geometry, similar to that presented in this study, is patterned with two opposing contacts oriented along the CISP maximum, and two other opposing contacts oriented along the orthogonal SO field maximum. The spin generation pulse polarizes spins very rapidly to the steady-state value in the plane of the sample. This pulse is then turned off, and soon after, in the orthogonal direction, the spin-orbit field pulse rotates the net spin polarization. This work was able to produce $\pi/2$ and $\pi$ rotation pulses. The spin relaxation times were significantly shorter than those measured in this dissertation. We believe with the spin relaxation times present in our samples ($\sim$ 10 ns) a $2\pi$ rotation pulse could be achieved without difficulty.

We also present a class of spin generation devices exploiting the anomalous current-

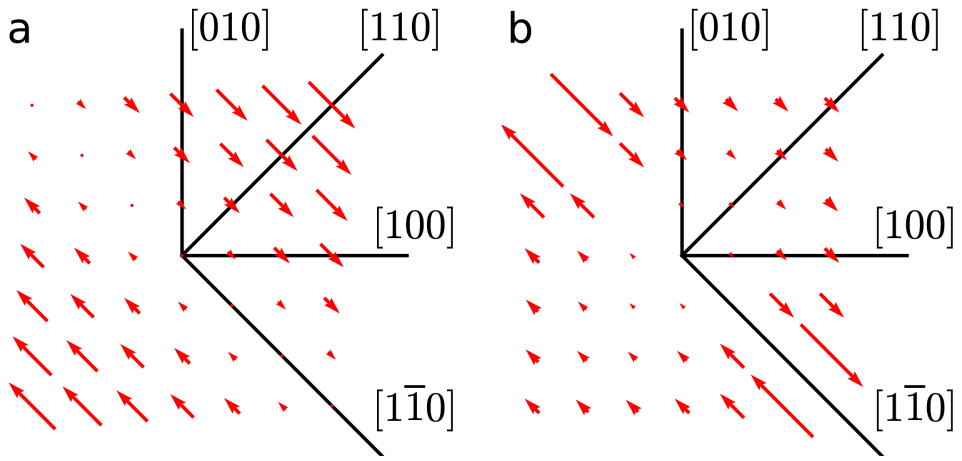


**Figure 7.2: SO and CISP field maps in spin-helix device:** (a) Spin-orbit field map for a sample exhibiting a spin-helix state. For all momenta, the spin-orbit field is either along or against [1$\bar{1}$0]. (b) Resulting current-induced spin polarization map based on an inverse relationship between the current-induced spin polarization coefficient $\eta$, and the spin-orbit field coefficient $\kappa$, as discovered in Sec. 6.6.4

induced spin polarization phenomenon based on the ability to fabricate a sample exhibiting a spin-helix state. That is, a sample for which the linear SIA and BIA spin-orbit field components are matched, as depicted in Fig. 7.2(a). The resulting current-induced spin polarization map is shown Fig. 7.2(b). A inverse relationship between the current-induced spin polarization coefficient ($\eta$) and the spin-orbit field coefficient ($\kappa$) is assumed, in qualitative agreement with the measurements presented in Sec. 6.6.4. Such a device is shown in Fig. 7.3(a).

For momentum along [$\bar{1}$10], the momentum-linear spin-orbit field vanishes, and as such the net current-induced spin polarization is expected to vanish as well. However, for momentum slightly deviated from this direction the spin-orbit field is weak, corresponding to a strong current-induced spin polarization (Fig. 7.2(b)). If the deviation is to the left, the spin polarization will be up, whereas if the deviation is to the right, the spins will be polarized down. This deviation could easily by modulated electrically using a pair of cross gates, in which case the sample design presented in this work is ideal.

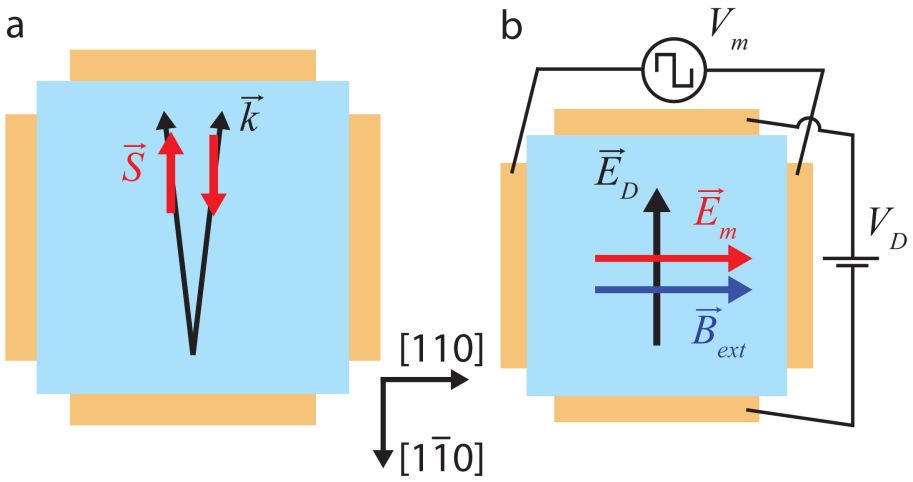


**Figure 7.3: CISP-based spin switching device:** Electron momentum is oriented along the direction of zero spin-orbit field ([$\bar{1}$10]). A slight deviation to the left (right) corresponds to current-induced spin polarization along [$\bar{1}$10] ([1$\bar{1}$0]). (b) Schematic for measuring low modulation field-induced CISP. DC driving field ($\vec{E}_D$, black) is oriented along [$\bar{1}$10]. External magnetic field ($\vec{B}_{ext}$, dark blue) and AC square wave modulation field ($\vec{E}_m$, red), are oriented along [110]. Spin polarization is modulated at AC frequency between spin up and spin down, as in (b). Measurement is conducted via optical Kerr rotation.

We present a suitable measurement geometry to test this effect in Fig. 7.3(b). The driving electric field ($E_D$) is oriented along the zero spin-orbit field direction. Meanwhile an external magnetic field, as well as the modulating electric field ($E_m$), are oriented orthogonal to $E_D$. $E_D$ is a DC field while $E_m$ is an AC square wave. The spin polarization will be modulated between spin up and spin down (along $E_D$) at the frequency given by $E_m$ and rotated out of the plane of the sample using the external magnetic field. This can be measured using the same Kerr rotation and lock-in detection scheme presented in this dissertation.

One practical consideration is the ability to fabricate devices which exhibit such a spin-helix. We propose that a sample which is nearly in a spin-helix state could be mechanically strained to tune the SIA spin-orbit splitting, as in Ref. [24], to reach such a state. To ensure minimal strain relaxation samples would need to be grown near or below the critical thickness. We point out that, due to the nature of current-induced spin polarization discovered in this work, a strong spin polarization could be generated and modulated very rapidly between up

and down spin using a weak modulation field, and as such, this effect has the potential to be extremely useful for the advancement of low power spintronics applications.

# Appendix A

# Computational Methods

In the course of the work presented in this dissertation it has been necessary to perform numerical algorithms for a few of the computational tasks that we encountered. These algorithms will be discussed here. The first is the relaxation method for determining the electric potential given a certain set of boundary conditions. This was performed to determine the suitable dimensions for the cross patterned samples (Ch. 5) to maximize the region of uniformity while minimizing power dissipation. It was also used to determine the magnitude and orientation of the electric field at the center of the sample. The second numerical algorithm is the fourth order Runge-Kutta method for solving ordinary differential equations in order to determine the temporal behavior of the dynamically generated spin polarization, as discussed in Ch. 6.

## A.1 Relaxation method for determining electric potential

The purpose of the relaxation method is to solve Poisson's equation, which is a second order partial differential equation given by

$$\nabla^2 \Phi\left(\vec{r}\right) = \frac{1}{\epsilon}\rho\left(\vec{r}\right) \tag{A.1}$$

where $\Phi(\vec{r})$ is the electric potential, $\epsilon$ is the dielectric constant, and $\rho$ is the charge density. We will begin with the assumption of space charge neutrality, namely $\rho = 0$. In truth we need to care about the free charge density. However, we take this to be uniform in space so the end result will simply be to multiply the resulting field by a constant. In this case, we have Laplace's equation

$$\nabla^2 \Phi\left(\vec{r}\right) = 0 \tag{A.2}$$

To approach the solution, one must first examine the symmetry of the problem to determine the appropriate coordinate basis. For our purposes, we are attempting to solve for the cross patterned sample which is best described using Cartesian coordinates. In this case, Eq. A.2 becomes

$$\left(\frac{\partial^2}{\partial x^2} + \frac{\partial^2}{\partial y^2} + \frac{\partial^2}{\partial z^2}\right)\Phi\left(x, y, z\right) = 0 \tag{A.3}$$

We make use of the symmetrized version of the second order ordinary differential equation using the finite differences approach, given by

$$\frac{\partial^2 f\left(x_n\right)}{\partial x^2} = \frac{f\left(x_{n+1}\right) - 2f\left(x_n\right) + f\left(x_{n-1}\right)}{\Delta_x^2} \tag{A.4}$$

where $n$ is the index referencing the $n^{th}$ element of position space, and $\Delta_x$ the finite difference separation in position space. Plugging Eq. A.4 into Eq. A.3, we get

$$\begin{aligned}
&\Phi\left(x_{m+1}, y_n, z_k\right) + \Phi\left(x_{m-1}, y_n, z_k\right) + \\
&\Phi\left(x_m, y_{n+1}, z_k\right) + \Phi\left(x_m, y_{n-1}, z_k\right) + \\
&\Phi\left(x_m, y_n, z_{k+1} + \Phi\left(x_m, y_n, z_{k-1}\right)\right) = 6\Phi(x_m, y_n, z_k). \qquad \text{(A.5)}
\end{aligned}$$

We notice Eq. A.5 as taking the potential at a point $(x_n, y_n, z_n)$ as being the average of all the surrounding points. This will be our prescription for determining $\Phi$, working our way from the known boundary conditions inward. We will work in two dimensions, approximating the $z$-dependence of $\Phi$ to be uniform.

Our general problem to solve is the cross patterned sample, where the ends of the cross are held at a known potential, and the edges running inward toward the center require no transverse electric field. The latter condition is a result of the etch and requires that no electrons enter or leave the InGaAs epilayer through the edge of the etched region. This is depicted in Fig. A.1(a).

The cross region of interest is broken into a two dimensional grid with finite differences $\Delta x = \Delta y$ chosen as large as possible to allow for the dimensions of the cross region. This is depicted in Fig. A.1(b). Using the relaxation method, we take each point to be the average of the 4 surrounding points. This is achieved by creating four temporary arrays, each one shifted one cell in the positive or negative direction along either the $x$ or $y$ axis from the array we wish to solve, and assigning to a new array the value of the average of the four temporary arrays. At this point the total change between the original array and the new array is calculated. This process is depicted by the following set of equations

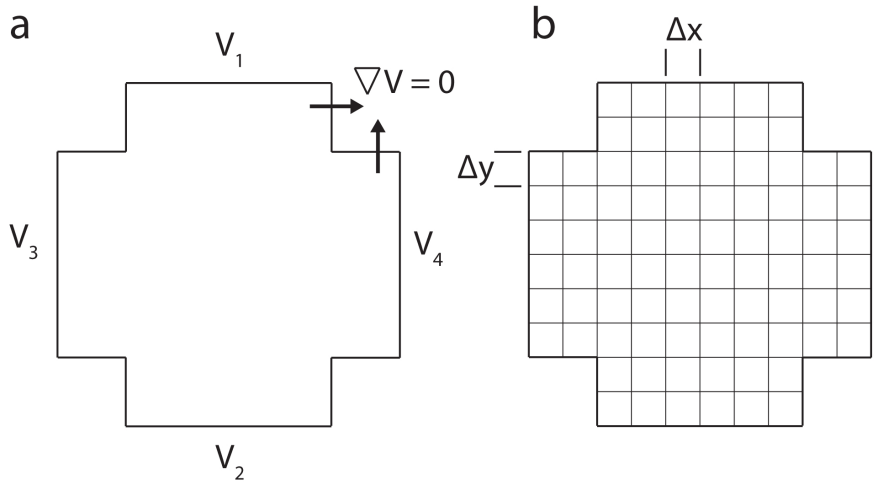


**Figure A.1: Relaxation method for cross pattern:** (a) Boundary conditions for cross pattern relaxation algorithm. Ends of cross are held at constant potential. Edges of etched region require no transverse potential gradient (depicted by arrows). (b) Grid method for setting up finite differences calculation. From the symmetry of the problem we choose $\Delta x = \Delta y$.

$$\Phi_{i+1}(x_m, y_n) = \frac{1}{4}\left[\Phi_i(x_{m-1}, y_n) + \Phi_i(x_{m+1}, y_n) + \Phi_i(x_m, y_{n-1}) + \Phi_i(x_m, y_{n+1})\right] \tag{A.6}$$

$$\Delta = \sum_{m,n} \left|\Phi_{i+1}(x_m, y_n) - \Phi_i(x_m, y_n)\right|. \tag{A.7}$$

The process is repeated until the change between iterations ($\Delta$) falls below a threshold value indicating convergence.

To avoid changing the grid points that we wish to remain constant, we build a mask. The mask is depicted in Fig. A.2. Notice that to fix the values of the voltages at the contacts, we must extend the grid by one grid point around the entire cross region. In the figure the cross pattern is depicted by a thicker solid black line. All unshaded grid points in the mask are allowed to change during each iteration according to Eq. A.6. The red points are fixed at the specified voltages and do not change during each iteration. Likewise the gray grid points are fixed at zero (though in truth their value doesn't matter). The blue grid points

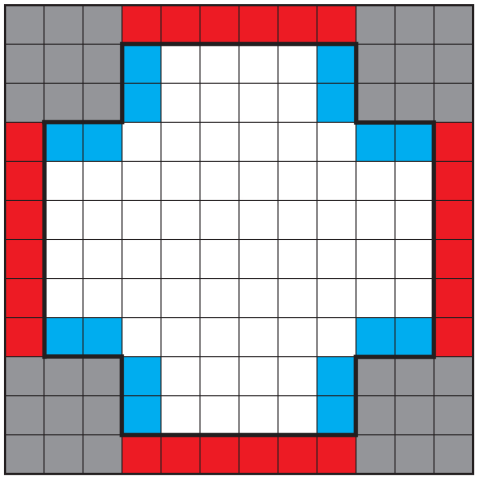

**Figure A.2: Cross pattern relaxation mask:** All unshaded grid points are changed during each iteration according to Eq. A.6. Red grid points are held constant during each iteration at the voltage values specified. Gray grid points are held at zero. After each iteration blue grid points are set to the values of the grid points one position inward from their adjacent edge. This ensures zero potential gradient at the edge of the etched region.

are set to the value of the grid points one position inward after each iteration. This ensures that the transverse potential gradient goes to zero at each edge of the etched region. The computational manifestation of the mask is an array of zeros, indicating which values remain fixed, and ones, indicating which values change during each iteration. During the iteration then, the average in Eq.A.6 is multiplied element-wise by the mask.

In general this problem can take a very long time to converge. We are setting values along the outer edges and waiting for successive averages to reach a convergence condition all the way in to the center. There are a few tricks we can perform to increase the computational efficiency. The first is known as the multi-grid method. This corresponds to successively waiting for the convergence condition to be met for a particular grid, and then cutting the grid size in half (i.e. turning each grid point into four grid points). From the grids depicted in Figs. A.1 and A.2, we can see that the resolution is significantly less than what we would

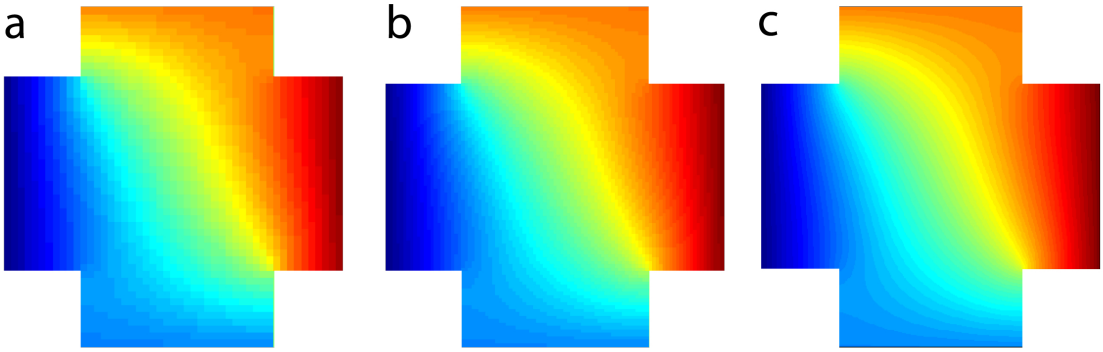


**Figure A.3: Multi-grid relaxation method:** Successive iterations using the multi-grid relaxation mechanism. Array sizes are $50 \times 50$ (a), $100 \times 100$ (b), and $400 \times 400$ (c). Voltages used are $\pm 1$ V vertically and $\pm 2$ V horizontally.

like in order to accurately depict a continuous electric potential map. Indeed we choose the largest possible finite difference ($\Delta x$) at the start to more quickly reach convergence, and then successively reduce the size of each grid point until the desired resolution is achieved. The relaxed potential maps for these successively reduced grid point sizes is shown in Fig. A.3. We can see that as we go to smaller grid points the resolution is improved. We also note that our boundary conditions are met, namely that the contacts are held at their proper voltages, and that the transverse electric field at the edges of the etched regions are zero. The latter is indicated by the fact that the equipotential lines are normal to these edges.

Another method for increasing the efficiency of the relaxation method is to perform what is known as Gauss-Seidel over-relaxation [136] (also called successive over-relaxation). In this case, instead of simply taking the average of neighboring points, we purposefully overshoot by a factor $r > 1$. We can express the original change in potential from each iteration as

$$\Delta\Phi_i\left(x_m, y_n\right) = \frac{1}{4}\left[\Phi_i\left(x_{m-1}, y_n\right) + \Phi_i\left(x_{m+1}, y_n\right) + \Phi_i\left(x_m, y_{n-1}\right) + \Phi_i\left(x_m, y_{n+1}\right)\right] - \Phi_i\left(x_m, y_n\right). \tag{A.8}$$

We then weight this change by the factor $r$ to achieve the new potential

$$\Phi_{i+1}(x_m, y_n) = \Phi_i(x_m, y_n) + r\Delta\Phi_i(x_m, y_n). \tag{A.9}$$

Thus the new potential for each iteration is given by

$$\begin{aligned}\Phi_{i+1}(x_m, y_n) = &(1-r)\,\Phi_i(x_m, y_n) + \\ &\frac{r}{4}\left[\Phi_i(x_{m-1}, y_n) + \Phi_i(x_{m+1}, y_n) + \Phi_i(x_m, y_{n-1}) + \Phi_i(x_m, y_{n+1})\right].\end{aligned} \tag{A.10}$$

For situations obeying a well-behaved geometry, this form of over-relaxation is stable for $r < 2$. We find, however, that the four points located on the corners of the cross (white grid point surrounded on two sides by blue in Fig. A.2) give rise to instabilities except for when $r \approx 1$. As such, we do not find over-relaxation to be a useful tool in this case.

The gradient of the electric potential is used to determine the electric field map. We can define a circle located at the center within which the electric field magnitude and orientation is defined to be uniform up to some threshold value. We choose this threshold value to be such that the electric field magnitude deviates by no more than 5% and the angle deviates by no more than 5°. For optical measurements we desire a radius of 35 $\mu$m for our region of uniformity. To achieve this we adjust the lengths of the contacts, as well as the overall size of the cross region. Obviously the larger the cross, and contacts, the larger the region of uniformity. However, the power dissipation, which contributes to heating, also scales with the size of the cross region. We calculate the power dissipation per unit volume from [123]

$$\frac{P}{V} = \frac{J^2}{\sigma} \tag{A.11}$$

where $J$ is the current density (current per unit area) calculated from the electric field using $J = \sigma E$, and $\sigma$ is the conductivity given by $\sigma = \rho\mu$ with $\rho$ the free charge density and $\mu$

the mobility. We have measurements of the mobility (Fig. 3.9) and estimate the free charge density to be the density of dopant carriers. With the electric field calculated from the relaxation simulation we can estimate the total power dissipated for a given set of voltages. We choose the dimensions shown in Figs. 5.3(a) and 6.1(b) such that the power dissipation remains below 15 mW for a potential difference of 2 V across each pair of orthogonal contacts and such that the radius of the region of electric field uniformity is at least 35 $\mu$m. Finally we can determine the magnitude of the electric field as a function of momentum direction $\phi$ by conducting relaxation simulations on various voltage settings. This is shown in Fig. 5.3(d).

## A.2 Runge-Kutta method for solving ODEs

The Runge-Kutta method is used throughout this work for solving ordinary differential equations for the spin polarization with respect to time. It is assumed that in the region of electric field uniformity, the spin polarization is uniform in space. However, if this condition is relaxed, then one must, in general, use a method for solving partial differential equations in space and time, such as the Crank-Nicolson method [137]. In this treatment, we shall maintain spatial uniformity. To introduce the Runge-Kutta method, we shall first start with the most basic forward Euler method using a finite difference in the time domain. We will conduct this analysis in the context of the spin polarization as it directly applies to our purpose.

The general form of the spin polarization is given by the set of equations (Eq. 6.10)

$$\frac{\partial S_x}{\partial t} = -\frac{S_x}{\tau_x} + \Omega_y S_z + \gamma_x \tag{A.12}$$

$$\frac{\partial S_y}{\partial t} = -\frac{S_y}{\tau_y} - \Omega_x S_z + \gamma_y \tag{A.13}$$

$$\frac{\partial S_z}{\partial t} = -\frac{S_Z}{\tau_z} + \left(\Omega_x S_y - \Omega_y S_x\right). \tag{A.14}$$

We begin with the definition of the forward Euler method for solving a differential equation of the form $\partial S/\partial t = f(S,t)$, given by

$$S\left(t_n + \Delta t\right) = S\left(t_n\right) + \Delta t f\left(S\left(t_n\right), t_n\right). \tag{A.15}$$

Hereafter we will denote the functional form of the time dependence of the spin polarization using subscripts. Namely $S_n = S(t_n)$, $S_{n+1} = S(t_n + \Delta t)$, etc. Then we have for the components of the spin polarization

$$S_{x,n+1} = S_{x,n} + \Delta t \left[-\frac{1}{\tau_x} S_{x,n} + \Omega_y S_{z,n} + \gamma_x\right] \tag{A.16}$$

$$S_{y,n+1} = S_{y,n} + \Delta t \left[-\frac{1}{\tau_y} S_{y,n} - \Omega_x S_{z,n} + \gamma_y\right] \tag{A.17}$$

$$S_{z,n+1} = S_{z,n} + \Delta t \left[-\frac{1}{\tau_z} S_{z,n} + \left(\Omega_x S_{y,n} + \Omega_y S_{x,n}\right)\right]. \tag{A.18}$$

In some cases simply using the forward Euler method is enough to solve for the time dependence of a function. However we can improve upon this by not just evaluating at the end times $t$ and $t + \Delta t$, but also by including the midpoint. This has the form

$$S_{n+1} = S_n + \Delta t f\left(S_{n+1/2}, t_n + \frac{\Delta t}{2}\right) \tag{A.19}$$

and is known as the Runge-Kutta method for solving first order ordinary differential equations [138]. We can, in turn use a forward Euler step to solve for the term on the right, given by

$$S_{n+1/2} = S_n + \frac{\Delta t}{2} f\left(S_n, t_n\right). \tag{A.20}$$

It is typical to make the following assignments,

$$k_1 = \Delta t f\left(S_n, t_n\right) \tag{A.21}$$

$$k_2 = \Delta t f\left(S_n + \frac{k_1}{2}, t_n + \frac{\Delta t}{2}\right) \tag{A.22}$$

which can be solved for, assuming the initial condition is known. Going back to Eq. A.19, we then have

$$S_{n+1} = S_n + k_2 \tag{A.23}$$

This is the form of the second order Runge-Kutta method. We can take the solution to arbitrarily higher orders, though it is common in practice to use the fourth order Runge-Kutta method, frequently referred to as RK4, given by

$$S_{n+1} = S_n + \frac{k_1}{6} + \frac{k_2}{3} + \frac{k_3}{3} + \frac{k_4}{6} \tag{A.24}$$

with

$$k_1 = \Delta t f\left(S_n, t_n\right) \tag{A.25}$$

$$k_2 = \Delta t f\left(S_n + \frac{k_1}{2}, t_n + \frac{\Delta t}{2}\right) \tag{A.26}$$

$$k_3 = \Delta t f\left(S_n + \frac{k_2}{2}, t_n + \frac{\Delta t}{2}\right) \tag{A.27}$$

$$k_4 = \Delta t f\left(S_n + k_3, t_n + \Delta t\right). \tag{A.28}$$

One can envision $k_1$ and $k_4$ as estimating the slope of the function (i.e. the derivative) at times $t$ and $t + \Delta t$, respectively, and $k_2$ and $k_3$ as evaluating the slope on either side of the midpoint. These parameters are evaluated for each of the spin components according to the form given in Eqs. A.16 - A.18. The Runge-Kutta method has significantly improved stability compared to the forward Euler method, particularly for functions that have an oscillatory time dependence for which the forward Euler method is unable to "keep up." Furthermore, it offers significantly higher efficiency when compared to implicit methods such as the backward Euler, or other predictor-corrector methods. The numerical evaluations of the spin polarization components, given a particular set of time-dependent parameters and initial conditions, is presented in Ch. 6.

# Bibliography


[1] Uhlenbeck, G. E. & Goudsmit, S. Spinning electrons and the structure of spectra. *Nature* **117**, 264–265 (1926).

[2] Gerlach, W. & Stern, O. The experimental proof of space quantization in a magnetic field. *Z. Phys.* **9**, 349–352 (1922). doi: 10.1007/BF01326983.

[3] Bose, S. N. Planck's law and the light quantum hypothesis. *Z. Phys.* **26**, 178–181 (1924). doi: 10.1007/BF01327326.

[4] Fermi, E. On the quantization of the monatomic ideal gas. *Z. Phys.* **36**, 902–912 (1926).

[5] Dirac, P. A. M. On the theory of quantum mechanics. *Proc. Roy. Soc. A* **112**, 661–677 (1926). doi: 10.1098/rspa.1926.0133.

[6] Pauli, W. On the connexion between the completion of electron groups in an atom with the complex structure of spectra. *Z. Phys.* **31**, 765 (1925).

[7] Zhirnov, V. V., Cavin, R. K., Hutchby, J. A. & Bourianoff, G. I. Limits to binary logic switch scaling - a gedanken model. *Proc. IEEE* **91**, 1934–1939 (2003). doi: 10.1109/JPROC.2003.818324 .

[8] DiVincenzo, D. P. Quantum computation. *Science* **270**, 255–261 (1926). doi: 10.1126/science.270.5234.255.

[9] Dresselhaus, G. Spin-orbit coupling effects in zinc blende structures. *Phys. Rev.* **100**, 580–586 (1955). doi: 10.1103/PhysRev.100.580.

[10] Bychkov, Y. A. & Rashba, E. I. Oscillatory effect and the magnetic susceptibility of carriers in inversion layers. *J. Phys. C* **17**, 6039–6045 (1984). doi:10.1088/0022-3719/17/33/015.

[11] Pikus, G. E. & Titkov, A. N. *Optical Orientation* (Elsevier Science, Amsterdam, 1984).

[12] D'yakonov, M. I. & Perel, V. I. Spin relaxation of conduction electrons in noncentrosymmetric semiconductors. *Sov. Phys. Solid State* **13**, 3023–3026 (1971).

[13] Elliot, R. J. Theory of the effect of spin-orbit coupling on magnetic resonance in some semiconductors. *Phys. Rev.* **96**, 266–279 (1954). doi: 10.1103/PhysRev.96.266.

[14] Yafet, Y. *Solid State Physics: g Factors and Spin-Lattice Relaxation of Conduction Electrons*, vol. 14 (Academic Press Inc., 1963). doi: 10.1016/S0081-1947(08)60259-3.

[15] Bir, G. L., Aronov, A. G. & Pikus, G. E. Spin relaxation of electrons due to scattering by holes. *Sov. Phys. JETP* **42**, 705–712 (1976).

[16] Kikkawa, J. M. & Awschalom, D. D. Resonant spin amplification in $n$-Type GaAs. *Phys. Rev. Lett.* **80**, 4313–4316 (1998). doi: 10.1103/PhysRevLett.80.4313.

[17] Jiang, L. & Wu, M. W. Control of spin coherence in $n$-type GaAs quantum wells using strain. *Phys. Rev. B* **72**, 033311 (2005). doi: 10.1103/PhysRevB.72.033311.

[18] Balocchi, A. *et al.* Full electrical control of the electron spin relaxation in GaAs quantum wells. *Phys. Rev. Lett.* **107**, 136604 (2011). doi: 10.1103/PhysRevLett.107.136604.

[19] Lampel, G. Nuclear dynamic polarization by optical electronic saturation and optical pumping in semiconductors. *Phys. Rev. Lett.* **20**, 491–493 (1967). doi: 10.1103/PhysRevLett.20.491.

[20] McCamey, D. R., Tol, J. V., Morley, G. W. & Boehme, C. Electronic spin storage in an electronically readable nuclear spin memory with a lifetime $> 100$ seconds. *Science* **330**, 1652–1656 (2010). doi: 10.1126/science.1197931.

[21] Crooker, S. A., Baumberg, J. J., Flack, F., Samarth, N. & Awschalom, D. D. Terahertz spin precession and coherent transfer of angular momenta in magnetic quantum wells. *Phys. Rev. Lett.* **77**, 2814–2817 (1996). doi: 10.1103/PhysRevLett.77.2814.

[22] Hilton, D. J. & Tang, C. L. Optical orientation and femtosecond relaxation of spin-polarized holes in GaAs. *Phys. Rev. Lett.* **89**, 146601 (2002). doi: 10.1103/PhysRevLett.89.146601.

[23] Crooker, S. A., Awschalom, D. D., Baumberg, J. J., Flack, F. & Samarth, N. Optical spin resonance and transverse spin relaxation in magnetic semiconductor quantum wells. *Phys. Rev. B* **56**, 7574–7588 (1997). doi: 10.1103/PhysRevB.56.7574.

[24] Sih, V. *et al.* Mechanical control of spin-orbit splitting in GaAs and $In_{0.04}Ga_{0.96}As$ epilayers. *Phys. Rev. B* **73**, 241316(R) (2006). doi: 10.1103/PhysRevB.73.241316.

[25] Salis, G. *et al.* Electrical control of spin coherence in semiconductor nanostructures. *Nature* **414**, 619–622 (2001). doi: 10.1038/414619a.

[26] Kato, Y., Myers, R. C., Gossard, A. C. & Awschalom, D. D. Coherent spin manipulation without magnetic fields in strained semiconductors. *Nature* **427**, 50–53 (2003). doi:10.1038/nature02202.

[27] Sih, V. *Electrical Manipulation of Spin-orbit Coupling in Semiconductor Heterostructures*. Ph.D. thesis, University of California, Santa Barbara (2006).

[28] Ohno, Y. *et al.* Electrical spin injection in a ferromagnetic semiconductor heterostructure. *Nature* **402**, 790–792 (1999). doi: 10.1038/45509.

[29] Kato, Y. K., Myers, R. C., Gossard, A. C. & Awschalom, D. D. Current-induced spin polarization in strained semiconductors. *Phys. Rev. Lett.* **93**, 176601 (2004). doi: 10.1103/PhysRevLett.93.176601.

[30] Kato, Y., Myers, R. C., Gossard, A. C. & Awschalom, D. D. Observation of the spin hall effect in semiconductors. *Science* **306**, 1910–1913 (2004). doi: 10.1126/science.1105514.

[31] Sih, V. *et al.* Generating spin currents in semiconductors with the spin hall effect. *Phys. Rev. Lett.* **97**, 096605 (2006). doi: 10.1103/PhysRevLett.97.096605.

[32] Binasch, G., Grünberg, P., Saurenbach, F. & Zinn, W. Enhanced magnetoresistance in layered magnetic structures with antiferromagnetic interlayer exchange. *Phys. Rev. B* **39**, 4828–4830 (1989). doi: 10.1103/PhysRevB.39.4828.

[33] Baibich, M. N. *et al.* Giant magnetoresistance of (001)Fe/(001)Cr magnetic superlattices. *Phys. Rev. Lett.* **61**, 2472–2475 (1988). doi: 10.1103/PhysRevLett.61.2472.

[34] Miller, R. C., Kleinman, D. A., Nordland, W. A. & Gossard, A. C. Luminescence studies of optically pumped quantum wells in GaAs-$Al_xGa_{1-x}As$ multilayer structures. *Phys. Rev. B* **22**, 863–871 (1980). doi: 10.1103/PhysRevB.22.863.

[35] Lewis, J. W. *et al.* Time-resolved circular dichroism spectroscopy: experiment, theory, and applications to biological systems. *J. of Phys. Chem.* **96**, 5243–5254 (1992). doi: 10.1021/j100192a016.

[36] Trowbridge, C. J. *et al.* Electron spin polarization-based integrated photonic devices. *Opt. Exp.* **19**, 14845–14851 (2011). doi: 10.1364/OE.19.014845.

[37] Ivchenko, E. L. & Pikus, G. E. New photogalvanic effect in gyrotropic crystals. *JETP Lett.* **27**, 604–607 (1978).

[38] Vorob'ev, L. E. *et al.* Optical activity in tellurium induced by a current. *JETP Lett.* **29**, 441–445 (1979).

[39] Aronov, A. G. & Lyanda-Geller, Y. B. Nuclear electric resonance and orientation of carrier spins by an electric field. *JETP* **50**, 431–434 (1989).

[40] Sih, V. *et al.* Spatial imaging of the spin hall effect and current-induced spin polarization in two-dimensional electron gases. *Nat. Phys.* **1**, 31–35 (2005). doi: 10.1038/nphys009.

[41] Koehl, W. F. *et al.* Current-induced spin polarization in gallium nitride. *Appl. Phys. Lett.* **95**, 072110 (2009). doi: 10.1063/1.3194781.

[42] Stern, N. P. *et al.* Current-induced polarization and the spin hall effect at room temperature. *Phys. Rev. Lett.* **97**, 126603 (2006). doi: 10.1063/1.3194781.

[43] Stepanov, I., Kuhlen, S., Ersfeld, M., Lepsa, M. & Beschoten, B. All-electrical time-resolved spin generation and spin manipulation in n-InGaAs. *Appl. Phys. Lett.* **104**, 062406 (2014). doi: 10.1063/1.4864468.

[44] Koralek, J. D. *et al.* Emergence of the persistent spin helix in semiconductor quantum wells. *Nature Lett.* **458**, 610–614 (2009). doi: 10.1103/PhysRevB.66.245204.

[45] Compton, A. H. The magnetic electron. *J. Franklin Inst.* **192**, 145–155 (1921).

[46] Dirac, P. A. M. The quantum theory of the electron. *Proc. Roy. Soc. (London)* **A117**, 610 (1928).

[47] Melissinos, A. C. & Napolitano, J. *Experiments in Modern Physics* (Academic Press, 2003), 2nd edn.

[48] Abers, E. S. *Quantum Mechanics* (Pearson Education, 2004).

[49] Schrödinger, E. R. J. A. Quantization as an eigenvalue problem. *Ann. Physik* **385**, 437–490 (1926). doi: 10.1002/andp.19263851302.

[50] Zeeman, P. About the influence of a magnetization on the nature of the emitted light by a substance. *Versl. Kon. Akad. Wetensch. Amsterdam* **5**, 242–248 (1896).

[51] Lundstrom, M. *Fundamentals of Carrier Transport* (Cambridge University Press, 2000), 2nd edn.

[52] Thomas, L. H. The motion of the spinning electron. *Nature* **117**, 514 (1926). doi:10.1038/117514a0.

[53] Sakurai, J. J. *Advanced Quantum Mechanics* (Addison Wesley, 1994).

[54] Kramers, H. A. General theory of the paramagnetic rotation in crystals. *Proc. Amsterdamn Acad.* **33**, 959–972 (1930).

[55] Wigner, E. About the operation of time reversal in quantum mechanics. *Nachr. Akad. Ges. Wiss. Gttingen* **31**, 546–559 (1932).

[56] Awschalom, D. D., Samarth, N. & Loss, D. *Semiconductor Spintronics and Quantum Computation* (Springer Verlag, 2002).

[57] Hahn, E. L. Spin echoes. *Phys. Rev.* **80**, 580–594 (1950). doi: 10.1103/PhysRev.80.580.

[58] Brillouin, L. *Wave propagation in periodic structures* (Dover Publications Inc., 1946).

[59] O'Reilly, E. *Quantum Theory of Solids* (CRC Press, 2003).

[60] Yu, P. Y. & Cardona, M. *Fundamentals of Semiconductors: Physics and Materials Properties* (Springer, 2010), 4th edn. doi:10.1007/978-3-642-00710-1.

[61] Singh, J. *Electronic and Optoelectronic Properties of Semiconductor Structures* (Cambridge University Press, 2007).

[62] Ashcroft, N. W. & Mermin, N. D. *Solid State Physics* (Brooks/Col Cengage Learning, 1976).

[63] Vurgaftman, I., Meyer, J. R. & Ram-Mohan, L. R. Band parameters for III-V compound semiconductors and their alloys. *J. Appl. Phys.* **89**, 5815–5875 (2001). doi:10.1063/1.1368156.

[64] Cohen, M. L. & Chelikowsky, J. R. *Electronic Structure and Optical Properties of Semiconductors* (Springer-Verlag, 1989).

[65] Kane, E. O. Energy band structure in p-type germanium and silicon. *J. Phys. Chem. Solids* **1**, 82–99 (1956). doi:10.1016/0022-3697(56)90014-2.

[66] Luttinger, J. M. Quantum theory of cyclotron resonance in semiconductors: General theory. *Phys. Rev.* **102**, 1030–1041 (1956). doi:10.1103/PhysRev.102.1030.

[67] Pfeffer, P. Effect of inversion asymmetry on the conduction subbands in GaAs-$Ga_{1-x}Al_xAs$. *Phys. Rev. B* **59**, 15902–15909 (1998). doi:10.1103/PhysRevB.59.15902.

[68] Datta, S. & Das, B. Electric analog of the electro-optic modulator. *Appl. Phys. Lett.* **56**, 665–667 (1990). doi: 10.1063/1.102730.

[69] Bir, G. L. & Pikus, G. E. *Symmetry and Strain Induced Effects in Semiconductors* (Wiley, New York, 1974).

[70] Dirac, P. A. M. The quantum theory of the emission and absorption of radiation. *Proc. R. Soc. A (London)* **114**, 243–265 (1927). doi: 10.1098/rspa.1927.0039.

[71] Fermi, E. *Nuclear Physics: A Course Given by Enrico Fermi at the University of Chicago* (University of Chicago Press, 1974).

[72] Joyce, W. B. & Dixon, R. W. Analytical approximations for the Fermi energy of an ideal Fermi gas. *Appl. Phys. Lett.* **31**, 354–356 (1977). doi: 10.1063/1.89697.

[73] Fox, M. *Optical Properties of Solids* (Oxford University Press, 2001).

[74] Ridley, B. K. *Quantum Processes in Semiconductors* (Oxford University Press, 2013), 5th edn.

[75] Ikoma, H. Electrical properties of $n$-type and $p$-type gallium arsenide. *J. Phys. Soc. (Japan)* **25**, 1069–1081 (1968). doi: 10.1143/JPSJ.25.1069.

[76] Mirlin, D. N., Sapega, V. F., Karlik, I. Y. & Katilius, R. Hot photoluminescence spectroscopy investigations of L-valley splitting and intervalley scattering in uniaxially stressed gallium arsenide. *Solid State Comm.* **61**, 799–802 (1987). doi: 10.1016/0038-1098(87)90481-9.

[77] Sclar, N. Neutral impurity scattering in semiconductors. *Phys. Rev.* **104**, 1559–1561 (1956).

[78] Dzhioev, R. I. *et al.* Low-temperature spin relaxation in $n$-type GaAs. *Phys. Rev. B* **66**, 245204 (2002). doi: 10.1103/PhysRevB.66.245204.

[79] Kersting, R., Heyman, J. N., Strasser, G. & Unterrainer, K. Coherent plasmons in $n$-doped GaAs. *Phys. Rev. B* **58**, 4553–4559 (1998). doi: 10.1103/PhysRevB.58.4553.

[80] Lundstrom, M., Jeong, C. & Kim, R. *Near-Equilibrium Transport: Fundamentals and Applications* (World Scientific Publishing Company, Inc., 2013).

[81] Huang, K. *Statistical Mechanics* (Wiley, 1987), 2nd edn.

[82] Measurements taken by Jason Stephens while working as a graduate student for Prof. D. D. Awschalom in 2005.

[83] Fabian, J. & Sarma, S. D. Spin relaxation of conduction electrons. *J. Vac. Sci. Technol. B* **17**, 1780–1715 (1999). doi: 10.1116/1.590813.

[84] Boguslawski, P. Electron-electron spin-flip scattering and spin relaxation in III-V and II-VI semiconductors. *Solid State Comm.* **33**, 389–391 (1980). doi: 10.1016/0038-1098(80)91177-1.

[85] Yokoyama, H. & Ujihara, K. (eds.) *Spontaneous Emission and Laser Oscillation in Microcavities* (CRC Press LLC, Boca Raton, FL, USA, 1995).

[86] Coherent, Inc. *Verdi V-8/V-10 Laser Operator's Manual* (2007).

[87] Alfrey, A. J. Simple 1 micron ring laser oscillators pumped by fiber-coupled laser diodes. *IEEE J. Quantum Electron.* **30**, 2350–2355 (1994). doi: 10.1109/3.328590.

[88] Kroemer, H. A proposed class of heterjunction injection lasers. *Proc. IEEE* **51**, 1782–1783 (1963). doi: 10.1109/PROC.1963.2706.

[89] Zelmon, D. E., Lee, J. J., Currin, K. M., Northridge, J. M. & Perlov, D. Revisiting the optical properties of Nd doped yttrium orthovanadate. *Appl. Optics* **49**, 644–647 (2010). doi: 10.1364/AO.49.000644.

[90] Coherent, Inc. *Operator's Manual: The Coherent Mira Model 900-P Laser* (2007).

[91] Hinds Instruments, Inc. *PEM 100 Photoelastic Modulator User Manual* (2006).

[92] Berman, P. R. & Malinovsky, V. S. (eds.) *Principles of Laser Spectroscopy and Quantum Optics* (Princeton University Press, 2011).

[93] Arfken, G. B. & Weber, H. J. *Mathematical Methods for Physicists* (Harcourt Academic Press, 2001), 5th edn.

[94] Kaufmann, B. Polarized photoluminescence of optically oriented electrons in PbTe epitaxial films. *Phys. Rev. B* **30**, 4640–4647 (1984). doi: 10.1103/PhysRevB.30.4640.

[95] Ohno, Y. *et al.* Electrical spin injection in a ferromagnetic semiconductor heterostructure. *Nature* **402**, 790–792 (1999). doi: 10.1038/45509.

[96] Faraday, M. Experimental researches in electricity. Nineteenth Series. *Philos. Trans. R. Soc. London* **136**, 1–20 (1846). http://www.jstor.org/stable/108303.

[97] Sajeev, J., Soukoulis, C., Cohen, M. H. & Economou, E. N. Theory of electron band tails and the Urbach optical-absorption edge. *Phys. Rev. Lett.* **57**, 1777–1780 (1986). doi: 10.1103/PhysRevLett.57.1777.

[98] Hecht, E. *Optics* (Addison-Wesley Longman, Inc., 2002).

[99] Guenther, R. D. *Modern Optics* (John Wiley and Sons, Inc., 1990).

[100] Kato, Y. *Electrical Manipulation of Electron Spin Coherence in Nonmagnetic Semiconductors*. Ph.D. thesis, University of California, Santa Barbara (2005).

[101] Ametek Advanced Measurement Technology, Inc. *Model 7265 DSP Lock-in Amplifier Instruction Manual* (2002).

[102] Oppenheim, A. V., Schafer, R. W. & Buck, J. R. *Discrete-time signal processing* (Prentice Hall, 1999).

[103] Zawadzki, W. *et al.* Temperature dependence of the electron spin $g$ factor in GaAs. *Phys. Rev. B* **78**, 245203 (2008). doi: 10.1103/PhysRevB.78.245203.

[104] Oestreich, M. & Rühle, W. W. Temperature dependence of the electron landé $g$ factor in GaAs. *Phys. Rev. Lett.* **74**, 2315–2318 (1995). doi: 10.1103/PhysRevLett.74.2315.

[105] Oestreich, M. *et al.* Temperature and density dependence of the electron landé $g$ factor in semiconductors. *Phys. Rev. B* **53**, 7911–7916 (1996). doi: 10.1103/PhysRevB.53.7911.

[106] Hohage, P. E., Bacher, G., Reuter, D. & Wieck, A. D. Coherent spin oscillation in bulk GaAs at room temperature. *Appl. Phys. Lett.* **89**, 231101 (2006). doi: 10.1063/1.2398909.

[107] Aronov, A. G., Pikus, G. E. & Titkov, A. N. Spin relaxation of conduction electrons in $p$-type III-V compounds. *Sov. Phys. JETP* **57**, 680–687 (1983). doi: 10.1103/PhysRevLett.80.4313.

[108] Glazov, M. M. & Ivchenko, E. L. Resonant spin amplification in nanostructures with anisotropic spin relaxation and spread of the electronic $g$ factor. *Semiconductors* **42**, 951–957 (2008). doi: 10.1134/S1063782608080137.

[109] Pursley, B., Luengo-Kovac, M., Vardar, G., Goldman, R. S. & Sih, V. Spin lifetime measurements in GaAsBi thin films. *Appl. Phys. Lett.* **102**, 022420 (2013). doi: 10.1063/1.4781415.

[110] Wolf, S. A. *et al.* Spintronics: A spin-based electronics vision for the future. *Science* **294**, 1488–1495 (2001). doi: 10.1126/science.1065389.

[111] Negulyaev, N. N., Stepanyuk, V. S., Hergert, W. & Kirschner, J. Electric field as a switching tool for magnetic states in atomic-scale nanostructures. *Phys. Rev. Lett.* **106**, 037202 (2011). doi: 10.1103/PhysRevLett.106.037202.

[112] Engels, G., Lange, J., Schäpers, T. & Lüth, H. Experimental and theoretical approach to spin splitting in modulation-doped $In_xGa_{1-x}As$/InP quantum wells for B$\rightarrow$ 0. *Phys. Rev. B* **55**, R1958–R1961 (1997). doi: 10.1103/PhysRevB.55.R1958.

[113] Nitta, J., Akazaki, T. & Takayanagi, H. Gate control of spin-orbit interaction in an inverted $In_{0.35}Ga_{0.47}As$ / $In_{0.52}Al_{0.48}As$ heterostructure. *Phys. Rev. Lett* **78**, 1335–1338 (1997). doi: 10.1103/PhysRevLett.78.1335.

[114] Nitta, J., Bergsten, T., Kunihashi, Y. & Kohda, M. Electrical manipulation of spins in the Rashba two dimensional electron gas systems. *J. Appl. Phys.* **105**, 122402 (2009). doi: 10.1063/1.3117232.

[115] Beck, M., Metzner, C., Malzer, S. & Döhler, G. H. Spin lifetimes and strain-controlled spin precession of drifting electrons in GaAs. *Europhys. Lett.* **75**, 597–603 (2006). doi: 10.1209/epl/i2006-10151-4.

[116] Crooker, S. A. & Smith, D. L. Imaging spin flows in semiconductors subject to electric, magnetic, and strain fields. *Phys. Rev. Lett.* **94**, 236601 (2005). doi: 10.1103/PhysRevLett.94.236601.

[117] Meier, L. *et al.* Measurement of Rashba and Dresselhaus spin-orbit magnetic fields. *Nat. Phys.* **3**, 650–654 (2007). doi: 10.1038/nphys675.

[118] Norman, B. M. *et al.* Mapping spin-orbit splitting in strained (In,Ga)As epilayers. *Phys. Rev. B* **82**, 081304(R) (2010). doi: 10.1103/PhysRevB.82.081304.

[119] Norman, B. M., Trowbridge, C. J., Awschalom, D. D. & Sih, V. Current-induced spin polarization in anisotropic spin-orbit fields. *Phys. Rev. Lett.* **112**, 056601 (2014). doi: 10.1103/PhysRevLett.112.056601.

[120] Ghosh, S. *et al.* Electrical control of spin coherence in ZnO. *Appl. Phys. Lett* **92**, 162109 (2008). doi: 10.1063/1.2913049.

[121] Bernevig, B. A. & Zhang, S. Spin-splitting and spin current in strained bulk semiconductors. *Phys. Rev. B* **72**, 115204 (2005). doi: 10.1103/PhysRevB.72.115204.

[122] Freund, L. B. & Nix, W. D. A critical thickness condition for a strained compliant substrate/epitaxial film system. *Appl. Phys. Lett.* **69**, 173–175 (1996). doi: 10.1063/1.117362.

[123] Jackson, J. D. *Classical Electrodynamics* (John Wiley and Sons, Inc., Cambridge, UK, 1999), 3rd edn.

[124] Awschalom, D. D. & Flatté, M. E. Challenges for semiconductor spintronics. *Nat. Phys.* **3**, 153–159 (2007). doi: 10.1038/nphys551.

[125] Chernyshov, A. *et al.* Evidence for reversible control of magnetization in a ferromagnetic material by means of spin–orbit magnetic field. *Nat. Phys.* **5**, 656–659 (2009). doi: 10.1038/nphys1362.

[126] Rashba, E. I. Theory of electrical spin injection: Tunnel contacts as a solution of the conductivity mismatch problem. *Phys. Rev. B* **62**, R16267–R16270 (2000). doi: 10.1103/PhysRevB.62.R16267.

[127] Baranova, N. B., Bogdanov, Y. V. & Zel'dovich, B. Y. New electro-optical and magneto-optical effect in liquids. *Sov. Phys. Usp.* **20**, 870–877 (1977).

[128] Yang, C. L. *et al.* Spectral dependence of spin photocurrent and current-induced spin polarization in an InGaAs/InAlAs two-dimensional electron gas. *Phys. Rev. Lett.* **96**, 186605 (2005). doi: 10.1103/PhysRevLett.96.186605.

[129] Chang, H. J. *et al.* Current and strain-induced spin polarization in InGaN/GaN superlattices. *Phys. Rev. Lett* **98**, 136403 (2007). doi: 10.1103/PhysRevLett.98.136403.

[130] Kuhlen, S. *et al.* Electric field-driven coherent spin reorientation of optically generated electron spin packets in InGaAs. *Phys. Rev. Lett.* **109**, 146603 (2012). doi: 10.1103/PhysRevLett.109.146603.

[131] Aronov, A. G., Lyanda-Geller, Y. B. & Pikus, G. E. Spin polarization of electrons by an electric current. *Sov. Phys. JETP* **73**, 537–541 (1991).

[132] Engel, H. A., Rashba, E. I. & Halperin, B. I. Out-of-plane spin polarization from in-plane electric and magnetic fields. *Phys. Rev. Lett.* **98**, 036602 (2007). doi: 10.1103/PhysRevLett.98.036602.

[133] Trowbridge, C. J., Norman, B. M., Kato, Y. K., Awschalom, D. D. & Sih, V. Dynamic nuclear polarization from current-induced spin polarization. *Phys. Rev. Lett.* (2014). Submitted.

[134] Korenev, V. L. Bulk electron spin polarization generated by the spin Hall current. *Phys. Rev. B* **74**, 041308(R) (2006). doi: 10.1103/PhysRevB.74.041308.

[135] Qi, Y. & Flatté, M. E. Spin gunn effect. *Phys. Rev. Lett.* **96**, 026602 (2006). doi: 10.1103/PhysRevLett.96.026602.

[136] Press, W. H., Teukolsky, S. A., Vetterling, W. T. & Flannery, B. P. *Numerical Recipes* (Cambridge University Press, 2007), 3rd edn.

[137] Crank, J. & Nicolson, P. A practical method for numerical evaluation of solutions of partial differential equations of the heat-conduction type. *Proc. Camb. Phil. Soc.* **43**, 50–67 (1947). doi: 10.1007/BF02127704.

[138] Kutta, M. W. Contribution for the approximate integration of total differential equations. *Z. Math. Phys.* **46**, 435–453 (1901).